Global models of accretion disc around compact objects

Marc Vanden Bossche

THÈSE

Pour obtenir le grade de

DOCTEUR DE L'UNIVERSITÉ GRENOBLE ALPES

École doctorale : PHYS - Physique
Spécialité : Astrophysique et Milieux Dilués
Unité de recherche : Institut de Planetologie et d'Astrophysique de Grenoble

Modèles globaux des disques d'accrétion autour d'objets compacts

Global models of accretion disc around compact objects

Présentée par :

Marc VANDEN BOSSCHE

Direction de thèse :

Geoffroy LESUR DIRECTEUR DE RECHERCHE, CNRS DELEGATION ALPES	Directeur de thèse
Guillaume DUBUS DIRECTEUR DE RECHERCHE, CNRS DELEGATION ALPES	Co-directeur de thèse

Rapporteurs :

HENRIK LATTER
FULL PROFESSOR, UNIVERSITY OF CAMBRIDGE
FABIEN CASSE
PROFESSEUR DES UNIVERSITES, UNIVERSITE PARIS CITE

Thèse soutenue publiquement le **10 juillet 2024**, devant le jury composé de :

GILLES HENRI, PROFESSEUR DES UNIVERSITES, UNIVERSITE GRENOBLE ALPES	Président
HENRIK LATTER, FULL PROFESSOR, UNIVERSITY OF CAMBRIDGE	Rapporteur
FABIEN CASSE, PROFESSEUR DES UNIVERSITES, UNIVERSITE PARIS CITE	Rapporteur
PEGGY VARNIERE, CHARGEE DE RECHERCHE, CNRS ILE-DEFRANCE VILLEJUIF	Examinatrice
JERÔME GUILET, INGENIEUR HDR, CEA CENTRE DE PARIS-SACLAY	Examinateur

GLOBAL MODELS OF ACCRETION DISC AROUND COMPACT OBJECTS

MARC VAN DEN BOSSCHE

Defended on July 10, 2024

ABSTRACT

Dwarf Novæ are eruptive binary systems comprised of a Roche-lobe overflowing solar-type star and an accreting white dwarf. Their recurrence time can be explained by a low-accreting phase called quiescence. During this phase the angular momentum transport parameter is inferred to be $\alpha = 10^{-2}$ by the Disc Instability Model (DIM) to reproduce observations. However, during this phase, the accretion disc is too cold, and too little ionised for the usual accretion driving mechanism, the Magneto-rotational Instability, to sustain turbulence and drive accretion. In this work, I explore two candidate mechanisms to explain the observed accretion during the quiescence phase, with the GPU-accelerated Idefix code. First, I study the accretion driven by spiral shock excited by the tidal potential. I show that the linear perturbative theory fails to predict the spirals wave behaviour in this cold regime. I then show that spiral shocks only achieve angular momentum transport an order of magnitude too low, at best, because these discs are so cold and thin ($H/R \approx 10^{-3}$) during quiescence. In a second part, I explore the possibility that an MHD wind arises and increases the angular momentum transport in low magnetic Reynolds number (Rm ≈ 100) regime. I quantify the efficiency of the arising MHD wind and compare the modelled transport parameter values to values inferred from observations by the DIM. I show that accretion is strongly enhanced by the presence of a magnetic wind, that launches even from a highly resistive disc. In magnetised simulations, a strong disc tilt develops. I examine different scenarii to understand the growth of this tilt.

REMERCIEMENTS

Je tiens ici à remercier toutes les personnes qui m'ont accompagné pendant cette thèse et qui ont participé à la merveilleuse ambiance que j'ai connue pour cette thèse.

D'abord, merci à vous Geoffroy et Guillaume pour ces trois années en votre compagnie. Vous m'avez fait confiance très rapidement pour que je m'ajoute à l'équipe, déjà bien remplie, de l'ERC de Geoffroy. La complémentarité de vos expertises, et parfois de vos curiosités, m'a permis de prendre du recul sur un grand nombre de questions. Je vous remercie pour votre aide du début à la fin, sans jamais renoncer à la rigueur nécessaire et toujours avec bienveillance.

Ensuite, en commençant par ordre chronologique, merci à Nico de m'avoir bien conseillé sur ses directeurs de thèse, puis pour ton aide quand tu es revenu au bercail.

Merci à Étienne, Ileyk et Enzo d'avoir partagé mon bureau. Merci pour toutes ces discussions qui, en fait, ne portaient que rarement sur de la physique !

Merci ensuite Adrien, Clément, Gaylor, John, Jonah qui avez été là les trois ans de ma thèse et que je suis venu quotidiennement embêter dans vos bureaux respectifs. Merci d'avoir écouté mes questions, et merci d'avoir fini par venir en poser à votre tour.

Merci à Myriam et Simon qui avez supporté mes blagues quasiment tous les midis et qui, pour une raison qui m'échappe, reveniez encore et encore. Merci pour vos discussions et pour vos recommandations musicales et littéraires.

Merci à Lucie, Thibault, Léopold, Filip, et tous les autres du bâtiment D, et même à celles et ceux du bâtiment A pour les moments passés ensemble.

Merci à toute l'équipe Sherpas de m'avoir accueilli, et pour toutes les discussions, scientifiques ou non, que j'ai pu avoir avec vous.

Merci à Baptiste, Léo et Magdy d'avoir été là de loin et même parfois de près.

Merci à ma sœur et à mes parents de m'avoir soutenu dans mes projets depuis toujours.

Merci à toutes celles et ceux qui ont passé du temps à m'expliquer les enjeux du moment de leur thèse. Merci à la team ciné de m'avoir attiré dans votre ~~secte~~ groupe. Merci aux joueurs et joueuses de jeu de rôle des deux campagnes et de tous les one-shots. Merci à celles et ceux avec qui j'ai partagé un bon nombre de soirées et d'après-midi jeux. Merci à la team pew-pew. Merci aux groupes de rando et de ski. Merci à toutes celles et ceux que je n'ai pas nommés ici mais qui ont été là ces trois ans. Merci d'avoir fait de ces trois années trois incroyables années.

CONTENTS

I CONTEXT 1

1 INTRODUCTION 3

1.1 First detections of variable stars . . . 3
1.2 Particularities of Dwarf Novæ . . . 4
1.3 Structure of the binary system . . . 13
1.4 Observations of outflows in dwarf novæ . . . 18
1.5 UV and X observations . . . 19
1.6 Summary . . . 21

2 HYDRODYNAMICS AND MHD OF ACCRETION DISCS 23

2.1 Analytical formulation . . . 23
2.2 The Disc Instability Model . . . 33
2.3 Accretion in magnetised discs . . . 39
2.4 State of the art in modelling dwarf novæ beyond the DIM . . . 43
2.5 Conclusion . . . 47

3 FINITE-VOLUME METHODS FOR FLUID DYNAMICS 49

3.1 Discretisation and Riemann solvers . . . 49
3.2 Strengths and limitations . . . 59
3.3 Numerical difficulties . . . 60
3.4 Numerical resources . . . 62

II RESULTS 65

4 SPIRAL SHOCKS IN THIN BINARY DISCS 67

4.1 Adding the secondary star . . . 67
4.2 Analytical derivation of spiral-wave solutions . . . 70
4.3 Collapse of linear theory: On the necessity of numerics . . . 74
4.4 Numerical setup . . . 75
4.5 Reproducing previous works . . . 78
4.6 Eccentric spirals . . . 82
4.7 Spiral transport . . . 90

4.8 Spiral shock heating . . . 95
4.9 Summary and consequences for future works . . . 99

5 MAGNETIC WINDS IN THIN BINARY DISCS 101
5.1 Numerical setup . . . 101
5.2 Magnetic accretion . . . 108
5.3 Disc tilt . . . 117
5.4 Summary . . . 142

III CONCLUSION AND PERSPECTIVES 147

6 CONCLUSION 149

7 PERSPECTIVES 151

IV APPENDIX 155

BIBLIOGRAPHY 157

A STATISTIC ON THE BIBLIOGRAPHY 175

B CARBON FOOTPRINT 181

C RÉSUMÉ EN FRANÇAIS 183
C.1 Introduction . . . 183
C.2 Hydrodynamique et Magnétohydrodynamique des disques d'accrétion . . . 185
C.3 Méthode des volumes finis pour la mécanique des fluides . . . 187
C.4 Chocs spiraux dans les disques minces de systèmes binaire . . . 189
C.5 Disques minces magnétiques dans les systèmes binaires . . . 191
C.6 Conclusion . . . 194
C.7 Perspectives . . . 195

LIST OF FIGURES

Figure 1.1 Historic light curve of SS Cygni. . . . 5
Figure 1.2 Light curve of Z Cam. . . . 7
Figure 1.3 Light curve of V1504 Cyg. . . . 7
Figure 1.4 Formation of a disc in a semi-detached binary system, from Verbunt (1982). . . . 9
Figure 1.5 Spectral evolution from quiescence to maximum of outburst for SS Cygni. . . . 12
Figure 1.6 Concept of eclipse mapping. . . . 14
Figure 1.7 Radial profile of the brightness temperature of Z Cha during outburst. . . . 15
Figure 1.8 Eclipse mapping observation of EX Dra at different times. . . . 16
Figure 1.9 Doppler map of U Gem during outburst. . . . 17
Figure 1.10 Visible and X-rays emission of SS Cyg. . . . 19
Figure 1.11 Visible, EUV and X-rays emission of SS Cyg during one outburst. . . . 20
Figure 1.12 Boundary layer at the interface of the accretion disc and the white dwarf. . . . 20
Figure 2.1 Opacity as a function of density and temperature of the gas 35
Figure 2.2 DIM S-curve. . . . 36
Figure 2.3 Density and temperature versus radius at different times. . . . 37
Figure 2.4 Mock visible light curve obtained with the DIM for two different values of $\dot{M}_{\rm ext}$. Figures taken from Hameury et al. (1998). . . . 38
Figure 2.5 Simplified picture of the MRI mechanism, taken from Lesur (2021). 41
Figure 2.6 Wind launching picture. . . . 42
Figure 2.7 Stability and instability with respect to the MRI in a resistive disc. 44
Figure 3.1 Godunov discretisation in finite volumes. . . . 51
Figure 3.2 Waves structures used by approximate Riemann problem solvers. . . . 53
Figure 3.3 Illustration of the CFL condition. . . . 55
Figure 3.4 Plots show the de-projected relative difference of the density to its azimuthal average for different advection velocities. . . . 63
Figure 3.5 Chequerboard features due to failure of the HLLD solver. . . . 64
Figure 4.1 Paczynski orbits & Roche potential. . . . 69
Figure 4.2 Moduli of W_m, Fourier modes of the tidal potential. . . . 72
Figure 4.3 Analytical theory spiral wavelength. . . . 75
Figure 4.4 Reproduction of three panels of Figure 12 of Ju et al. (2016) with the Idefix code. . . . 80
Figure 4.5 Reproduction of Figure 10 of Ju et al. (2016). . . . 81
Figure 4.6 Comparison of $\alpha_{\rm eff.}$ *vs.* $\alpha_{\rm SS}$ 83
Figure 4.7 Density maps for different simulations with different temperatures. 83
Figure 4.8 Spiral structure in the disc at different temperatures. . . . 85
Figure 4.9 Comparison of the density profile with and without a wave killing zone. . . . 86
Figure 4.10 Density maps for different simulations with different mass ratios and constant temperature. . . . 87
Figure 4.11 Lubow (1991a) eccentricity growth mechanism. . . . 87
Figure 4.12 Pitch angle measurement of spiral waves. . . . 88
Figure 4.13 Pattern speeds of the different modes for several mass ratios. . . . 89
Figure 4.14 Time evolution of α in the disc. . . . 91
Figure 4.15 Measure of α in the disc. . . . 92

Figure 4.16 Departure from the azimuthal density average at different times for the simulation restarted with no companion star. 92
Figure 4.17 Time evolution of α in the disc: comparison runs. 93
Figure 4.18 Time evolution of α with no secondary star. 94
Figure 4.19 Same plot as 4.15 including the high resolution Ma = 550 run. . . . 95
Figure 4.20 Constant opacity cooling temperature evolution. 96
Figure 4.21 Effective temperature at constant radius. 98
Figure 4.22 Constant opacity cooling temperature evolution (DBR) 98
Figure 5.1 Equation of state used in the 3D Ma = 100 simulations. 103
Figure 5.2 Initial profile of the magnetic Reynold number for resistive simulations. 104
Figure 5.3 Illustration of the grid used in the 3D simulations. 104
Figure 5.4 Principle of the grid-coarsening method. 105
Figure 5.5 Initial axisymmetric configuration at the 3D restart. 108
Figure 5.6 Evolution of the vertical and azimuthal average of the density close the midplane. 109
Figure 5.7 Evolution of the vertical magnetic flux through the mid plane. . . . 110
Figure 5.8 Evolution of the β_p in the midplane. 110
Figure 5.9 Dimensionless number characterising the initial axisymmetric state, with added magnetic field. 111
Figure 5.10 Maps of the azimuthal and time average of the density. 112
Figure 5.11 Pressure terms contributing to the vertical structure of the disc at different radii. 113
Figure 5.12 Vertical density profile averaged over 1 binary orbit. 113
Figure 5.13 Effective aspect ratio of the discs, averaged over 1 binary orbit. . . 114
Figure 5.14 Time-averaged accretion rate computed on spherical shells of radius r inside the disc. 115
Figure 5.15 Time-averaged outflow rate computed on spherical shells of radius r inside the disc. 116
Figure 5.16 Time-averaged of the radial matter flux $\langle \rho v_r \rangle_{\varphi,t}$. 116
Figure 5.17 Properties of the non-magnetic simulation. 117
Figure 5.18 Density slice of a snapshot of simulation RB3 at $\varphi \equiv \pi/4[\pi]$. The grey dotted line represents the orbital plane of the binary system. . 118
Figure 5.19 Altitude of the barycentre of a snapshot of simulation RB3. 118
Figure 5.20 Measure and fit of the latitude of the barycentre, from the same snapshot as figure 5.18 and 5.19. 119
Figure 5.21 Time evolution of the tilt parameters for the disc of simulation RB3 at different radii. 120
Figure 5.22 Evolution of local angular momentum components for disc rings, with time. 122
Figure 5.23 Same as figures 5.18 and 5.19 for the non-magnetic simulation HD. . 123
Figure 5.24 Time evolution of the tilt parameters for the disc of the non-magnetic simulation HD at different radii. 124
Figure 5.25 Evolution of local angular momentum components for disc rings, with time for the non-magnetic simulation HD. 125
Figure 5.26 Tilt parameters of the Ma = 50 magnetic simulation. 126
Figure 5.27 Euler angles nutation θ, precession ψ and intrinsic rotation ϕ. . . . 128
Figure 5.28 Potential energy landscape for an uniform ring. 130
Figure 5.29 Potential energy landscape for a non-axisymmetric ring $m = 1$. . . 131
Figure 5.30 Potential energy landscape for a non-axisymmetric ring $m = 2$. . . 132
Figure 5.31 Computed torques of corresponding to the different forces for a snapshot of RB3 at time $t = 14\ T_0$. 134
Figure 5.32 Vertical pressure forces on the disc at for simulation RB3, before the tilt growth. 135

Figure 5.33 Azimuthal average of the toroidal magnetic field for two snapshots of the RB3 simulation. . . . 135
Figure 5.34 First modes of the Fourier transform of vertical pressure forces on the disc for simulation RB3. . . . 136
Figure 5.35 Modified equation of state for the locally isothermal non-magnetic simulations. . . . 137
Figure 5.36 Tilt parameters of the reference simulation NBF. . . . 138
Figure 5.37 Tilt parameters of the simulations WBFw and WBFs. . . . 140
Figure 5.38 Altitude plot of the WBFw simulation and density slice. . . . 141
Figure 5.39 Bending wave propagation in the non-magnetic Ma = 10 simulations. . . . 141
Figure 5.40 Tilt parameters of the reference simulations WBFR2 and WBF100R2. . . . 143
Figure 5.41 Tilt parameters of the simulation IT. . . . 144
Figure 5.42 Tilt parameters of the simulation 50WBF. . . . 144
Figure A.1 Histogram of the publication year of the articles of the Bibliography. 176
Figure A.2 Histogram of the affiliation of the first author of the articles of the Bibliography. . . . 176
Figure A.3 Histogram of the journal of the articles of the Bibliography. . . . 177
Figure A.4 Histogram of the assumed gender of the first authors of the articles of the Bibliography. Non-binary authors are incorrectly assigned a gender for this plot. . . . 178
Figure A.5 Histogram of the assumed gender of the first authors of the articles of the Bibliography as a function of publication year, for recent articles only. Non-binary authors are incorrectly assigned a gender for this plot. . . . 178

LIST OF TABLES

Table 2.1 Typical physical scales of dwarf novæ **binary system**. 24
Table 2.2 Typical physical scales of dwarf novæ **disc** during quiescence and outburst. 24
Table 4.1 List of the isothermal 2D hydro simulations presented in this chapter. The simulations with 'WKZ' have a *Wave Killing Zone* as presented with equation (4.32). 78
Table 4.2 List of the non-isothermal 2D hydro simulations presented in this chapter. 78
Table 5.1 Runs presented in this paper. 106
Table 5.2 List of the non-magnetic 3D simulations presented in this section. . 137
Table B.1 Amount of computing time used for the simulations of this work. . 181
Table B.2 Carbon footprint of professional flight (round trip) taken for this PhD. 181

ACRONYMS AND CONVENTIONS

ACRONYMS

AAVSO American Association of Variable Star Observers

AGN Active Galactic Nucleus

CINES Centre informatique national de l'enseignement supérieur

CFL Courant-Friedrichs-Lewy

CPU Central Processing Unit

CV Cataclysmic Variable

DIM Disc Instability Model

FARGO Fast Advection in Rotating Gasesous Objects

GPU Graphical Processing Unit

GRICAD Grenoble alpes Recherche Infrasturcture de Calcul Intensif et de Données

HLL Harten-Lax-van Leer

HPC High-Performance Computing

IDRIS Institut du développement et des ressources en informatique scientifique

MHD Magneto-hydrodynamics

MRI Magneto-rotational instability

SPH Smoothed Particle Hydrodynamics

WKZ Wave Killing Zone

CONVENTIONS

— $\mathbb{N}$ is the set of all natural integers *including zero*.
— $M_\odot$ is the mass of the sun.

Part I

CONTEXT

1 INTRODUCTION

Contents

1.1 First detections of variable stars . . . 3
1.2 Particularities of Dwarf Novæ . . . 4
1.2.1 Observational characteristics . . . 6
1.2.2 Explaining the luminosity variations . . . 6
1.2.3 Different contributions to the emission . . . 11
1.3 Structure of the binary system . . . 13
1.3.1 Eclipse mapping . . . 13
1.3.2 Doppler tomography . . . 17
1.4 Observations of outflows in dwarf novæ . . . 18
1.4.1 Winds during outburst . . . 18
1.4.2 Winds during quiescence . . . 18
1.4.3 Jets . . . 19
1.5 UV and X observations . . . 19
1.6 Summary . . . 21

Monitoring stars has long been a human pastime. The oldest formal star maps and star registers we have discovered are as old as the oldest written records (Kansas, 2007), dating back to around 3000 BCE. Indeed, knowing the position of stars in the sky is quite handy as their movement is accurately predictable for most of them, and their evolution usually takes place on a timescale of tens of thousands of years. As a matter of fact, the constellations described by the Sumerians or the Vedic Indians are still very much observable today.

This clockwork regularity was already empirically observed back then, and star maps and registers were used to make calendars and to travel by night. In fact, this regularity inspired philosophical and religious traditions as well as the first attempts at empirical models of the skies, like the *musica universalis* of Pythagorean philosophers.

1.1 FIRST DETECTIONS OF VARIABLE STARS

It seems that Chinese astronomers were the first to note a discrepancy in this numbing regularity. During the 14th century BCE, they noted the appearance of a new star in the sky. We also have evidence that ancient Egyptians noticed a star with varying luminosity around 1200 BCE (Jetsu et al., 2013). Such events occurred on other occasions throughout recorded history, namely, amongst other less known events, in 1006 CE, 1054 CE, 1572 CE and 1604 CE. It is after the one of 1572 that the Danish astronomer Tycho Brahe published a book, *De Stella Nova* (1573) (Latin for *On the new star*), compiling observations of the event by contemporaneous astronomers. The event of a new star appearing took the name of a *nova*, the Latin word for *new*. More precisely, most of the observed events I mentioned above are now called *super novæ* because of the tremendous luminosity of the newly appeared star.

Nowadays, stars with varying luminosity are still an ongoing research topic for astronomers and astrophysicists. We call them *variable stars* and we have classified them into a wide range of categories (see for example Levy (2005) for an introduction to variable stars). The luminosity of these stars may vary for a lot of different reasons. The first

reason can be geometry. For example, when two stars form a binary system, it may happen that one star periodically eclipses the other. Some other stars, the *Cepheid variables*, have a changing luminosity because they undergo periodic contraction, changing both their radius and temperature. Another category of variable stars are the *flare variables* which feature strong, but irregular, increases in their luminosity. Finally, the category in which I am interested in this work are *cataclysmic variables*, or CVs for short. These stars are actually binary stars that can have dramatic changes in luminosity, so much so that some of them become visible to the naked eye when they do brighten.

The change in luminosity of cataclysmic variables is due to the interaction between the two stars. In these systems, one of the stars is always a white dwarf while there is no general rule for the second star, usually called the *companion star*. In all cases, the sudden increase in luminosity is caused by matter from the companion star falling onto the white dwarf. We call this process *accretion*, and it may take various forms. For example, in the case of classical novæ, which are a subcategory of cataclysmic variables, a thermonuclear explosion occurs when so much matter from the companion star has fallen onto the white dwarf that the bottom layers of accreted material reach the ignition temperature for thermonuclear reaction.

Cataclysmic variable stars have been long studied, and are now classified in the following categories (see Warner (2003) for example):

Classical novæ are systems with only one observed eruption. The luminosity variations of these systems are between 6 and 19 magnitude, and are the result of thermonuclear explosion on the white dwarf.

Recurrent novæ are previous classical novæ systems that go into outburst at least a second time.

Dwarf novæ are systems that go into regular outbursts with luminosity contrast of 2 to 5 magnitude. Each system has a well-defined outburst pattern, but across all dwarf novæ the time between two outbursts may vary from 10 days to tens of years. These outbursts usually last from 2 to 20 days, correlated with the time between two outbursts. The difference with regular novæ is made from observed spectra. During the outburst of a recurrent nova, material is ejected at high velocities; this is not the case for dwarf novæ and the light curves are very different. An example of typical dwarf novæ visible light emission is shown in figure 1.1.

Nova like are a wide category of cataclysmic variable stars. This category includes all the cataclysmic variables that do not go into outburst, but have similar spectra to that of novæ in ouburst. As such this category most likely includes pre-novæ, systems that have not been detected in outburst yet, and post-novæ, systems that underwent outburst which we never observed.

Magnetic CVs are systems where accretion occurs through magnetised accretion columns onto the white dwarf. Depending on the strength of the magnetic field, the accretion disc may be partially or totally disrupted. The two biggest subclasses of magnetic CVs are *polars* with no accretion disc signature, and *intermediate polars* with a truncated accretion disc. The suppression or truncation of the accretion disc is attributed to a strong magnetic field of the white dwarf. Polars are estimated to have magnetic field of $B \geq 1000$ T and intermediate polar $B \geq 100$ T. Magnetic CVs are sometimes included in the nova-like category.

1.2 PARTICULARITIES OF DWARF NOVÆ

In the present work, I am particularly interested in dwarf novæ systems, and I will restrict the discussion to these systems. They were first observed by Hind (1856) who thought he was witnessing a regular nova, but he noticed that it faded away only a few days later. This star was observed again three months later by Pogson, suggesting again a different behaviour than a regular nova. Pogson's observations were later compiled

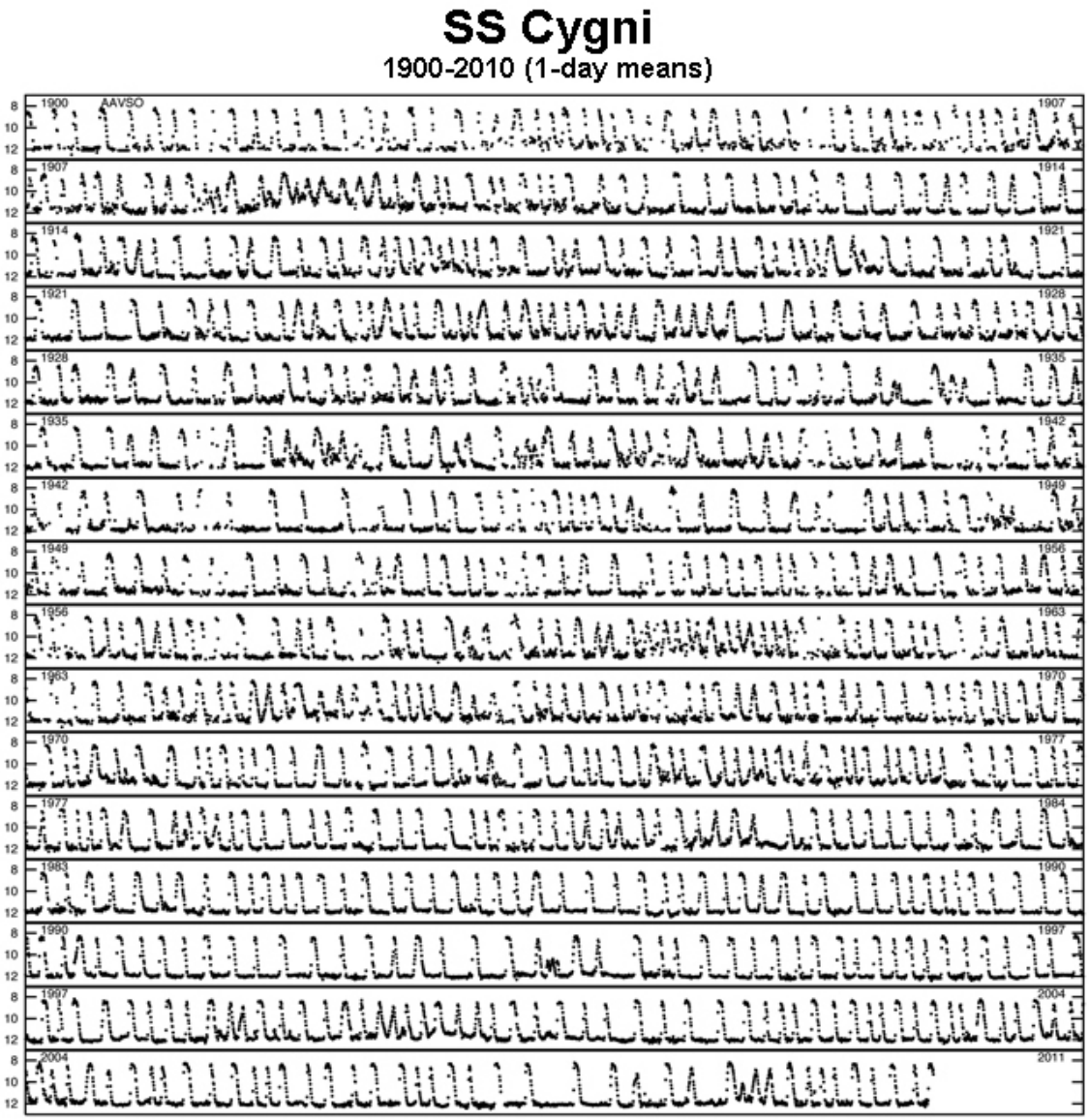

Figure 1.1 – Historic light curve of SS Cygni, a typical dwarf novæ system. Data compiled by the AAVSO, figure from their website https://www.aavso.org/vsots_sscyg.

by Turner (1906). This star, U Geminorum (U Gem), is now the prototypical dwarf nova system.

1.2.1 *Observational characteristics*

These systems featuring regular outbursts are now classified into three subcategories. These categories correspond to three general luminosity behaviours. Here we only consider the behaviour of their visible luminosity. The names of these categories are taken from the name of the prototypical system with this behaviour (Warner, 2003).

Z Cam star feature standstills at about 0.7 magnitude below their maximum brightness. During these standstills that can last days to years, there is no outburst. An example of the light curve of Z Cam is plotted on figure 1.2. The standstill after one of the outbursts is clearly identifiable.

SU UMa feature occasional *superoutbursts*. These superoutbursts are brighter than regular outbursts and are about five times as long. Figure 1.3 shows the lightcurve of V1505 Cyg, an example of SU UMa system. On this figure, one can recognise thirteen regular, short, outbursts and three superoutburts, lasting for much longer. During these superoutbursts, SU UMa systems also feature a lower-amplitude higher-frequency luminosity variation. These short periodic increases of luminosity during the superoutbursts are called *superhumps* and were first described by Vogt (1974).

U Gem dwarf novæ are all the other dwarf novæ. They typically outburst every month for about a week, but there can be strong variations within this class. On figure 1.1 is plotted the historical lightcurve of SS Cygni. This system is a U Gem type dwarf nova that has been continuously observed since Wells (1896). This system is bright enough to be observed by amateur astronomers, as a matter of fact, the plotted historic lightcurve is taken from the American Association of Variable Star Observers (AAVSO).

In this work, I will focus on describing U Gem dwarf novæ, and I will now discuss only them for the remainder of this introduction. These systems feature only two luminosity states differing by around 4 magnitudes; they can clearly identify on figure 1.1. The low luminosity state is called the *quiescence* phase, and the bright phase corresponds to the periodic *outbursts*. First, I will present the observational characteristics of this type of system. Then, I will discuss the proposed physical mechanisms to explain the observations. Chapter 2 presents a more in-depth theoretical lay of the land.

1.2.2 *Explaining the luminosity variations*

Since the 1920s, the spectral behaviour of cataclysmic variable stars was a puzzle for astronomers. Joy (1954) used spectra of AE Aquarii to show that this cataclysmic variable star was actually a binary star. They then applied a similar method to the dwarf nova SS Cygni to show that this star also was a binary star (Joy, 1956). Together with Walker (1954, 1956)'s works on DQ Her, these works led Kraft (1962) to speculate that 'that all cataclysmic variables might be binary systems'. They found that the systems they studied were composed of a *blue* (hot) component and a *red* (cold) component, and are of short orbital period, that is less 10 hours. They suggest that the blue stars may be white dwarfs. They observe that the red stars have a spectrum consistent with a 1 $M_\odot$ mass, but appear underluminous for their mass. They propose that the red stars overflow their Roche lobes and that the overflowing material forms a ring or a disc around the white dwarf. Nowadays, this binary system model is widely accepted, see for example see review by Ritter (2008) and Zorotovic and Schreiber (2020).

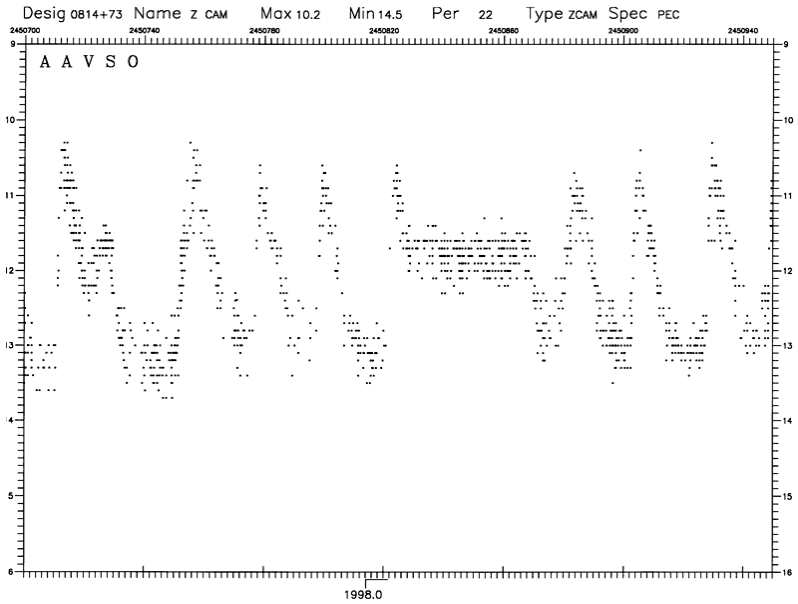

Figure 1.2 – Light curve of Z Cam, with a typical standstill. Figure from the AAVSO website https://www.aavso.org/vsots_zcam.

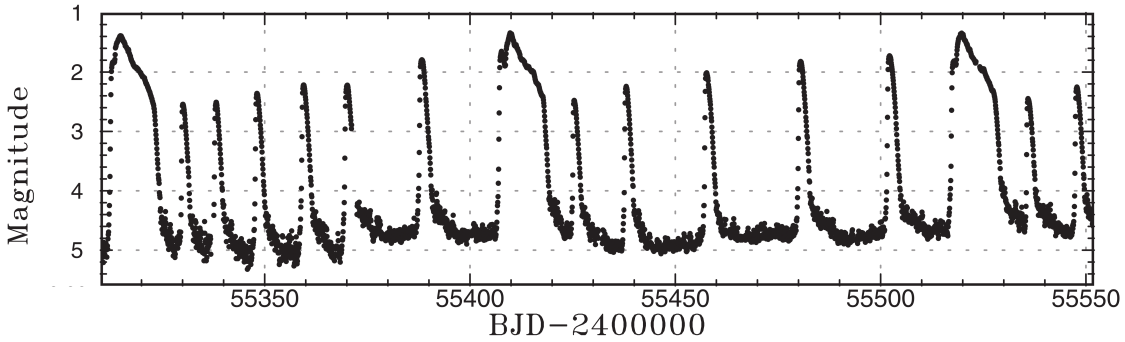

Figure 1.3 – Light curve of V1504 Cyg, a typical SU UMa system with long superoutbursts (here three). Figure from Osaki and Kato (2013).

1.2.2.1 *Roche lobe over flow: why do we think that ? How can it happen ?*

These binary systems where one of the components overflows from its Roche lobe are called *semi-detached* binaries. To obtain such systems from an initially wide binary system with a solar-type star and a white dwarf, there are two possible paths. One possibility is that the binary spirals in down to a separation where the solar-type star is larger than its shrinking Roche lobe. For the binary system to spiral in, some of its angular momentum must be expelled. This can occur through the emission of gravitational waves (Kraft et al., 1962) or from magnetic braking (Verbunt and Zwaan, 1981; Mestel and Spruit, 1987), *i.e.* from the magnetised wind of the stellar companion that is tidally locked to the white dwarf. The typical angular momentum loss timescale is estimated by these authors to be 10^8 years.

The other scenario that can produce a semi-detached binary is the expansion of the secondary star. The timescale of this growth is given by the nuclear evolution timescale of the star. For main sequence stars, this time is typically larger than one billion years. While possible, this second mechanism is less likely to produce cataclysmic variables because the angular momentum loss in a binary system is usually faster than stellar evolution timescale (Ritter, 2008).

The presence of a matter disc around the white dwarf is a direct consequence of the Roche lobe overflow. Its formation is summarised in figure 1.4. The overflowing matter circularises in a ring around the white dwarf. This ring then radially spreads: some matter loses its angular momentum and falls at lower radii, but the total angular momentum is conserved and the disc also spreads at larger radii. The point where the matter flux from the secondary star hits the disc is the *hot spot*. There, the disc is heated as some of the kinetic energy of the infalling matter is released in shock heating with the disc. This hot spot was initially thought to be on the surface of the white dwarf by Krzeminski (1965). Smak (1971) and Warner and Nather (1971) showed concomitantly that this bright spot was in fact in the outer regions of the disc.

1.2.2.2 *Which component is at the origin of the outburst ?*

The discovery that dwarf novæ were binary systems opened new possibilities to explain the recurrent increases of luminosity. The first interpretations of spectral evolution proposed that the white dwarf was the 'seat of the eruptions' (Zuckermann, 1961; Kraft, 1963). This mechanism relies on thermonuclear explosions at the surface of the white dwarf similar to novæ explosions. This model was not further explored when it appeared unlikely that it could produce short recurrence time between two outbursts (Osaki, 1974).

This interpretation was soon contested in favour of an explanation based on variations of the companion star (Krzeminski, 1964, 1965; Smak, 1969). One of their arguments that favoured an origin of the outbursts in the companion is the absence of an expanding shell like in other systems featuring novæ explosions. Paczyński (1965) and Bath (1969, 1972) proposed an instability mechanism of the outer layer of the companion star to explain the recurrent outbursts. They proposed that the outer convective layers of companion star pulsate. During a pulsating timescale, the star expands beyond its Roche lobe and produces an unstable outflow. That is, matter is removed from the outer layers of the companion star at a fast enough rate so that the expansion of the star due to this mass reduction is greater than the corresponding reduction in Roche lobe size. With this model, they were able to reproduce the rapid increases in luminosity of dwarf novæ. The recurrence time of the outburst is not well explained by this model as it mainly depends on the pulsating timescale of the companion star.

Osaki (1970) proposed another model where the companion star was at the origin of the outburst. He rules out any dynamical origin in the outburst because the thermal

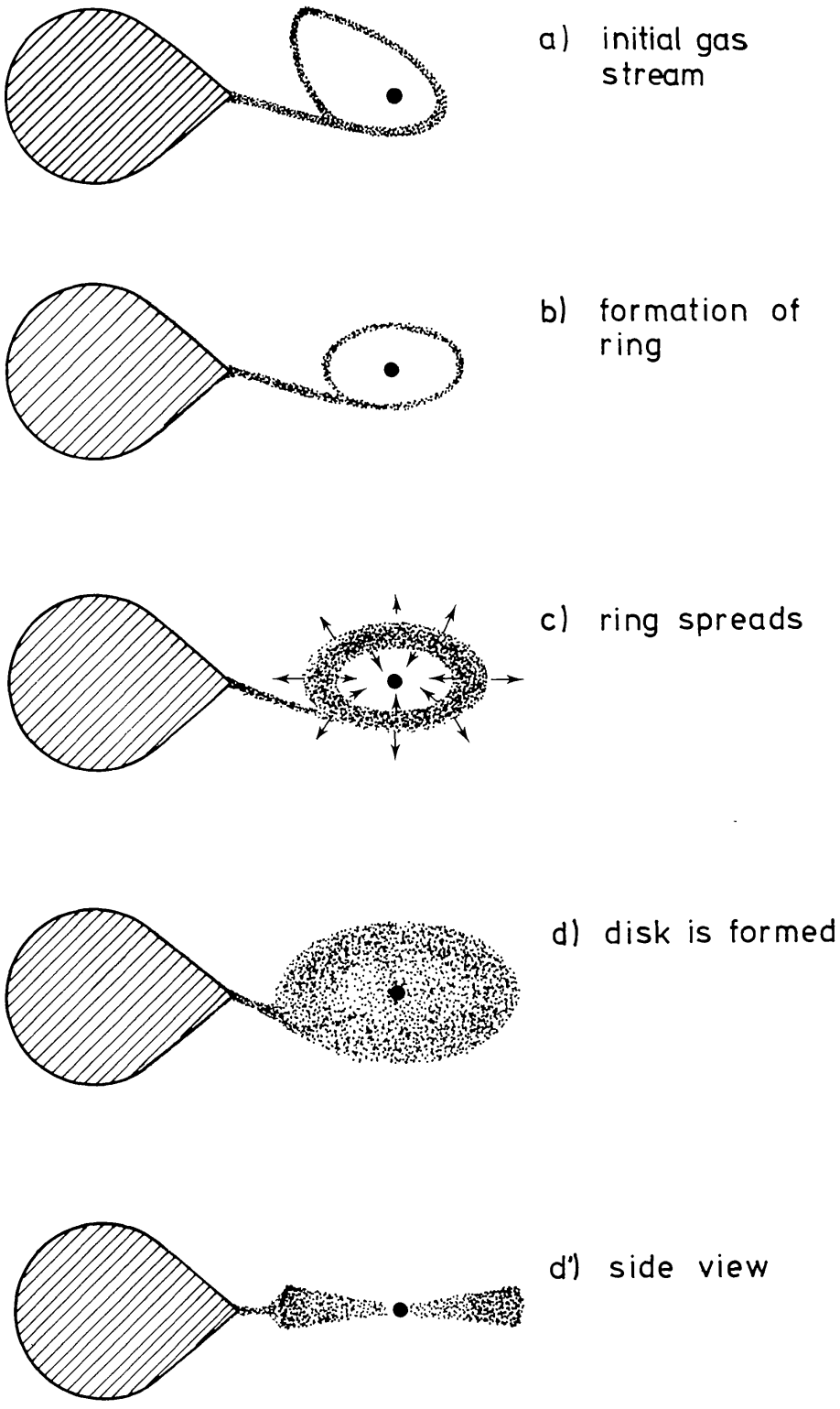

Figure 1.4 – Formation of a disc in a semi-detached binary system, from Verbunt (1982).

and nuclear timescales of solar-type stars are much longer than the recurrence times of dwarf novæ. In his scenario, he postulates that the outburst originates in a return to some equilibrium: When the companion star overflows its Roche lobe, the shear flow turbulence resulting from the mass loss regulates the star size as it temporarily increases energy transport. Consequently, the outburst corresponds to when the star is overflowing its Roche lobe, and the quiescence phase when not. With this model, Osaki (1970) was able to explain the short recurrence times of dwarf novæ. However, he could not produce outbursts with a strong enough luminosity increase.

Following the first accretion disc model for X-Ray Binaries (Pringle and Rees, 1972; Davidson and Ostriker, 1973; Lamb et al., 1973; Shakura and Sunyaev, 1973), Osaki (1974) proposed that a similar mechanism could explain the luminosity variation of dwarf novæ. He proposed that the mass flow from the companion star was constant, but that matter piling up in a ring around the white dwarf could undergo 'some kind of instability' and 'fall onto the white dwarf with a shorter timescale than that of piling up, resulting in sudden release of gravitational energy'. Our current understanding is now in line with this later model.

1.2.2.3 *Observed luminosity origin*

Like in the other types of accreting systems, the observed luminosity mostly originates in the release of gravitational potential energy of infalling matter onto the accreting object. In the case of dwarf novæ, this matter accretes through an *accretion disc* as first suggested by Kraft (1962), and eventually falls onto a white dwarf.

The matter from this disc slowly loses angular momentum and falls to lower radii eventually reaching the white dwarf surface. In a first approximation, the light we observe corresponds to the amount of potential energy lost by the infalling material. It can be simply evaluated, per unit mass, as $e = \Psi(r_{\mathrm{WD}}) - \Psi(r_{L_1})$, where Ψ is the potential including gravitational energy and rotation energy, and r_{WD} and r_{L_1} are the radii of the white dwarf and of the first Lagrange point of the binary system respectively. In these systems, the mass of the companion star is less than the mass of the white dwarf, and the Lagrange point is always such that $r_{\mathrm{WD}} \ll r_{L_1}$, and close to the white dwarf, other contribution to the gravitational potential, such as the secondary star, are negligible compared to the potential of the white dwarf. As a consequence, the potential energy released by the infalling matter, per unit mass, is

$$e \approx \frac{GM_{\mathrm{WD}}}{r_{\mathrm{WD}}} \tag{1.1}$$

which yields $e \approx 2 \times 10^{-4}\ c^2$ for a white dwarf of 1 $M_\odot$. The energy released by unit mass is only slightly less than the energy released by fusion reactions: for instance, Deuterium fusion D + D $\rightarrow$ He fusion releases $e_{\mathrm{fus}} \approx 0.006\ c^2$. In the case of accretion onto neutron stars or black holes, the energy released through accretion even surpasses the energy released by fusion reactions.

This estimate shows us the total (time-integrated) amount of energy released per unit mass of infalling matter. The emitted luminosity L, *i.e.* the amount of energy radiated away per unit time, depends on the rate at which matter is accreted onto the white dwarf.

$$L \approx \frac{GM_{\mathrm{WD}}}{r_{\mathrm{WD}}} \dot{M}_{\mathrm{WD}} \tag{1.2}$$

where $\dot{M}_{\mathrm{WD}}$ is the *accretion rate*, that is the amount of mass falling onto the white dwarf per unit time. For an axisymmetric disc of height H, this rate is $\dot{M} = -2\pi r_{\mathrm{WD}} H \rho v_R$ with

v_R the radial velocity of the accretion disc fluid, and ρ its density, whit the white dwarf centred in $r = 0$.

Osaki (1974)'s model was able to explain from basic arguments the fact that the observed luminosity was indeed a consequence of accretion. His idea was that after some time in quiescence, the matter accumulated in the accretion disc would be rapidly accreted onto the white dwarf. This can be more formally written as

$$\dot{M}_{\text{comp}} \tau_{\text{rec}} = \dot{M}_{\text{outburst}} \tau_{\text{outburst}} \tag{1.3}$$

where τ_{rec} the time between two outbursts and τ_{outburst} the duration of an outburst, and $\dot{M}_{\text{comp}}$ is the matter flow rate coming from the overflowing companion, and $\dot{M}_{\text{outburst}}$ is the accretion rate onto the white dwarf during an outburst. This equation is deducted by the conservation of mass. The left-hand side is the total mass provided by the companion in a recurrence time; the right-hand side is the total mass accreted onto the white dwarf during an outburst. If the only way to remove matter from the disc is for it to fall onto the white dwarf, we obtain this equation.

He then estimates the companion accretion rate with the luminosity of the hot spot, with

$$L_{\text{hot spot}} \approx \frac{G M_{\text{WD}}}{r_{\text{out}}} \dot{M}_{\text{comp}} \tag{1.4}$$

where r_{out} is the outer radius of the disc, where the hot spot is located. The accretion rate is not known, but their ratio corresponds to the ratio of the two characteristic times, hence the ratio of the luminosity during and outburst and the luminosity of the hot spot is

$$\frac{L_{\text{outburst}}}{L_{\text{hot spot}}} = \frac{r_{\text{out}}}{r_{\text{WD}}} \frac{\tau_{\text{rec}}}{\tau_{\text{outburst}}}. \tag{1.5}$$

By estimating $L_{\text{hot spot}}$ as one-half of $L_{\text{quiescence}}$, using a typical value of $r_{\text{WD}} = 5 \times 10^6$ m and $r_{\text{out}} = 10^8$ m, he obtained

$$\frac{L_{\text{outburst}}}{L_{\text{quiescence}}} \approx 160 \tag{1.6}$$

which matches the observation of dwarf novæ systems. The conclusion of this work is that an intermittent accretion through the disc onto the white dwarf is able to explain the change in luminosity of dwarf novæ. However, Osaki (1974) did not propose any instability mechanism that could explain this intermittent accretion. At the beginning of the 1980s, a model was proposed to explain this instability-like behaviour. This model is the Disc Instability Model, and is presented in details in section 2.2.

1.2.3 *Different contributions to the emission*

The emission described above accounts for most of the energy released through accretion. However, it is not the only emission channel in dwarf novæ. Let me rapidly review the different observable contributions of dwarf novæ systems.

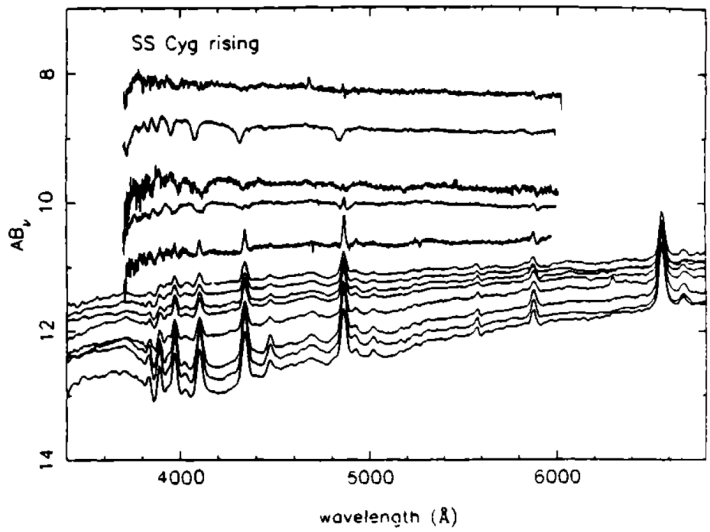

Figure 1.5 – Spectral evolution from quiescence (bottom spectrum) to maximum of outburst (top spectrum) for SS Cygni. Figure from Horne (1991).

Most of the radiation emitted by dwarf novæ accretion disc originates in the accretion disc. Local viscous or viscous-like heating releases the potential energy of matter and is radiated away. The simplest picture is to think of the accretion disc as a multi-temperature black body. Different radii have different viscous heating rates and thus radiate different amounts of energy, at different frequencies. In this picture, inner regions of the disc release more energy, being at higher temperature. They emit at shorter wavelengths than the outer regions of the disc. A method to probe the disc radial temperature profile is discussed in the following.

Wood et al. (1986) separated the relative optical contributions of the different components of the accreting system for Z Cha. During quiescence, the disc accounts for about 50% of the emitted flux, the hot spot contributes to close to 30% and the white dwarf to 20% of the luminosity. During outburst, the disc luminosity is so enhanced that the other contributions are negligible in comparison.

Additionally, the different elements of the gas, or rather plasma, or the accretion disc will also contribute to the emission through their atomic lines. Spectral lines provide precious information on the composition, temperature and density of the emitting region. First of all, they prove that the elements corresponding to the emission lines are present in the disc. Examples of spectra of SS Cyg are shown in figure 1.5. There, we see spectra at different epochs of the quiescence–outburst cycle. During the outburst phase, absorption lines are observed, whereas during quiescence emissions lines are observed because of a change in the temperature stratification and optical thickness of the emission region. The presence of atomic lines allows us to compare with the usually assumed solar composition of ≈70% Hydrogen, ≈28% Helium and ≈2% of heavier elements (in number density, see Grevesse and Sauval (1998) for example). Williams and Ferguson (1982) were the first to show a deviation from this composition. They showed that several CV systems they observed featured H I and He I lines that required an unexpectedly high Helium abundance: He/H $\gtrsim$ 100 in the disc. Done and Osborne (1997) showed with X-ray spectroscopy that the dwarf nova SS Cyg appeared to have a lower than expected abundance of heavy elements. More recently, Harrison (2016) showed that for the forty-one cataclysmic variables they observed, they found a subsolar metallicity composition of the companion stars, as well as subsolar hydrogen fraction. With near-infrared spectroscopy, Harrison and Marra (2017) note a small $^{12}C/^{13}C$ abundance ratio in the donor star of three cataclysmic variables. Together with recent studies (Godon and Sion, 2023; Yamaguchi et al., 2023), these results suggest that the companion star

is semi-detached binary systems may be evolved stars. This means that the formation channel of cataclysmic variable binaries may need to be revisited.

1.3 STRUCTURE OF THE BINARY SYSTEM

As detailed above, it is well established that dwarf novæ are binary systems composed of an accreting white dwarf surrounded by a disc which is fed by a Roche lobe overflowing-solar-type companion star. It is however possible to have a finer description of the structure of the systems thanks to several observational methods.

1.3.1 *Eclipse mapping*

This method was originally introduced by Horne (1985) for eclipsing systems, *i.e.* systems that are seen from a high enough inclination that the companion star periodically occults part of the disc and white dwarf component. See Baptista (2016) for a recent review.

This method relies on the fact that at different orbital phases, the companion star will hide different parts of the system. This method enables us to probe the structure of the accretion disc as different regions may emit different amounts of light.

A simulation of eclipse mapping observation is shown on figure 1.6. The right column shows a disc with a non-uniform emission pattern, represented by the colour. The occultation of the disc by the companion star is shown as an additional black region over the disc. This way, only the visible regions of the disc are coloured. This occulted region has a parabola shape. Its size depends on the size of the companion star, *i.e.* the mass ratio $q = M_s/M_{WD}$ of the binary system, and on the inclination under which the system is seen from Earth.

In practice, eclipse mapping observations work by finding a disc structure that is able to reproduce the observed light curve. This method assumes that the disc is razor-thin, and neglects its vertical extent to produce a two-dimensional structure. However, such a structure cannot be completely determined by a one-dimensional light curve. The remaining free parameters are selected among possible values using a Maximum Entropy Method.

Eclipse mapping produced a series of important results in the study of eclipsing cataclysmic variables. It was possible to show that the disc extends to approximately half the distance to the first Lagrange point in a variety of systems. Horne and Stiening (1985) showed it for the nova-like RW Tri, and Horne and Cook (1985) for the dwarf nova Z Cam during outburst.

Smak (1984) suggested that the disc size varies between the quiescence and outburst phases, with a larger disc during the outburst than during quiescence. This was later confirmed by the comparison of Horne and Cook (1985) who found $r_{out} \approx 0.6 r_{L_1}$ during outburst and Wood et al. (1986) who found $r_{out} \approx 0.37 r_{L_1}$ during the following quiescence of Z Cam.

These results were generalised to all dwarf novæ by followings work (Patterson, 1981; Wood et al., 1989a; Wood et al., 1989b; Rutten et al., 1992a,b; Baptista and Catalán, 2001; Vrielmann et al., 2002; Vrielmann and Offutt, 2003; Shafter and Misselt, 2006; Baptista et al., 2007). They confirmed the trend that, outbursting discs are larger that quiescent discs, even for the same system, between 25% to 70% of the distance to the first Lagrange point. They also noted that the measured size of the disc was dependent on the observation wavelength; discs appear larger at longer wavelengths because the outer discs are colder than the inner regions.

These size measurements are key to understanding the physics of these discs, for instance, they help constrain theoretical models of the truncation of the disc, like those

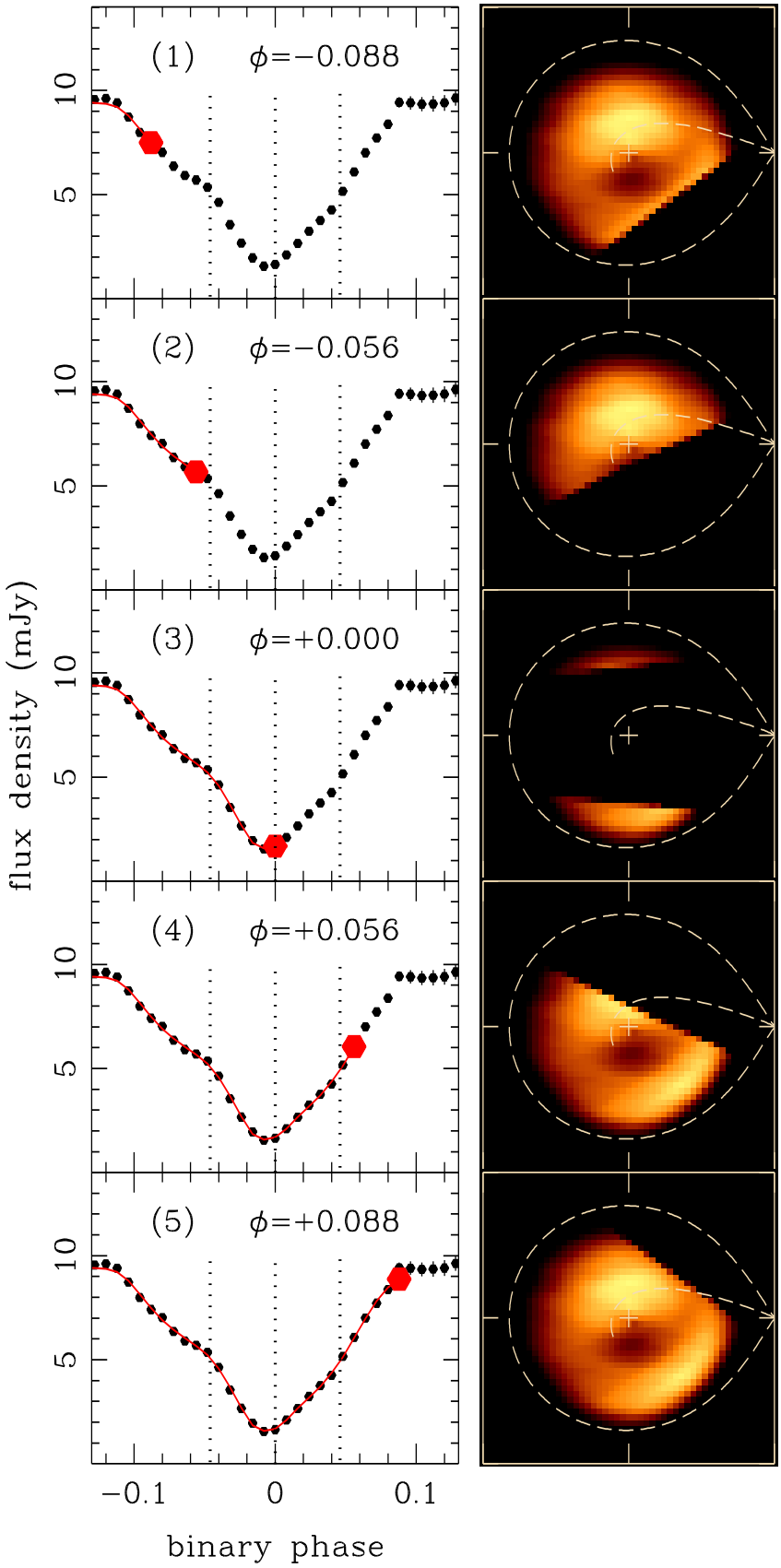

Figure 1.6 – Illustration of the concept of eclipse mapping with $q = 0.5$ and inclination of 81°. **Left:** Simulated observed light curve at different binary phases ϕ. The red hexagon shows the current phase. **Right:** Disc in false black body colour, the region of the disc occulted by the eclipsing companion is blackened. The yellow dashed lines show the Roche lobe and the ballistic trajectory of the mass flux from the companion star. The binary rotation is counter-clockwise. Figure from Baptista (2016).

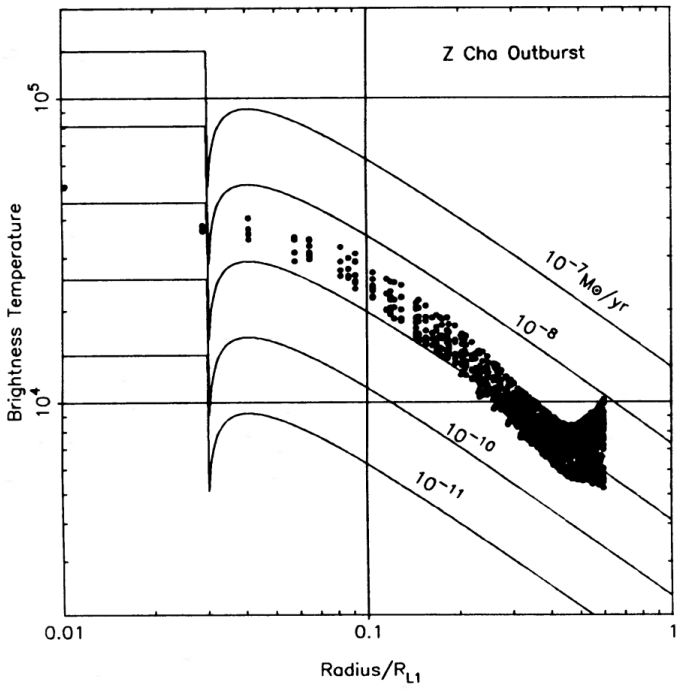

Figure 1.7 – Radial profile of the brightness temperature of Z Cha during outburst. The solid lines show the theoretical model (1.7) for different values of the accretion rate. Figure from Horne and Cook (1985).

discussed in chapter 2. The change in size with luminosity is also an important result as it can be easily compared to theoretical models too. For instance, a disc with high angular momentum transport will strongly accrete and also radially expand.

Additionally, eclipse mapping allows for a fine study of the structure of the bulk of the accretion disc and to derive properties of the accretion flow from it. For example, the radial profile of the accretion rate can be estimated from the observed brightness temperature. To do so, one compares the radial brightness temperature profile to theoretical estimates of this quantity. Assuming a steady disc with an optically thick, black-body emission due to viscous heating, Shakura and Sunyaev (1973) give

$$\sigma T_{\rm eff}^4 = \frac{3}{8\pi}\dot{M}\frac{GM_{\rm WD}}{r^3}\left[1-\left(\frac{r_{\rm WD}}{r}\right)^{1/2}\right] \tag{1.7}$$

where $T_{\rm eff}$ is the effective temperature, *i.e.* disc surface temperature, at radius r, and σ is Stefan's constant. $T_{\rm eff}$ and the mass of the white dwarf are deduced from observations, its radius is constrained by the white dwarf equation of state. An example of the estimation of the accretion rate in the disc of outbursting Z Cha is shown on figure 1.7. There, we see that the data is well fitted by the theoretical model for a steady viscous disc. We see that the accretion rate in this system is approximately $10^{-9} M_\odot/\mathrm{yr}$ during this outburst. For dwarf novæ, the typical accretion rate range from 10^{-14} $M_\odot/\mathrm{yr}$ to 10^{-10} $M_\odot/\mathrm{yr}$ during quiescence, and are typically $10^{-9} - 10^{-8}$ $M_\odot/\mathrm{yr}$ during outburst.

This study of the temperature structure of the disc can be conducted at different times during the outburst – quiescence cycle and provides information on where in the disc the outburst is first triggered. Figure 1.8 shows the evolution of the disc temperature during the whole cycle for the dwarf nova EX Dra. Baptista and Catalán (2001) observed with this technique the propagation of heating and cooling fronts in the accretion disc related to the beginning of the outburst and the return to quiescence. More recently, Court et al. (2020) showed that for this system, the outbursts seem to be consistently triggered in

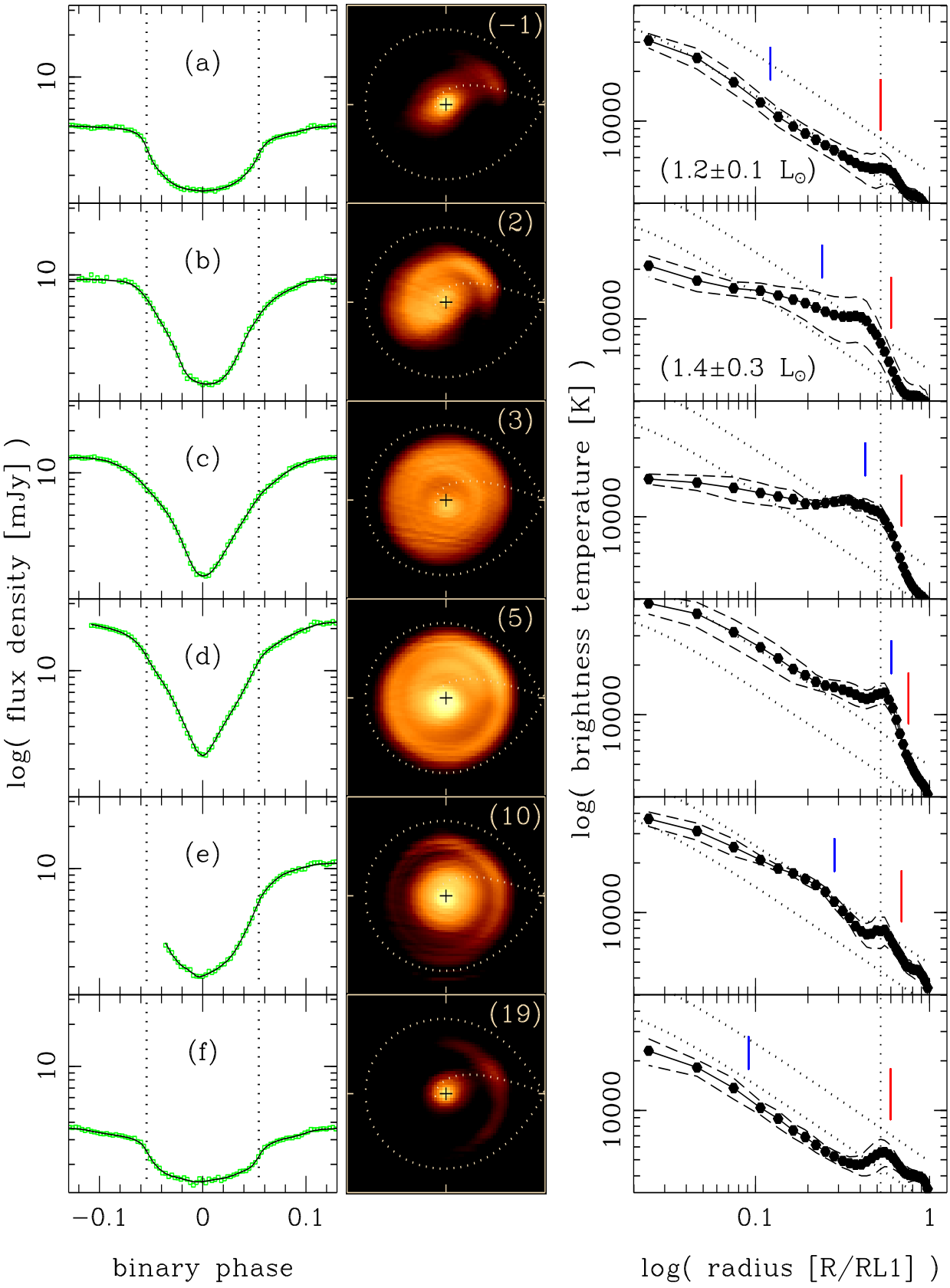

Figure 1.8 – Eclipse mapping observation of EX Dra at different times. **(a)** quiescence. **(b)** early rise. **(c)** late rise. **(d)** maximum of the outburst. **(e)** early decline. **(f)** late decline. **Left:** eclipse mapping observation data (green boxes) and model (solid line) **Middle:** Reconstructed eclipse maps, brightness temperature in false blackbody colour. **Right:** Azimuthal average of the brightness temperature. Figure from Baptista (2016).

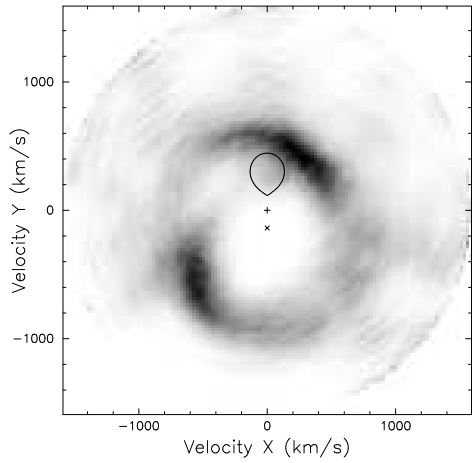

Figure 1.9 – Doppler map of U Gem during outburst using the He II λ4686 line, taken from Groot (2001). A spiral pattern is visible in the velocity space. The balloon shape represents the secondary star, which has the same shape as the Roche lobe because it is in co-rotation with the binary. The $+$ is the position of the centre of mass and the $\times$ is the position of the white dwarf.

the inner regions of the disc and the heating front propagates towards the outer radii. This type of outburst is called *inside out* outburst. On the contrary, outbursts seeded in outer regions are called *outside in* outbursts. This observational knowledge can then be confronted with theoretical modelling of dwarf novæ outbursts.

It is important to note however that results of eclipse mapping observation should be treated with caution as they rely on some strong assumptions. For instance, the measured brightness temperature is not a perfect proxy to measure the disc temperature. It is typically measured at a one wavelength assuming a perfect black body disc, which might not be the case. Moreover, the actual vertical structure of the disc is required to obtain the relation between the measured brightness temperature and the effective temperature (1.7). For example, Hirose et al. (2014) showed with numerical simulations with radiative transfer that the temperature at the centre of the disc can be upwards of five times larger than the disc surface temperature.

1.3.2 *Doppler tomography*

The Doppler tomography technique (see Marsh (2001), Echevarría (2012) for reviews) relies on the observed Doppler shifts of emission or absorption lines in cataclysmic variable systems. These shifts are measured during an orbital period along the projected line of sight and can then be used to detect structures in the accretion disc. By definition of this method, these structures are observed in a two-dimensional velocity space thanks to the rotation of the binary system. They are then translated into the real space using assumptions on the disc's general structure. Like eclipse mapping, this technique is only usable for systems observed under a high enough inclination.

The most prominent discovery made with this technique is the detection of spiral structures in dwarf novæ discs. They were first detected by Steeghs et al. (1997) in the IP Peg system. Spiral in cataclysmic variable discs were then observed in outbursting dwarf nova U Gem (Groot, 2001) and also in super-outbursting dwarf novæ (Baba et al., 2002). They were then also observed in novæ-like systems V3885 Sgr (Hartley et al., 2005), UX UMa (Neustroev et al., 2011). Figure 1.9 shows one of the Doppler maps of Groot (2001). The spirals appear to extend beyond the position of the companion star because this plot is in velocity space, not real space. In a (quasi-)Keplerian disc, higher

velocities correspond to radii closer to the central object. Spiral structures have also been observed during quiescence in the U Gem system (Neustroev et al., 2004). These results suggest that spiral waves are formed in the disc. These may have an impact on the disc dynamics. For instance, during quiescence, the usual mechanism driving accretion can not be sustained because the disc is too cold, as detailed further in chapter 2. Spiral shocks may then be a viable way to drive accretion in these cold discs. These observed structures are possibly related to tidally excited spirals that were extensively studied analytically (see for example Savonije and Papaloizou (1983) and Savonije et al. (1994)) as well as numerically (see for example Savonije et al. (1994) and Ju et al. (2016)). This possibility is extensively studied in chapter 4.

More recently, Ruiz-Carmona et al. (2020) vitiated the consensus of the systematic presence of spiral structures in dwarf novæ discs (in outburst). In their study of sixteen systems, they find non-axisymmetric structures in most of them but identified spirals in only two of them. They conclude that spirals may still exist in discs where they do not detect them, but they may not be luminous enough to be detected, or 'hidden' by some other disc condition.

1.4 OBSERVATIONS OF OUTFLOWS IN DWARF NOVÆ

Another feature of dwarf novæ system is the presence of large coherent outflows escaping the binary systems. They are mostly observed thanks to their Doppler-shifted spectrographic signatures and may play a key role in the accretion, as I will discuss in chapter 2.

1.4.1 *Winds during outburst*

The best direct evidence we have to confirm the presence of an outflow in accreting systems is the observation of *P Cygni profiles*. A P Cygni profile is an emission line accompanied by a blue-shifted absorption feature of the same line, and that was first observed in the P Cygni star by Maury and Pickering (1897). This spectrographic feature corresponds to a gas outflow towards the observer, absorbing the background emission of the star or the disc (Beals, 1929; McCrea, 1929), hence the blue-shifted absorption. With these features observed in UV emission, we detected outflows in dwarf novæ (Cordova and Mason, 1982; Mauche and Raymond, 1987; Drew, 1990). This type of outflow is usually classified as *wind* and not *jet* because they are not very collimated. Their measured velocity ranges from 3000 to 5000 km/s. These velocities correspond to the escape velocity close to the white dwarf, it is thus suspected that these winds originate from disc regions close to the white dwarf. P Cygni profiles were first observed in non-eclipsing systems with a high accretion rate ($> 10^{-9}\ M_\odot/\mathrm{yr}$). In high inclination systems, bipolar flows are proposed to explain the lack of detection of P Cygni profiles (Drew, 1990; Knigge and Drew, 1997). Hoare and Drew (1993) and Knigge and Drew (1997) estimate the mass loss due to these winds to be close to $10^{-9}\ M_\odot/\mathrm{yr}$, *i.e.* a few percent of the disc accretion rate. Recently, Cúneo et al. (2023) showed that several nova-like systems feature optical signatures of outflows. They report high outflow velocities (> 1000 km/s), consistent with disc winds. Winds appear to be a general feature of outbursting cataclysmic variables.

1.4.2 *Winds during quiescence*

To this day, there has not been any direct observation of winds in quiescent dwarf novæ systems. Perna et al. (2003) suggest that the broad O VII line they observed could be due to the presence of an outflow in WX Hyi in quiescence. According to them, the presence of an outflow is a compelling argument to explain the discrepancy in X-ray and UV accretion rates they witness. Hakala et al. (2004) report a possibly blue-shifted

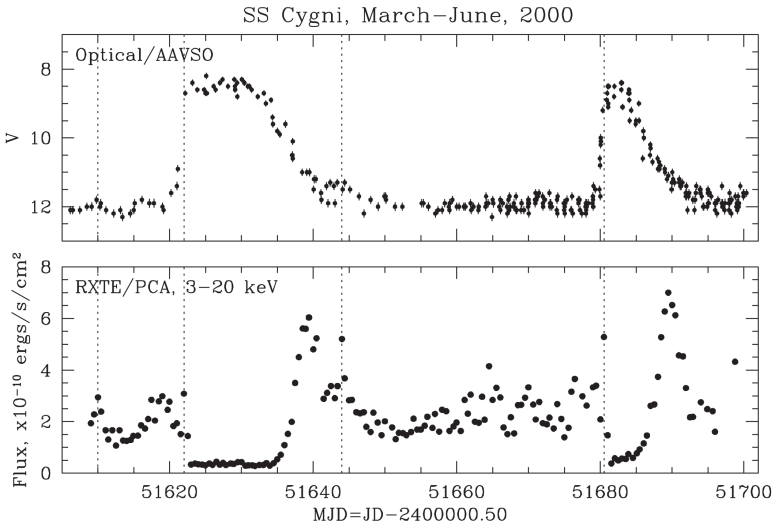

Figure 1.10 – Simultaneous lightcurves for two outbursts and a quiescence phase of SS Cyg. **Top:** Visible band emission (AAVSO). **Bottom:** X-rays flux (RXTE/PCA). Figure from McGowan et al. (2004). Note that the X-ray luminosity increase at the end of the outburst is not a general feature of dwarf novæ, but is particular to SS Cyg.

iron line, that could, here too, be due to the presence of an outflow in YZ Cnc during quiescence.

More recently, Hernández Santisteban et al. (2019) observed an illuminated distant bow shock in the V1838 dwarf nova during one of its outbursts. This bow shock appears too distant to have propagated during the outburst of the observation, rather they argue that a 'quasi-continuous outflow of material is required to sustain a standing bow shock with the interstellar medium'. This suggests that, in this system, a wind is also present during the quiescence phase.

We unfortunately lack further observations of winds during the quiescence phase. Either they are not present, but numerical studies suggest that they should (see Scepi et al. (2018a) and Scepi et al. (2019) for example), or they are too faint to be observed with current telescopes.

1.4.3 *Jets*

Contrarily to winds, jets are high velocity, low density, and collimated outflows. They are usually detected with radio emission attributed to synchrotron radiation.

The radio emission observed by Körding et al. (2008) during a 2007 outburst SS Cyg suggests that jets might also be present in dwarf novæ. Following this discovery, Harrison (2014) and Coppejans et al. (2015, 2016) showed that several other nova-like and dwarf novæ systems were also radio emitters, albeit at low power that prevented earlier detection. Körding et al. (2008), Russell et al. (2016) and Fender et al. (2019) argue that the radio emission in SS Cyg originates from synchrotron emission in a transient radio jet, similar to what is observed in X-ray binaries. However, contrarily to X-ray binaries, radio emission seems to linger well into the luminosity plateau of the outburst phase (Webb, 2023). A recent review by Coppejans and Knigge (2020) errs on the side of caution and advises that one should not conclude that all dwarf novæ emit jets just yet.

1.5 UV AND X OBSERVATIONS

Finally, dwarf novæ systems also feature higher energy wavelength emission. Indeed, basic accretion theory predicts that half of the gravitational energy (1.2) is released in

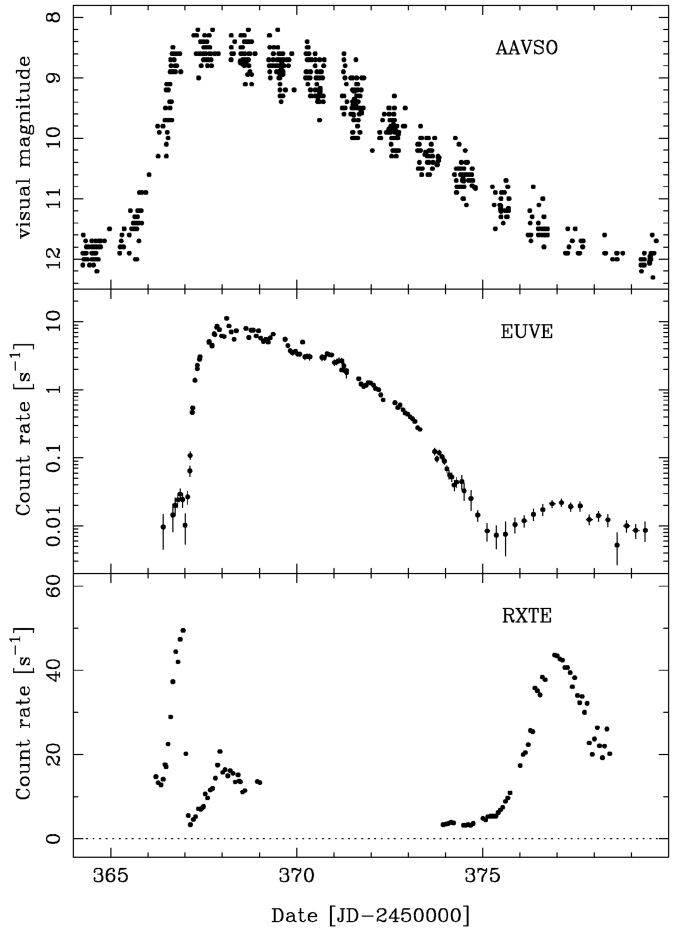

Figure 1.11 – Simultaneous lightcurves of SS Cyg during one outburst. **Top:** Visible band emission (AAVSO). **Middle:** EUV emission (EUVE from 0.1 keV to 0.2 keV). **Bottom:** X-rays flux (RXTE/PCA). Figure from Wheatley et al. (2003).

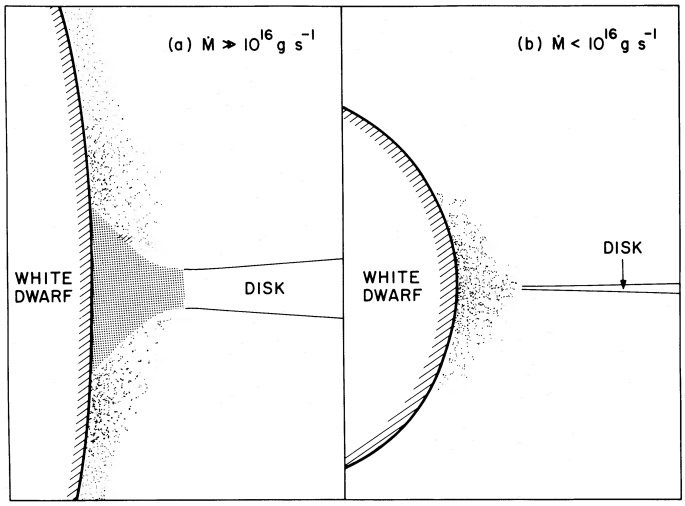

Figure 1.12 – Boundary layer at the interface of the accretion disc and the white dwarf. **Left:** High accretion rate regime with optically thick boundary layer (coloured region). **Right:** Low accretion rate with optically thin boundary layer (dotted region). Note that 10^{16} g/s $\approx 10^{-10}\ M_\odot$/yr. Figure from Patterson and Raymond (1985a).

accretion disc flow, while the other half is radiated away close to the white dwarf in the *boundary layer* between the accretion disc and the white dwarf (Lynden-Bell and Pringle, 1974). The light emitted by the inner regions of the disc is released in the form of ultraviolet radiation. The contribution of the boundary layer is emitted in Extreme Ultra Violet (EUV) radiation or X-rays.

During the low accretion quiescence phase, dwarf novæ emit soft X-rays [1] while during the high accretion outburst phase, the X-rays flux is suppressed and they emit EUV (Patterson and Raymond, 1985a,b; Wheatley et al., 1996; Wheatley et al., 2003; McGowan et al., 2004; Wheatley and Mauche, 2005; Fertig et al., 2011; Balman, 2015). Figure 1.10 and 1.11 show this behaviour. On figure 1.10, we see that X-ray emission is quenched during the high luminosity plateau of the outburst. On figure 1.11 we see that the EUV luminosity is increased during the outburst and decreases at the end of the outburst. The difference between these two regimes is well understood (Patterson and Raymond, 1985a,b), and is represented on figure 1.12. During the quiescence phase, when the accretion rate is $\lesssim 10^{-10}\ M_\odot/\mathrm{yr}$, the boundary layer has a low density, and is optically thin. As a consequence cooling is inefficient and the plasma emits a bremsstrahlung radiation in X-rays ($\lesssim 10$ keV). On the contrary, during the outburst, the boundary layer is optically thick and emits black body radiation in EUV ($\lesssim 100$ eV).

From the emission at these wavelengths, it is possible to have a second estimate of the accretion rate, independently of the optical emission estimate as they measure different phenomena. The EUV and X-rays emission come from the accretion onto the white dwarf, and thus depend on the chosen model for the boundary layer. On the other hand, the optical estimate depends on how accretion in the disc flow is modelled. For example, Pandel et al. (2005) computed the accretion rate of nine quiescent dwarf novæ from X-ray observations. They find accretion rates $10^{-12} - 10^{-10}\ M_\odot/\mathrm{yr}$. This range is consistent with the estimate of Wheatley et al. (2003), $5 \times 10^{-11}\ M_\odot/\mathrm{yr}$ for quiescent SS Cyg. In this latter work, they measure an accretion rate of $\approx 10^{-8}\ M_\odot/\mathrm{yr}$ during an outburst of SS Cyg with the same method.

1.6 SUMMARY

In this introduction, I presented the historical discovery of dwarf novæ and the observational state of the art for these systems. In the following chapters, I will present the theoretical and numerical works that have been carried out to best explain these observations. In the following, I will focus on describing only the accretion disc of dwarf novæ, and, at times, the matter flux from the companion star. The white dwarf, the boundary layer and the companion star, can impact the accretion disc (through illumination effects, amongst other effects), but will not be included in the following.

1. For Patterson and Raymond (1985a) 'hard X-rays' refer to the energy range 0.2-4.0 keV, which are usually called 'soft' X-rays, 'because the observations require or suggest hard spectra'. Unlike them, here, I use the usual nomenclature.

2

HYDRODYNAMICS AND MHD OF ACCRETION DISCS

Contents

2.1 Analytical formulation 23
2.1.1 Approximations and assumptions 23
2.1.2 Equations 27
2.1.3 Application to accretion discs 30
2.2 The Disc Instability Model 33
2.3 Accretion in magnetised discs 39
2.3.1 The magneto-rotational instability 39
2.3.2 Magnetic winds 41
2.3.3 Impact of resistivity 42
2.4 State of the art in modelling dwarf novæ beyond the DIM 43
2.4.1 Local simulations 44
2.4.2 Global models 46
2.5 Conclusion 47

We saw in chapter 1 that the behaviour of dwarf novæ system is tightly linked to the accretion disc that forms from the overflowing material of the companion star. In this chapter, I discuss the theoretical framework relevant to modelling these systems and in particular their accretion disc. We will see how the observations presented in the previous chapter constrain the theoretical model and motivate the theoretical developments I present here.

2.1 ANALYTICAL FORMULATION

2.1.1 *Approximations and assumptions*

Before diving into the analytical formulation of the problem at hand, let me first introduce the typical relevant scales for dwarf novæ systems.

For a quantity $q(\boldsymbol{r}, t)$, one can define typical variation length and time scales. I define the typical length scale over which this quantity varies as follows.

$$L \approx \frac{q}{|\boldsymbol{\nabla} q|} \tag{2.1}$$

I can do the same to define the typical variation time scale of this quantity.

$$\tau \approx \frac{q}{\partial_t q} \tag{2.2}$$

In dwarf novæ, these scales are closely related to the geometry of the accretion disc and the binary system. The orbital separation of the binary system gives us an upper estimate of the length scale. This scale is usually $a \approx 10^9$ m. Closely related to this scale is the orbital frequency of the binary system. This time is related to the binary separation and the mass of the binary components. The binary components usually have masses comparable to a solar mass, *i.e.* $M_{\rm WD} \approx 10^{30}$ kg. In any case, the mass of the white dwarf can not exceed the Chandrasekhar limit of $1.44\ M_\odot \approx 3 \times 10^{30}$ kg (Chandrasekhar, 1931). The companion star is usually a few tens of percent of the mass of the white dwarf

Length	Time	Mass	Magnetic field
$a \approx 10^9$ m	$T_0 \approx 10^4$ s	$M_{\rm WD} \approx 10^{30}$ kg	$B \approx 10^{-9}$ – 10 T

Table 2.1 – Typical physical scales of dwarf novæ **binary system**.

	Length	Time	Density	Temperature (Ma)
Quiescence	$H_{\rm in} \approx 10^4$ m	$T_{\rm in} \approx 10$ s – $T_{\rm out} \approx 1$ h	10^{-1} kg/m^3	$T \approx 2,000$ K (1000)
Outburst	$H_{\rm in} \approx 10^5$ m		10^{-2} kg/m^3	$T \approx 40,000$ K (100)

Table 2.2 – Typical physical scales of dwarf novæ **disc** during quiescence and outburst.

(Zorotovic et al., 2011). The binary system period is usually a few hours, that is $T_0 \approx 10^4$ s.

In these systems, it is also possible for a magnetic field to be present, and as I will discuss later, this has important consequences on the accretion disc. The magnetic field in cataclysmic variable systems is very loosely constrained. The lower estimate values come from typical interstellar medium values of $B_{\rm ISM} \gtrsim 10^{-9}$ T (Crutcher and Kemball, 2019). The upper estimation for the magnetic field is provided by a choice of my study. Here, I am interested in studying only *non-magnetic* systems. In other words, I am not interested in describing polars or intermediate polars, which have $B \geq 10^2$ T. As this field is evaluated on the white dwarf, it is an upper limit of the field in the disc even in those systems. In non-magnetic systems, if it does not come from the interstellar medium, the magnetic field originates from the components of the binary system, which are likely to have a dipolar field that can produce fields of at least $B \approx 10^{-2}$ T in the disc (Pearson et al., 1997).

The other relevant scales not only depend on the gravitational properties of the system, but also on the properties of the accretion disc. Most of the relevant scales I will discuss in the following have no hope of being resolved by current observational techniques, and we have to make assumptions on some of the disc properties. Here I assume a collisional fluid description of the accretion disc. I will present verifications that this assumption is compatible with the typical scales it allows us to compute.

For the accretion disc, an important length scale is its scale-height at the inner radius of the disc, that is at the radius of the white dwarf. This scale can be computed from the hydrostatic vertical equilibrium of the disc. Under the assumption that the disc is thin, *i.e.* $H/R \ll 1$, it can be computed as $H \approx \frac{c_{\rm s}}{\Omega_{\rm K}}$, with $c_{\rm s}$ the local sound speed in the gas and $\Omega_{\rm K} = \sqrt{GM_{\rm WD}/R^3}$ the local Keplerian frequency. Through the pressure (and here the sound speed), this scale directly depends on the temperature of the disc.

During the quiescence phase, we typically have a disc temperature around $T = 2,000$ K. Close to the white dwarf, this means that $H_{\rm in} \approx 10^4$ m. The corresponding aspect ratio of the disc is $R/H \lesssim 1000$. This aspect ratio also corresponds to the Mach number of the Keplerian flow $\mathrm{Ma} = \frac{v_{\rm K}}{c_{\rm s}}$, with $v_{\rm K}$ the Keplerian velocity. During the outburst phase, the disc is hotter and thus thicker. The typical outburst disc temperature is $T \approx 4 \times 10^4$ K, that is a disc height scale close to the white dwarf $H_{\rm in} \approx 10^5$ m, and a Mach number $\mathrm{Ma} \approx 100$. If the temperatures of these two phases are very different, the disc surface density predicted by the Disc Instability Model is the same $\Sigma \approx 10^3$ kg/m^2. This model is presented in section 2.2.

At the inner radius, the relevant timescale is the local Keplerian orbital period which is of a few tens of seconds, $T_{\rm in} \approx 10$ s. At the outer radius of the disc (close to 40% to 60% of the binary separation), this timescale is longer, close to one hour, that is $T_{\rm out} \approx 3 \times 10^3$ s.

The relevant scales of the system are summarised in table 2.2 for quantities relevant to the accretion disc, and in table 2.1 for the scales relevant to the binary system.

COMPACT SYSTEM, BUT RELATIVISTIC ? The above estimation relies on the computation of the Keplerian velocity close to the white dwarf. This velocity is typically of the order of a few percent of the speed of light, because the system is so compact. These velocities are however not high enough to require a relativistic description. With γ_L the Lorentz factor, we have $\gamma_L - 1 \lesssim 10^{-4} \ll 1$. In the following, I use a classical description of dynamics which is well justified.

CONTINUOUS MEDIUM DESCRIPTION In order to use a fluid description of the field q, the medium needs to be well described as a continuous medium, *i.e.* q being smooth enough. This can be quantified by the Knudsen number, and a fluid approximation is relevant when

$$\mathrm{Kn} = \frac{\ell}{L} \ll 1, \tag{2.3}$$

where ℓ is the mean free path of the particles of the medium. In this work, we will be interested in both an ionised plasma description of the medium as well as a non-magnetised gas, we can estimate the mean free path in both regimes. As we do not have access to the actual velocity distribution of the medium, we have to make assumptions to compute the mean free path. In both following cases, I assume that the medium is collisional, such that the temperature and pressure are well-defined, and verify that the obtained mean free path is not in contradiction with this assumption.

First, in the non-magnetic case, we can assume that the gas is an ideal gas as the particle sizes are much smaller than the inter-particle distances. We then have for an ideal gas (see for example Rohlf (1994))

$$\ell_{\mathrm{HD}} = \frac{k_B T}{\sqrt{2}\pi d^2 p}, \tag{2.4}$$

where k_B is Boltzmann's constant, T is the temperature, p is the pressure and d is the particle size. During the quiescence phase, for an atomic gas we typically have $\ell_{\mathrm{HD}} \leq 10^{-6}$ m.

At the other extreme of the fluid description, we have that for a fully ionised hydrogen plasma, dominated by Coulomb collision, we have that (see for example Spitzer (1956))

$$\ell_{\mathrm{plasma}} = \frac{(k_B T \epsilon_0)^2}{2\pi e^4 n_e \ln \Lambda}, \tag{2.5}$$

whereϵ_0 is the vacuum permittivity, m_e is the electron mass, e is the unit charge, n_e is the electron number density, and Λ is the plasma parameter. In quiescent dwarf novæ systems we have $\ell_{\mathrm{plasma}} \approx 10^{-14}$ m.

This means that between a fully ionised state and a non-ionised state we have $\ell \in [10^{-14}, 10^{-6}]$ m.

En passant, we have computed the typical time between two collisions which is

$$\tau_{\mathrm{coll}} = \ell \sqrt{\frac{\mu}{k_B T}} \tag{2.6}$$

with μ the molecular mass of the medium. We have $\tau_{\rm coll} \approx 10^{-10}$ s for the non-magnetic case; hence, much shorter than the typical time scales. We indeed have $\ell \ll L$ and $\tau_{\rm coll} \ll \tau$, that is no contradiction with the collisional fluid approximation.

NEGLECTING MOLECULAR VISCOSITY We further assume that the molecular viscosity is negligible compared to the effective viscosity arising from turbulence. Following the argument of Kato et al. (2008), one can estimate how they compare (see Goldreich and Schubert (1967) the original argument for star interiors). For instance, we can estimate them as $\nu = vl$ where v is the relevant velocity and l the relevant length scale. In both cases, the relevant velocity can be estimated to be the sound speed. For the molecular viscosity, the relevant length scale is $\ell_{\rm HD}$ the mean free path, and for the turbulent viscosity, it can be estimated to be H the local disc scale-height (see for example the review of Terquem (2002)). We then have

$$\frac{\nu_{\rm mol}}{\nu_{\rm turb}} = \frac{\ell_{\rm HD}}{H} \approx 10^{-10} \ll 1. \tag{2.7}$$

We can also evaluate the associated viscous timescales as $\tau_\nu = R^2/\nu$. We obtain $\tau_{\rm mol} = 3 \times 10^{16}$ s, that is approximately 100 million years. This is much larger than any relevant timescale for these systems. On the other hand, $\tau_{\rm turb} \geq T_{\rm in}$, that is $\tau_{\rm turb} \approx 1$ s.

LOW-FREQUENCY LIMIT We also assume that the microphysics related to electromagnetism and charged particles is taking place at much faster rate than the time scales that we are interested in. This means that we require

$$\omega_{\rm L}\tau \gg 1, \tag{2.8}$$

as well as

$$\omega_{\rm p}\tau \gg 1. \tag{2.9}$$

where $\omega_{\rm L}$ is the Larmor frequency, which corresponds to gyration frequency due to the magnetic field. $\omega_{\rm p}$ is the plasma frequency, that is the response time of charged particles in the medium. For typical regimes of dwarf novæ systems, we have $\omega_{\rm L} = 10^{11}$ Hz for electrons and $\omega_{\rm L} = 10^{8}$ Hz for heavier ions like Na^+. The plasma frequency is $\omega_{\rm p} = 10^{13}$ Hz. In both cases, the time scales we are interested in are much larger.

LARGE SCALE LIMIT Related to the above time scale are the following length scales which must be much smaller that the ones we are interested in studying.

$$L \gg \lambda_{\rm D}, \tag{2.10}$$

and,

$$L \gg \lambda_{\rm L}. \tag{2.11}$$

where $L \gg \lambda_{\rm D}$ is the Debye length, that is the screening length of the plasma. In this kind of system, we have $L \gg \lambda_{\rm D} = 10^{-8}$ m. $\lambda_{\rm L}$ is the Larmor length, which corresponds to the gyration scale due to the magnetic field. For typical regimes of dwarf novæ systems, we have $\lambda_{\rm L} = 10^{-6}$ m for electrons and $\lambda_{\rm L} = 10^{-4}$ m for heavier ions like Na^+. Even in

the case of extremely low magnetic field, at interstellar medium value of 10^{-7} T, we are lower than the typical length scale of dwarf novæ systems.

We see that all the relevant microphysics scales are much smaller than the scales that we are interested in describing. As a consequence, there is no contradiction in using a collisional plasma description for the material of the accretion disc. Moreover, the plasma scales are such that it can be considered a locally neutral medium and will be well-described by an inviscid (magneto-)hydrodynamics description.

SELF-GRAVITATING DISC ? When discs becomes cold enough, it is possible that its internal pressure is no longer able to counteract its own gravity. For a rotating disc, the relevant criterion is the Toomre criterion (Toomre, 1964). This criterion reads

$$\frac{c_s \kappa}{\pi G \Sigma} > 1 \Leftrightarrow \text{stable}, \tag{2.12}$$

where κ is the epicyclic frequency, G is the gravitational constant and Σ is the disc column density, which I assume to be constant for this estimate. This criterion can be translated into

$$\frac{M_{\text{disc}}}{M_{\text{WD}}} < \frac{H}{R} \Leftrightarrow \text{stable}. \tag{2.13}$$

For dwarf novæ, even during quiescence, when $H/R \approx 10^{-3}$, the mass of the disc is about 10^{18} kg and this criterion is satisfied. The accretion disc is not expected to be subject to gravitational instability. As a consequence, I will only take into account the gravitational potential of the stars of the binary.

2.1.2 *Equations*

Now that I have verified that a fluid description is appropriate, we know that the Euler equations (Euler, 1757) can be used to describe the evolution of the fluid. I will not repeat their general form, rather I present their most relevant version for this work.

In the non-magnetic case, we have

$$\partial_t \rho + \boldsymbol{\nabla} \cdot (\rho \boldsymbol{u}) = 0, \tag{2.14}$$

$$\partial_t \boldsymbol{u} + (\boldsymbol{v} \cdot \boldsymbol{\nabla}) \boldsymbol{u} = -\frac{1}{\rho} \boldsymbol{\nabla} p - \boldsymbol{\nabla} \Psi, \tag{2.15}$$

$$\partial_t \mathcal{E} + \boldsymbol{\nabla} \cdot (\mathcal{E} \boldsymbol{u}) = -\boldsymbol{\nabla} \cdot (\boldsymbol{u} p), \tag{2.16}$$

where ρ is the fluid density, p its pressure, $\boldsymbol{u}$ its velocity and $\mathcal{E}$ its energy per unit volume, and Ψ the gravitational potential.

The energy $\mathcal{E}$ includes the gas internal energy per unit volume ρe, the kinetic energy and the potential energy.

$$\mathcal{E} = \rho e + \frac{1}{2} \rho u^2 + \rho \Psi. \tag{2.17}$$

This equation system must be closed by an equation of state, and we use the ideal gas law.

$$p = \frac{\rho}{\mu} k_B T, \tag{2.18}$$

where T is the fluid temperature, and μ is the molecular mass of the fluid. For an ideal gas undergoing adiabatic transformation, we have that

$$\rho e = \frac{p}{\gamma - 1}, \tag{2.19}$$

with γ the heat capacity ratio of the gas.

In the magnetic case, we need to include the Maxwell equations (Maxwell, 1861) for the electric and magnetic fields $\boldsymbol{E}$ and $\boldsymbol{B}$.

$$\boldsymbol{\nabla} \cdot \boldsymbol{B} = 0, \tag{2.20}$$

$$\boldsymbol{\nabla} \cdot \boldsymbol{E} = 0, \tag{2.21}$$

$$\boldsymbol{\nabla} \wedge \boldsymbol{B} = \mu_0 \boldsymbol{j}, \tag{2.22}$$

$$\boldsymbol{\nabla} \wedge \boldsymbol{E} = -\partial_t \boldsymbol{B}, \tag{2.23}$$

where $\boldsymbol{j}$ is the electric current density, and μ_0 the vacuum magnetic permeability. The fact that we are interested in scales larger than the typical electric charge screening length of equation (2.10) translates in the absence of charge density in equations (2.21) and (2.22). Let us consider the simpler general case, where the plasma can not be considered a perfect conductive medium, rather it has a finite conductivity σ (and resistivity $\eta = 1/(\mu_0 \sigma)$). We have Ohm's law for a fluid at velocity $\boldsymbol{u}$.

$$\boldsymbol{j} = \sigma(\boldsymbol{E} + \mu_0 \boldsymbol{u} \wedge \boldsymbol{B}) \tag{2.24}$$

Hence we obtain from (2.23), (2.22) and (2.24) the magnetic field evolution equation.

$$\partial_t \boldsymbol{B} = \boldsymbol{\nabla} \wedge (\boldsymbol{u} \wedge \boldsymbol{B}) - \boldsymbol{\nabla} \wedge (\eta \boldsymbol{\nabla} \wedge \boldsymbol{B}) \tag{2.25}$$

This form includes the possible space variations of the Ohmic resistivity η.

Now, one still needs to include the Lorentz force $\boldsymbol{j} \wedge \boldsymbol{B}$ to the momentum balance (2.15). We obtain the following equation.

$$\partial_t \boldsymbol{u} + (\boldsymbol{u} \cdot \boldsymbol{\nabla})\boldsymbol{u} = -\frac{1}{\rho}\boldsymbol{\nabla} p - \boldsymbol{\nabla}\Psi + \frac{1}{\mu_0 \rho}(\boldsymbol{\nabla} \wedge \boldsymbol{B}) \wedge \boldsymbol{B} \tag{2.26}$$

The energy equation simply needs to be modified with $\mathcal{E} \mapsto \mathcal{E} + \frac{1}{2}\frac{B^2}{\mu_0}$ to include the local magnetic energy density, one also needs to include the Poynting flux. We thus have

$$\partial_t \mathcal{E} + \boldsymbol{\nabla} \cdot (\mathcal{E}\boldsymbol{u} + \boldsymbol{\Pi}) = -\boldsymbol{\nabla} \cdot (\boldsymbol{u}p), \tag{2.27}$$

where $\boldsymbol{\Pi} = \frac{\boldsymbol{E} \wedge \boldsymbol{B}}{\mu_0} = \eta \boldsymbol{j} \wedge \boldsymbol{B} + B^2 \boldsymbol{v} - (\boldsymbol{B} \cdot \boldsymbol{v})\boldsymbol{B}$ is the Poynting flux.

We also note that in practical applications, and in order to have a better intuition on the effect of the Lorentz force, we usually decompose it in two parts.

$$\frac{1}{\mu_0}(\boldsymbol{\nabla} \wedge \boldsymbol{B}) \wedge \boldsymbol{B} = -\frac{1}{2\mu_0}\boldsymbol{\nabla} B^2 + \frac{1}{\mu_0}(\boldsymbol{B} \cdot \boldsymbol{\nabla}) \cdot \boldsymbol{B} \tag{2.28}$$

The first term is the gradient of *magnetic pressure* and can be interpreted as pressure force like $-\boldsymbol{\nabla} p$. The second term is the *magnetic tension* and can be interpreted as an effect counteracting magnetic field line bending. Indeed, for a constant amplitude field, this term is $\frac{B^2}{\mu_0}\boldsymbol{K}$ with K proportional to the inverse of the curvature radius of the field lines.

NON-IDEAL MHD EFFECTS Above, I presented the equation for MHD that includes a dissipation term: the Ohmic resistivity, or simply resistivity, η.

It is relevant to include this term when the plasma is poorly ionised, but is not the only term that I could have included. When the plasma is not well ionised, the collisions between charged particles and neutral particles may become significant and change the dynamics. These terms are the difference between *ideal* MHD and *non-ideal* MHD. These non-ideal terms that arise due to this poor ionisation are a way to model the fact that the different species (electrons, ions and neutrals) are not perfectly coupled, while keeping the convenient one-fluid description.

For quiescent dwarf novæ systems, the ionisation fraction can be estimated for the plasma from the Saha equation (Saha, 1920). Using solar composition of Grevesse and Sauval (1998), that is hydrogen abundance $X = 0.7$ and metallicity $Z = 0.02$, Scepi et al. (2018a) find typical values around

$$\xi \approx 10^{-5}. \tag{2.29}$$

This value of $\xi \ll 1$ does not explicitly say whether the non-ideal effect will be relevant, but it certainly raises caution. Apart from the resistivity, two other non-ideal effects may be relevant in weakly ionised discs. Ohmic resistivity arises because of electron-neutral collisions whereas ambipolar diffusion arises from ion-neutral collisions, causing non-negligible ion-neutral drift. On the other hand, the Hall effect arises from a velocity drift between ions and electrons.

These two other non-ideal effects – the Hall effect (H) and Ambipolar diffusion (A) – are known to play an important role in protoplanetary discs (see for example Lesur et al. (2014) and Bai (2015) and reference therein). Balbus and Terquem (2001) propose a way to quantitatively measure their relative importance compared to Ohmic resistivity (O). They give

$$\frac{\mathrm{O}}{\mathrm{H}} = \left(\frac{\rho}{3\times10^{-3}\ \mathrm{kg/m^3}}\right)^{\frac{1}{2}}\left(\frac{c_\mathrm{s}}{v_\mathrm{A}}\right), \tag{2.30}$$

$$\frac{\mathrm{O}}{\mathrm{A}} = \left(\frac{\rho}{10^{-5}\ \mathrm{kg/m^3}}\right)\left(\frac{T}{10^3\ \mathrm{K}}\right)^{-\frac{1}{2}}\left(\frac{c_\mathrm{s}}{v_\mathrm{A}}\right)^2. \tag{2.31}$$

In these systems, the large-scale magnetic field is due to the dipole of the companion star and can be estimated as $B \approx 10^{-2}$ T (Pearson et al., 1997). In this case we have $\mathrm{O/H} \approx 10^2$ and $\mathrm{O/A} \approx 10^7$. From these estimates, it seems that the Hall effect may not be negligible. As discussed in Scepi et al. (2018a), the Hall effect is characterised by the Hall Lundquist number $\mathcal{L}_\mathrm{H}$. In dwarf novæ regimes, this number is $\mathcal{L}_\mathrm{H} \gg 1$ such that the actual effect of the Hall effect is in practice negligible (Sano and Stone, 2002; Kunz and Lesur, 2013). This confirms that the other non-ideal effects will have a lower impact on the dynamics. Furthermore, the above estimate for magnitude field amplitude does not take into account any disc dynamo effect, that can produce a stronger magnetic field. As $v_\mathrm{A} \propto 1/B$, a stronger field further reduces the relative impact of Hall effect and ambipolar diffusion. In this work, I do not take them into account.

The quantitative effect of the resistivity term included in the equation is discussed in the section on accretion in magnetised discs 2.3. There, I discuss the quantitative effect of resistivity on magnetic accretion-driving mechanisms.

2.1.3 *Application to accretion discs*

The Euler and Maxwell equations I presented above are the very general evolution equations for a magnetised fluid in a gravitational potential. In this work, I am more specifically interested in describing the evolution of an accretion disc. These particular objects have been modelled for almost eighty years (Weizsäcker, 1948), and the main problem we face to understand their evolution is to understand how angular momentum is redistributed inside the disc flow. Indeed, for matter to be able to lose some of its angular momentum and fall onto the central object, this angular momentum must be transferred to some other part of the flow.

A way to redistribute angular momentum in a flow is through some viscosity ν; this is what Lynden-Bell and Pringle (1974) proposed. At the time the physical origin of this viscosity was unknown. At around the same time, Shakura and Sunyaev (1973) proposed to quantify the angular momentum transport with a dimensionless parameter α. In fact, by construction, the two approaches are related as one can write the following relation.

$$\nu = \alpha c_\mathrm{s} H \tag{2.32}$$

where c_s is the sound speed and H is the disc thickness.

More recently, Balbus and Papaloizou (1999) formalised this approach making use of the weak turbulence formalism in the case of thin discs, *i.e.* when $H \ll R$. They were able to obtain the same dynamical equations as the previous models, but without using any *ad hoc* term. Namely, one can obtain the α parameter from first principles. I will use this formalism in the following. With this approach, I will derive a simple one-dimension model for an accretion disc. I however include the possibility of a vertical outflow in this picture, contrary to the first approach of Balbus and Papaloizou (1999).

As I am interested in understanding angular momentum transport, I will focus on the mass conservation equation (2.14) and the angular momentum equation. The latter is obtained from equation (2.26) and reads

$$\partial_t \left(R\rho u_\varphi\right) + \boldsymbol{\nabla}\cdot\left[R\rho u_\varphi \boldsymbol{u} - \frac{B_\varphi \boldsymbol{B}}{\mu_0}\right] + \rho\partial_\varphi P + \frac{\rho}{2\mu_0}\partial_\varphi B^2 = 0, \tag{2.33}$$

for a stationary central gravitational and axisymmetric potential.

Then, we write the quantities as some 'mean' field plus some perturbation to this field. In cylindrical coordinates (R, φ, z) we have

$$u_R = 0 + v_R, \quad u_\varphi = \Omega R + v_\varphi, \quad u_z = 0 + v_z, \tag{2.34}$$

where ΩR is the some azimuthal velocity. Note that I the 'mean' field taken here need not be the actual average of the flow, nor need the perturbation be of smaller amplitude than this 'mean' field [1]. In the following I assume $\partial_\phi \Omega = 0 = \partial_t \Omega$.

The angular momentum balance can be written with these new variables.

$$\partial_t \left(R\rho v_\varphi\right) + \boldsymbol{\nabla}\cdot\left[R\rho v_\varphi \boldsymbol{u} - \frac{B_\varphi \boldsymbol{B}}{\mu_0}\right] + \rho\boldsymbol{u}\cdot\boldsymbol{\nabla}(\Omega R^2) + \rho\partial_\varphi P + \frac{\rho}{2\mu_0}\partial_\varphi B^2 = 0, \tag{2.35}$$

We now introduce the following averages, to reduce the three-dimensional problem to just one spatial dimension.

$$\langle X\rangle = \frac{1}{2\pi}\int_0^{2\pi} X d\varphi \quad \text{and} \quad \overline{X} = \int_{-h}^{h}\langle X\rangle dz, \tag{2.36}$$

where h is some arbitrary height scale. For simplicity, we take $\partial_t h = \partial_\varphi h = \partial_R h = 0$. With these, we obtain a new form of the continuity equation

$$\partial_t \Sigma + \frac{1}{R}\partial_R\left(R\overline{\rho u_R}\right) + \left[\langle\rho v_z\rangle\right]_{-h}^{h} = 0, \tag{2.37}$$

where $\Sigma = \overline{\rho}$ the azimuthal average of the surface density. The angular momentum balance becomes

$$\begin{aligned}\partial_t(R\overline{\rho v_\varphi}) + \overline{\rho v_R}\partial_R\left(\Omega R^2\right) + \tfrac{1}{R}\partial_R\left[R^2\left(\overline{\rho v_\varphi v_R} - \tfrac{\overline{B_\varphi B_R}}{\mu_0}\right)\right] \\ + \left[R\left(\langle\rho v_\varphi v_z\rangle - \frac{\langle B_\varphi B_z\rangle}{\mu_0}\right)\right]_{-h}^{h} = 0.\end{aligned} \tag{2.38}$$

Here, the possibility of a wind arising translates in not assuming the surface terms $\left[...\right]_{-h}^{h}$ to be zero. Under this form, the angular momentum balance equation can be easily interpreted, as each contribution to the angular momentum change is isolated. Let me

1. Balbus and Papaloizou (1999) only assume $|\langle\boldsymbol{v}\rangle|^2 \ll \langle v^2\rangle$, *i.e.* that fluctuation motions are of small amplitude compared to the mean state.

decompose this balance equation in several terms to obtain a better understanding of the global picture.

First, let me focus on the *bulk* terms of this equation. They are related to the physics inside the accretion disc. They are directly related to the usual properties of accretion. For instance, for a stationary regime without wind, equation (2.38) reduces to

$$\dot{M} = \frac{2\pi}{\partial_R \left(\Omega R^2\right)} \partial_R \left[R^2 \left(\overline{\rho v_\varphi v_R} - \frac{\overline{B_\varphi B_R}}{\mu_0} \right) \right] \tag{2.39}$$

with $\dot{M} = 2\pi R \overline{\rho v_R}$ is the local accretion rate. This was the usual picture until recently. Based on the dimensional argument of Shakura and Sunyaev (1973), we define the α parameter as

$$\overline{\rho v_\varphi v_R} - \frac{\overline{B_\varphi B_R}}{\mu_0} = \alpha \overline{p} \tag{2.40}$$

In the case where accretion is driven by disc mechanisms, such as hydrodynamical or magnetic instabilities, this is a good description of accretion. This case corresponds to when the total angular momentum of the disc is conserved. In this case, it is simply redistributed at different radii. This model simply relates the radial advection of angular momentum $\overline{\rho v_R} \partial_R \left(\Omega R^2\right)$ to the gradient of stresses of the flow $1/R \partial_R (R^2 \alpha \overline{p})$. These stresses may be purely hydrodynamics, for example emerging from local turbulence, or arise from the magnetic fields.

A common abuse of terminology is to refer to α as directly quantifying the accretion. However, as we can see in equation (2.39) and (2.40) the value of α alone does not directly give the accretion rate. This abuse of terminology implicitly assumes that the disc is in a quasi-Keplerian steady state, with no radial variation of α, and a disc described by power-law profiles.

The α formulation of the stress is equivalent to a viscous model, provided that we use the effective viscosity of equation (2.32). Indeed, we can write the above stress as follows.

$$\alpha \overline{p} = -\frac{2}{3} \nu \Sigma \frac{d\Omega}{d \log R} \tag{2.41}$$

However, disc winds may also extract angular momentum as we can see in equation (2.38). Such an outflow effects translate in the presence of a *surface* term. This surface term is related to possible surface stresses that can locally remove angular momentum from the disc. Much like Shakura and Sunyaev (1973), Lesur (2021) proposed to introduce a dimensionless parameter υ to quantify the contribution of outflows to accretion, such that

$$\left[R \left(\langle \rho v_\varphi v_z \rangle - \frac{\langle B_\varphi B_z \rangle}{\mu_0} \right) \right]_{-h}^{h} = \upsilon p_{\mathrm{mid}} \tag{2.42}$$

where p_{mid} is the midplane pressure. This way, α quantifies the radial angular momentum transport, while υ quantifies the vertical transport. In the stationary regime, and when $\partial_z \Omega = 0$, this yields

$$\dot{M} = \frac{2\pi}{\partial_R \left(\Omega R^2\right)} \left[\partial_R (R^2 \alpha \overline{p}) + R^2 v p_{\rm mid} \right] \tag{2.43}$$

A similar treatment can be done to the energy equation. We obtain

$$\partial_t \overline{\mathcal{E}_{\rm m}} + \frac{1}{R} \partial_R (R \overline{\mathcal{F}_{{\rm m},R}}) + \left[\langle \mathcal{F}_{{\rm m},z} \rangle \right]_{-h}^{h} = \overline{p \nabla \cdot \boldsymbol{v}} - \left[\overline{\rho v_\varphi v_R} - \frac{\overline{B_\varphi B_R}}{\mu_0} \right] \frac{d\Omega}{d \log R} - \Lambda \tag{2.44}$$

with $\mathcal{E}_{\rm m} = \frac{1}{2}\rho v^2 + \frac{B^2}{2\mu_0}$ is the mechanical energy associated with the fluctuations, and $\boldsymbol{\mathcal{F}}_{\rm m} = \left(\mathcal{E}_m + p + \frac{B^2}{2\mu_0} \right) \boldsymbol{v} - \frac{\boldsymbol{v} \cdot \boldsymbol{B}}{\mu_0} \boldsymbol{B} - \frac{\boldsymbol{E} \times \boldsymbol{B}}{\mu_0}$ is the associated energy flux. Λ corresponds to possible losses, for example from Joule effect heating, viscous heating, radiative losses...

If we take this equation in a steady state, we see the losses are compensated for by the stress term $\alpha \frac{d\Omega}{d \log R}$. Moreover, when outflows are present, this local heating will be reduced, if the stress remains the same, as outflows do not locally contribute to heating, but can carry energy away. As a consequence, the observational signature of a disc will change depending on whether there is an outflow.

2.2 THE DISC INSTABILITY MODEL

When it comes to modelling accretion in dwarf novæ systems, the Disc Instability Model (DIM) provides an adapted theoretical one-dimensional framework. This model has been initiated more than forty years ago (Hōshi, 1979; Meyer and Meyer-Hofmeister, 1981; Cannizzo et al., 1982; Smak, 1982; Faulkner et al., 1983; Mineshige and Osaki, 1983) and explains the outburst-quiescence cycle by a thermo-viscous opacity hysteresis cycle (see Lasota (2001) and Hameury (2020) for reviews). This model can also be modified to describe some low-mass X-ray binary systems (van Paradijs and Verbunt, 1984; Cannizzo et al., 1985; van Paradijs, 1996). It has also been applied to FU Ori protoplanetary systems (Bell and Lin, 1994) and to active galactic nuclei (Janiuk et al., 2004; Hameury et al., 2009) with less success.

The DIM uses a non-magnetic description of the accretion disc, and uses a similar approach as presented in the previous section to obtain a one-dimensional problem. However, it includes additional effects relevant to dwarf novæ. The two first additional effects correspond to including the companion star in the picture. First, one should include the matter stream coming from this star as it provides both mass and angular momentum to the disc. Second, the tidal torque of the close companion also needs to be taken into account.

Finally, the last required addition is to the energy balance equation. We include a heating term Q^+, which is expressed under its viscous form, and we also include a black-body radiation cooling term Q^-. Note that in its original version the DIM does not include winds. In this case, we obtain the following equations.

$$\partial_t \Sigma + \frac{1}{R} \partial_R (R \Sigma v_R) = \frac{1}{2\pi R} \partial_R \dot{M}_{\rm ext}, \tag{2.45}$$

$$j \partial_t \Sigma + \frac{1}{R} \partial_R (R \Sigma j v_r) + \frac{3}{2R} \partial_R (R^2 \Sigma \nu \Omega_{\rm K}) = \frac{j_{\rm ext}}{2\pi R} \partial_R \dot{M}_{\rm ext} - \frac{1}{2\pi R} T_{\rm tid}, \tag{2.46}$$

$$\partial_t T_c + v_R \partial_R T_c + \frac{\Re T_c}{\mu C_P R} \partial_R (R v_R) = \frac{Q^+ - Q^-}{C_P \Sigma}, \tag{2.47}$$

where $\dot{M}_{ext}$ is the amount of matter per unit time coming from the companion star, $j = \sqrt{G M_{WD} R}$ is the local specific angular momentum, j_{ext} is the specific angular momentum of material coming from the companion star, Ω_K is the Keplerian angular frequency, T_{tid} is the tidal torque of the companion star, T_c is the disc central temperature. $Q^+ = 3\alpha\Omega\overline{p}$ is viscous heating. $Q^- = 2\sigma T_{eff}^4$ is the radiative cooling with σ the Stefan constant, and T_{eff} the disc surface temperature.

From these modified Euler equations alone, the outbursting nature of these systems can not be explained. It is in fact somewhat hidden in the surface temperature T_{eff}.

As its name suggests, this temperature is different from the disc central temperature T_c. As the (vertically) inner regions of the disc will heat through viscous heating, the heat will propagate more or less rapidly towards the upper and lower surfaces of the disc. This efficiency is mostly determined by the opacity of the disc's gas, κ. In the diffusion approximation, as the disc is optically thick, we have, for a constant opacity,

$$T_{eff}^4 = \frac{4}{3\kappa\Sigma} T_c^4 \tag{2.48}$$

As a consequence, one can compute the central equilibrium temperature of the disc T_{eq} by equating $Q^+ = Q^-$.

$$T_{eq} = \left(\frac{9}{8} \frac{\Omega\kappa}{\sigma} \frac{k_B}{\mu} \Sigma^2 \right)^{\frac{1}{3}} \tag{2.49}$$

where μ is the molecular mass of the fluid. However, it turns out that in the regime of dwarf novæ gas, there is an additional complication to this equilibrium. First, the opacity of the gas varies sharply by several orders of magnitude close to the temperature and density regime of dwarf novæ. This is because we are close to the ionisation temperature of hydrogen.

This rapid change in opacity is illustrated on figure 2.1. The opacity plotted on this figure is from Cox and Stewart (1970) and corresponds to Population II gas composition, that is hydrogen fraction $X = 0.8$, and metallicity $Z = 10^{-3}$, and helium fraction $Y = 0.199$. Depending on the ionisation fraction of the hydrogen, there will be a contribution to the opacity by atomic excitation and photo-ionisation, and free-free absorption (inverse Bremsstrahlung). Namely, as hydrogen ionises, the freed electrons increase significantly the inverse Bremsstrahlung opacity.

Second, to further complicate the matter, in addition to this sharp change in opacity, this regime of density and opacity is also such that for one single value of density, there exist several possible equilibrium temperatures such that $T/\sqrt{\kappa}$ is constant. This is what is illustrated on figure 2.1. Points a and b are on the same constant density curve, and have the same $T/\sqrt{\kappa}$, but different temperatures and opacities.

The stability of the accretion flow depends on whether the radiative losses of the disc can totally compensate for the viscous heating, that is the flow is stable if when the temperature changes, the heating terms are such that the state returns to equilibrium. However, this strongly depends on the value of the opacity and temperature for a given disc density. For example, point b on figure 2.1 may correspond to a stable opacity-

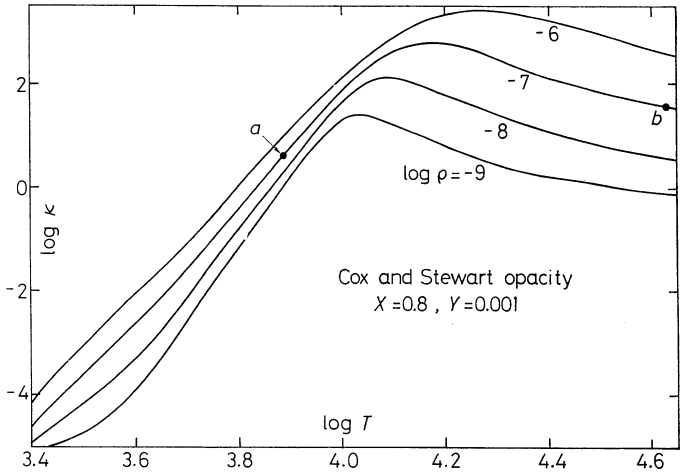

Figure 2.1 – Opacity as a function of density and temperature of the gas computed from Cox and Stewart (1970). The different solid lines correspond to different densities expressed in g/cm^3. The opacity is expressed in cm^2/g, and the temperature in K. Figure from Hōshi (1979).

temperature regime while point a may correspond to an unstable regime as they have the same $T/\sqrt{\kappa}$ but correspond to different $T_{\rm eff}$.

In the global picture, Hōshi (1979) showed that the accretion flow is stable if

$$\partial_T Q^+(T_{\rm eq}) \leq \partial_T Q^-(T_{\rm eq}) \tag{2.50}$$

where Q^+ may include additional heating terms, for example, heating due to the matter stream from the secondary star hitting and heating the disc at the hot spot. However, only heating terms that depend on the temperature may alter the stability of the equilibrium.

The *viscous* part of this thermo-viscous instability is captured by the criterion given by Lightman and Eardley (1974): the disc is stable if

$$\frac{\partial \Sigma \nu}{\partial \Sigma}(\Sigma_{\rm eq}) > 0, \tag{2.51}$$

where ν is the viscosity of the disc. If this criterion is not satisfied, the disc tends to break up into rings. In practice, for dwarf novæ, the thermal part of the instability captures most of the disc evolution.

The global picture is summarised in figure 2.2. First, this figure illustrates the three possible equilibrium temperatures of the disc at a given disc surface density Σ, radius R, and α. It also relates the different heating/cooling regimes to the ionisation of the hydrogen of the gas. Then, it shows the relation between the heating/cooling regime and the accretion rate of the disc. Finally, it introduces the comparison of this accretion rate with the matter flux rate from the companion star. Indeed, if $\dot{M}_{\rm ext} > \dot{M}$ the surface density of the disc will increase, conversely if $\dot{M}_{\rm ext} < \dot{M}$ it will decrease.

This figure also shows the fact that the three equilibrium temperatures only exist for a range of surface density $\Sigma \in [\Sigma_{\rm min}, \Sigma_{\rm max}]$. Outside this range, only one equilibrium temperature exists. Note that in this range, there are two *stable* temperatures (upper and lower branches) and one *unstable* temperature (middle branch).

This complete picture proposed by the DIM is summarised by the dashed arrows represented on figure 2.2. They show the full outburst-quiescence cycle following the equilibrium temperature curve.

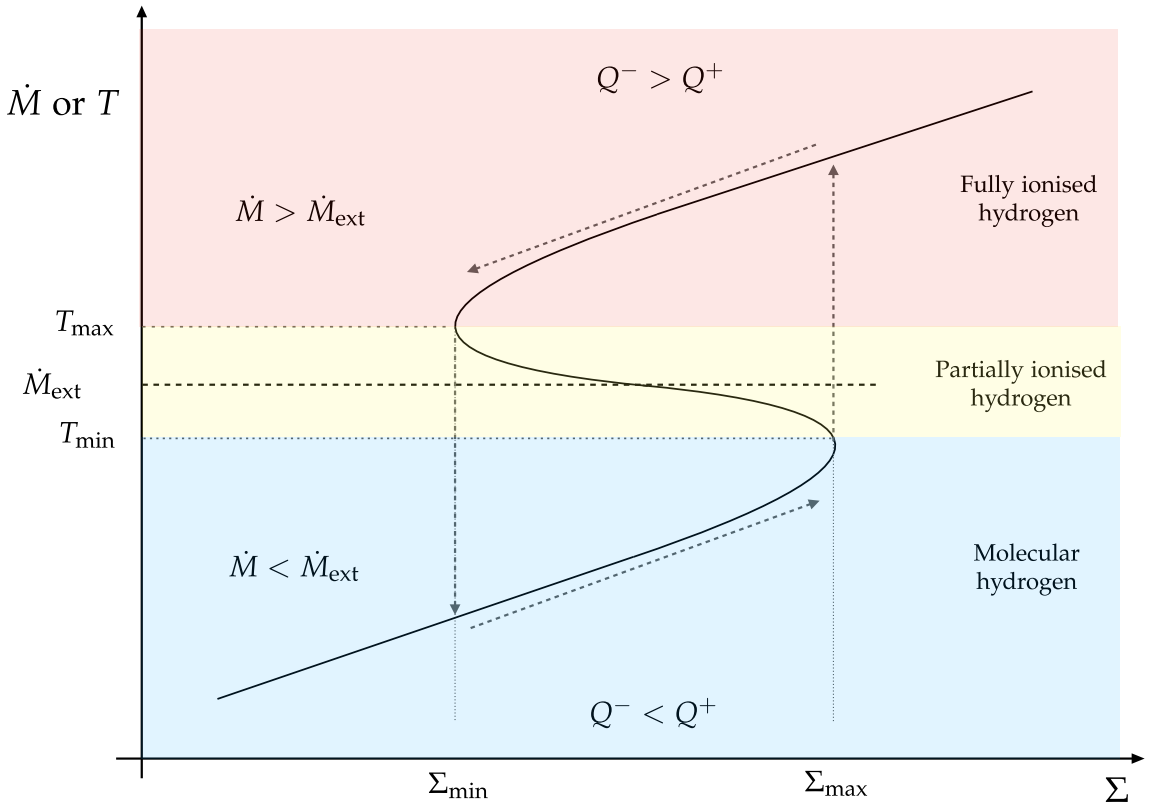

Figure 2.2 – S-curve in the surface density-temperature space, at constant radius and α. The black solid line represents the equilibrium temperature, *i.e.* where $Q^+ = Q^-$. The background colour represents the hydrogen ionisation state. The dashed arrows represent the outburst-quiescence cycle path. The hot branch corresponds to the outburst phase and the cold branch corresponds to the quiescence phase. Figure adapted from Scepi (2019).

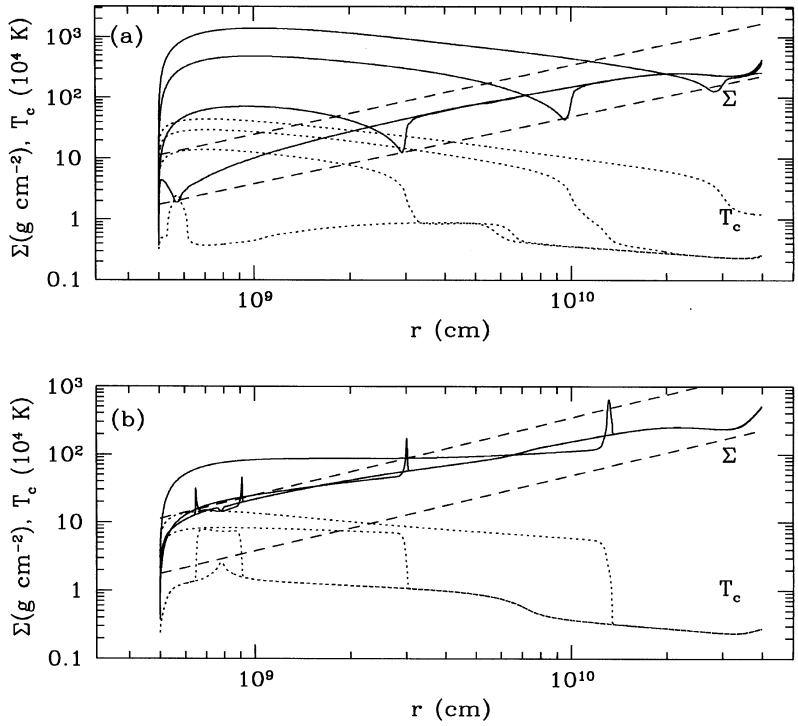

Figure 2.3 – Density (solid lines) and temperature (dotted lines) versus radius at different times. **Top:** Propagation of an inward cooling front and the associated density rarefaction wave. **Bottom:** Propagation of an outward heating wave and over-density. Figure from Hameury et al. (1998).

1. During the *quiescence* phase, the disc is cold and little ionised. The companion star provides more mass to the disc than the amount accreted onto the white dwarf. As a consequence, the surface density of the disc slowly increases. Its temperature also slowly increases.
2. When $\Sigma_{\rm max}, T_{\rm min}$ is reached, there no longer is a stable cold branch and an ionisation-opacity runaway is triggered: The disc is hot enough for the hydrogen to start ionising. The opacity of the gas is strongly enhanced, and the disc cooling drops in efficiency; the disc heats up even more. This triggers the outburst.
3. During the *outburst* phase, the disc is hot and fully ionised. Accretion is strong and so is the viscous heating. During this phase, more matter is being accreted than what is provided by the companion star. The surface density of the disc rapidly decreases.
4. When $\Sigma_{\rm min}, T_{\rm max}$ is reached, there is no more stable hot branch. The hydrogen recombines and the opacity of the disc decreases. The disc falls back to the quiescence phase.

Equations (2.45) – (2.47) can be solved to produce quantitative modelling of the evolution of a dwarf novæ disc. Such solutions, taken from Hameury et al. (1998), are plotted on figure 2.3. On this figure, we can see the density and temperature of the disc evolve with time. The most striking feature is the propagation of the cooling and heating fronts at the beginning and end of the outburst.

To produce these results, one has to make assumptions of the value of the local turbulent stresses α, as they can not be directly measured from an instantaneous observation of these systems. Indeed, the emitted spectrum does not depend on α. However, it is possible to estimate their value from the time variations of the emission. From the evolution equations, one can estimate a typical viscous timescale. For instance, neglecting

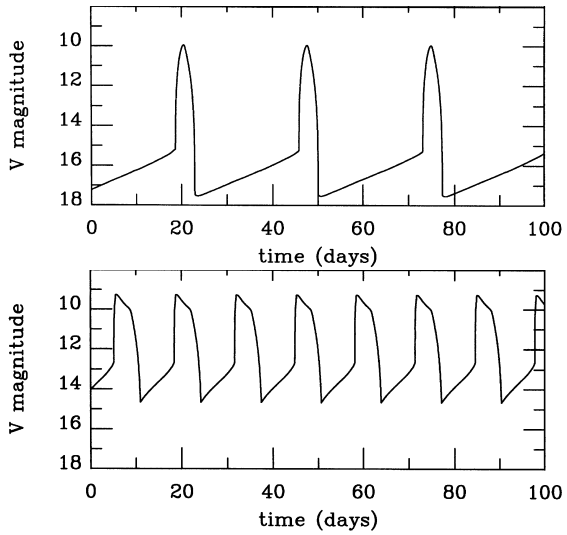

Figure 2.4 – Mock visible light curve obtained with the DIM for two different values of $\dot{M}_{\text{ext}}$. Figures taken from Hameury et al. (1998).

any possible outflow, and neglecting the time variation terms of the angular momentum balance, because $v \ll \Omega R$, one can obtain

$$\partial_t \Sigma = \frac{1}{R}\partial_R \left(\frac{1}{R\partial_R(R^2\Omega)} \partial_R \left(R^2 \alpha \overline{p} \right) \right). \tag{2.52}$$

Using that $\overline{p} \approx c_s^2 \Sigma$ and approximating the derivatives as division by the relevant timescale, we obtain

$$\tau_\nu = \frac{1}{\alpha\Omega}\,\mathrm{Ma}^2 \tag{2.53}$$

where $\mathrm{Ma} = \frac{\Omega R}{c_s} = \frac{R}{H}$ is the Mach number of the accretion flow.

From this estimate, it is possible to compute approximate values of the α parameter during the quiescence and outburst phases. The general idea is to equate the viscous timescale to the relevant time scale for each phase.

For the quiescence phase, Cannizzo et al. (1988, 2012) estimate from the recurrence time of dwarf novæ

$$\alpha_{\text{quiescence}} = 0.02 - 0.04. \tag{2.54}$$

From the decay time of the outburst, Smak (1999), King et al. (2007) and Kotko and Lasota (2012) estimate for the outburst

$$\alpha_{\text{outburst}} = 0.1 - 0.2. \tag{2.55}$$

One of the main strengths of the DIM is that using these parameters, it is able to produce disc oscillating between the outburst and quiescence state as shown on figure 2.4. It is then possible to tune the parameters of the model in order to best fit observed light curves and understand the physics of dwarf novæ discs. The main parameters that can be tuned are the α parameter values during quiescence and outburst, the size of the disc (inner and outer radii) and the matter flux from the secondary star.

The DIM is now widely accepted as a good model for recurrent outbursting systems (see for example Dubus et al. (2018) for a large-scale verification of the DIM with Gaia DR2 data (Gaia Collaboration et al., 2018; Lindegren et al., 2018)), and a number of refinements have been proposed in the last decades. I will not recall them here as they can be found in recent reviews like Hameury (2020), but they include effects like inner disc truncation, time variations of $\dot{M}_{\rm ext}$, irradiation by the disc or by the components of the binary systems...

What is most relevant to my work are the attempts at including disc winds in the DIM picture. As discussed above, wind can carry matter as well as angular momentum away from the system, and this can strongly change the emission of accreting systems. For instance, using the DIM Tetarenko et al. (2018) proposed that for X-ray binaries, the mass loss due to an outflow will significantly decrease the decay timescale of the luminosity peak. This allows us to explain very rapid decay time without requiring α values close to 1. To our current knowledge, such a high value of α can only be explained by strong magneto-rotational-instability-driven turbulence with a large-scale magnetic field, through the presence of substantial outflows (Bai and Stone, 2013a; Lesur et al., 2013; Salvesen et al., 2016), or with large scale convection (Hirose et al., 2014).

Concomitantly, Scepi et al. (2018b) used local models of the accretion flow of dwarf novæ to study the impact of magnetised winds. Their use of a vertical magnetic net flux allowed for MRI to develop in the hot branch, while being quenched in the cold branch by plasma resistivity, unless using strong magnetic fields. They then computed the expected light curves for such models of DIM including a magnetic wind in Scepi et al. (2019). They showed that the obtained light curves are compatible with observation. They propose that during the outburst, accretion is mostly driven by the MRI while being mostly driven by winds during the quiescence phase.

2.3 ACCRETION IN MAGNETISED DISCS

As we saw, the DIM requires that an effective viscosity, captured by the α parameter, is present in the disc, with different values during outburst and quiescence. Until the nineties, the physical origin of this viscosity was unknown; and the DIM was agnostic of the physical mechanism giving rise to it. In this section, I present mechanisms that can drive accretion in magnetised discs.

2.3.1 *The magneto-rotational instability*

It is only with the uncovering of a strong linear instability that can exist even in low magnetic field regime that we obtained the first plausible generic mechanism driving accretion in hot, well-ionised accreting systems discs.

The magneto-rotational instability (Velikhov (1959), Chandrasekhar (1961) and Balbus and Hawley (1991), MRI) is nowadays the widely accepted driving mechanism for accreting systems and has been extensively studied in a wide range of systems and regimes. In fact, it was its wide range of applications was already understood as it was first proposed by Balbus and Hawley (1991). Indeed, they write

> 'The instability has some extraordinary properties. It is present if a disk (1) is differentially rotating with a rate decreasing with distance from the center; and (2) has a weak (subthermal Alfvén speed) poloidal component. Remarkably, neither the growth rate of the most rapidly growing wavenumbers nor the stability criterion itself formally depend upon the magnetic field strength.'

These conditions apply to a wide variety of accretion discs, like AGN discs, protoplanetary discs or compact binary discs. The existence of this instability relies on an efficient coupling of the plasma of the disc and the magnetic field. When this coupling decreases, a minimal poloidal magnetic field amplitude, in terms of $2\mu_0 P/B_z^2$, is required to trigger this instability. In fact, in cold systems, where the plasma is poorly ionised, non-ideal MHD effects can quench this instability. This is for example the case for the *dead zone* of protoplanetary discs (Gammie, 1996), or during the quiescence phase of dwarf novæ systems (Gammie and Menou, 1998).

As my work focuses on global mechanisms driving accretion rather than local, turbulence driving mechanisms, I will not re-derive the linear stability analysis of the MRI here. Let me simply recall the stability criterion in the case where a vertical magnetic field is present, *i.e.* the *net flux* case. This criterion is expressed in the Hill approximation at radius R, we have the criterion

$$(k_z V_{\mathrm{A},z})^2 < 2q\Omega^2 \Leftrightarrow \text{mode } k_z \text{ is unstable} \tag{2.56}$$

where k_z is the vertical wave vector, and $V_{\mathrm{A},z} = B_z/\sqrt{\mu_0\rho}$ is the vertical field Alfvén velocity. Ω is the local angular frequency of the flow at radius R, and q is the local shear rate at radius R

$$q = -\frac{d\log\Omega}{d\log R} \tag{2.57}$$

From this criterion, we understand that for a quasi-Keplerian flow, *i.e.* with $q \approx 3/2$, one can always find a large enough vertical scale so that the corresponding mode is unstable. In a disc, however, the vertical scale is limited by the thickness of the disc $H = \frac{c_s}{\Omega}$. We can thus obtain a criterion on the vertical plasma parameter.

$$\frac{4\pi^2}{q} < \beta_z \Leftrightarrow \text{the disc is unstable} \tag{2.58}$$

where $\beta_z = \frac{2\mu_0 c_s^2 \rho}{B_z^2}$ the vertical plasma parameter. This criterion can be translated as follows.

$$B_z < \frac{1}{\pi}\frac{H}{R}\frac{GM_{\mathrm{WD}}\rho}{2R} \Leftrightarrow \text{the disc is unstable} \tag{2.59}$$

For typical outbursting dwarf novæ regime, this means $B_z \lesssim 1$ T for the disc to be unstable. This value of the magnetic field is compatible with the estimates of the local magnetic field in these systems.

The fundamental mechanism behind the MRI can be understood in simple terms. Let us consider the stability of a couple of fluid particles along the same vertical magnetic field line at a given radius. This simplified description of the MRI is represented on figure 2.5. By angular momentum conservation, if one particle falls to a lower radius, the other one will go to a further radius. The magnetic tension will act as a spring and counteract their relative drift. For a strong enough magnetic field, this is a stabilising effect. Otherwise, this effect, will further remove angular momentum of the inner-radius

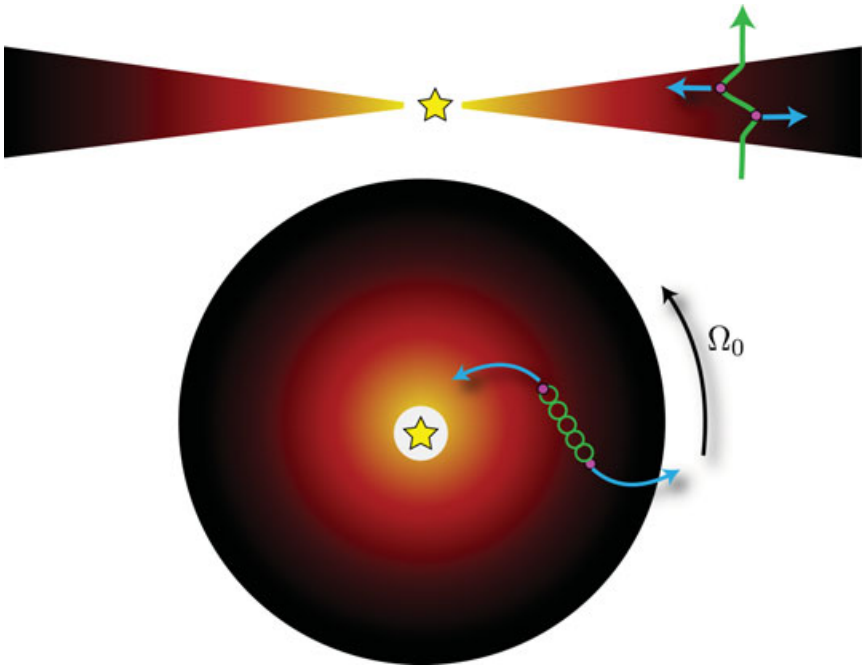

Figure 2.5 – Simplified picture of the MRI mechanism, taken from Lesur (2021).

particle and give it to the outer-radius particle. This will increase their relative drift into a positive feedback loop.

In the linear picture, the MRI can grow indefinitely, but of course, this instability will eventually saturate. Goodman and Xu (1994) showed that this saturation is mostly due to parasitic instabilities. This saturation will yield a turbulent saturation regime of the MRI. As such, the MRI-driven turbulence, and thus the MRI, can be reduced to an α parameter description. The first model of this instability required no mean magnetic field, as it can be kickstarted from a finite amplitude perturbation. Then the 'MRI dynamo' produces the field necessary to sustain the turbulent regime (Hawley et al., 1996). In this case, they measured an angular momentum transport parameter $\alpha \approx 0.01$. But it was later realised that this value depended on the numerical resolution (Fromang and Papaloizou, 2007).

It is also possible to study the MRI when a mean magnetic field is present. Hawley et al. (1995) showed with local simulations of accretion flow that the obtained value of α depends on the amplitude of the magnetic field. They studied the case where a mean vertical field was present as well as when a mean toroidal field was present. In this work, I only consider the mean vertical field case, as the more likely origin for this field in dwarf novæ is the dipole or either binary component.

Including corrections of local simulations by Bodo et al. (2008) to the work of Hawley et al. (1995), Lesur (2021) estimates that in the net flux case, for $\beta_z \in [400, 50000]$, we have

$$\alpha \approx 3.3\beta_z^{-1/2} \tag{2.60}$$

2.3.2 *Magnetic winds*

The second effect that can arise in an accretion disc when a large-scale vertical magnetic field is present is magnetic outflow. When deriving the equations relevant for accretion discs I mentioned possible vertical *outflows*. Magnetic winds[2] are a type of such outflows. Other possible outflows are thermal winds (Parker, 1958) and line-driven

2. The distinction between *winds* and *jets* is not clear cut as it mainly depends on the angle of the outflow. Jets are typically fast, low-density and collimated; winds may carry more mass and are not collimated.

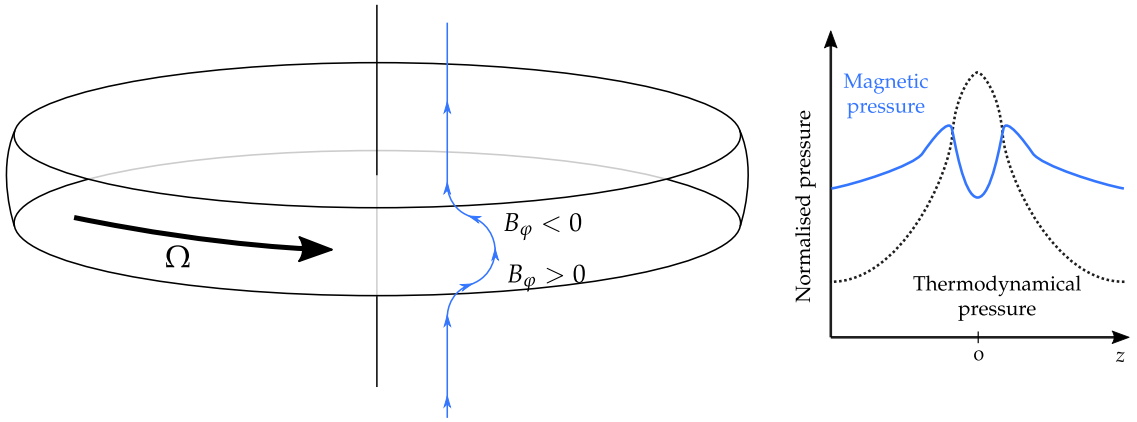

Figure 2.6 – Wind launching picture. The radial shear creates $B_\varphi \neq 0$ from radially advected field. The vertical gradient of magnetic pressure field pushes matter away from the disc. If the disc is isothermal, the thermodynamic pressure is proportional to the disc density.

winds (Lucy and Solomon, 1970). While these may be relevant for dwarf novæ observations, they do not apply a torque to the accretion disc, and as such do not contribute to the angular momentum transport and I will not consider them here.

Note that, the contribution of these outflows to accretion is not captured by the α parameter, as they correspond to a *surface* torque rather than a bulk torque. As mentioned above an analogous parameter υ can be introduced to describe their contribution.

The mechanism described by Blandford and Payne (1982) for the magnetic launching of a wind is rather simple. If the magnetic field lines are frozen in the accretion disc, as is the case in ideal MHD, some material will be ejected from the disc along the field lines like a 'bead on a rigid wire' because of the centrifugal force.

An equivalent picture can be drawn from MHD properties of the flow. The accretion taking place in the disc will create a radial component of the magnetic field by advection. Then, the radial shear will produce a toroidal magnetic field from this radial field as represented on figure 2.6. This is the usual Ω dynamo effect. As a consequence, the magnetic pressure will be maximal at the surface of the disc. The magnetic pressure gradient, $\boldsymbol{\nabla} B^2/2\mu$, will push matter out from the disc. As shown on figure 2.6, there also is a magnetic pressure gradient directed towards the midplane inside the disc. In cases where the magnetisation of the disc is weak, *i.e.* $\beta \gg 1$, the disc remains supported by the thermodynamic pressure.

In fact, the creation of the toroidal magnetic field is associated with a radial current density. The Lorentz force corresponding to this current and to the toroidal magnetic field corresponds to the vertical magnetic pressure gradient. This picture is similar to induction braking in Faraday's wheel experiment (1831).

As detailed above, the contribution of this outflow to angular momentum transport can be quantified with the dimensionless parameter υ (2.42)

Note that the simplified picture of figure 2.6 does not take turbulent effects into account. See Jacquemin-Ide et al. (2021a) for a more detailed vertical structure that includes the turbulent fluctuations of the magnetic field.

2.3.3 *Impact of resistivity*

The accretion driving mechanisms presented in this section both rely on an efficient coupling of the plasma to the ambient magnetic field. However, during the quiescence

phase of dwarf novæ systems, the plasma is cold little ionised as I extensively discussed above. This means that the coupling of the magnetic field to the plasma will be decreased. For example for the MRI, Gammie (1996) showed that for the cold, little ionised *dead zone* of protoplanetary disc, this enhanced resistivity killed the MRI altogether. Above, I wrote that the ionisation fraction was $\xi \ll 1$, but I did not quantitatively discuss the consequences of this poor ionisation. In fact, the effect of the resistivity is best captured with another dimensionless number: the magnetic Reynolds number.

$$\mathrm{Rm} = \frac{v_K H}{\eta} \tag{2.61}$$

Much like the usual Reynolds number, if $\mathrm{Rm} \gg 1$ this means that the effect of the dissipative term, here resistivity, is small compared to the advection term of Navier-Stokes equation, here the induction equation (2.25). On the other hand, when $\mathrm{Rm} \ll 1$ the resistivity will strongly modify the flow compared to an ideal MHD flow.

IMPACT ON THE MRI The picture of the MRI presented above was developed for a fully ionised plasma with no Ohmic resistivity. Gammie and Menou (1998) however showed that during the quiescence phase of dwarf novæ systems resistivity plays an essential role in quenching this instability.

Like with the hydrodynamic Reynolds number, the flow is expected to be laminar if $\mathrm{Rm} \ll 1$ while it is expected to be turbulent when $\mathrm{Rm} \gg 1$. Also like for the usual Reynolds number, the transition to turbulence does not occur at $\mathrm{Rm} \approx 1$ but rather at some critical Rm_c. For accretion disc, this transition regime depends on the exact field amplitude β, but is typically around $\mathrm{Rm}_c \approx 10^3$.

The exact criterion for MRI stability in a resistive disc is

$$\mathrm{Rm} > \frac{\beta_{\mathrm{mean}}}{\sqrt{\frac{3}{2\pi^2}\beta_{\mathrm{mean}} - 4}} \Rightarrow \text{unstable} \tag{2.62}$$

where $\beta_{\mathrm{mean}} = 2\mu_0\langle P\rangle / \langle B\rangle^2$. This criterion is illustrated on figure 2.7. This figure also shows an intermittent turbulence regime. In this regime turbulence is not fully developed, as showed by Fleming et al. (2000).

This means that for cold, poorly ionised discs, the MRI can only survive in regions where the disc is somehow heated or ionised by some external source, such as central star irradiation or the hot spot in dwarf novæ systems, or in regions where enough magnetic flux has been accumulated.

IMPACT ON MAGNETIC WINDS The wind launching mechanism can be understood as a saturation effect of the MRI, according to Lesur (2021)'s interpretation. As such, if the disc is too resistive for MRI to be triggered, no outflow will be launched. However, even with non-ideal effects the MRI can be triggered at the surface of the disc, and launch an outflow from there, possibly with a non-turbulent disc. See for example the MRI stability analysis figure 26 of Lesur (2021) that proposes another interpretation of the winds launched simulations of Bai and Stone (2013b).

2.4 STATE OF THE ART IN MODELLING DWARF NOVÆ BEYOND THE DIM

When it comes to modelling dwarf novæ discs, the DIM is a simple one-dimensional model that achieves to reproduce the outburst quiescence cycle. However, as intrinsically one-dimensional, it can not capture a lot of relevant physical effects. For example, the

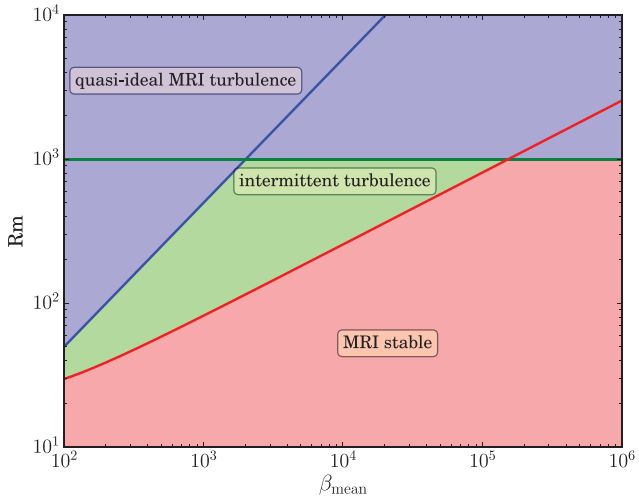

Figure 2.7 – Stability and instability with respect to the MRI in a resistive disc; β_{mean} is defined as in the text. Figure from Lesur (2021).

secondary star induces fundamentally non-axisymmetric perturbations in the disc, like the tidal truncation of the disc or the matter flow from the companion. Another example is that the heating and cooling fronts (see for example figure 2.3) are barely wider than the disc height scale, suggesting that adding the vertical dimension of the disc may help understand the physics of these. Finally, effects like the MRI or disc winds can not arise *ab initio* from the full three-dimensional flow and magnetic field geometry. They can only be included with a by-hand prescription. Here, I present past efforts to take into account these effects. First, I discuss local models focusing on understanding the underlying mechanisms driving the accretion, that can then be included in the DIM as educated prescriptions. Second, I present global models of dwarf novæ disc that try to understand large-scale accretion in dwarf novæ systems.

2.4.1 *Local simulations*

Because of the high numerical cost of numerical simulations, a particular effort has been carried out in the accretion disc community to produce local simulations of the accretion flow. With these, one focuses on understanding the local properties of the flow, like local instabilities cascading to turbulence. If they do not capture the global properties of the accretion flow, they achieve the great resolution necessary to resolve such instabilities. These simulations use the *shearing box* framework first developed by Hawley et al. (1995) to study the MRI. This framework corresponds to the Hill approximation.

The shearing box model is based on a Taylor expansion of the flow around a radius R. The simulation domain is a cuboid with special boundary conditions. In three dimensions, the coordinates used are (x, y, z) and they correspond to the local cylindrical coordinates (R, φ, z). The gravitational potential in this model is the Hill potential, that is a local second-order Taylor expansion of the potential at radius R. The y and z boundary conditions are taken to be periodic. The x boundary conditions are also periodic, but with a twist. To represent to local Keplerian shear in which the domain is embedded, the flow properties across the x boundary are periodic but shifted of a number of cells corresponding to the shear between the two x sides of the box. Note this number of cells may not be an integer. Some models also include a vertical dependency on gravity and

non-periodic vertical boundary conditions. The latter ones are referred to as *stratified* shearing box models.

More particularly for dwarf novæ, King et al. (2007) compiles previous simulations that focused on the MRI-driven turbulence in a not vertical magnetic net flux model. They showed with shearing box simulation, that they were not able to produce the α values required to match the DIM estimates during the outburst phase.

At around the same time, Fromang and Papaloizou (2007) raised caution about the fact that the α measured from local simulations appeared to be dependent on the numerical parameters of the simulations. This was later confirmed by Shi et al. (2016) who showed that this low measured effective viscosity is a numerical artefact due to the chosen aspect ratio of the simulation domain. In the meantime, Davis et al. (2010) showed that in stratified shearing box simulations, the restoration of the vertical gravity allowed for numerical convergence. However, they used periodic vertical boundary conditions for numerical simplicity; they point out that this is unrealistic for stratified shearing box simulations. Then, Bodo et al. (2014) and Ryan et al. (2017) produced stratified shearing box simulations with an outflow boundary condition in the vertical direction. They showed that the measured α parameter was also dependent on the chosen resolution, the latter found $\alpha \propto N^{-1/3}$ with N the number of grid cells per disc height scale H. At this point in time, the numerical convergence problem of shearing box simulations, stratified or not, has not been completely elucidated. At the same time, it was also shown the turbulent properties of the MRI were dependent on the magnetic Prandtl number $P_\mathrm{m} = \nu/\eta$, the ratio of viscosity to resistivity. The change of saturation of the MRI may play a critical role, given that the Prandlt number varies dramatically depending on the accreting system, with $P_\mathrm{m} \ll 1$ in young stellar objects and P_m in active galactic nuclei or proto-neutron stars. Studying these regimes is computationally expensive, as one needs to have a fine enough grid to resolve the very small scales introduced by either low viscosity or low resistivity. Recently, Meheut et al. (2015) achieved regimes with $P_\mathrm{m} \lesssim 10^{-2}$ and observed a low-P_m saturation of the α parameter in the presence of a mean magnetic field. On the other hand Guilet et al. (2022) examined $P_\mathrm{m} \gtrsim 100$ and found a high-P_m saturation independent of the Reynolds number. Fromang et al. (2007) also found that there is no MRI in $P_\mathrm{m} < 1$ regimes with no magnetic net flux.

In the beginning of the 2010s, it was shown from local simulations that it was in fact possible to explain the outburst-quiescence cycle. Latter and Papaloizou (2012) showed that even with MRI-driven turbulence and simple treatment of opacity and cooling, they were able to reproduce S-curve equilibrium. This was not obvious as turbulence-induced fluctuation could have killed this particular equilibrium state.

Using a more accurate radiative transfer model, Hirose et al. (2014) then showed that large-scale convection during the outburst phase of dwarf novæ could possibly enhance accretion and bridge the order of magnitude gap between the α values of the DIM of around 0.2. Prior to this work, shearing box simulation only achieved α values of around 0.02.

More recently, Scepi et al. (2018a) added the effect of cold quiescence temperature on the disc plasma. During this phase, the hydrogen of the disc is poorly ionised, so much so that the plasma is not well coupled to the magnetic field. Quantitatively, this means $\mathrm{Rm} \leq 10^4$. They showed, in agreement with the argument of Gammie and Menou (1998), that during the quiescence phase, MRI-driven turbulence is completely quenched and could not explain the α of the DIM.

Scepi et al. (2018b) then showed that provided a large-scale vertical magnetic field is present, a wind may be launched from the disc. During the quiescence phase, this wind is the main contributor to angular momentum transport in the accretion flow. As I discussed above, a such wind can however not be reduced to an α prescription, because, amongst other reasons, it does not contribute to heating the disc.

Recently, Held and Latter (2018, 2021) emphasised the impact of hydrodynamical as well as magnetohydrodynamical convection in angular momentum transport. They showed that convection can produce large-scale structures as well enhance angular momentum transport by nearly an order of magnitude. They were able to confirm the picture of Hirose et al. (2014) when a strong resistivity is included in the model, but not with a low resistivity.

Finally, Suzuki (2023) tried to make a step towards having a better global picture of local turbulence. They restored the curvature terms to the shearing box approximation and observed that the radial variation of the epicyclic frequency enhanced non-linear processes in the flow. They report stronger 'time variability, intermittency, and localized substructures' compared to traditional shearing box models.

2.4.2 *Global models*

On the other hand, some effects are fundamentally large-scale mechanisms and can not be captured by local models like shearing box simulations. Here, I present a chronological series of global models used to describe dwarf novæ systems. Their objective are various, but they all share the necessity to use a global approach to address a given physical question.

In fact, the first global simulations of such binary system discs predate local simulations by more than two decades (Lin and Pringle, 1976). The first step they undertook was to understand whether an accretion disc formed in these binary systems. How to interpret the accretion conclusions of these very early numerical models is debatable (see discussion at the end of the article), however, they show that a disc can indeed be formed from a Roche lobe overflowing companion. Not much later, Paczyński (1977) showed that the maximum radial extent of the disc was dictated by the tidal potential's influence on the fluid particle orbits[3].

With the advent of Smoothed Particle Hydrodynamics methods (SPH, Gingold and Monaghan (1977) and Lucy (1977)), it became possible to produce more reliable models of accretion discs. These simulations enable them to produce simulations of the entirety of the accretion disc with an improved description of the fluid. Whitehurst (1988a,b) improved this method and applied it right away to dwarf novæ systems. They were particularly interested in understanding the sumperhump behaviour of UM UMa stars. A few years before, Vogt (1982) and Osaki (1985) had proposed that this behaviour could be explained by an eccentric disc. Studying these required the use of global simulations. Lubow (1991a) proposed a theoretical model to explain this eccentricy due to a tidal coupling to the disc. Concomitantly, they produced SPH simulation that validated their model (Lubow, 1991b). The properties of these eccentric discs have been studied extensively with global simulations; to mention only a few Kunze et al. (1997), Murray (1998), Smith et al. (2007) and Kley et al. (2008). Note that the last one of these articles differs from the others as the numerical method changed. Rather than SPH simulations, they produced finite-volume Godunov simulations. These are better suited to study sharp pressure structures compared to SPH models. This type of method is presented extensively in chapter 3.

The other large-scale mechanism that has been studied with global models is spiral density waves. They are a type of tidal interaction with the binary companion star. This type of interaction has been long studied (Darwin, 1879) in the context of planet-satellite interaction or star binary evolution. Cowling (1941) showed that such interaction could excite oscillatory modes in a polytropic gas body like a star.

Goldreich and Tremaine (1980) and then Papaloizou and Lin (1984) showed that this tidal coupling could excite density waves in the context of accretion discs. These density waves are spirals shaped, and propagate from the exterior of the disc towards inner

3. More details about the tidal truncation of the disc are presented in chapter 4.

regions. Sawada et al. (1986a,b) were the first to produce numerical simulations to specifically study these waves in semi-detached binaries. They showed that for hot discs ($\mathrm{Ma} \leq 10$) these spiral waves could propagate to the inner regions of the disc and carry a significant amount of angular momentum. Spruit (1987) then showed that in the case where these waves become sonic, they will steepen into shocks and will contribute to angular momentum transport in the disc. They estimate that the resulting transport scales as $\alpha \propto \mathrm{Ma}^{-3/2}$.

These waves were then studied through linear theory by Savonije et al. (1994), but also in full non-linear models. Savonije et al. (1994) produced finite-difference simulations of such disc and Artymowicz and Lubow (1994) studied them with SPH simulations. The former were particularly interested in understanding the efficiency of these waves in angular momentum transport. They concluded that for 'cold' discs with $\mathrm{Ma} \geq 25$ these wave produce only little accretion.

More recently Ju et al. (2016, 2017) produced global simulations of dwarf novæ discs to tie local and global effects together. Here again, they shifted towards a finite volume method (Athena++) rather than SPH method. Their first article focused on the dynamics driven by the spiral waves. First, they show that with temperatures relevant for the outburst phase spiral-driven accretion is already weak. They measure $\alpha \lesssim 0.05$. These values are closer to what is expected during the quiescence phase, but they explore a hot disc regime, with $\mathrm{Ma} \approx 50$ at the inner radius. They were not able to probe realistic temperature regime, that is a much thinner disc, for quiescence. However, they show that with decreasing temperature, angular moment transport decreases too. They report that the shock model from Spruit (1987) is not a good fit for the spirals they observe. They conclude however that the linear theory of Savonije et al. (1994) provides a satisfactory fit. They speculate, in agreement with linear theory, that in the colder quiescence phase, spiral-driven transport is very weak and may not be able to explain the values required by the DIM. In section 4.5, I present how I was able to reproduce their results.

In their second paper, they include the coupling to magnetic field, and compare the efficiency of MRI-driven accretion with spiral-driven accretion. They produce hot disc simulations with $\mathrm{Ma} \approx 10$. In this simulation, they see that the MRI-driven accretion and spiral-driven accretion are comparable when $\beta = 400$. They note that when increasing the magnetic field to $\beta = 100$ MRI-driven accretion surpasses spiral-driven accretion. They then attempted to produce a colder simulation with $\mathrm{Ma} \approx 20$, however, due to the increased numerical cost of this simulation they were not able to integrate long enough to reach a steady state. They observe however that in this colder simulation the spiral waves are more tightly wound, as expected from linear theory, and contribute less to angular momentum transport.

Finally, Pjanka and Stone (2020) produced global 3D MHD simulations of hot dwarf novæ discs. They produce a simulation with $\mathrm{Ma} \approx 5$ and a simulation with $\mathrm{Ma} \approx 10$. They found that accretion was highly variable on all timescales. Moreover, they find that the vertical position of the spiral pattern varies quickly on sonic timescale, but they do not mention any coherent global motion. They also find that above a couple of thermal scale-heights, there is a highly magnetised region or 'corona'. They report that this corona contributes to 30% to 50% of the measured accretion. Due to the high numerical cost of such simulations, they are only able to integrate them for 10 binary orbits. They believe that longer-term simulations should be carried out to explore the existence of a steady state, especially in low-temperature regimes.

2.5 CONCLUSION

From all the works presented in this chapter, we see that we have a rather good understanding of the accretion dynamics in dwarf novæ. The disc instability model provides a model for the periodic outburst-quiescence cycle. This model has some shortcomings,

but I will not repeat them here (see section 5 of Hameury (2020) for a review of those). Then, models focusing on more precise aspects of the dynamics of dwarf novæ discs were able to furnish physical mechanisms to explain the observed accretion during the outburst-quiescence cycle.

Indeed, during the outburst phase, we now know that the main accretion-driving mechanism is the magneto-rotational instability. As detailed above, this has been confirmed by both zoomed-in local simulations and global simulations. During this phase, it has been shown that the tidally-excited spiral waves still exist but do not contribute much to accretion compared to the MRI.

The quiescence phase, however, is still a blind spot of the models. Scepi et al. (2018b) and Scepi et al. (2019) showed that magnetic winds could be included in the DIM picture and were a possible accretion-driving mechanism during this phase. During this phase, the disc is cold and the MRI is quenched, so it also remains possible that spiral-driven accretion can drive the little accretion required by the DIM. Analytical and numerical estimates predict that this is not the case, but no model has explored realistic temperature regime for this phase yet ($\mathrm{Ma} \lesssim 1000$). It also remains to be shown that MHD winds survive in a global model during the quiescence phase; and their possible large-scale impact on such razor-thin resistive accretion discs are completely unknown to this day.

This is in this context that my PhD work comes in. In this work, I focus on understanding the accretion-driving mechanism relevant to the cold and poorly ionised quiescence phase. With the methods presented in the next chapter, I study dwarf novæ accretion discs at temperatures low enough to model the quiescence phase.

3

FINITE-VOLUME METHODS FOR FLUID DYNAMICS

Contents

3.1 Discretisation and Riemann solvers **49**
3.1.1 Finite-volume method 50
3.1.2 Godunov method 50
3.1.3 Fargo advection scheme 55
3.1.4 Constrained transport 57
3.1.5 Non-ideal MHD term: Ohmic resistivity 59
3.2 Strengths and limitations **59**
3.3 Numerical difficulties **60**
3.3.1 Floors and limiters 60
3.3.2 Fargo 60
3.3.3 High magnetisation 61
3.4 Numerical resources **62**

As presented in the previous chapter, there are several different ways to numerically study fluid dynamics for accretion discs. In this chapter, I present the method I used in this work, at the core of the Idefix code (Lesur et al., 2023)[1].

3.1 DISCRETISATION AND RIEMANN SOLVERS

The Euler equations presented in the previous chapter can be written as a hyperbolic partial differential equation system of the following form.

$$\partial_t \boldsymbol{q} + \boldsymbol{\nabla} \cdot \boldsymbol{F}(\boldsymbol{q}) = \boldsymbol{S} \tag{3.1}$$

where $\boldsymbol{q} = (\rho, \rho\boldsymbol{v}, \mathcal{E}) \in \mathbb{R}^{d+2}$ the local state of the flow and $\boldsymbol{F} : \boldsymbol{q} \mapsto (\rho\boldsymbol{v}, \rho\boldsymbol{v} \otimes \boldsymbol{v} + p\boldsymbol{I}_d, (\mathcal{E} + p)\boldsymbol{v}) \in \mathbb{R}^{d(d+2)}$ the corresponding fluxes, for a d-dimensional flow, that is $\boldsymbol{v} \in \mathbb{R}^d$. $\boldsymbol{S}$ is a possible source term. In the case of the MHD equations $\boldsymbol{q}$ and $\boldsymbol{F}(\boldsymbol{q})$ have additional dimensions to describe the magnetic field. Additionally, the magnetic energy and forces are included in relevant components of $\boldsymbol{q}$ and $\boldsymbol{F}(\boldsymbol{q})$.

Gravity also requires a special treatment. In Idefix, the potential energy is not included in the internal energy $\mathcal{E}$. Rather, the work of gravitational forces $\rho\boldsymbol{v} \cdot \boldsymbol{\nabla}\Psi$ are included as source terms are included as a source term. This means that the time variations of the potential energy $\rho\Psi$ are neglected. In general, this assumption is reasonable as the gravitational potential varies much more slowly than the other forms of energy. In the present work, I use a reference frame such that the potential is constant with respect to time. The gravitational forces $-\rho\boldsymbol{\nabla}\Psi$ are also included as source terms in the relevant equations.

1. The source code and documentation are available at https://github.com/idefix-code/idefix.

Additional terms that arise from non-Cartesian coordinate systems, *i.e.* curvature terms, are also included as source terms. Inertial forces arising from the choice of a rotating reference frame are included as source terms as well.

The variables in $\boldsymbol{q}$ are called the *conservative* variables, as equation (3.1) is a conservation equation. The usual variables of Euler equations $\rho, \boldsymbol{v}, p$ are the *primitive* variables, and going from one to the other is quite simple.

3.1.1 *Finite-volume method*

The idea of the finite-volume method is to discretise the integration domain in small volumes $\mathcal{V}_i$. We integrate equation (3.1) over such a volume and, in the case where there is no source term, we obtain

$$\int_{\mathcal{V}_i} \partial_t \boldsymbol{q} dV + \oint_{\mathcal{S}_i} \boldsymbol{F}(\boldsymbol{q}) \cdot d\boldsymbol{S} = 0. \tag{3.2}$$

with $\mathcal{S}_i = \partial\mathcal{V}_i$. We write the average of $\boldsymbol{q}$ over $\mathcal{V}_i$, $\boldsymbol{Q}_i = \frac{1}{V_i}\int_{\mathcal{V}_i} \boldsymbol{q} dV$ where $V_i = \int_{\mathcal{V}_i} dV$ is the measure of $\mathcal{V}_i$.

We now have discretised the flow state $\boldsymbol{q}$ over space, and obtained the following evolution equation.

$$\frac{d\boldsymbol{Q}_i}{dt} = -V_i \oint_{\mathcal{S}_i} \boldsymbol{F}(\boldsymbol{q}) \cdot d\boldsymbol{S} \tag{3.3}$$

In the above equation, I ignored the time-discretisation, to emphasise how the space-discretisation is carried out. by integrating this equation between t and $t + dt$, where t is some time and dt a discretised time step, this discretisation is restored. If the right-and-side is known for all times t, the time-integration is straightforward and can be carried out with any standard method be it a first time order Euler method (Euler, 1768) or a higher order Runge-Kutta method (Runge, 1895; Kutta, 1901). In this work, I use an order two Runge-Kutta method implemented in IDEFIX.

The space discretisation is done accordingly to this $\mathcal{V}_i$-$\mathcal{S}_i$ decomposition. In one dimension, we will write x_i the position of the centre of the volume element $\mathcal{V}_i$, and we will write $x_{i-\frac{1}{2}}$ and $x_{i+\frac{1}{2}}$ the positions of its boundaries $\mathcal{S}_i$. These lower indices will be used for any discrete field evaluated at cell centre or cell boundaries.

The remaining difficulty is to evaluate the fluxes $\boldsymbol{F}(\boldsymbol{q})$ on the boundaries $\mathcal{S}_i$ of our discretised volume elements $\mathcal{V}_i$, that is to compute $\boldsymbol{F}_{i\pm\frac{1}{2}}$.

3.1.2 *Godunov method*

The solution proposed by Godunov (1959) is to compute these fluxes as the solution of local Riemann problems (Riemann, 1860). This problem amounts to describing the time evolution of a fluid at a discontinuity. In the discretised picture, in one dimension with no source term, equation (3.1) becomes

$$\boldsymbol{q}_i^{n+1} = \boldsymbol{q}_i^n + \frac{\Delta t}{\Delta x}\left(\boldsymbol{F}^n_{i-\frac{1}{2}} - \boldsymbol{F}^n_{i+\frac{1}{2}}\right), \tag{3.4}$$

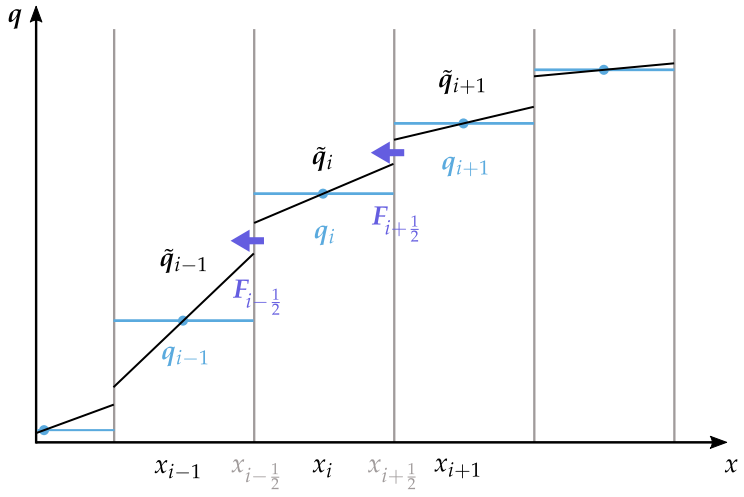

Figure 3.1 – Godunov discretisation in finite volumes, with average values $\boldsymbol{q}_i$ (light blue horizontal lines) used in the original Godunov method, reconstructed values $\tilde{\boldsymbol{q}}_i$ (black slanted lines) used by second-order Godunov methods and inter-cell fluxes $\boldsymbol{F}_{i\pm\frac{1}{2}}$ (dark blue arrows).

where the intercell fluxes $\boldsymbol{F}^n_{i\pm\frac{1}{2}}$ are computed as solutions of the Riemann problem at the interfaces between cells $i \pm 1$ and i. The upper index denotes the time step index. This discretisation is depicted on figure 3.1.

3.1.2.1 *Isolated Riemann problem*

Formally, the Riemann problem is the following one-dimensional initial-boundary value problem. With $x \in [x_L, x_R]$, with $x_L < 0 < x_R$.

$$\partial_t \boldsymbol{q} + \partial_x \boldsymbol{F}(\boldsymbol{q}) = 0, \tag{3.5}$$

with initial-boundary conditions

$$\boldsymbol{q}(x,0) = \begin{cases} \boldsymbol{q}_L, & \text{if} \quad x < 0, \\ \boldsymbol{q}_R, & \text{if} \quad x > 0, \end{cases} \tag{3.6}$$

$$\forall t \geq 0, \begin{cases} \boldsymbol{q}(x_L, t) = \boldsymbol{q}_L, \\ \boldsymbol{q}(x_R, t) = \boldsymbol{q}_R. \end{cases} \tag{3.7}$$

The solution to this problem involves several waves of density, pressure and velocity propagating from the discontinuity interface $x = 0$. In general, there will be waves propagating towards both negative x and positive x. The exact velocity, amplitude and type of these waves depend on the initial condition.

Depending on the equations solved, there will be different waves. In the pure hydrodynamics case, there will be two sound waves as well as an entropy wave. In the ideal magnetohydrodynamics case, there are in total seven waves: two Alfvén waves, two slow magnetosonic waves, two fast magnetosonic waves and an entropy wave.

When the systems is linear, *i.e.* when $\partial_x \boldsymbol{F}(\boldsymbol{q})$ can be written as a linear operation $\mathcal{L}_{\boldsymbol{F}} \partial_x \boldsymbol{q}$, the eigenvalues of $\mathcal{L}_{\boldsymbol{F}}$ give us the velocities of the different waves.

When the system is not linear, the waves may interact and produce more complex waves. In hydrodynamics, there can be shock waves, rarefaction waves and contact

waves. In the magnetohydrodynamics case, there may additionally be hybrid waves (Brio and Wu, 1988) and overcompressive shock waves (Liu, 1993).

Unfortunately, there is no general analytical solution for this problem (Toro, 1999) and we have to resort to numerical evaluation methods.

There exist *exact* solvers that can reach any arbitrary precisions (*e.g.* Godunov (1959) and Godunov et al. (1976)). These are however quite computationally heavy and are not used in large-scale fluid simulations. For large-scale simulations, like in this work, we use approximate Riemann problem solvers.

3.1.2.2 *Approximate Riemann solvers*

The most simple of these *Riemann solvers* is the Harten, Lax, van Leer (HLL) solver (Harten et al., 1983). This solver only uses a two-wave structure and approximates the regions between the wave fronts as homogeneous. This last approximation, of a piece-wise-constant description of the wave-fan remains in all solvers derived from the HLL solver like HLLC, HLLD, ... The structure used by this solver is shown on figure 3.2. In the HLL approximation, the left and right domains of the flow are identical to the corresponding initial condition. Between these regions is a mixed state $\boldsymbol{q}_{\mathrm{HLL}}$. Depending on the sign of the wave velocities, one can compute the flux at the $x = 0$ interface from either the left $\boldsymbol{q}_L$, the right $\boldsymbol{q}_R$ or the mixed $\boldsymbol{q}_{\mathrm{HLL}}$ state.

Using the above-mentioned assumption that the three regions, one can compute the state of the middle region. Assuming that the wave did not propagate to the boundaries, that is

$$x_L \leq TS_L, \quad \text{and} \quad x_R \geq TS_R \tag{3.8}$$

with S_L and S_R being the fastest signal velocities, we can integrate equation (3.3)

$$\int_{x_L}^{x_R} \boldsymbol{q}(x,T)dx = \int_{x_L}^{x_R} \boldsymbol{q}(x,0)dx + \int_0^T \boldsymbol{F}(\boldsymbol{q}(x_L,t))dt - \int_0^T \boldsymbol{F}(\boldsymbol{q}(x_R,t))dt. \tag{3.9}$$

The right-hand term is evaluated as follows.

$$\int_{x_L}^{x_R} \boldsymbol{q}(x,T)dx = x_R\boldsymbol{q}_R - x_L\boldsymbol{q}_L + T(\boldsymbol{F}_L - \boldsymbol{F}_R) \tag{3.10}$$

and the right-hand term yields

$$\int_{x_L}^{x_R} \boldsymbol{q}(x,T)dx = \int_{x_L}^{TS_L} \boldsymbol{q}(x,T)dx + \int_{TS_L}^{TS_R} \boldsymbol{q}(x,T)dx + \int_{TS_R}^{x_R} \boldsymbol{q}(x,T)dx \tag{3.11}$$

$$= \int_{TS_L}^{TS_R} \boldsymbol{q}(x,T)dx + (TS_L - x_L)\boldsymbol{q}_L + (x_R - TS_R)\boldsymbol{q}_R \tag{3.12}$$

where for $x \in [TS_L, TS_R]$, $\boldsymbol{q}(x,T) = \boldsymbol{q}_{\mathrm{HLL}}$ by definition. Hence, we have

$$\boldsymbol{q}_{\mathrm{HLL}} = \frac{S_R\boldsymbol{q}_R - S_L\boldsymbol{q}_L + \boldsymbol{F}_L - \boldsymbol{F}_R}{S_R - S_L} \tag{3.13}$$

and then the flux at $x = 0$,

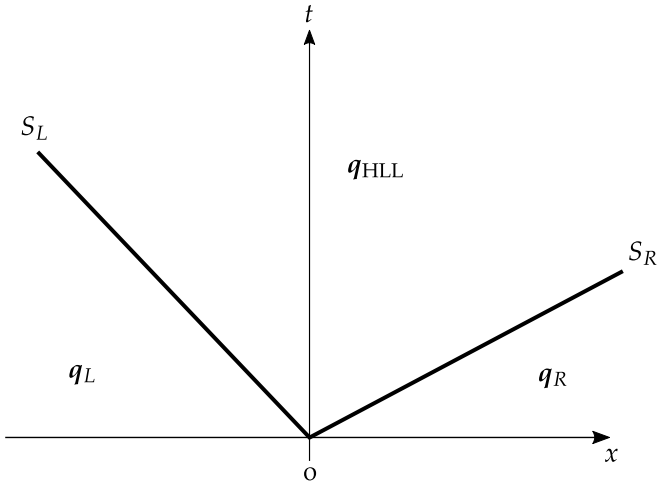

(a) HLL approximate solver wave structure.

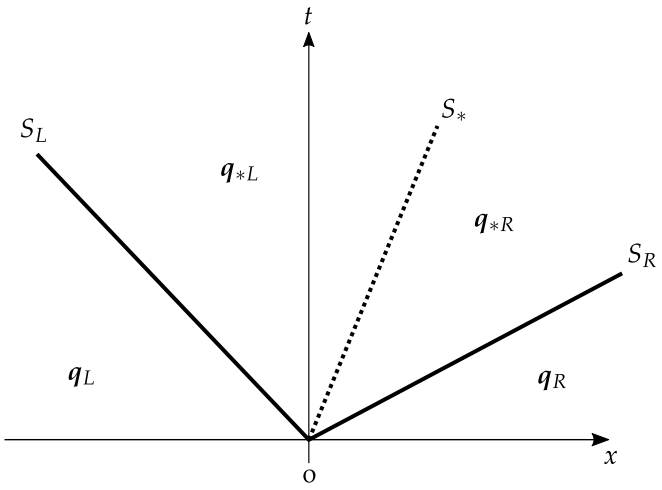

(b) HLLC approximate solver wave structure.

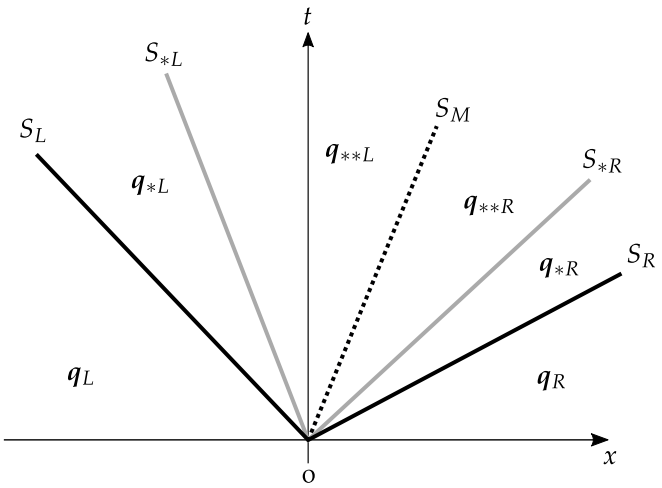

(c) HLLD approximate solver wave structure.

Figure 3.2 – Waves structures used by approximate Riemann problem solvers. The velocities of the waves are constant and the domains they separate are homogeneous in state.

$$\boldsymbol{F}_0^{\mathrm{HLL}} = \begin{cases} \boldsymbol{F}_L, & \text{if} \quad S_L \geq 0 \\ \dfrac{S_R \boldsymbol{F}_L - S_L \boldsymbol{F}_R + S_L S_R (\boldsymbol{q}_R - \boldsymbol{q}_L)}{S_R - S_L}, & \text{if} \quad S_L \leq 0 \leq S_R \\ \boldsymbol{F}_R, & \text{if} \quad S_R \leq 0 \end{cases} \tag{3.14}$$

In the case where $S_L \leq 0 \leq S_R$ this value comes from the Rankine-Hugoniot (Rankine, 1870; Hugoniot, 1889) condition on the shock front.

A more refined approximate solver is the HLLC solver (Toro et al., 1994) which restores the entropy (contact) wave of the Euler equation. The structure used in this approximate Riemann solver is shown on figure 3.2. In this work, I used the HLLC solver for all non-magnetic simulations.

In the magnetohydrodynamics case, additional waves need to be taken into account. The HLLD developed by Miyoshi and Kusano (2005) uses a five-wave structure (out of seven waves) to approximate the Riemann problem solution of ideal magnetohydrodynamics. In this solver, the waves taken into account are the fast-magnetosonic waves, the Alfvén waves and the contact wave; only the slow magnetosonic waves are ignored.

3.1.2.3 *Practical application*

In the above-mentioned approximate solutions, the values of the wave velocities S_L, S_R, S_*, ... were assumed to be known. As mentioned earlier, in the non-linear case, these velocities will differ from what the characteristic method [2] yields. In practice, the velocities are approximated to be the minimal and maximal sound wave velocity for the hydrodynamics case, and the minimal and maximal magnetosonic wave velocity for the magnetic case, from each state $\boldsymbol{q}_L$ and $\boldsymbol{q}_R$ as proposed by Davis (1988).

These wave velocities are also used for the Courant-Friedrichs-Lewy (CFL) condition (Courant et al., 1928). This condition ensures that no wave travels across more than one grid cell during one time step. It can be written as follows.

$$\Delta t \leq C_{\mathrm{CFL}} \frac{\Delta x}{S_{\max}}, \tag{3.15}$$

where $C_{\mathrm{CFL}} \in [0, 1[$ is the CFL number, and $S_{\max}$ is the maximum signal velocity in the cell of size Δx. If this condition is not satisfied, two wave fronts may cross and not interact when they should. This condition is illustrated on figure 3.3.

The approximate solutions presented above assume that the state of a cell is a homogeneous state. In practice, we use a linear reconstruction scheme inside the cells (van Leer, 1979) as illustrated on figure 3.1. This produces a second-order scheme thus improving the precision of the method. After this linear reconstruction, there still is a Riemann problem to be solved at each boundary. For a series of homogeneous states $\boldsymbol{q}_i$, the linear reconstruction yields $\tilde{\boldsymbol{q}}_i$, which is linear and defined for $x \in [x_{i-\frac{1}{2}}, x_{i+\frac{1}{2}}]$. The left and right states used in the approximate solver are, for the Riemann problem between cells i and $i+1$

2. This method allows computing the linear wave propagation velocities for a linear partial differential equation system. These velocities are the eigenvalues of the Jacobian of this system. For linearised Euler equations around a flow at v, the wave velocities are $\pm c_s + v$ with multiplicity 1, and v with multiplicity d.

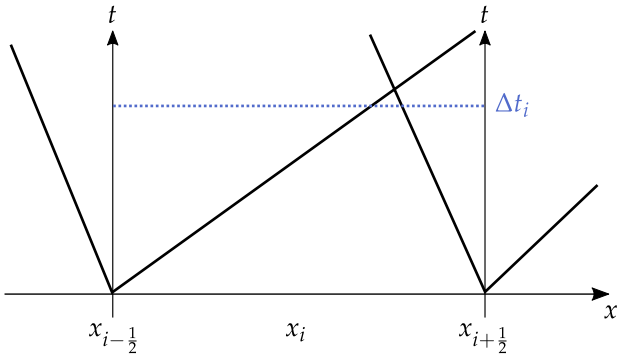

Figure 3.3 – Illustration of the CFL condition (3.15). The grey solid lines correspond to the wave propagating. For cell i, the time step Δt_i should be smaller than the time at which wavefronts will cross the opposite cell boundary.

$$\begin{cases} \boldsymbol{q}_L &= \tilde{\boldsymbol{q}}_i(x_{i+\frac{1}{2}}) \\ \boldsymbol{q}_R &= \tilde{\boldsymbol{q}}_{i+1}(x_{i+\frac{1}{2}}) \end{cases} \tag{3.16}$$

The fluxes $\boldsymbol{F}_L$ and $\boldsymbol{F}_R$ are computed as $\boldsymbol{F}(\boldsymbol{q}_L)$ and $\boldsymbol{F}(\boldsymbol{q}_R)$ respectively. Note that in IDEFIX, the reconstruction step is done on the *primitive* variables. In some other codes, this reconstruction is carried out on the characteristics variables[3]. It is only after this reconstruction step, that $\boldsymbol{q}_L$ and $\boldsymbol{q}_R$ are computed from the primitive variables for the inter-cell Riemann problems.

Finally, the reconstruction step has to satisfy several criteria to avoid Gibbs phenomenon (Wilbraham, 1848; Gibbs, 1898, 1899). In particular, it has to be *total variation diminishing* (TVD). This means that the total variation defined as $\mathscr{T} = \sum_i |\boldsymbol{q}_i - \boldsymbol{q}_{i+1}|$ must decrease at each time step.

$$\forall n \in \mathbb{N},\ \mathscr{T}^{n+1} \leq \mathscr{T}^n. \tag{3.17}$$

This condition together with the other stability conditions, which I do not repeat here (see chapter 13 of Toro (1999) for more details), do not fully constrain the reconstruction. This means that there are several possible TVD reconstruction schemes with different properties. By default, IDEFIX uses the van Leer reconstruction scheme (van Leer, 1974). It can also use the minmod scheme (Roe, 1986) in cases detailed in the following. This latter reconstruction method is more diffusive than the former.

3.1.3 *Fargo advection scheme*

In hydrodynamic systems where the Mach number is Ma $\gg 1$, the time step is mainly constrained by the fluid velocity rather than the sound speed. As discussed in the previous chapters, this is the case for quiescent dwarf novæ discs which have Ma $\gg 10$. Moreover, in this type of accretion disc, the flow velocity is mainly dominated by the azimuthal velocity, *i.e.* $|v_\varphi| \gg |v_R|$. In order to circumvent this limitation, one can split the evolution operator in two parts, a mean operator and a fluctuation one.

In practice this amounts to splitting $\boldsymbol{F}(\boldsymbol{q}) = \overline{\boldsymbol{F}}(\boldsymbol{q}) + \boldsymbol{F}'(\boldsymbol{q})$. As the limiting velocity is some advection velocity, this translates as

3. These are the variables corresponding to eigenvectors of the characteristic method.

$$\boldsymbol{\nabla} \cdot (\rho \boldsymbol{v}) = \boldsymbol{w} \cdot \boldsymbol{\nabla} \rho + \boldsymbol{\nabla} \cdot (\rho [\boldsymbol{v} - \boldsymbol{w}]) \tag{3.18}$$

where $\boldsymbol{w}$ is the advection velocity. In practice, this means that the flow is advected at $\boldsymbol{w}$ and the Riemann problem is solved only for the fluctuation part: $\boldsymbol{\nabla} \cdot (\rho [\boldsymbol{v} - \boldsymbol{w}])$.

This is the FARGO (Fast Advection in Rotating Gaseous Objects) algorithm developed by Masset (2000). In theory, any axisymmetric advection velocity can be used, or more generally an advection velocity such that $\partial_t \boldsymbol{w} = \boldsymbol{\nabla} \cdot \boldsymbol{w} = 0$. Practical uses of non-Keplerian velocities are discussed in section 3.3.2. The version of this advection scheme implemented in IDEFIX is close to the one implemented in PLUTO (Mignone et al., 2007, 2012a,b). This scheme is also compatible with MHD, but as will be discussed later, I only used it in non-magnetic simulations.

Let us here assume that the advection is along the x direction. The advection of the fluid at w corresponds to a shift of $\Delta x = w \Delta t$ at each time step. In general, this does not correspond to an integer number of cells. Rather, it corresponds to a shift of $m \in \mathbb{N}$ cells plus a residual δx. Along the advection direction, we have the following linear transport equation.

$$\partial_t \boldsymbol{q} + w \partial_x \boldsymbol{q} = 0 \tag{3.19}$$

Using the fact that for this linear step, we have

$$\forall\ t, \Delta t,\ \boldsymbol{q}(x, t + \Delta t) = \boldsymbol{q}(x - w\Delta t, t) \tag{3.20}$$

we can discretise the transport equation as follows.

$$\boldsymbol{q}_i^{n+1} = \boldsymbol{q}_{i-m}^{n} - \frac{\delta x}{\Delta x} \left[H_{i-m+\frac{1}{2}} - H_{i-m-\frac{1}{2}} \right] \tag{3.21}$$

where $H_{i+\frac{1}{2}} = \frac{1}{\delta x} \int_{y_{i-\frac{1}{2}}}^{y_{i+\frac{1}{2}}} \boldsymbol{q}^n(x) dx$. The second term of the right-hand side corresponds to the fact that the advection does not correspond to an integer number of cells. To compute this quantity, one needs to choose a reconstruction method for $\boldsymbol{q}$ inside the cells. In this work, I use the piecewise linear method implemented in IDEFIX.

Here, as we are working in the rotating reference frame we used $\boldsymbol{w} = (v_\mathrm{K} - \omega R) \boldsymbol{e}_\varphi$, the Keplerian velocity modified by the rotation of the frame.

This algorithm is implemented to be compatible with any MPI (MPI Forum, 2021) domain decomposition. However, a large amount of cells may need to be exchanged when used together with an azimuthal domain decomposition. This can significantly slow down the execution. As a consequence, azimuthal domain decomposition should be used with care when using the FARGO scheme.

Using this algorithm thus allows for increased time step, as we now use the modified CFL condition

$$\Delta t \leq C_\mathrm{CFL} \frac{dx}{|\boldsymbol{S}_\mathrm{max} - \boldsymbol{w}|} \tag{3.22}$$

where $S_{\max}$ is the fastest wave, and w is chosen such that $|S_{\max} - w| \ll |S_{\max}|$. This scheme also reduces the numerical diffusivity compared to not using the scheme (Masset, 2000).

An added benefit of using this scheme is that the quantities that we are interested in measuring often correspond to the departure to the advection flow. For instance, measuring the accretion properties of the flow requires measuring quantities arising from $v - w$. This is the case for $\dot{M}$ or α. When using the FARGO algorithm, these quantities are readily available as the outputs of the Riemann solvers.

3.1.4 *Constrained transport*

When solving for the magnetohydrodynamics equations, one needs to evolve the magnetic field in addition to the hydrodynamics fields. Doing so in a naive fashion will not ensure that $\boldsymbol{\nabla} \cdot \boldsymbol{B} = 0$, and this is why we need to use a finer method like *constrained transport* to evolve the magnetic field as proposed by Evans and Hawley (1988). To do so, we compute the electric fields on the edges of the cells and the magnetic fields on the faces of the cells.

For instance, using a tridimensional cell face $\mathcal{S}$, we can write the surface-integrated induction equation

$$\partial_t \int_{\mathcal{S}} \boldsymbol{B} \cdot d\boldsymbol{S} = - \oint_{\mathcal{C}} \boldsymbol{E} \cdot d\boldsymbol{l}, \tag{3.23}$$

with $\mathcal{C} = \partial\mathcal{S}$. The right-hand side can be space-discretised. To simplify the notation we have that $\mathcal{V}$ is homeomorphic to a cube $\mathcal{V} \cong [x^-, x^+] \times [y^-, y^+] \times [z^-, z^+]$. Let z be the direction normal to the cell face $\mathcal{S} \cong [x^-, x^+] \times [y^-, y^+]$. x and y are the two other dimensions, such that (x, y, z) is direct.

$$\oint_{\mathcal{C}} \boldsymbol{E} \cdot d\boldsymbol{l} = E_x^- dx^- - E_x^+ dx^+ + E_y^+ dy^+ - E_y^- dy^- \tag{3.24}$$

As the faces of $\mathcal{V}$ have common edges, the integrated electric fields will cancel out, ensuring $\partial_t \int_{\partial\mathcal{V}} \boldsymbol{B} \cdot d\boldsymbol{S} = 0$. As a consequence, the divergence of the magnetic field is conserved at machine precision, and provided it is initially zero it will remain that way.

This relies on the fact that the electric fields on the same cell edge have the same value regardless of the face used to compute it. One-dimensional Riemann solvers presented here however yield the values of the electric fields on the face surfaces and not on the edges. These values need to be evaluated on the cell edges. There are several ways to do so, and I used two different methods in this work. The first one is an averaging procedure proposed by Gardiner and Stone (2005), formally this is a constrained transport algorithm that includes a contact wave, propagating at S. In this case, the electric fields are first computed on each cell face and at cell centres, and then computed on cell edges.

$$
\begin{aligned}
E_{i+\frac{1}{2},j+\frac{1}{2}} &= \frac{1}{2}\left(E_{i,j+\frac{1}{2}} + E_{i+1,j+\frac{1}{2}} + E_{i+\frac{1}{2},j} + E_{i+\frac{1}{2},j+1}\right) \\
&\quad -\frac{1}{4}\left(E_{i,j} + E_{i+1,j} + E_{i,j+1} + E_{i+1,j+1}\right) \\
&\quad +\frac{S}{8}\left(B^x_{i+\frac{1}{2},j} - B^x_{i,j} - B^x_{i+\frac{1}{2},j+1} + B^x_{i,j+1}\right) \\
&\quad +\frac{S}{8}\left(B^x_{i+\frac{1}{2},j} - B^x_{i+1,j} - B^x_{i+\frac{1}{2},j+1} + B^x_{i+1,j+1}\right) \\
&\quad +\frac{S}{8}\left(B^y_{i+1,j+\frac{1}{2}} - B^y_{i+1,j} - B^y_{i,j+\frac{1}{2}} - B^y_{i,j}\right) \\
&\quad +\frac{S}{8}\left(B^y_{i+1,j+\frac{1}{2}} - B^y_{i+1,j+1} - B^y_{i,j+\frac{1}{2}} + B^y_{i,j+1}\right)
\end{aligned}
\tag{3.25}
$$

where E is the electric field along the third dimension z, which not indexed here. B^x and B^y are the components of the magnetic field in the x and y directions. The other method I used is taken from Londrillo and del Zanna (2004) and Mignone and Del Zanna (2021) and is more computationally expensive as it relies on solving two-dimensional Riemann problems. As this second method is more expensive, I only used it when the previous method failed and produced either very large $\boldsymbol{\nabla} \cdot B$ values, or straight-up NaNs (Not-a-Number), which can occur when the computed pressure ends up being negative because of truncation errors.

In practice, even with these methods, round-off errors can and will accumulate in the divergence of the magnetic field. When the simulations require billions of time steps, the accumulated error may become significant. To circumvent this problem, I use the vector potential formalism, with $\boldsymbol{A}$ such that $\boldsymbol{B} = \boldsymbol{\nabla} \wedge \boldsymbol{A}$ and $\boldsymbol{E} = -\partial_t \boldsymbol{A}$. This has an additional computational cost as it requires storing more fields, but proved necessary in this work. In this case, the procedure is as follows.

1. Compute the electric field $\boldsymbol{E}(t + \Delta t)$ on the cell edges with the chosen method.
2. Evolve the potential vector $\boldsymbol{A}(t + \Delta t) = -\int_0^{t+\Delta t} \boldsymbol{E}(\tau) d\tau$ on the cell edges.
3. Compute the magnetic field $\boldsymbol{B}(t + \Delta t) = \boldsymbol{\nabla} \wedge \boldsymbol{A}(t + \Delta t)$ from the new vector potential.
4. Reconstruct the cell-centred magnetic field.

This means that the initial magnetic field condition has to be given in terms of $\boldsymbol{A}$ rather than $\boldsymbol{B}$. This method, however, is not infallible. As $\boldsymbol{A}(t) = -\int_0^t \boldsymbol{E}(t) d\tau$, if there is a constant electric field, the value of the vector potential can become very large with time. This may lead to truncation errors when computing $\boldsymbol{\nabla} \wedge \boldsymbol{A}$ and cause an increased value of the divergence of the magnetic field. I indeed see a noticeable increase in the value of $\boldsymbol{\nabla} \cdot \boldsymbol{B}$, but that remains reasonably small compared to $B/\Delta x$.

3.1.5 *Non-ideal MHD term: Ohmic resistivity*

In this work, the only non-ideal magnetohydrodynamic term used is Ohmic resistivity. Its effect is to add an electric field $\eta \boldsymbol{j}$ to the induction equation. This term is added between steps 1 and 2 of the procedure described above.

The values of the Ohmic resistivity η are interpolated from a precomputed table of solution of Saha equation (Saha, 1920). The tables used are the same as in Scepi (2019), and assume solar composition of Grevesse and Sauval (1998), that is hydrogen abundance $X = 0.7$ and metallicity $Z = 0.02$. Hence, the local value of the Ohmic resistivity depends on the local density and temperature. Further specifics of the resistivity implementation are discussed in chapter 5.

To properly capture this parabolic term of the partial differential equation, there is an additional CFL condition that constrains the global simulation time step. Here we want to resolve the diffusion time scale associated with this term, *i.e.* we must have

$$\Delta t \leq C_{\mathrm{CFL}} \frac{\Delta x^2}{2\eta}, \tag{3.26}$$

where η is the Ohmic resistivity, Δx is the cell size, and $C_{\mathrm{CFL}} \in [0, 1[$ is the CFL number. In practice, the global time step of the code is computed as

$$\Delta t = C_{\mathrm{CFL}} \left(\max_{\mathscr{V}} \left[\sum_d \left(\frac{c_{\mathrm{max},d}}{\Delta x_d} + \frac{2\eta}{\Delta x_d^2} \right) \right] \right)^{-1} \tag{3.27}$$

where $\mathscr{V}$ is the whole simulation domain, c_{max} is the fastest signal velocity in a cell, and d indexes the dimensions.

3.2 STRENGTHS AND LIMITATIONS

Like any method, finite volume methods have strengths and weaknesses. It is important to keep them in mind to be able to use the best method to address a given physics problem.

The main advantage of finite-volume method is that it readily includes a proper description of (magneto-) hydrodynamics shocks. There is no intrinsic problem caused by the discontinuity of the evolved fields as the Riemann problem is in itself a type of discontinuity problem. This means that entropy is not artificially conserved when it should not be, as it can be the case in Hamiltonian methods. Hence, there is no need to add *ad hoc* dissipation terms of unknown physical origin.

Grid-based methods are however not flawless either. For instance, in the case of IDEFIX, the grid is static during the simulation. This means that if thin structures develop in low-resolution regions of the grid, they will be poorly resolved. This is not the case with Adaptive Mesh Refinement methods like ATHENA++. However, this feature is not implemented in IDEFIX for the time being, meaning that we have to try and anticipate where the thin structure will develop. This problem will be relevant in chapter 5.

Another known limitation of finite volume methods arises in magnetic simulations, in regions with low pressure and strong magnetic field, *i.e.* when $\beta \ll 1$. Miyoshi and Kusano (2005) proved the positivity-preserving property of the HLLD solver in one dimension, however this property is not guaranteed in higher dimensions. As I use one-

dimensional Riemann solvers, this problem can not occur in my simulations. However, when the energy equation is solved for, it may occur that the field values produced by the Riemann solver are such that the reconstructed pressure is negative as :

$$P = (\gamma - 1)\left(e - \frac{1}{2}v^2 - \frac{B^2}{2\mu_0}\right) \tag{3.28}$$

this error is especially likely to occur in highly magnetised regions where $\frac{B^2}{2\mu_0} > P$. This means that the behaviour of finite-volume methods in highly magnetised regions should be interpreted with caution. Using a more diffusive solver like HLL can mitigate this effect, at the price of increased numerical diffusion.

Finally, these methods also include a numerical dissipation, be it because of the error of the numerical evolution scheme, because of the spatial discrete grid or because of the properties of the chosen approximate Riemann solver. These effects are often hard to quantify and can sometimes hinder the convergence of simulation. See for example McNally et al. (2019) for a discussion on the effect of numerical viscosity or Nixon et al. (2024) for a discussion on numerical resistivity. These highlight the necessity of some kind of convergence tests for numerical works.

3.3 NUMERICAL DIFFICULTIES

Here, I present some of the numerical difficulties I encountered in this work and the solutions I used to circumvent them.

3.3.1 *Floors and limiters*

In all simulations presented in this work, I impose some kind of density floor. In non-magnetic simulations, a density floor is necessary to prevent the apparition of a very sharp gradient over a few radial cells at the outer truncation of the disc. In magnetic simulations, in order to limit the influence of the Alfvén velocity on the time step, I also impose an Alfvén velocity limiter. The density floors I use are implemented in such a way that some of the fluid momentum is conserved by the transformation. In the magnetic case, to limit the Alfvén velocity, I change the density of the cell.

The specifics about these floors and limiters are detailed in the relevant section of part ii.

3.3.2 *Fargo*

The first numerical difficulty I encountered is relevant to the results presented in chapter 4. For these two-dimensional non-magnetic simulations, I made extensive use of the FARGO algorithm presented above. Indeed, in the non-magnetic case, the limiting constraint to the time step is the azimuthal velocity of fluid. This velocity is approximately Keplerian, and is much greater than all other velocities. As a matter of fact, for a 1024^2 simulation, I obtained a speed-up factor of about 30 when using this algorithm.

However, as the dwarf novæ discs are tidally truncated at some outer radius, the outer regions of the simulation domain are not actually being advected at v_K. Moreover, the Keplerian velocity rapidly decreases away from the inner radius, and thus the time step constrain rapidly relaxes at larger radii. Hence, there is no point in using the advection scheme in the outermost parts of the simulation box.

As presented in Masset (2000), the advection velocity used in the advection scheme needs only be axisymmetric. I thus implemented a more relevant advection velocity of the following form.

$$\boldsymbol{w}(R) = \frac{1}{2}\left[v_\mathrm{K} - \omega R\right] \times \left[1 - \tanh\left(\frac{R - R_\mathrm{v}}{h_\mathrm{v}}\right)\right] \boldsymbol{e}_\varphi \tag{3.29}$$

where $v_\mathrm{K} = \sqrt{\frac{GM_\mathrm{WD}}{R}}$ is the Keplerian velocity, ω is the angular frequency of the binary system, R_v is the transition radius above which the advection velocity decreases to zero, an h_v is the width of the transition.

Using this advection scheme shortened the run time of my simulations. Indeed, in the outer regions, the fluid velocity differs from the Keplerian velocity by a large amount, *i.e.* $|\boldsymbol{v} - \boldsymbol{v}_\mathrm{K}| \ll \boldsymbol{v}_\mathrm{K}$. This means that, in this region, the modified CFL condition of the FARGO scheme (3.22) is no longer relevant, and produces a time step larger than the regular CFL condition (3.15) would. However, it also produced some artefacts in the flow structures as shown on figure panel (b) of 3.4.

I tested a wide range of parameters to understand the apparition of these wave-like artefacts, but I did not find any way to predict whether it would appear or not in a given simulation. For instance, I initially thought that it only appeared when $h_\mathrm{v} \leq H$, the disc height scale, but I also observed this behaviour in simulations with $h_\mathrm{v} \gg H$.

As a consequence, I only used a Keplerian (that is $v_\mathrm{K} - \omega R$) advection velocity for this work. As shown on figure 3.4, this advection velocity does not produce these artefacts, and the spiral structure is very close to the spiral structure I obtain when do not use the FARGO advection algorithm at all. In the magnetic simulations of chapter 5, the time step was no longer constrained by the Keplerian flow, so I did not use this algorithm.

3.3.3 *High magnetisation*

In my magnetic simulations, I observed the apparition of sharp density variations over the scale of one cell. These sharp structures are poorly resolved and can not be interpreted physically.

Typical structures that can arise are chequerboard features in the density field, as illustrated on panel (a) of figure 3.5. On this figure, it is very clear that they appear only in regions where $\beta_\mathrm{p} \ll 1$. These structures are unphysical and need to be avoided.

A way to avoid them is to use the HLL solver rather than the HLLD solver. The former being much more diffusive, such structures will be smoothed out. However, this means increasing the numerical diffusivity everywhere in the simulation domain, even in the disc where there is no problem as $\beta \gg 1$.

To circumvent this, Scepi et al. (2018a) chose to change the approximate solver used depending on the Riemann problem to solve. For instance, when the pressure difference between two adjacent cells is "large", they use the more diffusive HLL solver to avoid possible failures of HLLD. This feature is not implemented in IDEFIX because it is in strong contradiction with the Single Instruction Multiple Data (SIMD) paradigm of GPU architecture, doing so would very strongly decrease the performances of the code.

Instead, I implemented a simpler solution making use of the `shockFlattening` option of IDEFIX. This feature enables to use the minmod limiter when shocks are considered strong, that is when $|\boldsymbol{\nabla} P/P|$ exceeds a user-specified value, thus increasing the numerical diffusivity. As shown on panel (b) of figure 3.5, using this option as is, is not enough. In order to smooth these structures, one would need to use a very small threshold of $|\boldsymbol{\nabla} P/P|$, thus smoothing all small-scale structures of the simulation.

In order to more effectively smooth the shocks in highly magnetised regions, and not use too small a threshold that would smooth the disc structures, I implemented a custom version of this module. With this version, the user can specify the condition that a shock

must satisfy to be targeted for the use of the minmod limiter. This new feature is now publicly available.

For my simulations, the shocks have to satisfy either following conditions to be smoothed by the minimod limiter:
— it must be "strong", that is $|\boldsymbol{\nabla} P/P| > 1$, or
— it must occur in a highly magnetised region, that is $\beta < 10^{-1}$.

These values were chosen after several test runs. The condition needed to be strong enough such that the chequerboard pattern is smoothed, but does not smooth out small disc structures. The results of this method are shown on panel (c) of figure 3.5. On this figure, we see that the chequerboard structures in high magnetisation regions have disappeared. We also see that the very thin density structures close to the disc have been smoothed a little but remain clearly visible.

3.4 NUMERICAL RESOURCES

In this PhD work, I used the resources of different computing clusters. For the simulations of 4, I mostly used the local meso-centre from the Université Grenoble Alpes: GRICAD (Grenoble alpes Recherche Infrasturcture de Calcul Intensif et de Données)[4], in particular the computing clusters Dahu and Bigfoot. These clusters are equipped with V100 and A100 Nvidia GPUs.

I also use the V100 Nvidia GPU installed at the French national computing centre IDRIS, on the Jean Zay supercomputer[5] for the largest simulation of chapter 4 and for the initial computation of simulations of chapter 5.

Finally, I used the Mi250 AMD GPU installed in the Adastra machine of the French national computing CINES[6] for most of the work presented in chapter 5.

4. https://gricad.univ-grenoble-alpes.fr/
5. http://www.idris.fr/jean-zay/
6. https://www.cines.fr/calcul/adastra/

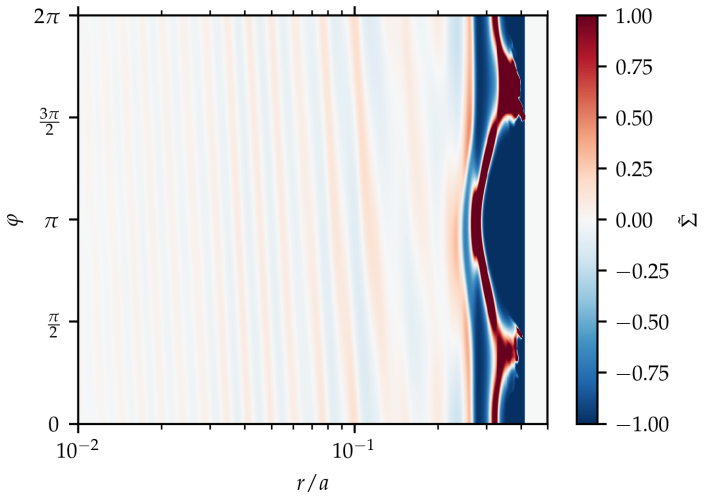

(a) De-projected density profile with FARGO disabled.

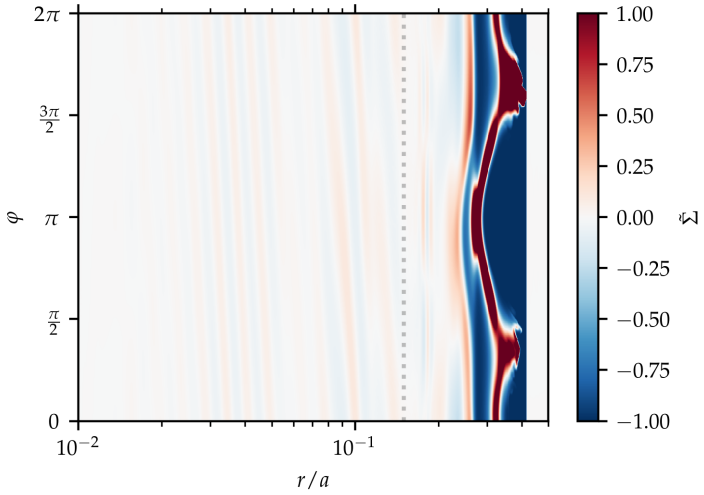

(b) De-projected density profile with vanishing FARGO velocity.

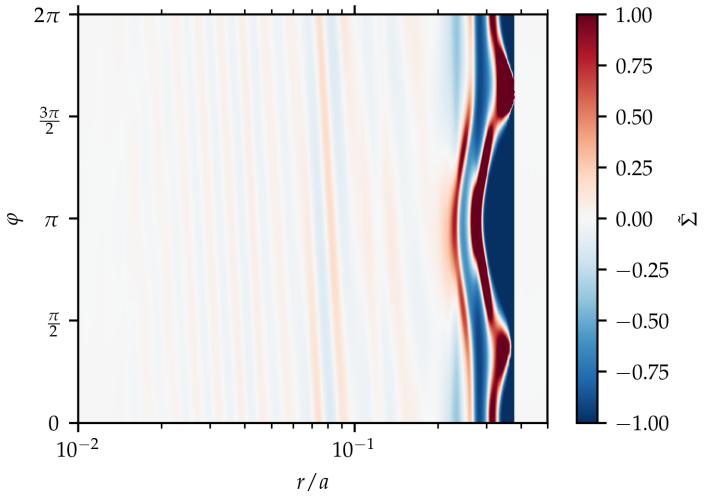

(c) De-projected density profile with keplerian FARGO velocity.

Figure 3.4 – Plots show the de-projected relative difference of the density to its azimuthal average after 20 binary orbits for different advection velocities. Here $R_v = 0.15$ (grey dotted line on panel (b)). Differences between the plots are clearly visible at $R \approx 0.15$ and $R \approx 0.06$ where the spirals appear to fade.

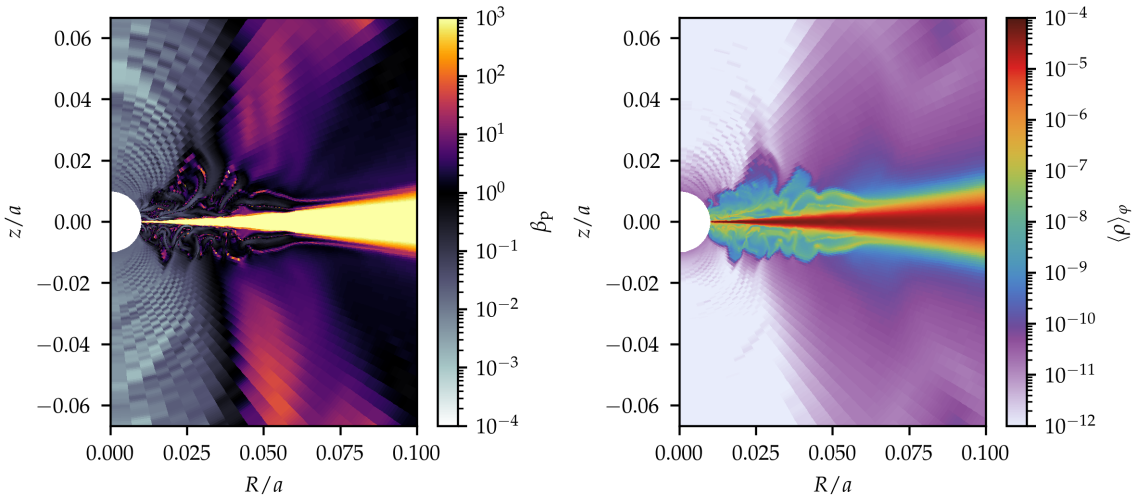

(a) With no `shockFlattening`.

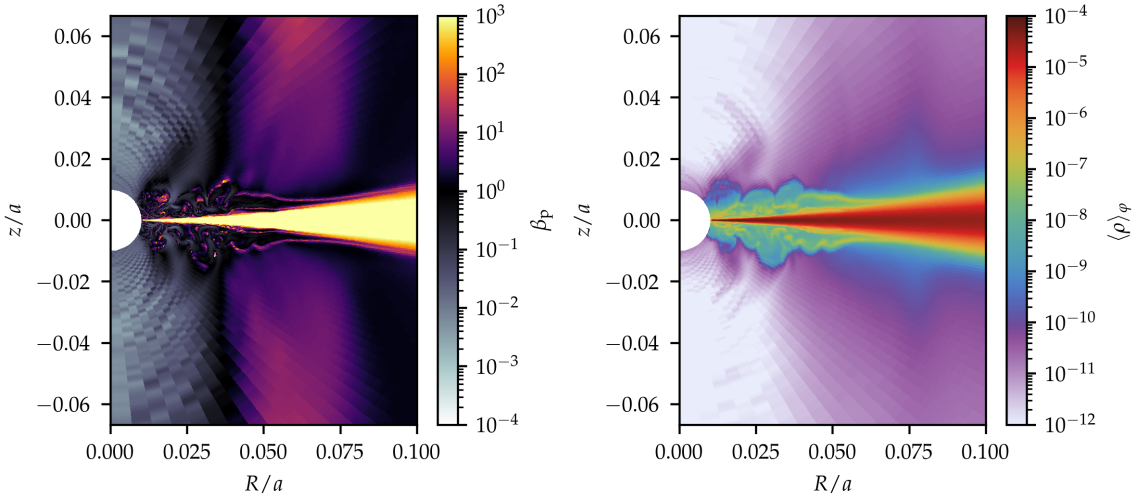

(b) With the original `shockFlattening`.

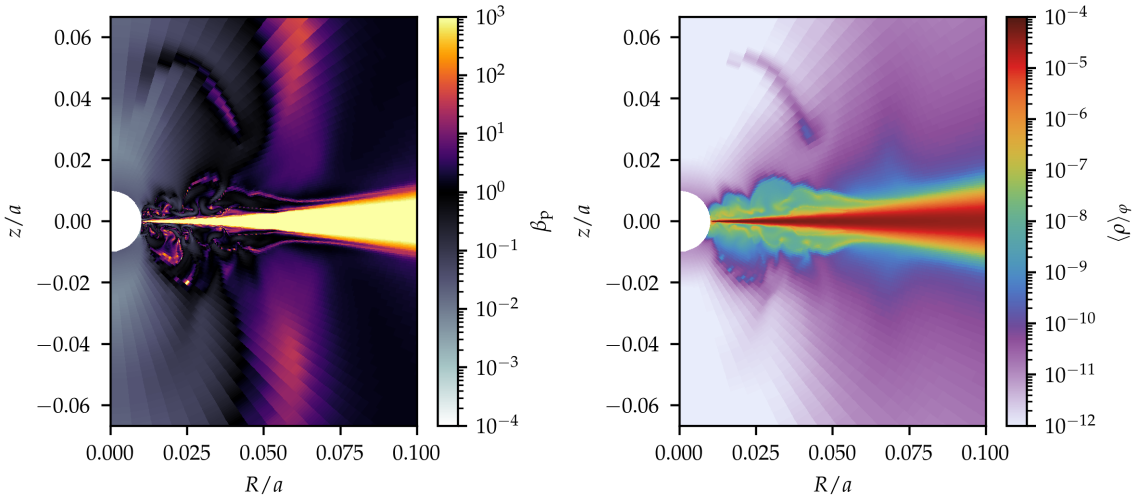

(c) With the custom `shockFlattening`.

Figure 3.5 – Consequences of unphysical results yielded by the approximate Riemann solvers. These snapshots are taken from three resistive simulations with initial $\beta_{\mathrm{p}} = 10^{4}$ and 0.03 binary orbits after the initial condition. **Left:** Poloidal β plasma parameter. **Right:** Azimuthal average of the density.

Part II

RESULTS

4

SPIRAL SHOCKS IN THIN BINARY DISCS

Contents

4.1 Adding the secondary star **67**
4.1.1 Gravitational potential 68
4.1.2 Reference frame 68
4.1.3 Matter stream 70
4.2 Analytical derivation of spiral-wave solutions **70**
4.2.1 Equations 71
4.2.2 Spiral waves 71
4.2.3 Linear order approximation 71
4.2.4 Results 73
4.3 Collapse of linear theory: On the necessity of numerics **74**
4.4 Numerical setup **75**
4.4.1 Grid and units 75
4.4.2 Boundary conditions 76
4.4.3 Initial condition 76
4.4.4 Handling of the tidal truncation 77
4.4.5 Inertial forces 77
4.4.6 List of simulations 77
4.4.7 Averaging methods 78
4.5 Reproducing previous works **78**
4.6 Eccentric spirals **82**
4.6.1 Eccentricity growth and mass ratio 86
4.6.2 Spiral pattern speed 88
4.7 Spiral transport **90**
4.7.1 Relaxation time 90
4.7.2 Angular momentum transport 91
4.7.3 Removing the secondary star 92
4.7.4 Resolution test 94
4.8 Spiral shock heating **95**
4.8.1 On the importance of thermodynamics 95
4.8.2 MRI unstable regions ? 99
4.9 Summary and consequences for future works **99**

DURING QUIESCENCE, the accretion disc of dwarf novæ systems is cold, poorly ionised and highly resistive. As a consequence, during this phase, magnetic accretion mechanisms have a reduced efficiency compared to during the outburst. In this chapter, I explore a purely hydrodynamical global accretion-driving mechanism: spiral-shock-driven accretion. As this mechanism does not require any coupling to the magnetic field, its relative contribution to accretion is highest during the quiescence phase. Most of the results presented in this chapter are published in Van den Bossche et al. (2023).

4.1 ADDING THE SECONDARY STAR

As I discussed in the introduction chapters, in order to have a complete picture of the accretion in compact binaries systems, and in particular in semi-detached binaries,

it is crucial to take into account the presence of a close companion star. As discussed in section 2.2, the Disc Instability Model does so while being a purely one-dimensional model. Here, as I aim to obtain a global, multidimensional description of the accreting system, the description of the companion star needs to be refined.

4.1.1 *Gravitational potential*

The first of these effects is the strong gravitational influence of the secondary star. In dwarf novæ systems, the radial extent of the disc is usually comparable to the separation of the binary system. We can typically have the disc extending up to half the binary separation. This means that in these regions of the disc, the gravitational pull of the secondary star should not be neglected. More quantitatively, in these systems, the ratio of the gravitational force of the secondary star to the gravitational pull of the white dwarf can reach 30% in the outer disc.

The potential of the secondary star is approximated as another point-mass potential. This way, the total gravitational potential of the system is the sum of the potentials of both stars $\psi = \psi_{\mathrm{WD}} + \psi_{\mathrm{s}}$,

$$\psi(\boldsymbol{r}) = -\frac{GM_{\mathrm{WD}}}{|\boldsymbol{r} - \boldsymbol{r}_{\mathrm{WD}}|} - \frac{GM_{\mathrm{s}}}{|\boldsymbol{r} - \boldsymbol{r}_{\mathrm{s}}|}, \tag{4.1}$$

where G is the gravitational constant, M_{WD} and M_{s} the masses of the white dwarf and the secondary star respectively, and $\boldsymbol{r}_{\mathrm{WD}}$ and $\boldsymbol{r}_{\mathrm{s}}$ their positions. Note that this potential does not describe regions inside the stars. Note also that this potential is not spherically symmetric.

The most striking effect of the potential of the secondary star is that it limits the size of the accretion disc around the white dwarf. Indeed, an accretion disc inside a binary system can not extend beyond the first Lagrange point.

In fact, the maximum extent of the accretion disc is even smaller than the radius of the L_1 point. Paczyński (1977) gives an estimation of this truncation radius. Their argument relies on the orbits of test masses in the binary potential. Close to the white dwarf, the test-mass orbits are almost Keplerian and circular, as the influence of the secondary star is negligible. However, at radii further away from the white dwarf, the orbits are distorted, as shown on figure 4.1; so much so that outer orbits intersect inner orbits. The radius given by Paczyński (1977) corresponds to the outermost radius for non-intersecting orbits. Like the L_1 point radius, this outermost radius scales with the mass ratio of the binary system. For the mass ratio range $q \in [0.03, 0.7]$ relevant for dwarf novæ, this truncation radius is close to 70% of the distance to the first Lagrange point. This means that the disc extends at most to radii ranging from 60% to 40% of the binary orbital separation. Although not a direct illustration of Paczyński (1977)'s model, we can already understand the change in disc size with mass ratio clearly visible on figure 4.10 with this model.

4.1.2 *Reference frame*

In order to simplify our study, we choose to work in a reference frame centred on the white dwarf. At times, we will also choose a rotating reference frame, in which the secondary star is stationary.

It is crucial to note that neither of these reference frames is inertial (Galilean), as they are not centred on the centre of mass of the binary system. To compensate for this, we have to include inertial forces. When the reference frame is not rotating, it is enough to add an *indirect potential* term.

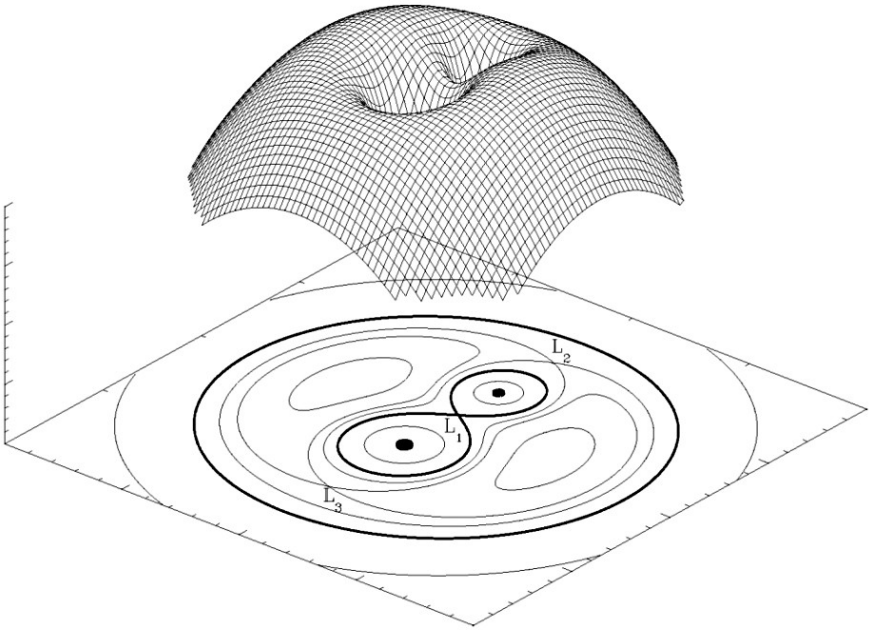

(a) Roche potential.

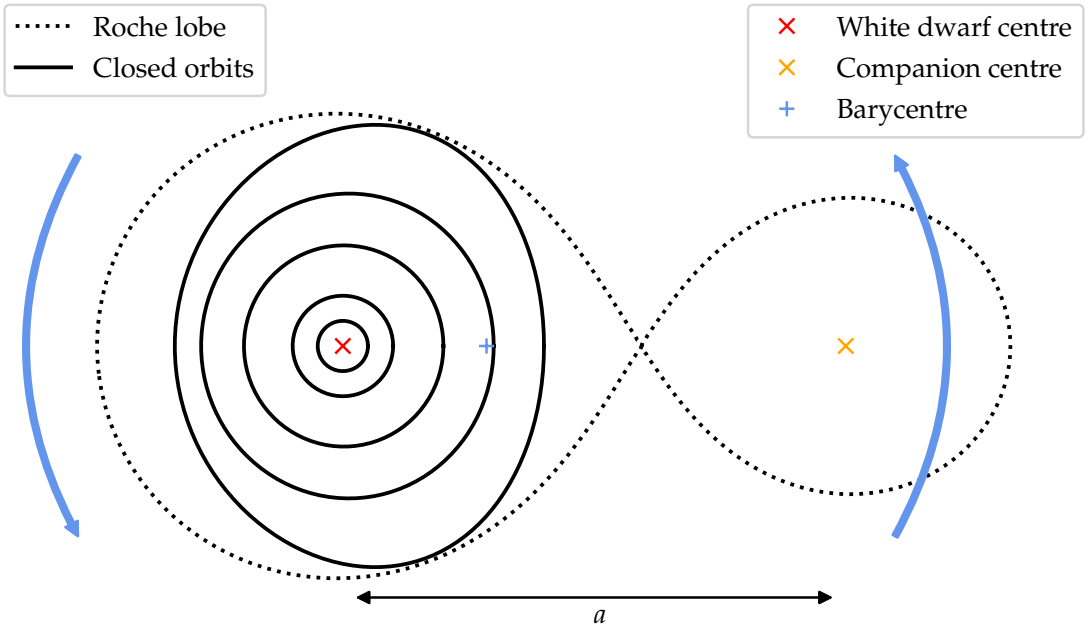

(b) Closed orbits in a tidal potential.

Figure 4.1 – **Top:** Roche potential, including the tidal forces and the centrifugal force in a reference frame centred on the centre of mass of the system. The contours are isopotential curves in the binary plane. The first three Lagrange points are represented at the intersection of these contours. **Bottom:** Closed prograde orbits inside the Roche potential at different radii. At radii away from the white dwarf, the orbits are distorted compared to Keplerian circular orbits. The represented orbits, Roche lobe, and centre of mass position are computed for the same potential, with $q = 0.4$. The arrows represent the orbital motion of the binary around its barycentre.

$$\Psi(\boldsymbol{r}) = -\frac{GM_{\mathrm{WD}}}{|\boldsymbol{r}-\boldsymbol{r}_{\mathrm{WD}}|} - \frac{GM_{\mathrm{s}}}{|\boldsymbol{r}-\boldsymbol{r}_{\mathrm{s}}|} + \frac{GM_{\mathrm{s}}}{a^3}\boldsymbol{a}\cdot\boldsymbol{r} \tag{4.2}$$

where $\boldsymbol{a} = \boldsymbol{r}_{\mathrm{s}} - \boldsymbol{r}_{\mathrm{WD}}$ is the binary separation. Note that we will always assume that the binary has a circular orbit, that is that a is a constant.

The thus obtained total potential is a tidal potential in that the force derived from it is exactly the tidal forces of a binary system.

When the reference frame is rotating, one needs to include the centrifugal force as well as the Coriolis force. The former can be written as deriving from a potential. The potential obtained when including the centrifugal force is called Roche potential; however, the Roche potential is usually expressed in an inertial reference frame, without the indirect term.

Each potential well is called *Roche lobe*. One usually takes the 8-shaped iso-potential surface crossing the first Lagrange point to define them, as shown on figure 4.1.

4.1.3 *Matter stream*

Because of the two-well potential, an expanding companion star will eventually overflow from its Roche lobe. Most of the matter from the expanding companion will flow through the first Lagrange point towards the white dwarf. This matter flow has several effects on the accretion disc.

First, the companion star is the matter reservoir of the accretion disc, and the matter flux is what determines the outburst–quiescence cycle for the DIM, as we discussed in section 2.2.

The matter stream will also collide on the external part of the accretion disc, creating a *hot spot*. This hot region may heat the neighbouring regions of the disc and as we will discuss later, it might help seed the outburst.

To measure the importance of the matter stream on the accretion disc in terms of matter flux, I define the following timescale. It corresponds to the time it would take for the matter flux to totally replenish the initial accretion disc.

$$\tau_{\mathrm{stream}} = \frac{M_{\mathrm{disc}}}{\dot{M}_{\mathrm{stream}}} \tag{4.3}$$

where M_{disc} is the mass of the accretion disc, and $\dot{M}_{\mathrm{stream}}$ is the matter flux from the secondary star. Using estimates of Hameury et al. (1998), this timescale is typically of thousands to tens of thousands of binary orbits. Numerical simulations are usually run for, at the very best, hundreds of binary orbits. On these timescales, the amount of matter brought by the matter stream will be negligible compared to the initial disc mass.

To circumvent this problem, one usually artificially increases the strength of the matter flux, so that its effects can be observed on the simulation timescale. For example, Ju et al. (2016) use a very strong mass flow with $\tau_{\mathrm{stream}} \approx 50\ T_0$.

4.2 ANALYTICAL DERIVATION OF SPIRAL-WAVE SOLUTIONS

The first approach I used to assess the efficiency of spiral-wave-driven accretion is analytical. Here, I present the derivation of the spiral-waves solutions excited by the tidal potential in an accretion disc. This derivation follows Savonije et al. (1994) but also relies on Savonije and Papaloizou (1983).

4.2.1 *Equations*

We can write the Euler equations for an isothermal disc including the tidal potential of the secondary star, described in equation (4.2). As we are only interested in describing the radial and azimuthal behaviour of the disc, we vertically integrate the Euler equations. We have the vertically integrated quantities $\Sigma = \int \rho dz$, and $P = \int p dz$.

The set of equations we want to solve is the following.

$$\begin{cases} \partial_t \Sigma + \dfrac{1}{r}\partial_r(\Sigma r v_r) + \dfrac{1}{r^2}\partial_\varphi(\Sigma r v_\varphi) = 0 \\ \partial_t v_r + v_r \partial_r v_r + \dfrac{v_\varphi}{r}\partial_\varphi v_r - \dfrac{v_\varphi^2}{r} = -\dfrac{1}{\Sigma}\partial_r P - \partial_r \Psi, \\ \partial_t v_r + v_r \partial_r v_\varphi + \dfrac{v_\varphi}{r}\partial_\varphi v_\varphi + \dfrac{v_\varphi v_r}{r} = -\dfrac{1}{r\Sigma}\partial_\varphi P - \dfrac{1}{r}\partial_\varphi \Psi. \end{cases} \tag{4.4}$$

We additionally assume an arbitrary barotropic equation of state $P(\Sigma)$.

However, as is, this system of equations can not be solved analytically. We need to make further assumptions to find an analytical solution.

4.2.2 *Spiral waves*

Let us now realise that spiral waves are well described with an azimuthal Fourier expansion of the field of interest. Indeed, for a generic real-valued field ϕ of $\mathbb{R}^2$ using polar coordinates (r, φ), this azimuthal Fourier expansion reads

$$\phi(r, \varphi) = \sum_{m=0}^{\infty} \phi_m(r) e^{im\varphi}, \tag{4.5}$$

with ϕ_m a complex-valued function. If $\arg \phi_m$ is not constant, this means that the phase of the m^{th} mode of ϕ changes with radius. If this phase is a monotonic function, the m^{th} mode then represents an m-armed spiral.

4.2.3 *Linear order approximation*

Here, we want to develop a perturbation theory: we assume that the flow can be described as a mean-field term plus a deviation from this state. The mean state we choose is the solution for an isolated disc, *i.e.* with no companion star, $(\Sigma_0, P_0, v_r, v_\varphi)$ such that

$$\begin{cases} v_r = 0, \\ \dfrac{v_\varphi^2}{r} = \dfrac{1}{\Sigma_0}\dfrac{dP_0}{dr} + \dfrac{d}{dr}\psi_{\text{WD}}. \end{cases} \tag{4.6}$$

We write the deviations from this state as $v_r', v_\varphi', \Sigma', P'$. Our perturbation theory can be understood as an asymptotic development in q, the binary mass ratio, as the tidal potential is proportional to q for a fixed M_{WD}. In our perturbation theory, we make one further assumption: we want to find a 'steady' state solution. This 'steady' state only

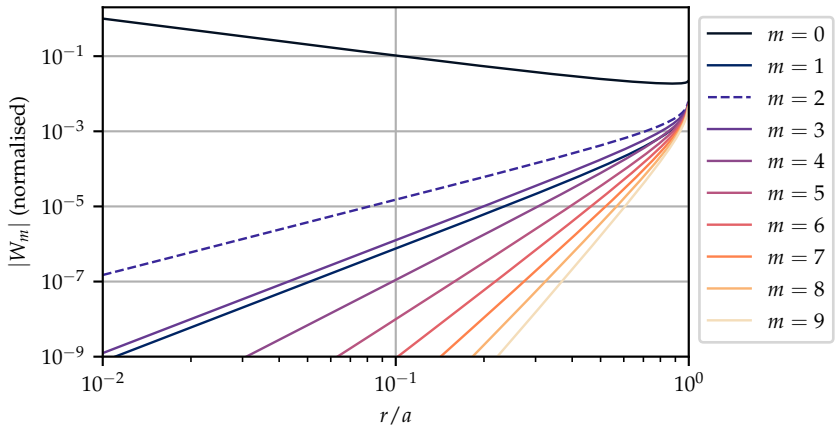

Figure 4.2 – Moduli of W_m, Fourier modes of the tidal potential. The $m = 2$ is highlighted as it is the one on which the linear theory focuses. The normalisation factor is $|W_0(a/100)|$.

makes sense in the frame rotating with the binary system. This remark will guide us in choosing an appropriate corotating Fourier basis.

As explained above, we now expand the quantities in Fourier series. We write $\Omega = v_\varphi/r$.

We change variables to $K_m = \frac{\Sigma'_m c_s^2}{\Sigma_0}$ and $\xi_m = \frac{(v'_r)_m}{im(\Omega-\omega)}$. The m subscript denotes the m^{th} Fourier mode. ω is the binary angular frequency, and $c_s^2 = \frac{dP}{d\Sigma}$ is the sound speed. To take into account the time periodicity of the position of the companion star, we use a slightly different Fourier function basis: $e^{im(\varphi-\omega t)}$. This basis is relevant as we want to find a corotating steady-state solution. For example, the tidal potential is expanded as

$$\Psi(r,\varphi,t) = \sum_{m=0}^{\infty} W_m(r) e^{im(\varphi-\omega t)} \tag{4.7}$$

Following, Savonije and Papaloizou (1983), we expect the dominant Fourier mode to be the $m = 2$ mode. In the linear pictures, modes do not couple, and we choose to solve the dynamics for this mode only. We have $W_2(r) = -\frac{3}{4}\frac{GM_s}{a^3}r^2 + o\left(\left(\frac{r}{a}\right)^2\right)$. The moduli of the first ten modes are plotted on figure 4.2. There, we see that the $m = 2$ mode (dashed line) is the non-axisymmetric mode with the largest amplitude.

We can now rewrite the system (4.4) with the new variables. Here we want to develop a linear order perturbation theory. Hence we now assume that the perturbed quantities are of small amplitude compared to the mean state. We thus neglect all non-linear order terms.

It is possible to obtain one single equation.

$$\frac{d^2\xi_m}{dr^2} + A(r)\frac{d\xi_m}{dr} + B(r)\xi_m = D(r) \tag{4.8}$$

where

$$A(r) = \frac{\Sigma_0 r}{\beta}\frac{d}{dr}\left(\frac{\beta}{\Sigma_0 r}\right) + \frac{2}{\Sigma_0 r}\frac{d}{dr}(\Sigma_0 r), \tag{4.9}$$

$$B(r) = \frac{d^2}{dr^2}(\Sigma_0 r) + \left[\frac{1}{\beta}\frac{d}{dr}\left(\frac{\beta}{\Sigma_0 r}\right) + \frac{2\Omega}{r(\Omega-\omega)\Sigma_0 r}\right]\frac{d}{dr}(\Sigma_0 r) - \frac{4\Omega^2}{r^2(\Omega-\omega)^2} - \frac{m^2(\Omega-\omega)^2-\Omega^2}{\beta}, \tag{4.10}$$

$$D(r) = -\frac{1}{\beta}\left[\frac{dW_m}{dr} + \frac{2\Omega W_m}{r(\Omega-\omega)} - \frac{d}{dr}\left(\frac{W_m\beta}{r^2(\Omega-\omega)^2}\right) - \frac{2\Omega W_m\beta}{r^3(\Omega-\omega)^3}\right], \tag{4.11}$$

with $\beta = \frac{c_s^2 r^2(\Omega-\omega)^2}{c_s^2 - r^2(\Omega-\omega)^2}$. Note that the r dependency of Ω is not written for readability.

4.2.4 *Results*

Let us first find a homogeneous solution of the ordinary differential equation (4.8), that is a solution where $\forall m \in \mathbb{N},\ W_m = 0$, even for $m = 2$.

We also work under the assumption that we are close to the white dwarf, that is $r \ll a$. This implies $r^2(\Omega-\omega)^2 \gg c_s^2$. We then have $\beta \approx -c_s^2$.

Furthermore, we use the additional assumption that the Mach number of the flow is large. This means that β is a small parameter which we can use to produce a WKB solution. We find, for the homogeneous equation, the following solution.

$$X_m(r) = \frac{\eta_1 e^{i\mu(r)} + \eta_2 e^{-i\mu(r)}}{Q(r)} \tag{4.12}$$

η_1 and η_2 are integration constants determined by the boundary conditions. $Q(r) = \left[m^2(\Omega-\omega)^2 - \Omega^2\right]^{1/4}$ and $\mu(r) = -\int_r^{r_1} \frac{\sqrt{m^2(\Omega-\omega)^2-\Omega^2}}{c_s} dr$, with r_1 an arbitrary radius.

From this homogenous solution, using the methods of variation of parameters, one can find a general solution.

$$\xi_m(r) = \frac{\eta_1 e^{i\mu(r)} + \eta_2 e^{-i\mu(r)}}{Q^{1/4}(r)} \int_{r_0}^{r} e^{-\int_{r_0}^{\rho}\left(2\frac{\dot{X}}{X}+A\right)ds} \int_{r_0}^{\rho} \frac{D(R)Q^{1/4}(R)e^{\int_{r_0}^{R}\left(2\frac{\dot{X}}{X}+A\right)dx}}{\eta_1 e^{i\mu(R)} + \eta_2 e^{-i\mu(R)}} dR d\rho \tag{4.13}$$

This standing spiral-wave solution has a local dispersion relation given by the integrand of $\mu(r)$.

$$k^2(r)c_s^2 = m^2[\Omega(r)-\omega]^2 - \Omega^2(r) \tag{4.14}$$

This allows us to compute the theoretical wavelength of the linear spiral wave. We have, for $m \geq 2$,

$$\lambda(r) = \frac{2\pi}{\sqrt{m^2-1}}\frac{c_s}{\Omega(r)} + \mathcal{O}\left(\frac{\omega}{\Omega(r)}\right). \tag{4.15}$$

This will be of use when choosing the resolution of my numerical discretisation.

4.3 COLLAPSE OF LINEAR THEORY: ON THE NECESSITY OF NUMERICS

Let us now take a step back and look at what we have obtained so far. We have derived a linear steady-state standing spiral wave solution of Euler equations One of the strongest assumptions we made for linear theory to hold is that the amplitude of deviations from the mean state has to remain small compared to the mean state. Otherwise, the non-linear, higher-order terms that we have neglected will no longer be small.

I introduce $\sigma = \frac{\Sigma'}{\Sigma_0}$, a dimensionless parameter which quantifies whether we satisfy this assumption. Linear theory holds if and only if $\sigma \ll 1$.

I can estimate its value using the following approximations

$$\int_{r_0}^{r} d\rho \approx r \quad \text{and} \quad \frac{d}{dr} \approx \frac{1}{r}. \tag{4.16}$$

I also use, $\Omega \gg \omega$, with ω the angular frequency of the binary system, and $\mathrm{Ma} = \frac{\Omega r}{c_s} \gg 1$, which I already assumed. I obtain

$$\sigma(r) = \frac{3}{4}\frac{GM_s}{a^3 c_s^2} r^2 = \frac{3}{4(1+q)} \left(\frac{\omega}{\Omega(r)}\right)^2 \mathrm{Ma}^2(r) \tag{4.17}$$

where $q = \frac{M_s}{M_{WD}}$ the mass ratio of the binary system.

For typical dwarf nova systems, the radius of a white dwarf is about one earth radius, the mass of the companion star is around one solar mass, and the binary separation is around one solar radius.

We obtain the following estimate.

$$\sigma(r) = \frac{3}{4} \left(\frac{r}{r_{WD}}\right)^2 \left(\frac{4000\ \mathrm{m/s}}{c_s}\right)^2 \approx \frac{3000\ \mathrm{K}}{T} \left(\frac{r}{r_{WD}}\right)^2, \tag{4.18}$$

where r_{WD} is the white dwarf radius. For typical quiescence regime where the temperature is such that $T \lesssim 3000$ K, we obtain

$$\sigma_{\text{quiescence}}(r_0) \gtrsim 1. \tag{4.19}$$

This means the perturbations have amplitudes comparable to the mean state. Furthermore, note that this linear development should best hold at small radii; indeed we have $\sigma \propto r^2$. We thus expect that linear theory fails to properly describe spiral waves in cold quiescent discs.

Note that for the outburst regime, when the disc is much hotter with temperatures upwards of 10^4 K, the linear theory should hold.

Solving exactly a non-linear system like (4.4) is unfortunately not possible analytically without strong assumptions like we made here. It is thus necessary to use methods that allow to study the full non-linear solution of the disc flow.

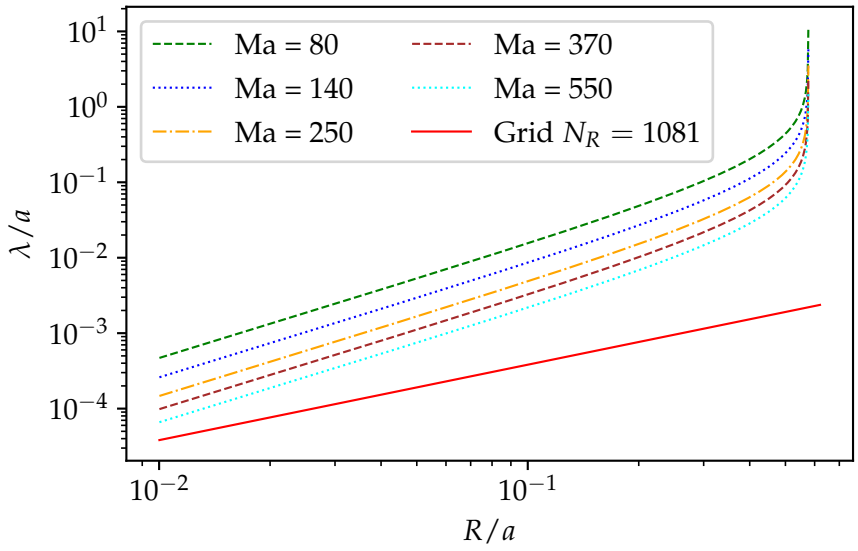

Figure 4.3 – Wavelength of the spiral wave at different Mach numbers (dashed lines), compared to the resolution used in most simulations (red).

4.4 NUMERICAL SETUP

To solve the non-linear Euler equations (4.4), I use the IDEFIX code presented in chapter 3. We solve the vertically integrated Euler equations in polar coordinates (R, φ) in a global 2D geometry.

4.4.1 *Grid and units*

Here, I wish to study the dynamics driven by the shocks caused by the spiral waves. To do so, one ought to satisfy the Nyquist criterion for these waves everywhere in the disc. As computed in equation (4.15), this criterion is most constraining in the inner regions of the disc.

I choose a grid with with logarithmic spacing in the radial direction, with $\Delta R \propto R$. This enables me to have a fine resolution in the innermost regions, where it is required. I use a uniform spacing in the azimuthal direction. This grid is such that the aspect ratio of cells is constant with radius. Figure 4.3 compares the radial resolution I used to the theoretical spiral-wave wavelength.

The units I use here are scaled on SS Cyg. The length unit is the binary orbital separation $a \approx 1.37 \times 10^9$ m, and the time unit is the binary period $T_0 \approx 6.6$ h.

The innermost radius of the grid corresponds to the outer radius of the white dwarf, and the outermost radius corresponds to the radius of the first Lagrange point. In code units, the radial range spans from $r_0 = 0.01\ a$ to $r_{L_1} \approx 0.6\ a$ depending on the mass ratio of the binary system. The whole azimuthal direction is solved for.

This grid is the first difference with previous works like Ju et al. (2016) or Pjanka and Stone (2020). In this work, I describe the accretion disc down to the radius of the white dwarf. In their work, their inner radius is twice as large with $r_{\rm in}/a = 0.02$. Going to lower radii puts a stronger constraint on the time step via the CFL condition, because

the Keplerian velocity increases at smaller radii $v_K \propto r^{-1/2}$ and the cell size decreases $\Delta x = r d\varphi$.

As shown in table 4.1, the resolution of my simulations changes with the mass ratio q used. The integration domain extends to the Lagrange point in each case, but this distance changes with q of the simulation. The modification of the grid between these simulations is simply to remove or append cells. This way the inner region always has the same grid, independently of the mass ratio.

4.4.2 *Boundary conditions*

I use periodic boundary conditions for the azimuthal direction. The radial boundary conditions I use here are *Keplerian outflow* conditions, which are a modified version of the usual *outflow* boundary conditions. These boundary conditions impose a no-inflow condition by imposing $v_R = 0$ in the ghost cells when there would be an outflow. When there would be an inflow, these boundary conditions impose $\partial_R v_R = 0$. Additionally, they impose the azimuthal velocity of the fluid to be the local Keplerian velocity in the corotating frame $v_\phi(R) = \sqrt{\frac{GM_{WD}}{R}} - \omega R$.

At the inner radius, the gravitational influence of the companion star is negligible compared to the gravity of the white dwarf so this velocity is a good approximation of the expected fluid velocity. This however does not take into account possible boundary layer effects close to the white dwarf. For example matter close to the white dwarf could possibly be corotating with the white dwarf. At the outer radius, this boundary condition is not as good an approximation. I did not note any obvious numerical artefacts as a consequence of this choice. At the outer radius, the effect of this boundary condition is also mitigated by the very low density due to the tidal truncation of the disc. This boundary condition is similar to the one used by Ju et al. (2016).

4.4.3 *Initial condition*

The initial condition of my simulations is an isothermal disc with constant surface density $\Sigma = 1$ rotating at the local Keplerian velocity, with no radial flow. The isothermal hypothesis is inspired by the results of the DIM for the quiescence phase. As can be seen on figure 2.3 (bottommost dashed line of the top panel, after the propagation of the cooling front), during the quiescence phase, the temperature of the disc does not vary with radius. Moreover, as shown by Ju et al. (2016) and as presented later in this chapter, when energy is solved for, a cooling mechanism has to be introduced because otherwise spiral shock would heat the disc at temperatures much higher than the initial temperature. To circumvent this they use an artificially low heat capacity ratio γ. I discuss later in this chapter the case when this assumption is relaxed and energy is solved for.

Regarding the density profile, an initially uniform surface density is not quite in agreement with the DIM. Indeed, as shown on 2.3, during the quiescence phase, we expect $\Sigma \propto R$. This initial condition however allows for comparison with previous simulations of Ju et al. (2016).

This initial flow is not an equilibrium state because of the tidal potential of the secondary star. It will relax to another state, which we hope to be a steady state. To reduce the time spent in the transient state, I impose an external truncation of the disc. I apply to following mask to the density profile.

$$\mu(R) = \frac{1}{2}\left(1 - \tanh\left(\frac{R - r_T}{\delta_T}\right)\right) \tag{4.20}$$

WI take r_T the truncation radius to be approximately the truncation radius computed in Paczyński (1977) depending on the mass ratio of the simulation, and $\delta_T = 0.01$. This initial truncation helped reduce the duration of the initial transient state compared to preliminary simulations not using this initial truncation. I also note that the final truncation radius of the disc is the same whether I use this initial truncation or not, confirming that this does not affect the disc after the initial transient regime.

4.4.4 *Handling of the tidal truncation*

As a consequence of the tidal truncation of the disc, there are regions of extremely low density in my integration domain. To avoid the appearance of infinitely strong density gradients at the outer edge of the disc, we impose a numerical density floor. If the density in a cell reaches values below $\Sigma_{\rm floor} = 10^{-6}$ we use this density value instead. This density floor is implemented such that the momentum of each cell is conserved by rescaling the amplitude of the fluid velocity, that is if the density Σ is below the floor value, the velocity will become

$$\boldsymbol{v}_{\rm new} = \frac{\Sigma}{\Sigma_{\rm floor}} \boldsymbol{v}_{\rm old} \tag{4.21}$$

Note that for the initial condition, after the mask (4.20) is applied, regions with density lower than the floor value are set to $\Sigma_{\rm floor}$. In this particular instance, the velocity of the fluid is not modified.

4.4.5 *Inertial forces*

As before, here the equations are solved in a reference frame centred on the white dwarf, and include the tidal potential (4.2).

Here I use a rotating reference frame. I specify to Idefix that the angular frequency of the frame is $\omega = 2\pi$ in our units, and Coriolis, $\boldsymbol{F}_{\mathscr{C}}$, and centrifugal, $\boldsymbol{F}_{\rm c}$, forces are added in the solver. These forces read as follows.

$$\boldsymbol{F}_{\mathscr{C}} = 2\Sigma \boldsymbol{v} \wedge \omega \boldsymbol{e}_{\varphi} \tag{4.22}$$

$$\boldsymbol{F}_{\rm c} = \Sigma \omega^2 R \boldsymbol{e}_R \tag{4.23}$$

These forces are included as source terms in the Riemann problem picture presented in chapter 3.

4.4.6 *List of simulations*

Tables 4.1 and 4.2 present a list of the 2D non-magnetic simulations I produced. I explored two directions in the parameter space.

The first direction is the temperature of the disc, with Mach numbers ranging from 80 to 550. With this range, we extend from previous works (namely Ju et al. (2016) at Ma ≈ 80, *i.e.* $T \approx 2 \times 10^5$ K) to realistic temperature for quiescent discs with Ma $= 550$, *i.e.* $T \approx 4000$ K.

We then explore the effect of the binary mass ratio on the disc dynamics. For instance, previous works have shown that systems with small mass ratios are prone to developing an eccentric disc (Kley et al., 2008, for example).

Inner radius Ma	Resolution ($N_R \times N_\varphi$)	q	Note
80	1081×1024	0.3	
140	1081×1024	0.3	
250	1081×1024	0.3	
370	1081×1024	0.3	
550	1081×1024	0.3	Under resolved
250	1137×1024	0.05	
250	1119×1024	0.1	
250	1042×1024	0.7	
250	1081×1024	0.3	WKZ 1
250	1081×1024	0.3	WKZ 2
550	4096×4096	0.3	

Table 4.1 – List of the isothermal 2D hydro simulations presented in this chapter. The simulations with 'WKZ' have a *Wave Killing Zone* as presented with equation (4.32).

Initial temperature	Resolution ($N_R \times N_\varphi$)	q	γ	Note
3000 K	4096×4096	0.3	1.4	constant κ_P
3000 K	4096×4096	0.3	1.4	tabulated $T_{\text{eff.}}$

Table 4.2 – List of the non-isothermal 2D hydro simulations presented in this chapter.

4.4.7 *Averaging methods*

Here we want to have a time resolution fine enough to resolve the dynamics in the entire disc. This means that the time resolution has to be at most 1/10 the Keplerian timescale at the inner radius. As we wish to study the state reached during the quiescence phase, not the idealised initial condition, we need to carry out the simulation to dozens of binary orbits. Both constraints together implies a time scale separation of at least five orders of magnitude.

Producing outputs at this rate for a simulation of 100 binary orbits is not reasonable. First, the amount of data produced would be enormous, of approximately 30 To per simulation; and it would be very long to analyse thoroughly. Second, writing data, even though parallelised with MPI is slow. Writing data at this frequency would slow the code to a halt, being bottlenecked by output writing.

To circumvent this problem, I implemented *on-the-fly* averaging to readily output reduced data. I store to memory the azimuthally averaged fields of interest every $1/10{,}000^{\text{th}}$ of binary orbits. These azimuthal averages are then averaged over $1/100^{\text{th}}$ of a binary orbit. The time and azimuthal averages are then output every $1/100^{\text{th}}$ of a binary orbit.

This proved to be a sufficient time sampling method to resolve the rapid inner region dynamics of the disc.

Additionally, full snapshots are produced every $1/10^{\text{th}}$ of a binary orbit.

4.5 REPRODUCING PREVIOUS WORKS

The first part of this numerical work was to make sure that the new, and at the time, still under development, IDEFIX code could reproduce the results of previous works. This step is especially important for a new code; together with the tests mentioned in chapter 3 this ensures us that we are able to produce sensible results.

In this section, I present how I reproduce the results from Ju et al. (2016), which focus on spiral shocks in dwarf novæ disc, albeit in much higher temperature regimes. In their work, they use the ATHENA++ finite-volume code; even though the method is the same, variation in implementation can produce measurable differences.

First, note that the time unit and the potential / reference frame used in that paper are different from what I presented above. Indeed, in their units, $T_0 = 2\pi$, whereas I chose the more convenient $T_0 = 1$ to count binary system orbits. They also use a time-varying potential rather than working in the corotating frame. I modified the above-described setup to match their work by using a non-rotating frame and a rotating tidal potential.

Even though my study focused on an isothermal model, I tried to reproduce the results of the runs 'iso $c_s = 0.1$' as well as the run 'adi $\gamma = 1.1$' (with and without matter stream from the companion) from their paper. In the latter case, the code additionally solves the energy equation, with adiabatic index $\gamma = 1.1$. This allows us to compare the shock heating efficiency of both codes.

The results I obtain are very satisfactory. I am able to closely reproduce their results as can be seen on Figure 4.4. I obtain the same density, accretion rate, and effective viscosity profiles after the same integration time, and using the same averaging procedures. I also note that a low-density cavity forms at the inner boundary. This drop in density is neither visible on Figure 4.4 nor on the Figure of their paper, as the radial domain if the plot stops at radii greater than their inner boundary.

We note some slight differences that can be attributed to implementation differences between IDEFIX and ATHENA++. One of the measurable differences is clearly visible on the top panel of 4.4 and is the fact that the density peak at around $R/a = 0.2$ is stronger in their simulation than what I obtain with IDEFIX. The accretion rate and effective α parameters also show slight differences but remain in good agreement overall.

To verify more precisely that IDEFIX is able to reproduce their data, I reproduce the angular momentum balance shown on figure 4.5. I reproduce the total angular momentum budget of both their non-isothermal runs with $\gamma = 1.1$, with and without matter inflow from the companion star.

The different terms plotted on this figure correspond to the different terms of the angular momentum balance equation. They read as follows using the writing convention of chapter 2.

$$\mathrm{AM}_t(R) = \partial_t \langle \rho R v_\varphi \rangle_{\mathrm{Ju}} R \tag{4.24}$$

$$\mathrm{AM}_{\dot{M}}(R) = -\langle R \rho v_R \rangle_{\mathrm{Ju}} R \dot{M} \partial_R (R v_{\mathrm{K}}) \tag{4.25}$$

$$\mathrm{AM}_{FH}(R) = -\partial_R (R^2 \langle \rho v_R v_\varphi \rangle_{\mathrm{Ju}}) \tag{4.26}$$

$$\mathrm{T}(R) = \langle \boldsymbol{R} \wedge \boldsymbol{F}_{\mathrm{ext}} \rangle_{\mathrm{Ju}} R \tag{4.27}$$

where the average $\langle X \rangle_{\mathrm{Ju}} = \int_{z_{\mathrm{min}}}^{z_{\mathrm{max}}} \int_0^{2\pi} X d\varphi dz \Delta R$ where $z_{\mathrm{max}}, z_{\mathrm{min}}$ are the vertical boundaries of their simulation, and ΔR is the radial size of the cells at radius R. With these terms, the angular momentum balance equation reads as follows.

$$\mathrm{AM}_t = \mathrm{AM}_{\dot{M}} + \mathrm{AM}_{FH} + \mathrm{T} \tag{4.28}$$

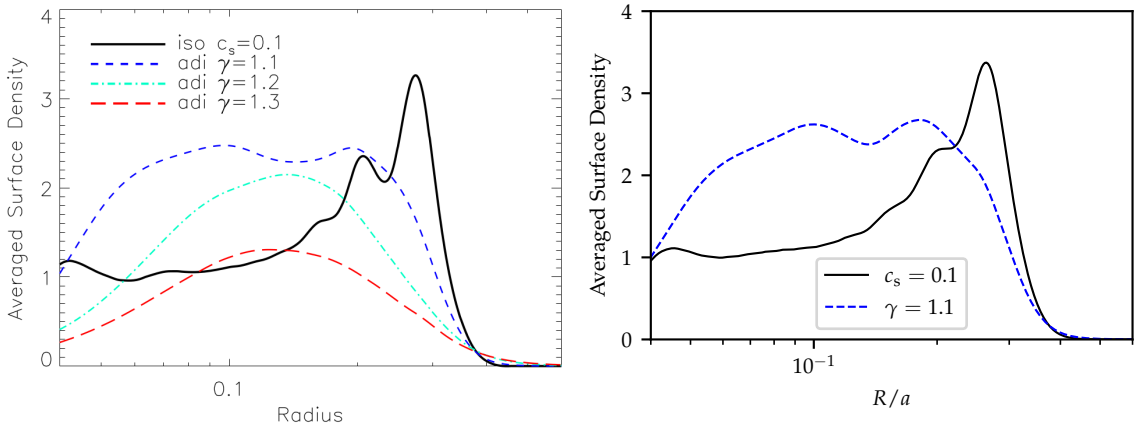

(a) Density profile.

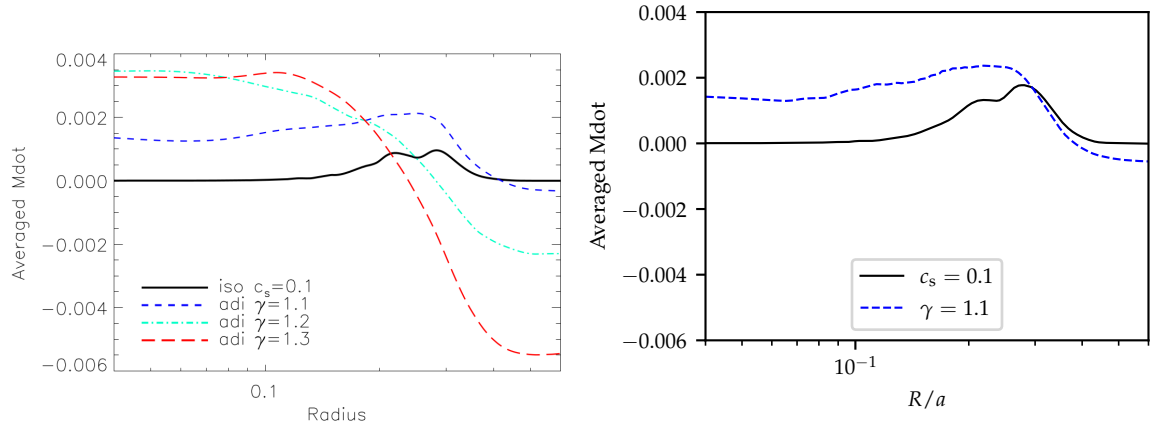

(b) Accretion rate profile.

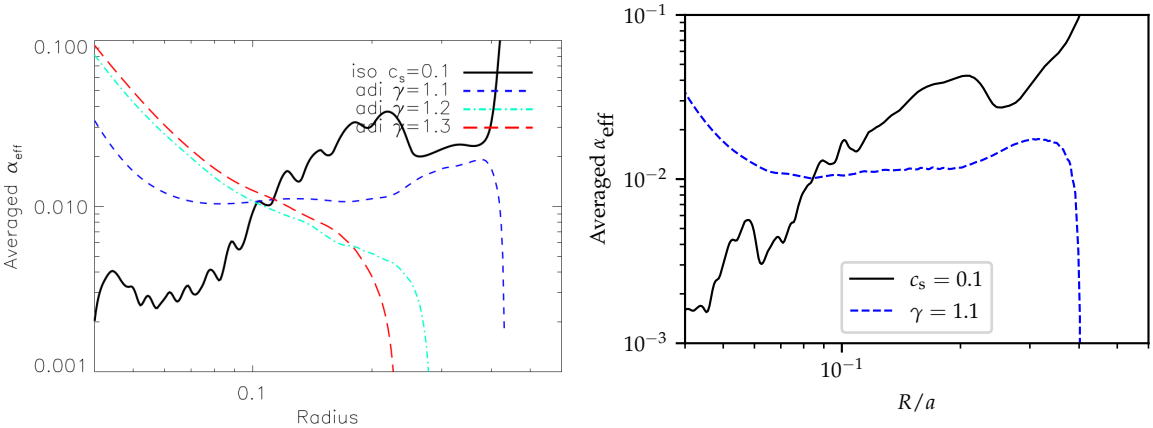

(c) Effective α profile.

Figure 4.4 – **Left:** Selected panels of Figure 12 of Ju et al. (2016). **Right:** Reproduction of these panels with the IDEFIX code.

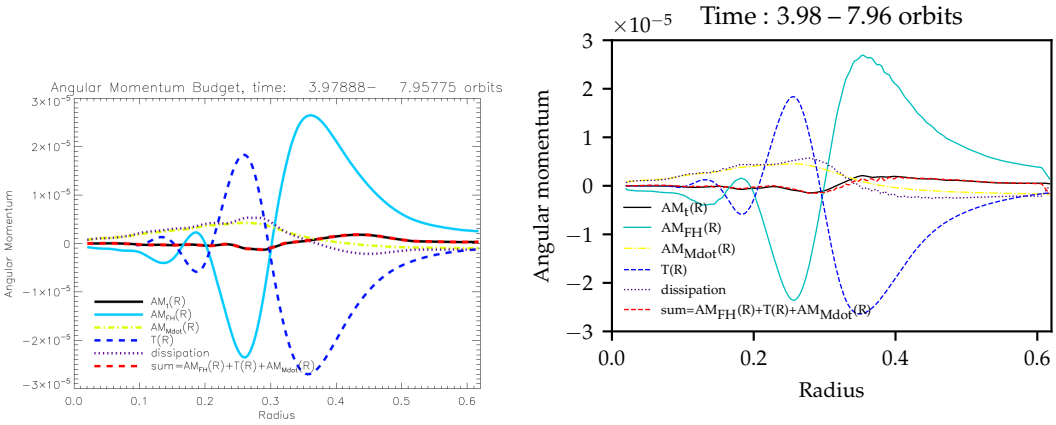

(a) No-inflow simulation.

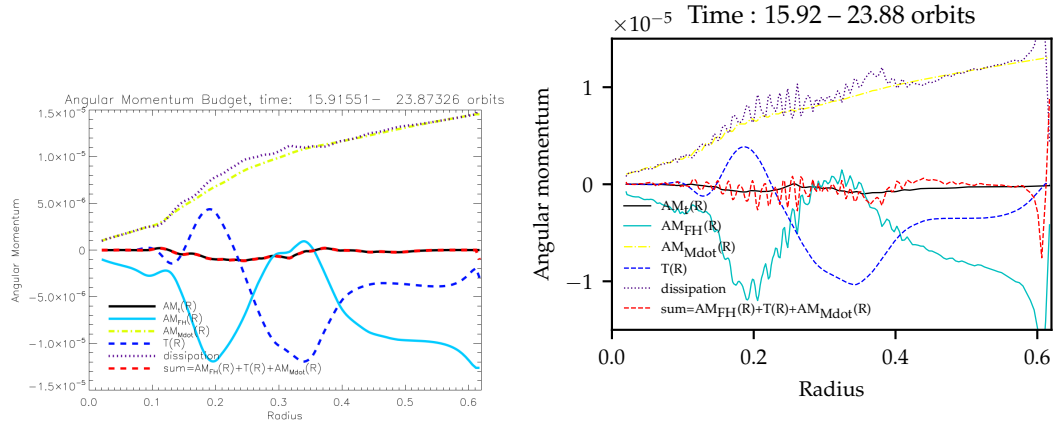

(b) With inflow simulation.

Figure 4.5 – **Left:** Figure 10 of Ju et al. (2016). **Right:** Reproduction with the IDEFIX code. Note that a minus sign needed to be added to the dissipation term.

where I dropped the radial dependency of every term. On figure 4.5 we first see that angular momentum balance is verified, as the solid black line (left-hand side of (4.28) is superimposed to the dashed red line (right-hand side of (4.28)). The dissipation term plotted is $-\mathrm{AM}_{FH} - \mathrm{T}$.

Here as well, the results produced by IDEFIX are in good agreement with their work. I observe however that for the with-inflow simulation, my angular momentum budget is noisier than theirs.

The ability to closely reproduce previous work gives us confidence in the new IDEFIX code. I can now produce new simulations and explore regimes more relevant for the quiescence phase of dwarf novæ.

ALTERNATIVE DEFINITION OF α Before I present the results I obtain for the newly explored quiescence regime, I want to discuss the definition of the α parameter used in Ju et al. (2016) and in my work.

As presented in chapter 2, one usually quantifies accretion with the dimensionless α parameter of Shakura and Sunyaev (1973). In Ju et al. (2016) however, they use a different definition for their $\alpha_{\mathrm{eff.}}$. They argue that for such binary systems, this quantity should be defined from the accretion rate rather than from the Reynolds and Maxwell stresses. They use

$$\alpha_{\mathrm{eff.}} = \frac{\dot{M}}{3\pi\Sigma c_s H}. \tag{4.29}$$

Both this $\alpha_{\mathrm{eff.}}$ and the α_{SS} from Shakura and Sunyaev (1973) can be obtained from the angular momentum balance equation. In fact, we have.

$$\alpha_{\mathrm{eff.}} = \frac{2}{3}\alpha_{\mathrm{SS}} - \frac{2}{3}\frac{\int R\langle \boldsymbol{R}\wedge\boldsymbol{F}\rangle dR + C}{\Sigma c_s H}. \tag{4.30}$$

with $\boldsymbol{F}$ any external force, here, the tidal force of the secondary star. C is an integration constant. This is obtained assuming a steady state as well as no radial dependency for the accretion rate $\dot{M}$. Here, α_{SS} corresponds to the α parameter defined earlier in equation (2.40). In the following, I drop the subscript.

However, in my simulation, as will be discussed below, the disc does not reach a steady state. In this case, the definition from the accretion rate no longer decomposes easily in a stress term plus a torque term. Moreover, the measured accretion rate also varies strongly with radius.

Nonetheless, this difference in definitions does not change the conclusions presented in this chapter. As shown on figure 4.6, in both cases we measure $\alpha \ll 10^{-2}$ at late times.

4.6 ECCENTRIC SPIRALS

The density maps of Figure 4.7 clearly show the spiral waves in the accretion disc. We can see, as expected, that the colder the disc is, the more tightly wound the spiral waves are. The hottest simulation at $\mathrm{Ma} = 80$ corresponds to the regime of Ju et al. (2016), and I go to colder temperatures from there.

In the linear theory, we only examined the evolution of the $m = 2$ spiral mode because it corresponds to the dominant potential mode, as shown on figure 4.2. Here, I see that the dominant spiral mode is not an $m = 2$ spiral mode. On the density map, this is most

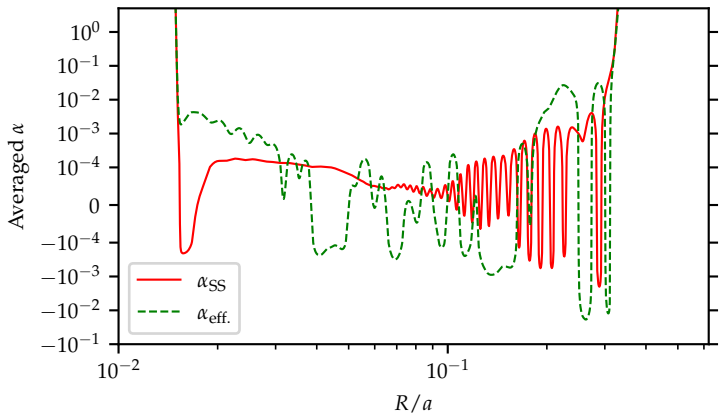

Figure 4.6 – Comparison of the two definitions of the angular momentum transport parameter in the run with Ma = 250 and $q = 0.3$ averaged over 10 binary orbits.

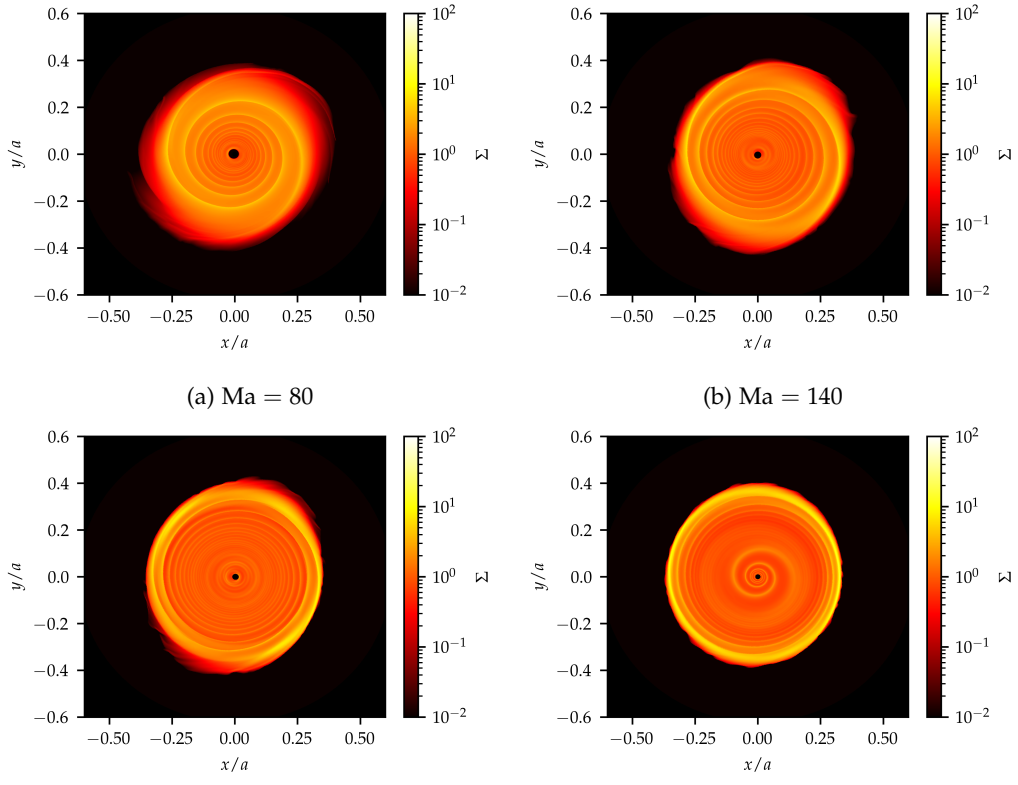

(a) Ma = 80

(b) Ma = 140

(c) Ma = 250

(d) Ma = 370

Figure 4.7 – Density maps for different simulations with decreasing temperature (a to d) 10 binary orbits after the initial condition.

clearly visible on the Ma = 370 panel in the inner part of the disc. The right column of figure 4.7 is a de-projected plot of the density perturbation defined as follows.

$$\tilde{\Sigma} = \frac{\Sigma - \langle\Sigma\rangle_\varphi}{\langle\Sigma\rangle_\varphi} \tag{4.31}$$

where $\langle\Sigma\rangle_\varphi$ is the azimuthal average of the surface density.

To quantify the amplitude of the different spiral modes, it is natural to do an azimuthal Fourier transform of the density maps, as shown on Figure 4.8. Both on figure 4.7 and 4.8, we see that at all temperatures the $m = 1$ mode dominates over the $m = 2$ in the inner parts of the disc. The transition radius at which the dominant mode changes becomes larger in colder discs. In the Ma = 370 simulation, we see that the whole disc is dominated by the $m = 1$ mode.

An $m = 1$ spiral wave is an eccentricity mode of the disc. However, the simulations presented above are not expected to feature an eccentric instability, as discussed below. To make sure that this one-armed spiral wave was not an effect of my inner radius boundary condition I produced further test simulations at Ma = 250.

These simulations have a modified inner boundary condition tuned to damp waves and prevent reflection and the artificial excitation of eccentric mode. To do so, I use a *wave killing zone* type boundary condition.

We use a smooth mask

$$\lambda(R) = \begin{cases} 1 - \sin^2\left(\dfrac{\pi}{2}\dfrac{R - r_0}{r_{\mathrm{WKZ}} - r_0}\right) & \text{if } R \leq r_{\mathrm{WKZ}}, \\ 0 & \text{if } R \geq r_{\mathrm{WKZ}}, \end{cases} \tag{4.32}$$

where r_0 is the internal boundary radius and r_{WKZ} is the radial extension of the wave killing zone. This method is inspired by de Val-Borro et al. (2006)'s method to damp planetary wakes in the context of protoplanatary disc-planet interaction. For a velocity field in direction X the boundary condition is

$$\begin{cases} \delta\rho(R) & = \frac{\lambda(R)}{\tau_{\mathrm{WKZ}}}\left(\rho - \rho^{\mathrm{t}}\right) \\ \rho^{\mathrm{new}}(R) & = \rho(R) - \delta\rho(R)dt \\ \delta F_X(R) & = \frac{\lambda(R)}{\tau_{\mathrm{WKZ}}}\rho(R)\left(v_X(R) - v_X^{\mathrm{t}}(R)\right) + v_X\delta\rho \\ F_X^{\mathrm{new}}(R) & = F_X(R) - \delta F_X(R)dt, \end{cases} \tag{4.33}$$

where the superscript t denotes target values, τ_{WKZ} is the relaxation time. Note that here, I modify the *inter-cell flux* from its value computed by the Riemann solver, not the cell-centred values in the ghost zones.

Hence, the parameters of the wave-killing zone are its size, the relaxation time and the target values. We use target values corresponding to a Keplerian flow. The relaxation time is 1/10 Keplerian orbital time at the inner radius. For the radial extension, I use $1.2r_0$ and $2r_0$. The latter case is plotted on figure 4.9 for a comparison with the simulation without wave-killing zone.

To be effective, the size of a wave-killing zone should be larger than the wavelength of the wave one wishes to dampen. The theoretical wavelength of the spiral wave is plotted on figure 4.3 with its Ma dependency. With a size of $1.2r_0$, no difference in the dynamics is observed, which is why I tried a larger damping region. But here as well there was

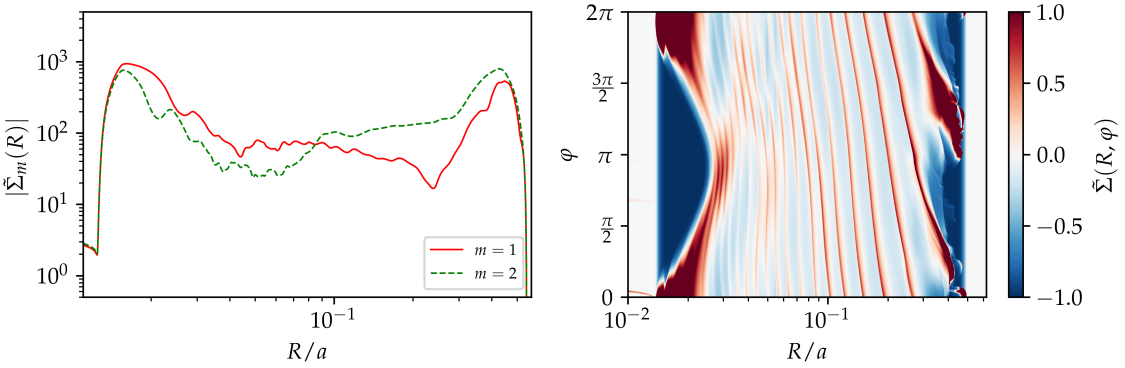

(a) Ma = 80

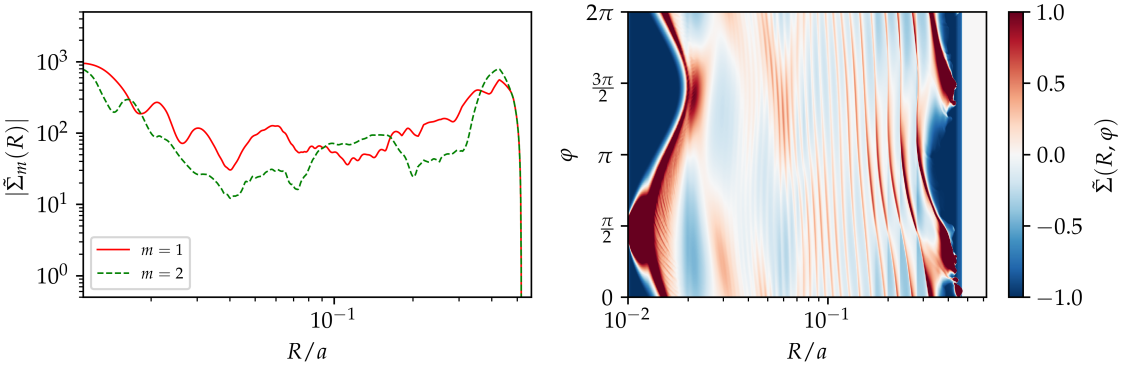

(b) Ma = 140

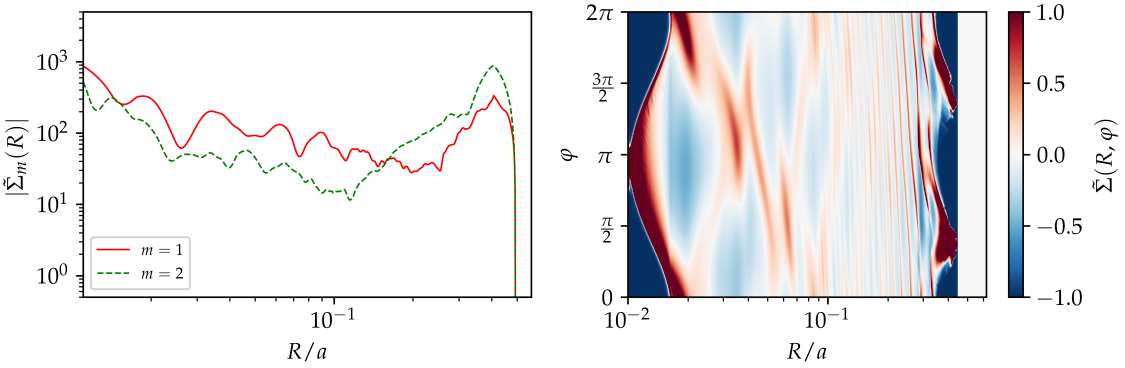

(c) Ma = 250

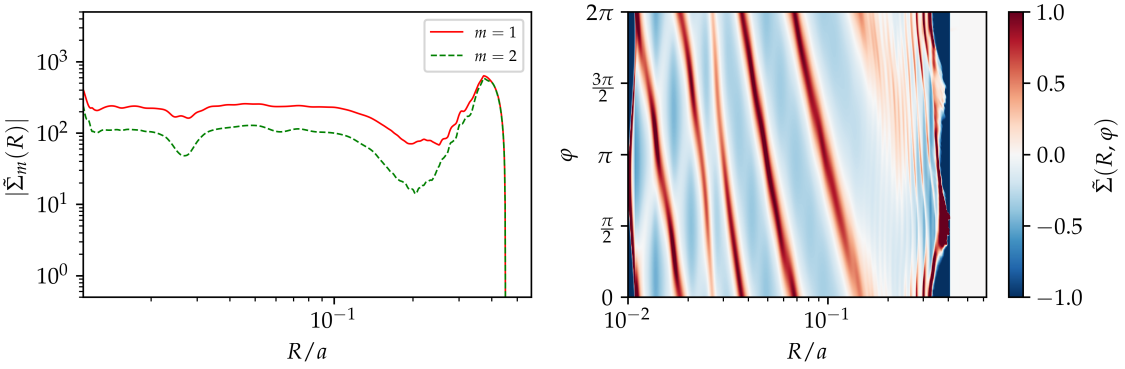

(d) Ma = 370

Figure 4.8 – **Left:** Amplitude of the azimuthal Fourier transform of the density maps of Figure 4.7. **Right:** De-projected density perturbation to the azimuthal average.

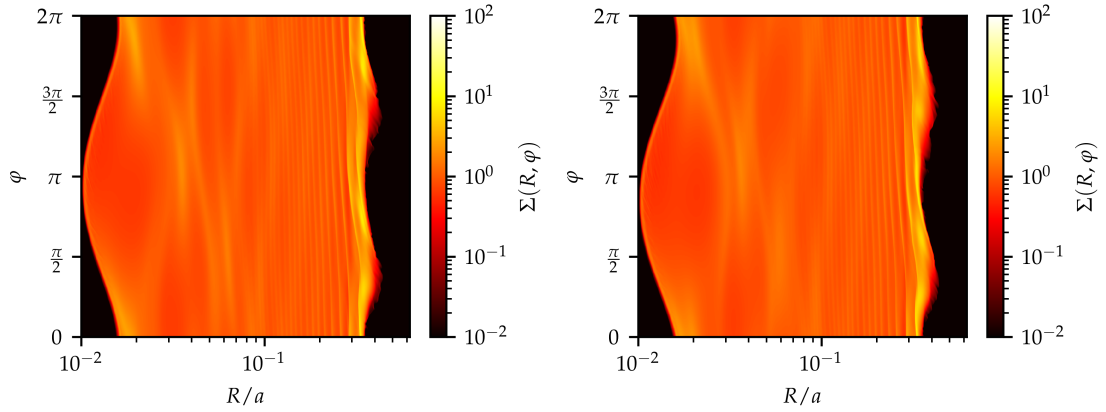

(a) No WKZ simulation

(b) Simulation with WKZ ($r_{\mathrm{WKZ}} = 2r_0$)

Figure 4.9 – Comparison of the density profile with and without a wave killing zone.

no noticeable difference in the dynamics, as can be seen on figure 4.9. The inner edge cavity is present in both cases, and the spiral structure is unaffected. I conclude from this that the $m = 1$ mode is not due to a simple reflection of the excited waves on the inner boundary.

4.6.1 *Eccentricity growth and mass ratio*

As discussed in the introduction SU UMa type cataclysmic variables feature superhumps that have so far been explained by eccentric discs, as they are found in systems with mass ratio $q \leq 0.3$.

In binary systems with such mass ratio, the tidal truncation radius occurs at radii sufficiently large such that the 3:1 resonance radius lies inside the disc. This radius corresponds to the radius at which the Keplerian angular frequency (with respect to the white dwarf) is exactly 3 times the binary orbital frequency. When this resonance lies within the disc, it couples to the tidally excited waves to produce eccentricity. This mechanism is depicted on figure 4.11. This mechanism driving eccentricity growth is now well established and has been observed in several numerical works (Lubow, 1991b; Kley et al., 2008; Oyang et al., 2021).

This mechanism can be understood as a second-order development to the linear theory presented in section 4.2. As we did before, the fields describing the disc can be expanded in azimuthal Fourier series $e^{i(k\varphi - l\omega t)}$ where ω is the binary angular frequency and (k, l) is analogous to a wave vector. k corresponds to the azimuthal wave number and l corresponds to a temporal wave number, *i.e.* a frequency. This (k, l) is the integer couple represented on figure 4.11. On one hand, as the tidal forces are locked in phase with the companion star, they will have a wave vector (m, m) with both wave numbers equal. On the other hand, a stationary (in inertial frame) eccentric mode has wave vector $(1, 0)$. $k = 1$ corresponds to the azimuthal symmetry of eccentricity and $l = 0$ corresponds to the stationarity of this mode.

These two may be non-linearly coupled, in this case, the produced mode corresponds to the product of these modes. The resulting wave vector is the sum (or difference) of the wave vectors of the interacting modes, that is $(m - 1, m)$. In the case where $m = 2$, we find a positive feedback loop: The tidal mode with wave vector $(2, 2)$ interacts with the eccentric mode $(1, 0)$. Then, this produces a response in the disc with wave vector $(1, 0)$, *i.e.* an eccentric mode.

However, in my work, I do not observe a global growth of disc eccentricity, as can be seen on figure 4.10. In my simulations with $q = 0.05$ and $q = 0.1$ we expected to

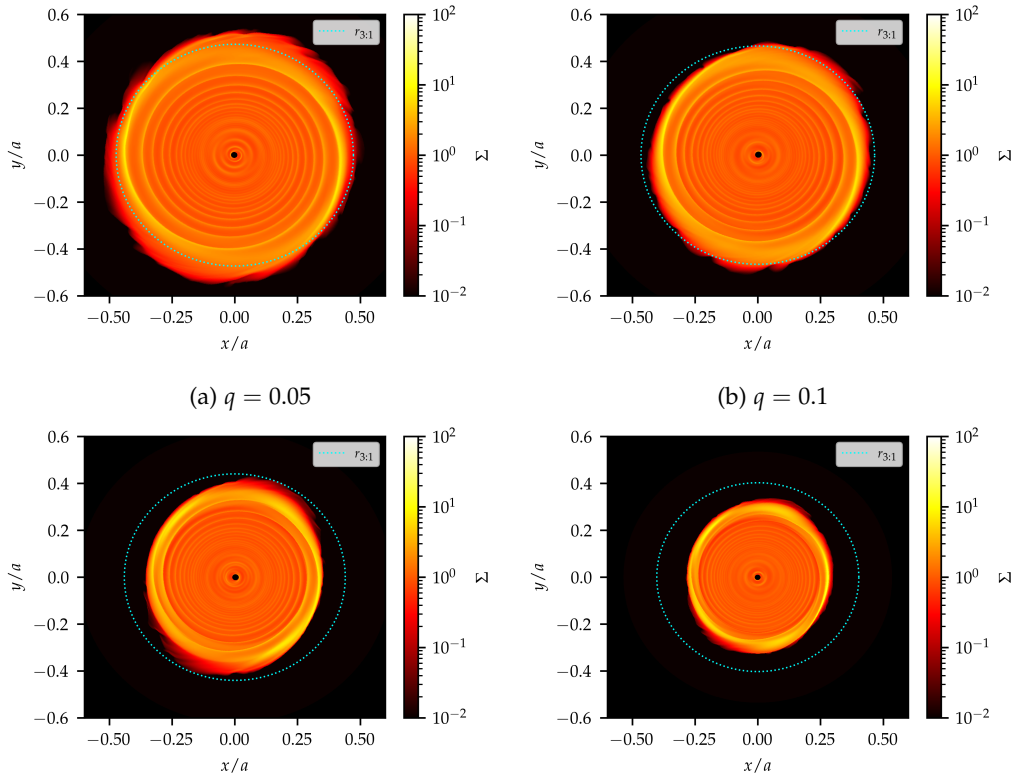

(a) $q = 0.05$ (b) $q = 0.1$

(c) $q = 0.3$ (d) $q = 0.7$

Figure 4.10 – Density maps for different simulations with increasing mass ratio (a to d) 10 binary orbits after the initial condition and Ma = 250. Because the tidal potential geometry is not the same, the discs have different sizes depending on the mass ratio q; at lower q the disc is truncated further away from the white dwarf. The cyan dashed circle corresponds to the 3:1 resonance radius at each mass ratio. This radius lies inside the disc only when $q < 0.3$.

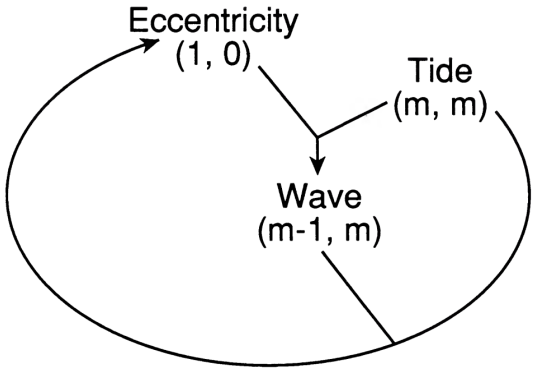

Figure 4.11 – Coupling mechanism of an eccentric mode and tidal mode. The numbers represent the wave number: the first one is the azimuthal wave number, and the second one is the time wave number. The eccentric mode has a zero temporal wave number because it is assumed to be stationary in an inertial reference frame. Figure from Lubow (1991a).

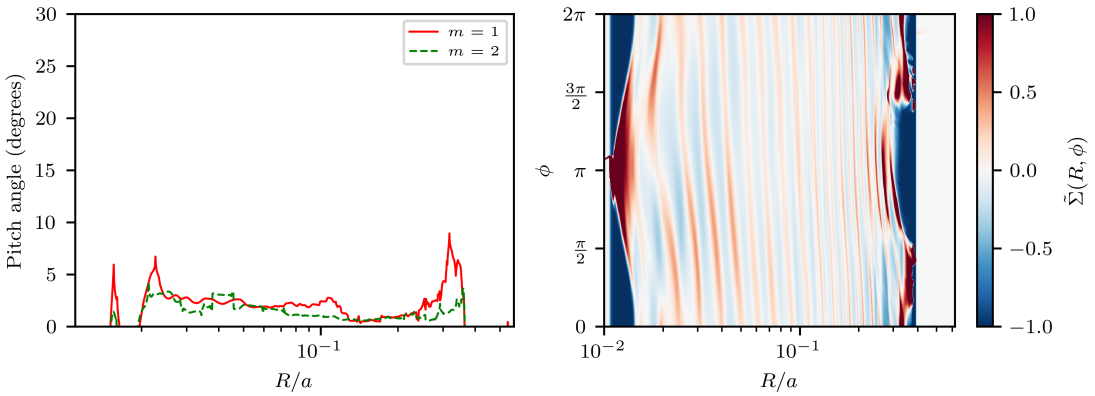

Figure 4.12 – Pitch angle measurement of the run with Ma = 250 for modes $m = 1$ and $m = 2$, after 38.8 binary orbits. For the m^{th} mode, the pitch angle θ_m is computed from the phase of the Fourier transform of the density Σ_m and is such that $\tan\theta_m = \frac{1}{R\partial_R \arg\Sigma_m}$. Figure from Van den Bossche et al. (2023).

observe such a growth, as the resonance radius remains within the disc for 60 to 100 binary orbits. Kley et al. (2008) have simulations in comparable regimes of mass ratio where they observe an eccentric instability on comparable timescales.

The main difference with their work is that my simulations are at much colder temperatures as I want to model the quiescence phase, and not superhumps. Indeed, their coldest simulation has $H/R = 0.02$, which translate to Ma = 50. In my case, the eccentric spiral waves are very tightly wound around the disc with pitch angle of values $< 5°$ for the simulation Ma = 250, as shown on figure 4.12. This very small pitch angle possibly explains why the eccentricity mode does not produce a globally eccentric disc. They note that the eccentricity growth rate increases linearly with Ma, but are not able to conclude on the final eccentricity state of low-temperature disc due to insufficient resolution. I did not produce simulations with $q < 0.3$ at different temperatures than Ma = 250, so I can not answer this question either.

The other important difference with their simulation is that my discs are inviscid. The only contribution to an effective viscosity is the shocks produced by the spiral wave, whereas they include a viscosity. In their setup, the viscosity's main role is to ensure that the disc viscously spreads beyond the resonance radius. Nonetheless, they note that a lower viscosity produces a slower growth of the eccentricity. This is because their argument is that viscosity is necessary for the disc to spread up to the 3:1 resonance radius. As shown on figure 4.10, even with no viscosity included this radius remains within my discs with $q < 0.3$.

As I will discuss below, I see that the relaxation behaviour of angular momentum transport are different for the low mass ratio simulations. This suggests that the coupling to the resonance might change the transport properties even without producing a global eccentric disc.

4.6.2 *Spiral pattern speed*

The properties of the spiral wave have been extensively studied. For instance, their pattern speed can be very informative of the process exciting them. For instance, the coupling of the disc eccentricity and the tidal potential described above can be described produced a wave of the form $e^{i([m\pm1]\phi - m\omega t)}$ with phase velocity

$$\Omega_m^{\text{inertial}} = \frac{m}{m \pm 1}\omega. \tag{4.34}$$

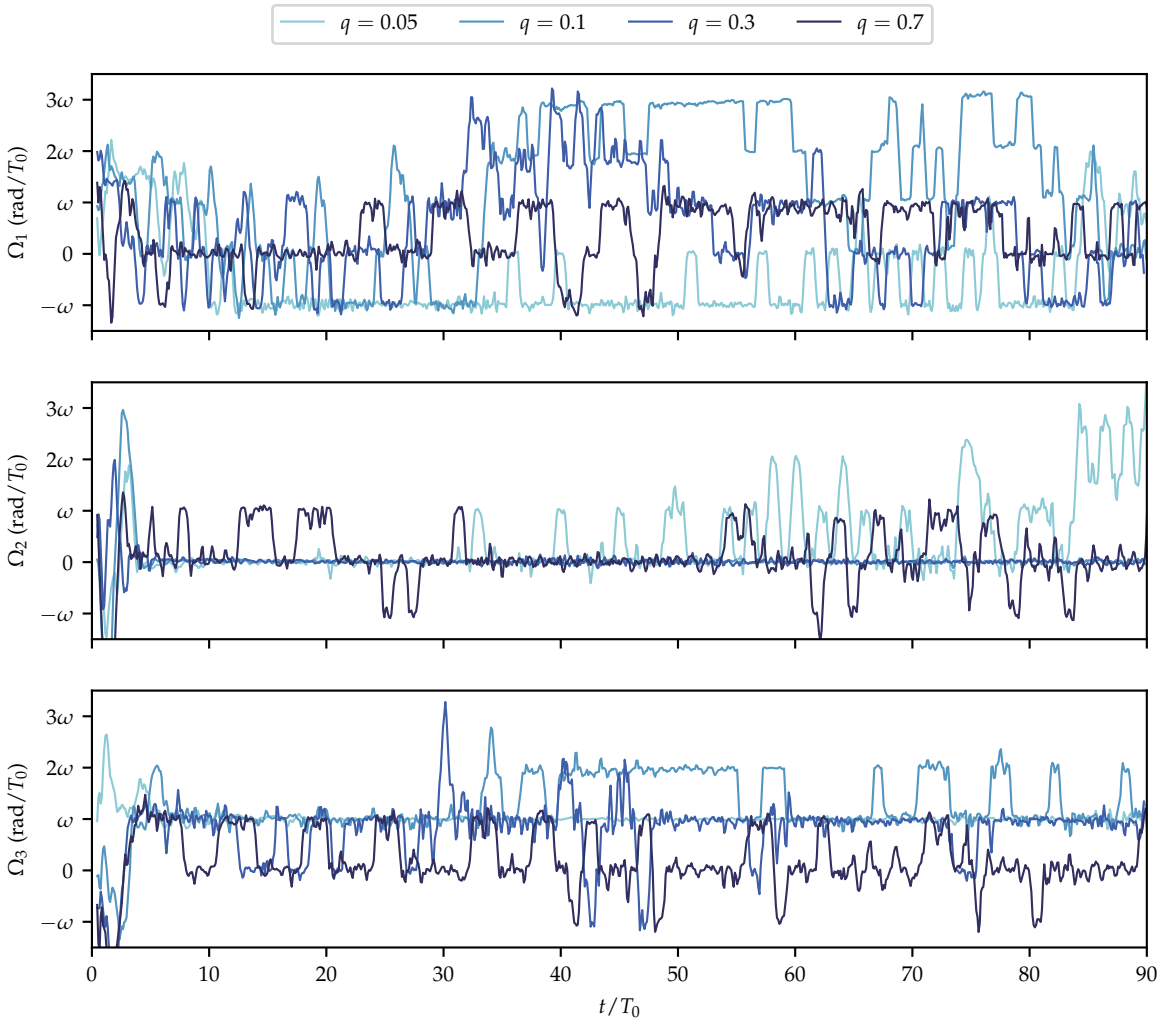

Figure 4.13 – Pattern speeds of the different modes for several mass ratios at $R = 0.2$. **Top:** $m = 1$ mode. **Middle:** $m = 2$ mode. **Bottom:** $m = 3$ mode. The phases Φ_m are smoothed over 1 binary orbit before taking their time derivative Ω_m.

This pattern speed is in the inertial reference frame. To work in the rotating reference frame, one needs to subtract the binary frequency ω. For comparison purposes, I work in the rotating frame in the following. In the rotating frame, (4.34) becomes

$$\Omega_m = \frac{\mp 1}{m \pm 1}\omega. \tag{4.35}$$

This pattern speed can be measured from the simulations using the time evolution of the phase of the azimuthal Fourier transform of density profile $\Sigma_m(R,t)$. For a mode m,

$$\Phi_m(R,t) = \arg \Sigma_m - \omega t \tag{4.36}$$

$$\Omega_m(R,t) = \frac{d}{dt}\Phi_m(R,t). \tag{4.37}$$

The measured pattern speed for the first azimuthal modes are shown on Figure 4.13. There, we see different features.

— First, the $m = 2$ mode is locked in phase with the companion star. This is what is expected from the linear theory, and previous numerical works (Ju et al., 2016). This

differs from second-order coupling, but as it is a higher-order effect, this expected amplitude is also expected to be lower. In previous simulations like in mine, very visible two-armed spirals at outer radii remain stationary in the rotating frame.

— Second, there seem to be several intermittent regimes of pattern speeds for the $m = 1$ mode. These modes do not match the theoretical $\frac{\mp 1}{m \pm 1}\omega$ pattern velocities. For $q = 0.05$ run, this eccentric mode appears to be mostly stationary in inertial space ($\Omega_1 = -\omega$).

— Lastly, looking at the 3:1 resonance radius for low mass ratio runs, the $m = 3$ mode has an intermittent pattern speed of $0 - \omega$. This is not consistent with the effect of the 3:1 resonance.

It seems that the theoretical pattern speeds at small mass ratios are not reproduced in my simulations. This can be the result of one of several possibilities. The eccentricity can already be saturated in a non-linear regime, or possibly, not have reached a stationary state yet. Kley et al. (2008) integrate for several hundreds of binary orbits with an arbitrary viscosity. As I do not impose such a viscosity reaching such a state might take even longer. It is also possible that strong non-linear coupling in my simulation, coupled with the low effective viscosity, stabilises the disc with respect to the eccentricity growth.

However, from Figure 4.13 there seems to be something at play which could be disentangled, in future works. The pattern speed almost always are integer ($\in \mathbb{Z}$) multiple of the binary frequency hinting that there are some preferred mode or modes. We also see that a lot of pattern speeds feature two or three regimes, and in some cases oscillate between the two even at late times.

4.7 SPIRAL TRANSPORT

As discussed in the introduction, the accretion can be measured with the α parameter introduced by Shakura and Sunyaev (1973). Here because we are using a finite-volume method, we have access to the inter-cell flux as well as the reconstructed cell-centred properties of the flow. To be more precise in the evaluation of the α parameter, we use the stress provided by the inter-cell fluxes. We can write

$$\alpha = \frac{\langle \rho v_R v'_\varphi \rangle_{t,\varphi}}{\langle \rho c_s^2 \rangle_{t,\varphi}}. \tag{4.38}$$

like in chapter 2, $v'_\phi = v_\varphi - v_K$ is the fluctuations in azimuthal velocity compared to the local Keplerian velocity. I average over the whole azimuthal domain. I also use a time-moving average to smooth the high-frequency dynamics' variations.

4.7.1 *Relaxation time*

Figure 4.14 shows the time evolution of this parameter for different simulations. In all simulations, we observe an initial transient regime. During this regime, angular momentum transport greatly increases to values of $\alpha \approx 0.01$.

However, this regime then relaxes to a state of low accretion. As the initial state of my simulations is an idealised axisymmetric Keplerian disc, it is expected to observe a strong initial transient state. The relaxation timescale appears to be very long and dependent of the disc temperature. For colder discs, this timescale reaches hundreds of binary orbits, the difference in relaxation time between the Ma $= 250$ and Ma $= 370$ simulations can be seen on figure 4.14. For the simulation with Ma $= 80$ the relaxation time is less than 10 binary orbits.

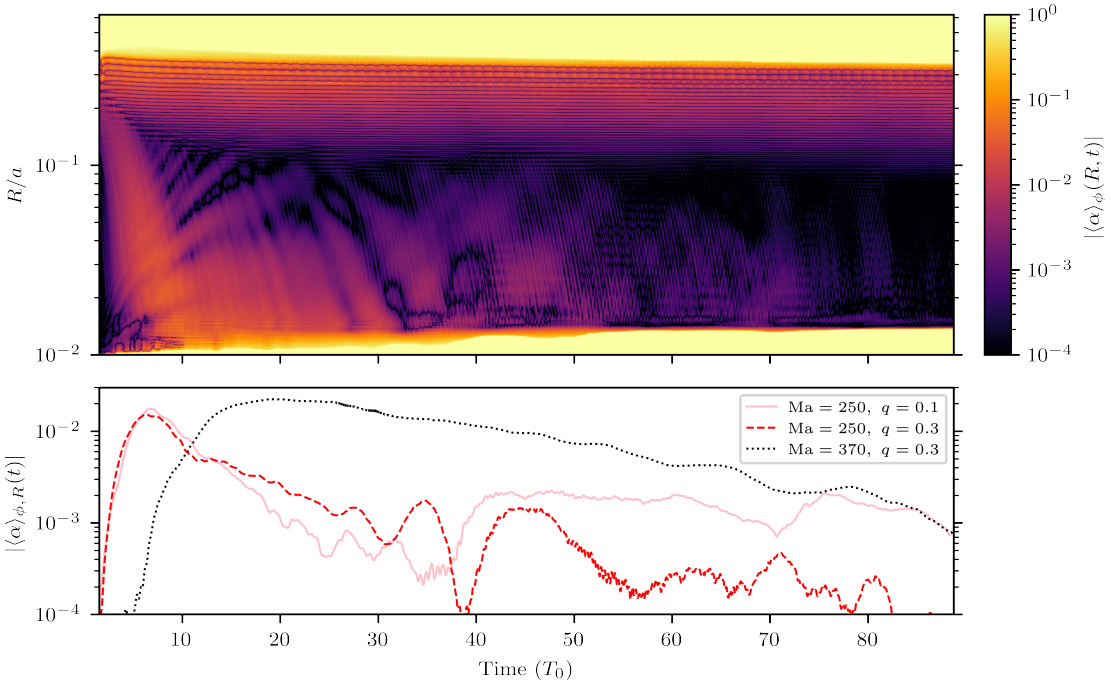

Figure 4.14 – **Top:** azimuthal average of the α parameter over radius and time for the simulation with Ma $= 250$ and $q = 0.3$, smoothed over three binary orbits. **Bottom:** Radial (for $0.02 \leq R \leq 0.1$) and azimuthal average of the angular momentum transport parameter for different runs. Figure from Van den Bossche et al. (2023).

This very long relaxation time has values comparable to the time between two outbursts in these systems. For example, SS Cyg has a recurrence time close to 200 of its binary orbits. Here, we aimed to find a steady state for the quiescence phase, but if the relaxation time is so long, this means that the disc may not be able to reach a steady state between two outbursts. This can produce memory effects from one outburst to the next, possibly modifying the observable emissions.

We also observe that the simulation with small mass ratio $q = 0.1$ reaches an α steady state after approximately 40 binary orbits. As mentioned above, this can be due to the coupling to the 3:1 resonance that lies within the disc at this mass ratio, and may increase accretion.

4.7.2 *Angular momentum transport*

In order to minimise the effect of the idealised initial condition on my measurements, I measure the final accretion regime of my simulations, averaged from $t = 80$ to $t = 89.9$. The values obtained are shown on figure 4.15.

In all cases, we see that the final value of the α parameter is well below the 10^{-2} value required by the DIM during quiescence. The state during which we measure the value of the α parameter is not a steady state, as discussed in the previous section. However, its value is decreasing during most of the simulation time. The value that we obtain at this time is thus an upper estimation of the angular momentum transport parameter α. Here too we see that the simulations with $q = 0.05$ and $q = 0.1$ have a $10\times$ increased accretion compared to the other at the same temperature. Even in this case, we barely reach $\alpha = 10^{-3}$.

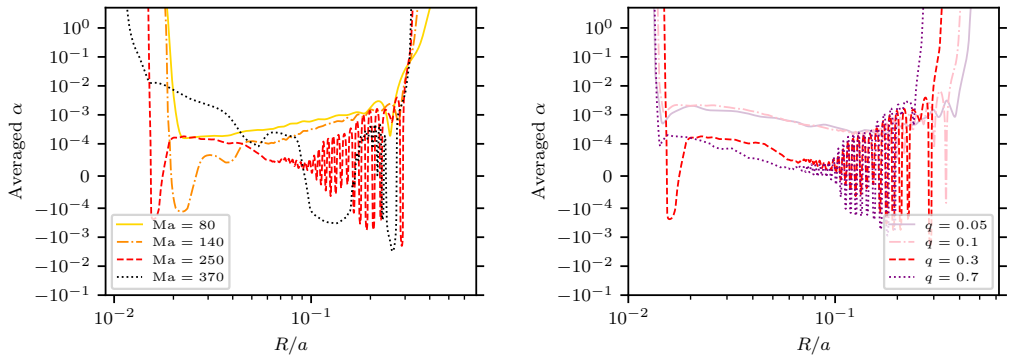

(a) Simulations with $q = 0.3$.

(b) Simulations with Ma $= 250$.

Figure 4.15 – Measure of the angular momentum transport parameter at late time of the simulation, averaged between $t = 80$ and $t = 89.9$ and over azimuth. The two panels explore different parameter variations. Figure (a) from Van den Bossche et al. (2023).

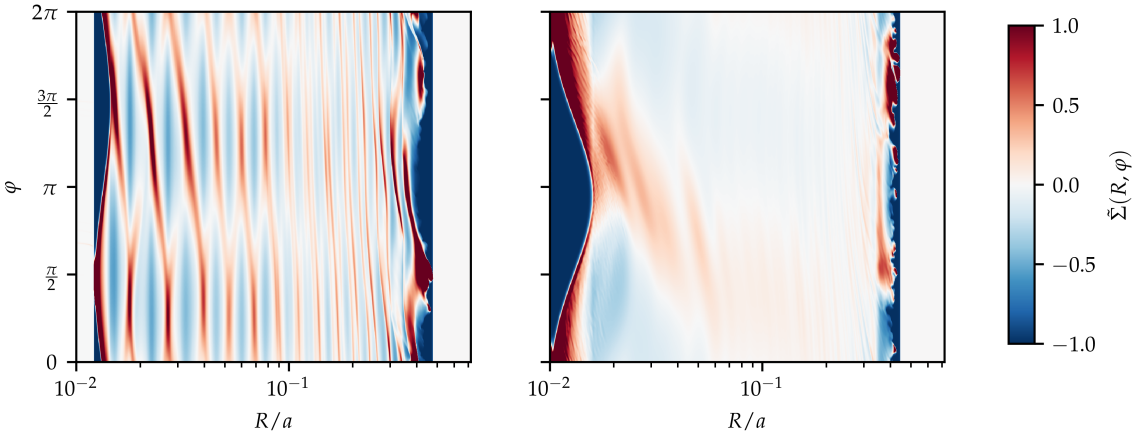

Figure 4.16 – Departure from the azimuthal density average at different times for the simulation restarted with no companion star. **Left:** Immediately after the restart. **Right:** After 50 binary orbits with no tidal potential.

4.7.3 *Removing the secondary star*

The results shown on Figures 4.14 and 4.15 for the simulations with $q = 0.05$ and $q = 0.1$ were at first somewhat puzzling. Indeed, the spiral waves are excited by the tidal potential. This means that we expect them to be weaker when the mass of the secondary star decreases.

In order to more thoroughly examine this phenomenon, I produce a series of simulations that start from the same state at $t \approx 49$. I modify the potential such that the mass of the white dwarf is unchanged but the mass of the companion star is set to zero.

The spiral waves obtained in this way are plotted on figure 4.16. We see that the spiral regime dramatically changes. We still have clear $m = 1$ spiral wave, but this time they are not as tightly wound as before. More surprisingly, we observe that the α parameter increases again after the secondary star is removed as can be seen on figure 4.17.

This can be due to several phenomena which we explored.

OUTER AND INNER EDGE RWI Like in Lesur et al. (2015), I have an infall of the matter surrounding the disc. This is due to the way I impose momentum conservation with the density floor in the tidally truncated region. At the outer edge of the disc, I also have a strong shear because of the density floor. This means that a Rosby Wave Instability (RWI) might develop there. This instability is characterised by the growth of large-scale ($m = 1$)

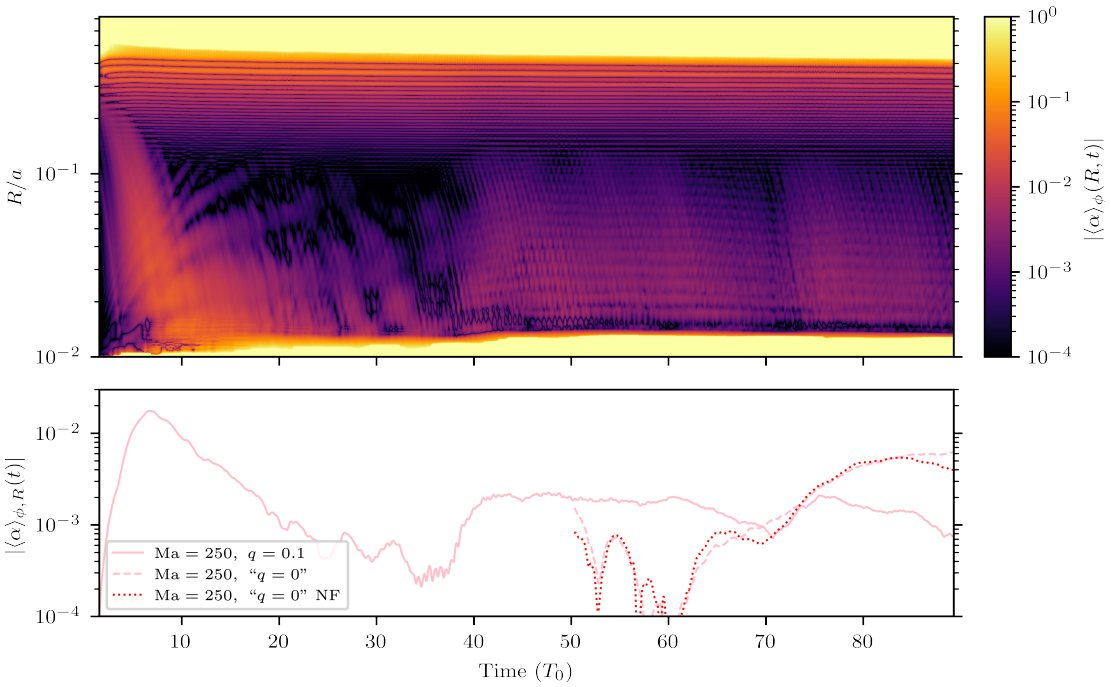

Figure 4.17 – Angular momentum parameter, similar to Figure 4.14. Here both panels correspond to the simulation with no tidal potential. On the bottom panel, this simulation with no tidal potential is denoted "$q = 0$". The simulation denoted "$q = 0$ NF" is also restarted with tidal potential, but without the FARGO scheme.

vortices. Lovelace et al. (1999) gives a criterion to recognise the RWI based on the local vorticity of the flow.

$$\mathscr{L} = \frac{1}{2}\frac{\Sigma}{(\boldsymbol{\nabla} \wedge \boldsymbol{v}) \cdot \boldsymbol{e}_z} S^{2/\gamma} \tag{4.39}$$

where S is the local entropy, and γ is the adiabatic index of the gas. The criterion reads as follows.

Unstable with respect to the RWI $\Rightarrow$ $\mathscr{L}$ has a local extremum.

Note that this criterion is not an equivalence relation. It is thus possible for $\mathscr{L}$ to have a local extremum without RWI.

In the simulation, I indeed see a local maximum in the inverse potential vorticity of the flow at the outer edge of the disc. This is due to the strong shear, but also to the fact that matter accumulated at the outer edge both because of the spiral waves and the matter infall producing a local over density. I also note a maximum of the inverse potential vorticity at the inner edge of the disc. This suggests that the RWI may be triggered at these radii. This is however not a definitive proof as the criterion is not an equivalence relation.

FARGO ? I also observe that the inner edge eccentric cavity grows beyond its initial size. As discussed in section 3.3.2, I suspected the FARGO advection scheme to change the dynamics of discs. Here, I reran the same simulation with the FARGO scheme disabled to measure its effect. We observed some differences in the measured α but we still observed the same general behaviour when removing the tidal potential as shown on figure 4.17. The α parameter increases after the restart in the same way whether FARGO is activated or not.

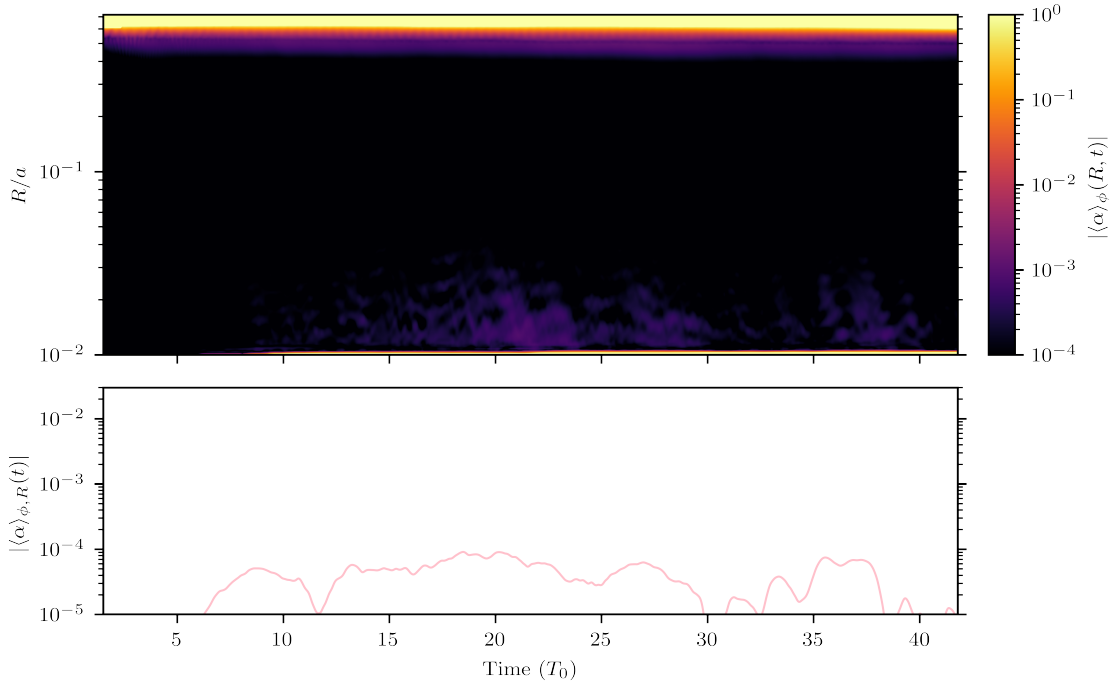

Figure 4.18 – Angular momentum parameter, similar to Figure 4.14. Here both panels correspond to the simulation with no tidal potential from the beginning.

WAVE REFLECTION I also produced a simulation implementing a wave-killing zone, like described before. Here as well the results did not change. I still see the growth of the inner edge eccentric cavity as well as an increased accretion regime.

NO SECONDARY STAR Finally, I produced simulations with no secondary star from the beginning. In these simulations, we obtain results very similar to Lesur et al. (2015). The resulting accretion of $\alpha < 10^{-4}$ is lower than what is observed after the presence of the binary. The transport properties of this simulation are shown on figure 4.18.

The fact that a disc in a tidal potential has to relax to a different state after the gravitational potential is changed is not surprising. It is also consistent with the transient accreting regime that I observed at the beginning of my simulation. In this case, as well the disc is a stable state for a different gravitational potential and has to reshape to the new potential.

This means that the outer edge instability drives only little accretion on its own, *i.e.* when there is no companion star from the beginning. It is possible that the tidal potential selects and excites a mode of this instability. This could possibly explain the dominant $m = 1$ spiral mode I observe. This excited mode then relaxes when the secondary star is removed as shown on figure 4.17.

4.7.4 *Resolution test*

As discussed in section 4.4, I chose the resolution of the numerical simulations using the linear theory criterion. I showed in the above, that my results strongly deviate from the linear theory predictions. I thus produced an additional simulation to verify that the resolution used in the simulation was fine enough.

This resolution test was also motivated by the run with Ma $= 550$. According to the linear theory, the resolution of 1081×1024 should have been sufficient to resolve the spiral wave dynamics everywhere in the disc. However, its transport properties are

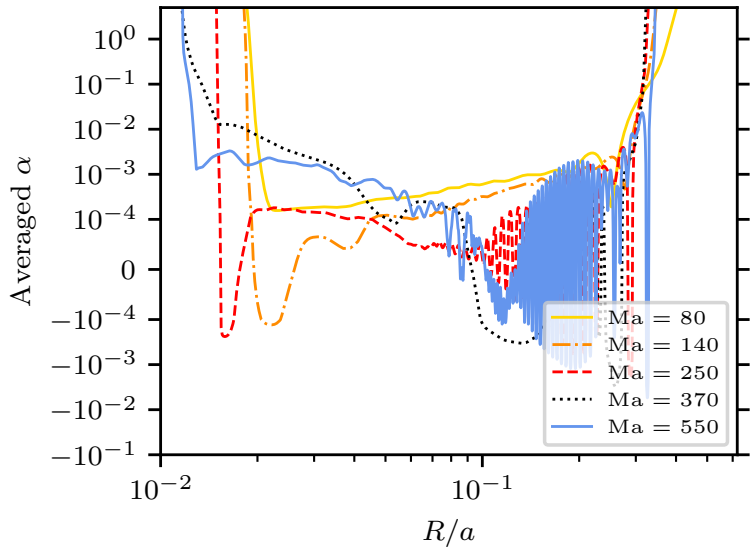

Figure 4.19 – Same plot as 4.15 including the high resolution Ma = 550 run.

dramatically different from the other simulations: in this simulation, I obtain values $\alpha \gg 1$. On figure 4.19 is plotted the higher resolution Ma = 550 run.

The resolution test simulation has an approximately $(4, 4)\times$ the resolution of the runs presented so far. On this run, we see the same spiral behaviour as in the low-temperature runs. I note that the relaxation time appears to be increased in the higher resolution run, possibly due to the increase in numerical diffusivity. In this run too, I reach $\alpha \ll 10^{-2}$ after 100 binary orbits consistently with the lower resolution runs, as can be seen on figure 4.19. The rapidly oscillating behaviour is a consequence of the very tightly wound spiral waves. This concludes that my resolution was sufficient and that the low accretion obtained is not a resolution artefact.

4.8 SPIRAL SHOCK HEATING

In this part, I present simulations where the disc thermodynamics is solved for. First, I study the thermodynamics of discs heated solely by spiral shocks. Then, I explore the consequences of such heating.

4.8.1 *On the importance of thermodynamics*

Ju et al. (2016) showed in their work that the heating of spiral shocks is important in their regimes. So much so that they could not produce long adiabatic simulations with realistic adiabatic index γ because the disc heats up too quickly. This heating can be clearly seen on their figure 7: the higher the γ they use, the less tightly wound the spiral waves are. As shown in section 4.5, I was able to reproduce their adiabatic simulations with the IDEFIX code.

This means that in order to run simulations on long timescales of several tens of binary orbits, one needs to introduce some cooling of the disc matter. This amounts to adding a cooling term to the energy equation.

In dwarf novæ systems, the dominant cooling channel of the disc is black-body radiation of the fluid. The cooling can thus be included in the energy equation with a term of the following form.

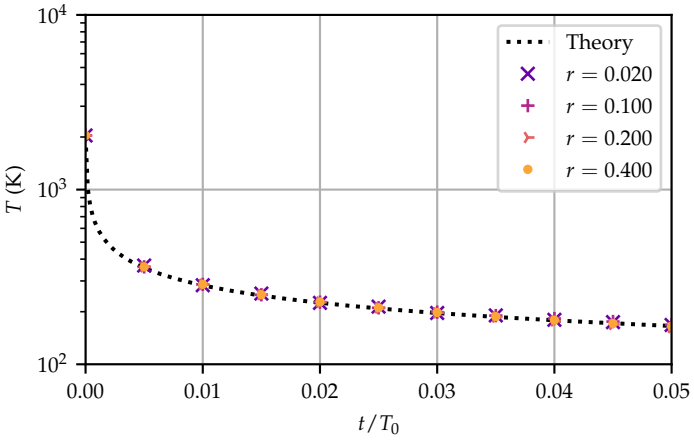

Figure 4.20 – Time evolution of the disc temperature at different radii for the constant opacity cooling function. As explained in the text, the cooling occurs at the same rate everywhere in the disc.

$$\frac{dE}{dt} = -4\sigma\kappa\rho T^4 \tag{4.40}$$

where σ is the Stefan constant and κ is the gas opacity, which may depend on different parameters. As I am doing 2D simulations, I use $\rho = \frac{\Sigma}{H}$ where $H = \frac{c_s}{\Omega_K}$ the disc height scale.

As presented with the DIM in section 2.2, one important question is to know whether we are able to find an equilibrium state where the disc heating (here, by spiral shocks) is balanced by the radiative cooling. The DIM only explored this question in a one-dimensional approach, however, spiral waves are fundamentally non-axisymmetric features. Their inclusion in thermodynamics remains open.

In the following, I start with the simplest model for a cooling function, that is with constant opacity. I then refine this model using tabulated values of the opacity to better match the actual opacity regime of the gas.

4.8.1.1 *Constant opacity model*

During the quiescence phase, the disc is expected to be marginally optically thin. My first cooling model uses a constant opacity for an optically thin disc. As a consequence, I use a Planck oppacity of $\kappa_P = 7$ cm^2/g. This value is computed from typical density and temperatures for the quiescence phase: $\Sigma = 100$ g/cm^2 and $T = 3000$ K. I used tabulated values of the opacity in Scepi (2019). For $T \in [10^{2.7}, 10^{4.5}]$ K they are taken from Ferguson et al. (2005), for $T \in [10^{3.75}, 10^{8.7}]$ K they are taken from OPAL (Iglesias and Rogers, 1996). Like in the latter, the opacity also depends on the medium density through[1] $\log\left(\rho/(10^{-6}\ T)^3\right)$ ranging from -8.0 to 1.0. Between the domains Scepi (2019) used a linear interpolation, and a zero-gradient extrapolation outside the domains.

Figure 4.20 shows the evolution of the temperature of the disc. We can see that the disc cools extremely rapidly to very low temperatures. This cooling is consistent with theoretical expectations. For a gas cooling with no, or negligible, heating, one has the following.

1. The quantities are expressed in CGS units.

$$\frac{dT}{dt} = -4\frac{\sigma\kappa_P\mu}{k_B}(\gamma-1)T^4 \tag{4.41}$$

with μ the molecular mass of the fluid, k_B the Boltzmann constant, and γ the adiabatic index. We obtain the following solution for the time evolution of the temperature.

$$T(t) = T_0\left(\frac{3t}{\tau}+1\right)^{-\frac{1}{3}} \tag{4.42}$$

where T_0 is the initial temperature and τ is a typical cooling time computed from the differential equation.

$$\tau = \frac{k_B}{4\sigma\kappa_P\mu(\gamma-1)T_0^3}. \tag{4.43}$$

We see on figure 4.20 that the temperature evolution is very close to this prediction. This means that the disc will eventually cool to 0 K if no heating occurs. Here, after a few hundredths of a binary orbit, the disc already reaches temperatures of 200 K, which are lower than quiescence disc temperature by an order of magnitude. The fact that there is no dependency on the radius is explained by the fact that τ is the same everywhere, because the disc is assumed to be globally isothermal.

This means that either the black body cooling with a constant opacity is a bad approximation and overestimates the actual cooling, or that there is some heating process that is not included in my simulation. As I want to focus on hydrodynamics-only simulations in this part, I explore the first possibility.

I then slightly modify this cooling model to include a temperature background. This is implemented as a cooling function of the form

$$\frac{dE}{dt} = -4\sigma\kappa\rho\left(T^4 - T_{bg}^4\right) \tag{4.44}$$

This produces results very similar to those above, but the temperature stops decreasing at $T_{bg} = 500$ K. This temperature background represents physical process that I ignore in my simulations. For instance, it is expected that the irradiation from the stars of the binary system heats the disc and prevents the gas from reaching a 0 K temperature.

It also turns out that the value of using a Planck opacity of $\kappa_P = 7$ cm^2/g is not self-consistent. Indeed, this assumes that the medium is optically thin, however for a typical surface density of $\Sigma = 100$ g/cm^2 (I assumed an initially constant surface density), this would yield an optical depth of $\kappa_P\Sigma > 1$ which contradicts the optically thin assumption.

Moreover, as the disc cools the opacity is expected to drop significantly, as shown on figure 2.1.

This indicates that the constant opacity model was too simplified to properly capture spiral shock heating and the associated radiative cooling.

4.8.1.2 *Tabulated effective temperature*

Here, I modify the cooling model, to have a more realistic description of the thermodynamics. I use a simple 1D radiative transfer model to compute the local equilibrium

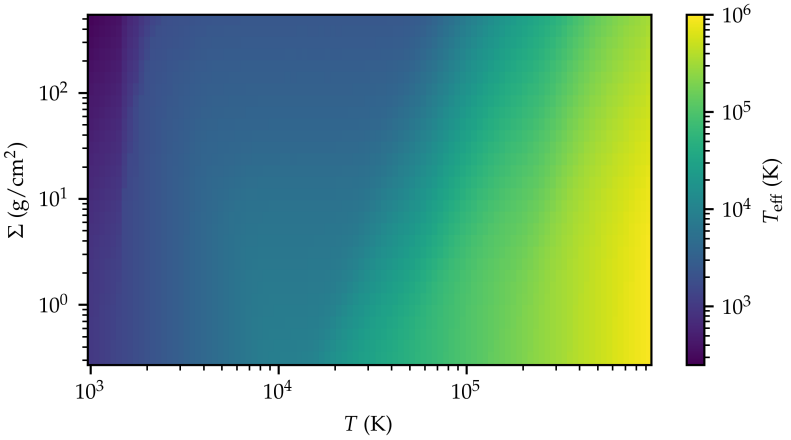

Figure 4.21 – Effective $T_{\rm eff.}$ as a function of surface density and disc temperature, computed at constant radius $R = 10^{9.7}$ cm.

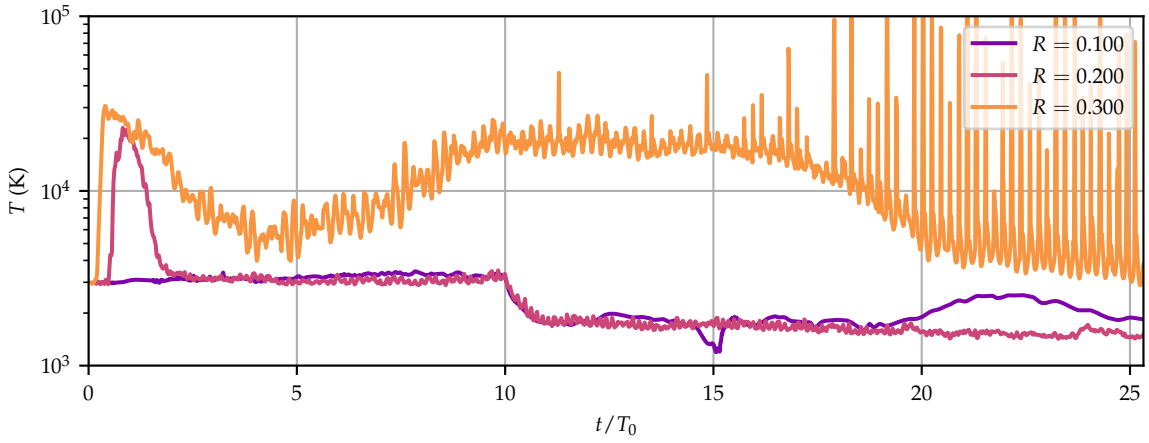

Figure 4.22 – Time evolution of the disc temperature at different radii for the tabulated effective temperature cooling function. Note that $R = 0.3$ remains inside the disc at all times.

effective temperature of the disc depending on the radius away from the white dwarf, the local surface density and midplane disc temperature. This model uses both Rosseland and Planck opacities. We thus have the following cooling term.

$$\frac{dE}{dt} = -4\sigma\kappa\rho\left(T_{\rm eff.}^4 - T_{\rm bg}^4\right) \tag{4.45}$$

where $T_{\rm eff.}$ is computed as a function of the local radius, temperature and surface density, in a similar to Hameury et al. (1998) in the thick atmosphere approximation (not the grey atmosphere approximation). A slice at constant radius of this effective temperature function is shown on figure 4.21. To compute this effective temperature, we assume vertical hydrostatic equilibrium.

The results obtained with this more realistic cooling function are shown on figure 4.22. Here I also implement a temperature floor that changes with time. For the ten first binary orbits, the temperature floor is set at 3000 K, the expected quiescence temperature. I do so in order to let possible spiral waves form. I then lower the temperature background to 500 K to observe whether spiral shocks are able to produce sufficient heating to compensate for the cooling.

We see on figure 4.22 that the steady state temperature reached by the disc is > 1000 K, that is not limited by the temperature background. This means that spiral shocks alone are sufficient to produce enough heating to reach realistic quiescence temperature.

4.8.2 *MRI unstable regions ?*

On figure 4.22, I also observe that the outermost part of the disc reaches very high temperatures, much higher than temperatures expected during the quiescence phase. This is the case even after the temperature background is lowered.

This is an effect of the tidal truncation of the disc. The disc has a non-circular shape because of the non-axisymetrical potential and strong shocks are produced at its outer edge. This may be a consequence of my idealised circular disc initial condition and of the infalling outer low-density regions. These non-axisymmetric features coupled to a slight precession of the disc also explain the very strong spikes seen at $R = 0.3$ on figure 4.22.

However, if one were to include a matter stream from the companion star, there would be a strong shock heating in these regions too.

If a quiescent disc reaches temperatures of 10^4 K in some regions, it means that the gas may be ionised enough to produce MRI-driven turbulence. This possible ionising effect was not taken into account in the argument of Gammie and Menou (1998). They discard such effect on grounds that thin discs couple 'only weakly to the tidal potential and suffers no global instability.'

4.9 SUMMARY AND CONSEQUENCES FOR FUTURE WORKS

In this chapter, I presented my work on 2D hydrodynamics simulations of dwarf novæ discs. The results can be summarised as follows.

1. The dominant spiral wave mode in cold quiescent discs is the $m = 1$ mode, not the $m = 2$ predicted by linear theory, which fails in quiescent regimes.
2. The spiral waves I observe deviate strongly from quasi non-linear coupling theory. The pattern speeds are integer multiples of the binary frequency but are yet to be explained.
3. Spirals shocks drive only weak accretion, and fail to explain the $\alpha = 10^{-2}$ required to explain recurrence times.
4. I observed a very long relaxation time in low-temperature disc, suggesting that the quiescence state might not be a steady state. This implies that there can be memory effects from one outburst to the next.
5. Spiral shocks alone are able to sustain quiescence disc bulk temperature of upwards of 1000 K. The hot spot and tidal truncation may be able to produce MRI unstable regions even during quiescence.

A new analytical framework needs to be developed to better understand the dynamics of tidally excited spiral waves. The $m = 2$ spirals seem to merge into $m = 1$ due to non-linear effects, which can not be captured in simple linear theories. Cimerman and Rafikov (2024) observe a similar phenomenon in circumbinary disc. In their case too, the region where the tidal torque is the strongest (for them: the inner disc) features $m = 2$ spiral waves, which evolve to a $m = 1$ spiral wave in the rest of the disc (for them: the outer disc).

As discussed in the introduction, recent observational work (Ruiz-Carmona et al., 2020) showed that for outbursting dwarf novæ, spiral waves are not seen as often as they are expected. In this regime, the spiral waves are expected to have a wide opening

angle. During the quiescence phase, the more tightly wound spiral waves would be even more difficult to resolve; and for the time being, it would be very challenging to have observational confirmation of the $m = 1$ spiral mode.

Additionally, the very long relaxation time that I observed in my cold simulations raises caution about future numerical works. If the quiescence phase is not a steady state, particular care will have to be paid to the initial condition of simulations. They will have to reproduce as closely as possible the final state of an outbursting disc, otherwise one might only measure the transient regime from an idealised initial state.

5

MAGNETIC WINDS IN THIN BINARY DISCS

Contents

5.1 Numerical setup **101**
5.1.1 Plasma parameter definitions 101
5.1.2 Equation of state 102
5.1.3 Ohmic resistivity 103
5.1.4 Grid 103
5.1.5 Units 106
5.1.6 Algorithm 106
5.1.7 Boundary conditions and density floor 106
5.1.8 Initial conditions 107
5.2 Magnetic accretion **108**
5.2.1 Disc evolution 108
5.2.2 Disc vertical structure 111
5.2.3 Outflow and accretion 114
5.2.4 Disc magnetisation 115
5.2.5 Comparison with the non-magnetic case 117
5.3 Disc tilt **117**
5.3.1 Description of the tilt 118
5.3.2 Understanding the tilt 126
5.4 Summary **142**

In this chapter, I present three-dimensional simulations of dwarf novæ discs. As we saw in chapter 4, spiral-driven accretion is not strong enough to explain the observed accretion of these systems during quiescence. Here, I include the third dimension as well as magnetic field to the picture of the previous chapter. This will allow me to study possible wind launching from quiescent dwarf nova discs.

5.1 NUMERICAL SETUP

Here I solve the full three-dimensional Euler MHD equations with the IDEFIX code, as presented in chapter 3. I work in spherical coordinates (r, θ, φ).

5.1.1 *Plasma parameter definitions*

As presented above, the main control parameter for both MRI and wind launching is the plasma β parameter. The definition of this parameter is not the same across literature, so for the sake of clarity, I present the precise definition I use in this work.

The relevant control parameter for the physical mechanisms at hand is the β parameter *of the mean field*, that is

$$\beta_{\text{mean}} = \frac{2\mu_0 \langle P \rangle}{\langle B \rangle^2}. \tag{5.1}$$

This parameter is the ratio of the *mean thermodynamical pressure* and the magnetic pressure *of the mean field*. Unless otherwise written, all β parameters in the following are

defined as such. Note that with this definition, the plasma parameter does not take into account local perturbation of the fields, for example, due to turbulence. The average $\langle \dots \rangle$ are usually space averages. For β, we usually take an azimuthal average of its equatorial value. In the following, I will always specify over which set the average is computed.

I then make the difference between the *poloidal* β parameter and the *total* β parameter. The former is a relevant control parameter for accretion physics through the MRI and magnetic winds, while the latter is simply the ratio of thermodynamical to magnetic pressure.

$$\beta = \frac{2\mu_0 \langle P \rangle}{\langle B \rangle^2} \tag{5.2}$$

is the total plasma parameter, taking into account all dimensions of the magnetic field $\boldsymbol{B} = B_r \boldsymbol{e}_r + B_\theta \boldsymbol{e}_\theta + B_\varphi \boldsymbol{e}_\varphi$, and B its magnitude

$$\beta_\mathrm{p} = \frac{2\mu_0 \langle P \rangle^2}{\langle B_\mathrm{p} \rangle^2} \tag{5.3}$$

is the poloidal plasma parameter, taking into account only the poloidal dimensions of the magnetic field, with $\boldsymbol{B}_\mathrm{p} = B_r \boldsymbol{e}_r + B_\theta \boldsymbol{e}_\theta$ the poloidal magnetic field, and B_p its magnitude. It is often more relevant to look only at the poloidal component of the magnetic field as the B_ϕ is a consequence of the shear flow, and is not a relevant control parameter from wind launching and MRI.

5.1.2 *Equation of state*

The Euler equations system is closed with a two-temperature barotropic equation of state.

A two-temperature equation of state proved necessary from preliminary simulations because I use a density floor. Indeed, because of the density floor, the *isothermal* vertical hydrostatic equilibrium of the disc is not possible. Such a vertical profile requires $\rho_\mathrm{eq}(r,z) \approx \rho_0(r) \exp\left(-\frac{z^2}{2H^2}\right)$ with $H = \frac{c_\mathrm{s}}{\Omega_\mathrm{K}}$. For $z \gg H$ the density will inevitably be lower than the imposed density floor. As a consequence of having $\rho = \rho_\mathrm{floor} \gg \rho_\mathrm{eq}$ in the atmosphere, the vertical hydrostatic equilibrium is not achieved, and the "massive" atmosphere is not supported by its lower layers. This means that the atmosphere collapses onto the disc, while being continuously replenished by the density floor.

The chosen equation of state is the following.

$$p = c_\mathrm{s}^2(\rho)\rho, \tag{5.4}$$

with

$$c_\mathrm{s}(\rho) = c_\mathrm{d} + \frac{1}{2}\left[1 - \tanh\left(\frac{\log\frac{\rho}{\rho_\mathrm{c}}}{\Delta}\right)\right](c_\mathrm{c} - c_\mathrm{d}), \tag{5.5}$$

where c_d and c_c are the high-density (disc) and low-density (corona) sound speeds respectively. ρ_c is the transition density, and Δ is the transition width. This equation of state corresponds to a cold disc at $T_\mathrm{d} \propto c_\mathrm{d}^2$ and a hot corona, or disc atmosphere, at $T_\mathrm{c} \propto c_\mathrm{c}^2$. I choose ρ_c such that we have several orders of magnitude between the initial

density profile and ρ_c, and likewise between ρ_c and the density floor of the simulation. Δ is chosen such that $\frac{\partial P}{\partial \rho} > 0$ for all densities to avoid instability. This two-temperature equation of state is illustrated on figure 5.1. In the simulations of this chapter, I do not solve the energy equation. Consequently, the fluid temperature is fully determined by its density.

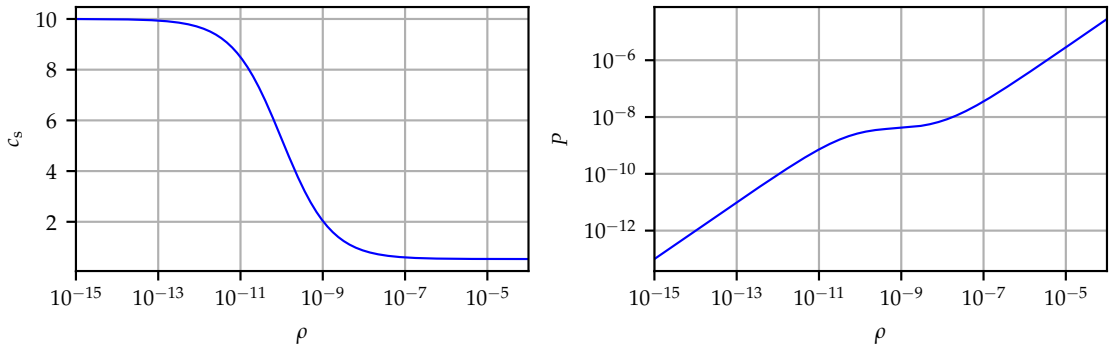

Figure 5.1 – Equation of state used in the 3D Ma $= 100$ simulations. Note that $\forall\, \rho \in \mathbb{R}^+$, $\frac{\partial P}{\partial \rho} > 0$. The density floor used is $\rho_{\text{floor}} = 10^{-15}$ and the initial disc density at the inner edge is $\rho = 10^{-4}$.

The choice of this equation of state is physically motivated by the fact that the low-density material above the disc plane is heated (and ionised) by the white dwarf. In the Ma $= 100$ simulations, I use c_d such that $\text{Ma}_d(r_{\text{in}}) = \frac{v_K}{c_d} = 100$ and c_c such that $\text{Ma}_c(r_{\text{in}}) = \frac{v_K}{c_c} \approx 5$. I use $\rho_c = 10^{-10}$ such that there are several orders of magnitude of density at high density and low temperature for an isothermal regime. I use $\Delta = 1.2$ such that for these sound speeds this equation of state is bijective.

5.1.3 *Ohmic resistivity*

The magnetic diffusivity defined in Eq. (2.25) is computed from tabulated solutions of Saha equation. However, it is still too computationally expensive to produce disc simulations with $\text{Ma}_{\text{real.}} \approx 10^3$ so I have to rescale the computed resistivity in order to obtain a realistic magnetic Reynolds number for quiescence $\text{Rm} = \frac{\Omega_K H^2}{\eta} \lesssim 100$ in the inner disc. The initial profile of the Reynolds number is shown on figure 5.2. The rescaling procedure can be described as follows

$$\eta_{\texttt{code}} = \epsilon\, \eta_{\text{Saha}}(\rho, T_{\texttt{code}}/\epsilon), \tag{5.6}$$

with $\epsilon = \left(\frac{\text{Ma}_{\text{real.}}}{\text{Ma}_{\texttt{code}}}\right)^2 = \frac{T_{\texttt{code}}}{T_{\text{real.}}}$ the ratio of the realistic Mach number, and the Mach number of the simulation $\text{Ma}_{\texttt{code}}$, related the aspect ratio of the disc defined in Eq. (5.9). I impose η to be exactly zero in the cells adjacent to the axis, at $\theta \equiv 0\ [\pi]$. The regularisation scheme used around the axis that was implemented in Idefix at the time (described in the next subsection) is only known to be exact in ideal MHD.

5.1.4 *Grid*

For the simulations presented in this chapter, I use a logarithmic grid for the radial dimension, with $\Delta r \propto r$. This non-uniform grid enables us to better capture the small-scale dynamics of the inner regions without having a very fine, and computationally expensive, grid at the outer edges where it is not necessary. The inner radius of the domain is set at $r_0 = 0.01\ a$, at the outer radius of the white dwarf. The outer radius of

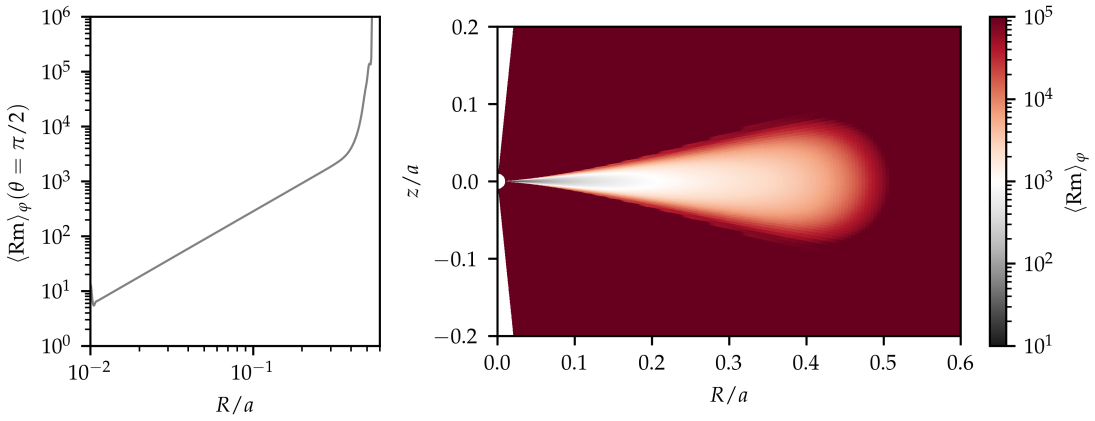

Figure 5.2 – Initial profile of the magnetic Reynold number for resistive simulations. Close the axis, the resistivity is zero, and the $\mathrm{Rm} = \infty$. **Left:** Rm in the midplane of the disc. **Right:** Azimuthal average of the magnetic Reynolds number, the high-density disc is recognisable, at low Rm.

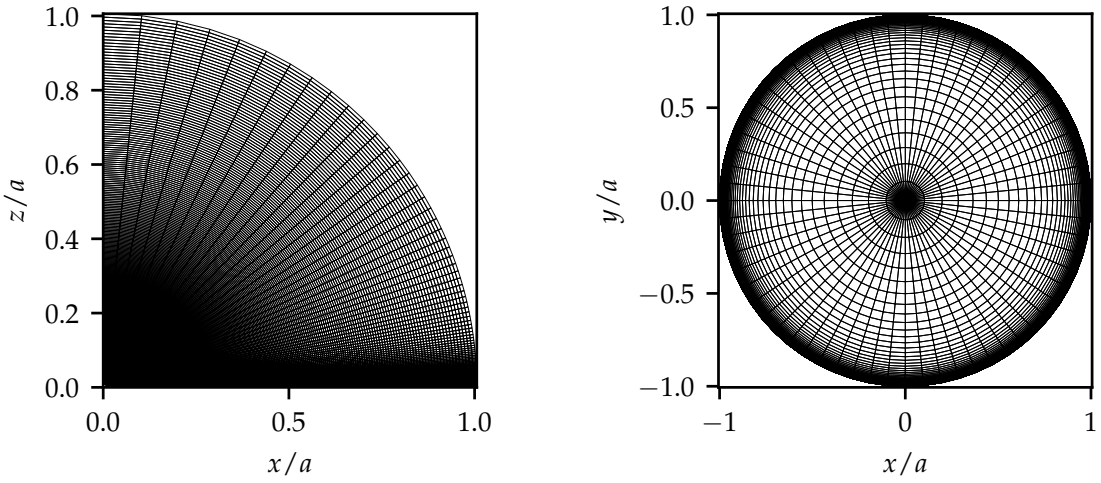

Figure 5.3 – **Left:** Poloidal ($x - z$) slice of the grid. **Right:** Top view ($x - y$) of the grid. On the latter, we see the $\theta - \phi$ grid of the external radius of the grid. On the right panel, only 1 in 10 azimuthal cells is represented for legibility.

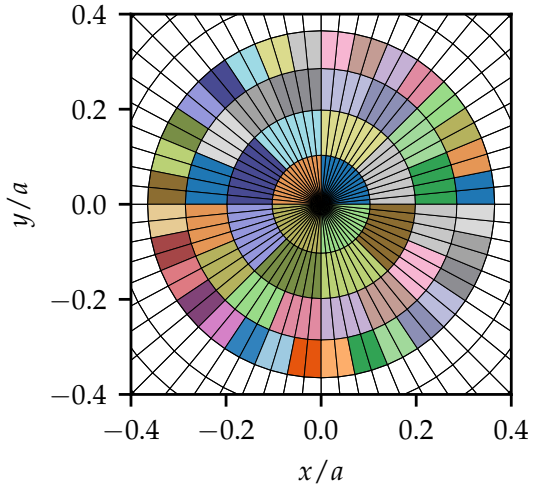

Figure 5.4 – Principle of the grid-coarsening method: at a given θ, adjacent cells with the same colour have the same average quantity, with grouping size increasing closer to the pole. This illustration is not a representation of the actual levels used in the simulations. Here the level is $\ell = 4$ adjacent to the pole, and decreases by one with each θ step. White cells are not grouped.

the domain is set at $r = a$. This means that the simulation domain extends in regions where the secondary star should be present, I comment on this choice in more detail in Sect. 5.2.2.1.

For the latitudinal direction, I use a concatenation of stretched grids near the poles, and a uniform grid around the equatorial plane. The stretched grid is used from the pole, down to a latitude corresponding to $4 \times h(r_0)/r_0$ on either side of the midplane. For the longitudinal direction, I use a uniform grid. The global grid has size $(N_r, N_\theta, N_\varphi) = (512, 192, 640)$. With this grid, at $r = r_0$, there are approximately 1.1 grid cell per scale-height in the azimuthal direction, 1 point per scale-height in the radial dimension and 8 points per scale-height in the latitudinal direction.

For the azimuthal direction, in order to reduce the impact of the small cells close to the axis, I use a static coarsened grid such that the coarsening level ℓ is

$$\ell = \left\lfloor 1 + \log_2 \left(\frac{1}{\sin\theta} \right) \right\rfloor . \tag{5.7}$$

The effect of this grid-coarsening is to average neighbouring cells by groups of power of 2, and maintains $\nabla \cdot \boldsymbol{B} = 0$. Figure 5.4 illustrates the grouping method.

This method allows me to use a modified CFL condition, such that the time step is limited by

$$dt = \min \left[\min \left(\frac{2^{\ell-1} dx}{c} \right) + \min \left(\frac{2^{2(\ell-1)}}{\eta} \right) \right] . \tag{5.8}$$

c is the fastest signal speed, and η is the Ohmic resistivity. In practice, the time step is limited by the Alfvén velocity of the plasma rather than by the parabolic CFL condition due to Ohmic resistivity.

Table 5.1 – Runs presented in this paper.

Name	Ma(r_0)	Resolution (N_r, N_θ, N_ϕ)	q	Ohmic resistivity	Initial β_p
RB3	100	$(512, 192, 640)$	0.4	Yes	10^3
iB3	100	$(512, 192, 640)$	0.4	No	10^3
RB4	100	$(512, 192, 640)$	0.4	Yes	10^4
iB4	100	$(512, 192, 640)$	0.4	No	10^4
HD	100	$(512, 192, 640)$	0.4	N/A	non − magnetic
R50	50	$(512, 192, 640)$	0.4	Yes	10^3

5.1.5 *Units*

In this chapter, the chosen time unit is the binary period $T_0 = \frac{2\pi}{\omega} = 2\pi\sqrt{\frac{a^3}{G(M_\mathrm{s}+M_\mathrm{WD})}}$. The natural length unit is the binary separation a. Like in chapter 4, these units are scaled on the dwarf nova system SS Cygni, where T_0 is approximately 6.6 hours and a is 1.37×10^{11} cm (Bitner et al., 2007).

In this paper, I use the Mach number at the inner edge as a reference for the thickness of the disc, as $\mathrm{Ma} = \frac{r}{h}$, the inverse of the disc aspect ratio.

$$\mathrm{Ma} = \frac{\Omega_K(r_0) r_0}{c_\mathrm{s}} \approx 364 \left(\frac{M_\mathrm{WD}}{1\,M_\odot}\right)^{1/2} \left(\frac{10^9\,cm}{r_0}\right)^{1/2} \left(\frac{10^4\,K}{T}\right)^{1/2}, \tag{5.9}$$

where $\Omega_K(R) = \sqrt{GM_\mathrm{WD}/R^3}$ is the Keplerian angular frequency for the white dwarf's potential. Note that this definition depends on the chosen inner boundary of the simulation; for instance, in an isothermal setup $\mathrm{Ma} \propto \sqrt{r_0}$. This must be kept in mind when comparing to previous work. In particular, Pjanka and Stone (2020) set their inner boundary further out, at $r_0 = 0.05\,a$, with a the binary separation.

5.1.6 *Algorithm*

Here, I use the HLLD approximate Riemann solver (Miyoshi and Kusano, 2005). The parabolic terms of the Ohmic resistivity are solved using an explicit scheme.

5.1.7 *Boundary conditions and density floor*

In the azimuthal direction, I use periodic boundary conditions. In the latitudinal direction, I use the `axis` boundary condition described in Lesur et al. (2023), which follows Zhu and Stone (2018). In the radial direction, I use a custom outflow boundary condition. This condition is such that, at the inner radius, the azimuthal velocity is set to be Keplerian, $v_\phi = \sqrt{\frac{GM_\mathrm{WD}}{r}} - \omega R$. The toroidal magnetic field is set to zero and all other fields are set to have zero gradient. At the outer radius, we use the same condition, except for the density, which I set to the density floor. This is such that the pressure gradient is always directed towards the exterior of the simulation domain. This is especially important in order to model escaping winds.

Additionally, I use a density floor at $\rho_\mathrm{floor} = 10^{-15}$ such that if the density of a cell drops below this threshold, it is automatically set to this density.

I also use an Alfvén speed limiter such that the Alfvén speed in a cell never exceeds $\max(v_{A,max}, dx/dt_{\min})$, where $v_{A,max}$ is set to the liberation velocity at the inner radius, $dt_{\min}$ is specified by the user, and dx is the smallest edge of the cell, taking the grid-coarsening procedure into account. When triggered, the Alfvén velocity limiter increases the density of the cell such that the local Alfvén velocity abides by our criterion. Compared to an Alfvén speed limiter using a uniform velocity ceiling, this criterion allows for larger Alfvén velocity in larger cells, where a higher signal speed does not lower the timestep of the simulation. Using this limiter limits greatly the quantity of mass added by the Alfvén speed limiter compared to a limiter which limits the Alfvén velocity everywhere.

Both the density floor and Alfvén speed limiter are implemented in such a way that the poloidal momentum of the cell is always conserved. The azimuthal velocity is left unchanged to minimise the effect of the density floor on the angular momentum of the cell.

5.1.8 *Initial conditions*

The simulations in this chapter are all restarted from an axisymmetric 2.5D hydrodynamics-only run. The hydrodynamics run is integrated for ten binary orbits and is then restarted in full 3D with a magnetic field and a non-axisymmetric potential.

5.1.8.1 *Hydrodynamics initial condition*

The 2.5D hydrodynamics run is started with the density profile from the hydrostatics isothermal vertical equilibrium. With the chosen equation of state, there is no radial dependency of the sound speed inside the disc. This is, however, not the actual hydrostatic equilibrium solution for our equation of state, because with such a density profile, there is a vertical variation of temperature.

$$\rho(R,z) = \rho_0 \left(\frac{R}{r_0}\right)^{\frac{3}{2}} \exp\left[\frac{GM_{\rm WD}}{c_{\rm s}^2}\left(\frac{1}{\sqrt{R^2+z^2}} - \frac{1}{R}\right)\right], \tag{5.10}$$

where $(R,z) = (r\sin\theta, r\cos\theta)$ are the cylindrical coordinates. I use $\rho \propto R^{\frac{3}{2}}$ such that the initial surface density of the disc is $\Sigma = \int \rho dz \propto R$ as predicted by the DIM during quiescence (Hameury et al., 1998). At first non-vanishing order in z/R, this profile yields $\rho \propto \exp(-z^2/2H^2)$ where $H = c_{\rm s}/\Omega_K(R)$ is the hydrodynamics vertical equilibrium height-scale, related to the Mach number by $\mathrm{Ma}(R) = R/H(R)$.

I set the initial flow to be purely Keplerian, $v_\phi = \sqrt{\frac{GM_{\rm WD}}{r} - \omega R}$, with no vertical or radial velocity. This does not exactly match the radial equilibrium of the disc, as it does not compensate for any radial pressure gradient.

Following the same procedure as in chapter 4, I pre-truncate the disc at the tidal truncation radius r_T predicted for our mass ration (Paczyński, 1977). This step is done in anticipation of the tidal potential introduced at the 3D restart with magnetic fields. The mask I apply to truncate the disc is the same as before. As discussed in chapter 4, this shortens the initial transient tidal truncation regime.

$$\mu(R) = \frac{1}{2}\left(1 - \tanh\left(\frac{R - r_T}{\delta_T}\right)\right) \tag{5.11}$$

I use $\delta_T = 0.05$

The simulation is then integrated for ten binary orbits in order to reach an axisymmetric quasi-steady state, consistent with our initial truncated disc and the barotropic

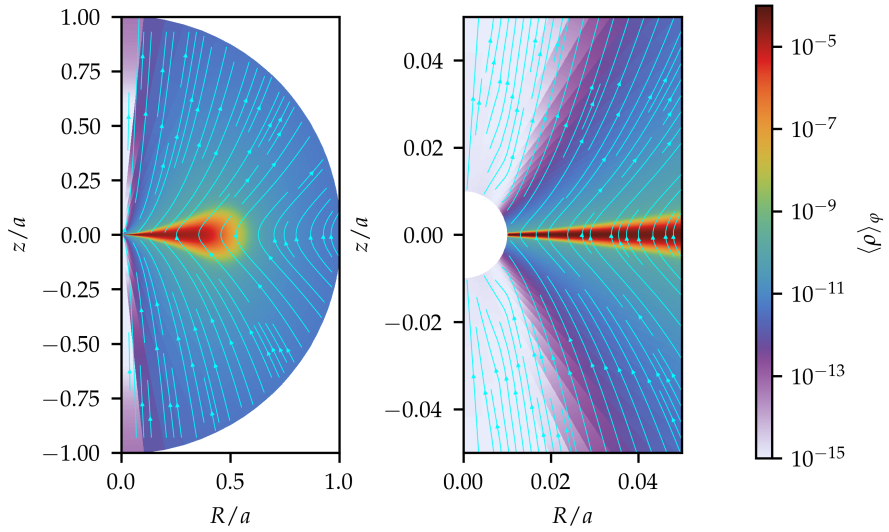

Figure 5.5 – Initial axisymmetric configuration at the 3D restart. The cyan streamlines show the magnetic field lines from equation (5.12). **Left:** Global picture. **Right:** Zoom on the inner regions of the simulation. Note that on this figure, the density colourbar goes down to the density floor.

equation of state. During this step, a thermal wind is launched. Such a wind does not contribute to angular momentum transport, as it imposes no torque on the disc.

5.1.8.2 *3D Magnetic restart*

After ten binary orbits, I restart from the state obtained from the 2.5D hydrodynamics run. I add a slanted poloidal magnetic field adapted from Zanni et al. (2007). The magnetic field is initialised with the potential vector $\boldsymbol{A}$.

$$A_r = A_\theta = 0, \quad A_\phi = \frac{4}{3} B_0 \left(\frac{R}{r_0}\right)^{m+2} r_0^2 \frac{\kappa^{5/4}}{(\kappa^2 + z^2/R^2)^{5/8}/R} \tag{5.12}$$

where κ is the typical kink scale of the magnetic field line in units of the binary separation, we use $\kappa = 0.3$. B_0 is the magnetic field strength at the inner radius. m is the power law index of the magnetic field in the midplane, we use $m = 1/4$ such that the initial plasma β is constant in the disc midplane. With this magnetic field prescription, the initial magnetic field is purely vertical in the disc midplane. The magnetic field geometry corresponding to this vector potential is shown on figure 5.5.

I emphasise that the magnetic field is only included in the 3D simulation and not in the 2D preliminary run to avoid the creation of rings due to the accumulation of the magnetic flux due to the constrained geometry (Riols and Lesur, 2019).

5.2 MAGNETIC ACCRETION

5.2.1 *Disc evolution*

Here I describe the evolution of the disc in three dimensions, once the magnetic field is added. This evolution is separated into two parts. In the present section, I present the properties of the accretion disc during the first orbits after the magnetic field, tidal potential and third dimension are introduced. In a second evolution phase, the disc develops a rapidly increasing tilt with respect to the binary orbital plane. During the first evolution phase, that is for $t < 14 - 15\ T_0$ across all simulations, the tilt is small. Quantitatively,

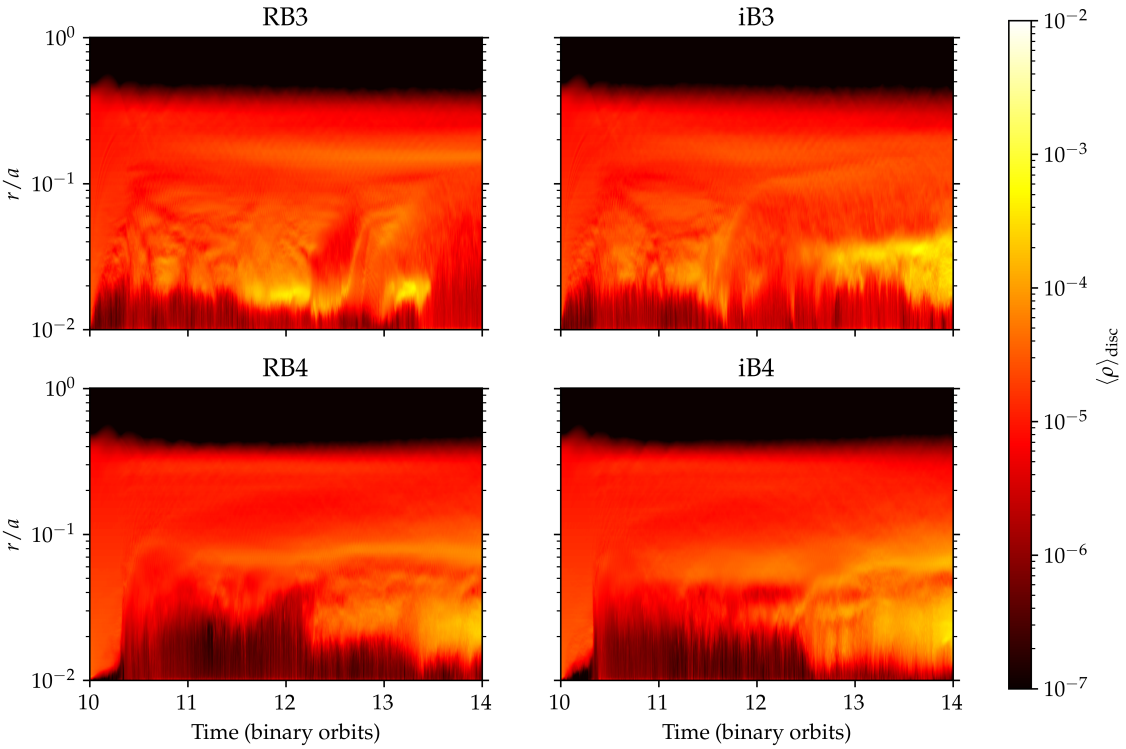

Figure 5.6 – Evolution of the vertical and azimuthal average of the density close the midplane, between ± 4 the hydrostatic scale-height. **Left:** Runs with resitivity. **Right:** Ideal MHD runs. **Top:** Runs with initial $\beta = 10^3$. **Bottom:** Runs with initial $\beta = 10^4$.

this means that the angle the disc makes with the binary plane is indistinguishable from the noise fluctuations due to the turbulent flow. I discuss the strong tilt phase in the next section. In the present section, I focus on the first phase of evolution, at times $t \leq 14\ T_0$. Here, the disc lies in the binary orbital plane.

The disc density evolution is presented on figure 5.6. On this figure, we see that after less than a binary orbit, the density in the inner region of the disc appears to be greatly reduced compared to the initial hydrodynamics state across all four simulations. The regions at radii $r < 0.02$ develop an eccentric cavity like the two-dimensional simulations of chapter 4. The radius of this cavity is consistent with the two-dimensional simulations. The radius of this low-density region is greater in the $\beta = 10^4$ simulations for a few orbits, and settles to $r \approx 0.02$ like the $\beta = 10^3$ after a few more binary orbits.

On figure 5.7 is plotted the vertical magnetic flux in the midplane. We can see that the initial magnetic field is rapidly advected towards the inner regions of the disc. This step comes together with a diminution of the density. As a consequence, the plasma magnetisation in the inner regions of the disc dramatically increases from its initial value, see figure 5.8.

After a few binary orbits, the disc has settled in a two-region state. The inner cavity of the disc has low density and high magnetisation, with $\beta_{\mathrm{p}} \ll 1$, i.e. a magnetically dominated region. The outer region of the disc remains thermally dominated, with $\beta_{\mathrm{p}} \gg 1$, but lower than its initial value, and surface density closer to the initial state.

In both simulations with initial $\beta = 10^3$, we can see that after being initially advected onto the white dwarf, the poloidal magnetic field lines are advected back into the disc after a couple of binary orbits. In the lower magnetisation simulations, with $\beta = 10^4$, this does not happen. On the contrary, the magnetic field flux further decreases because poloidal magnetic field loops form close to the midplane. This also occurs at a lower rate in the $\beta = 10^3$ simulations after some of the field lines are advected back in the disc.

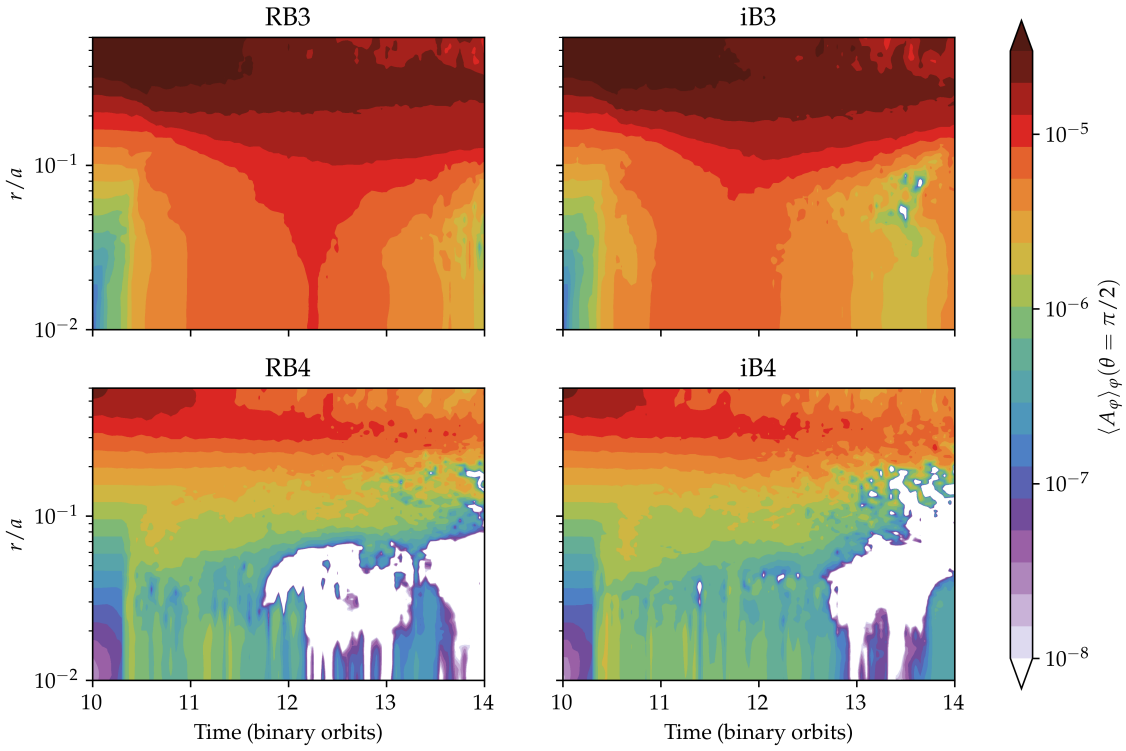

Figure 5.7 – Evolution of the vertical magnetic flux through the mid plane. The iso-contours correspond to magnetic field lines. **Left:** Runs with resistivity.**Right:** Ideal MHD runs. **Top:** Runs with initial $\beta = 10^3$. **Bottom:** Runs with initial $\beta = 10^4$.

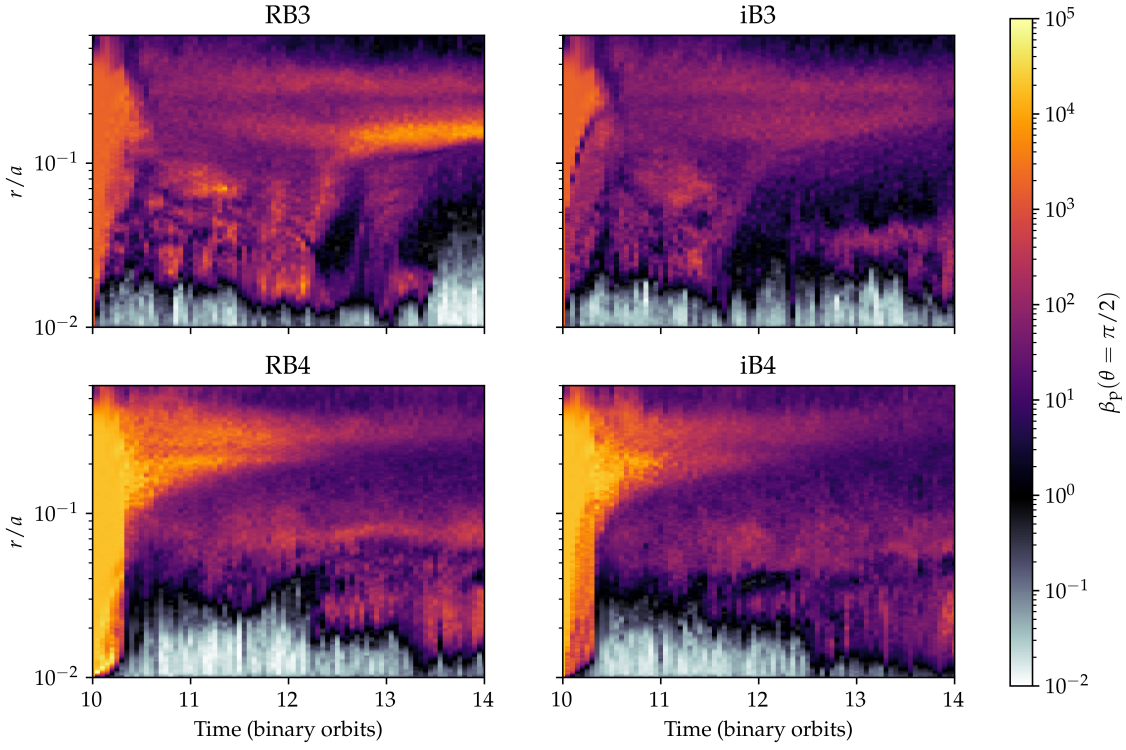

Figure 5.8 – Evolution of the β_p in the midplane. **Left:** Runs with resitivity. **Right:** Ideal MHD runs. **Top:** Runs with initial $\beta = 10^3$. **Bottom:** Runs with initial $\beta = 10^4$.

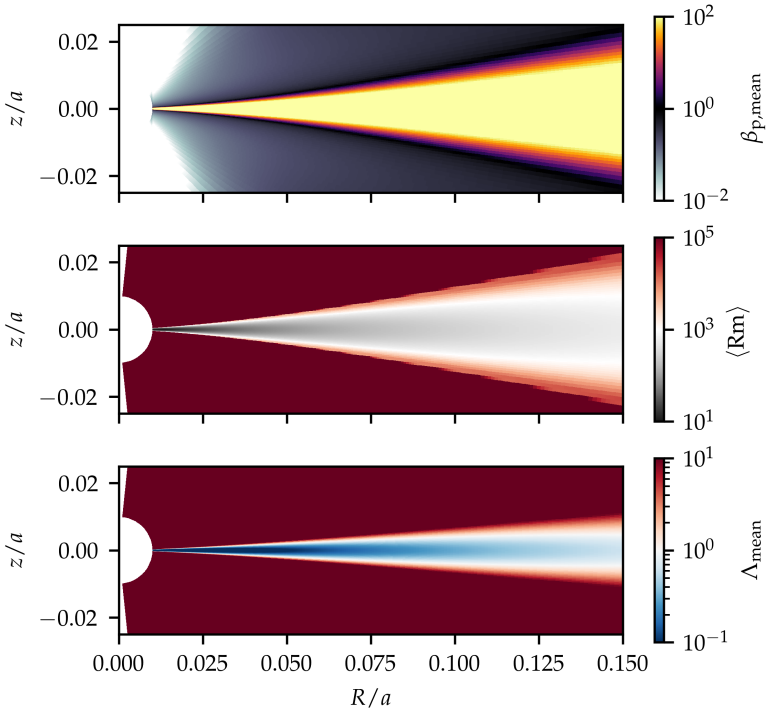

Figure 5.9 – Dimensionless number characterising the initial axisymmetric state, with added magnetic field. **Top**: Poloidal β parameter of the mean field. **Middle:** Mean magnetic Reynolds number. **Bottom:** Ohmic Elsasser number.

I also note that even though the disc midplane is highly resistive, very clear MRI channel modes develop on both surfaces of the disc, both in resistive and ideal simulations. There, the resistivity is lower and the β is lower; this allows for the MRI to develop as the local Ohmic Elsasser number $\Lambda = 2\,\mathrm{Rm}\,/\beta_\mathrm{p} > 1$, as shown on figure 5.9. As a consequence, and as will be discussed below, I see no major difference between the resistive and ideal MHD simulations in terms of turbulent accretion. I will not further discuss the MRI as the low disc resolution necessary for global simulation implies that MRI turbulence will be poorly resolved, if at all. Indeed, in the ideal MHD case, Latter et al. (2010b) shows that for $\beta = 10^3$, at least 50 points per scale-height are required to resolve the fastest growing channel mode; here, I only have 8.

5.2.2 *Disc vertical structure*

5.2.2.1 *Wind geometry*

As shown on Fig. 5.10, a wind is launched above and below our disc. The wind launching surface is somewhat far from the density bulk, at an altitude ranging from $|z| \gtrsim 0.1$ in inner radii to $|z| \approx 0.2$ at further radii. At lower altitudes, matter is falling towards the midplane. This structure is somewhat reminiscent of Jacquemin-Ide et al. (2021b) with the magnetic wind launching far above the disc. However, the flow inside the density bulk appears to be different in here than in their simulations. As discussed below, this difference in behaviour is also observed in the dominant pressure term inside the disc (see figure 5.11).

As a consequence of the elevated wind launching surface, I extended the outer radius of the simulation domain. Preliminary test runs with a smaller outer radius $r_\mathrm{out} = r_{L_1}$ for the simulation zone (not shown here) showed that this outer radius was not far enough for the wind to launch, because the outer boundary condition polluted the outflow.

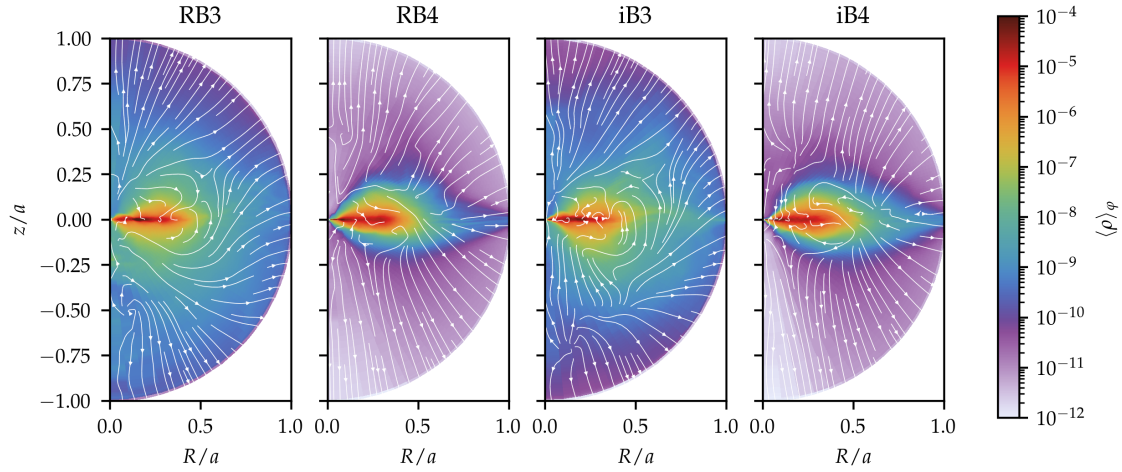

Figure 5.10 – Maps of the azimuthal and time average of the density. The over-plotted streamlines correspond to the azimuthal and time average of the poloidal velocity field. **RB3:** resistive simulation with $\beta = 10^3$. **RB4:** resistive simulation with $\beta = 10^4$. **iB3:** ideal simulation with $\beta = 10^3$. **iB4:** ideal simulation with $\beta = 10^4$. For reference, the first Lagrange point is around $r/a = 0.6$.

5.2.2.2 *Vertical equilibrium*

When it comes to the vertical equilibrium, I find that the disc can be separated in two radial regions, as shown on figure 5.11. The two top panels correspond to the inner region of the disc (but not to the cavity), where the vertical support of the disc is ensured by the magnetic pressure, both laminar and turbulent. There, the thermodynamic pressure is smaller than the magnetic pressure.

The two bottom panels correspond to the outer disc. There, the disc is vertically supported by the thermodynamic pressure. The laminar magnetic pressure reproduces the expected behaviour, as previously shown on figure 2.6. In this region, the turbulent magnetic pressure $\langle \delta B^2 \rangle$ is sub-dominant by a factor of about ten (see Fig. 5.11). This outer region is similar to the simulations of Jacquemin-Ide et al. (2021b).

In this simulation, the transition radius between the magnetically dominated region and the thermally dominated region is around $R = 0.1 - 0.2$. At this radius, $\langle P \rangle = \langle \delta B^2 \rangle$.

As a consequence of being magnetically supported, the inner disc structure dramatically changed from the initial hydrostatic profile. The inner regions of the disc become strongly puffed-up or 'elevated', and lose some of their top-bottom symmetry. The initially thin disc now has effectively a much larger aspect ratio than the initial hydrostatic $\mathrm{Ma}^{-1} = 0.01$. This is clearly visible in figure 5.12. On this figure, we can see that the vertical density profile at radii $r \leq 0.1$ is much wider than the hydrostatic equilibrium at this radius. On the contrary, in outer regions of the disc $r \geq 0.2$, the disc density profile corresponds to this hydrostatic profile. Note that the deviation from this profile at outer radii away from the midplane is due to the barotropic equation of state; the low-density matter is at higher temperature and is not expected to fit the isothermal hydrostatic profile.

I define an effective height scale $H_\sigma(R)$ from the vertically integrated density.

$$I_R(H_\sigma) = \langle \int_{z_0 - H_\sigma}^{z_0 + H_\sigma} \rho(z, R) dz \rangle_\varphi, \tag{5.13}$$

where z_0 is the vertical position of the maximum of the azimuthally averaged density at fixed cylindrical radius R. The effective height scale is such that $I_R(H_\sigma)$ is approximately 68% of the total azimuthally averaged surface density. Formally, $H_\sigma = I_R^{-1}(0.68)$. I also

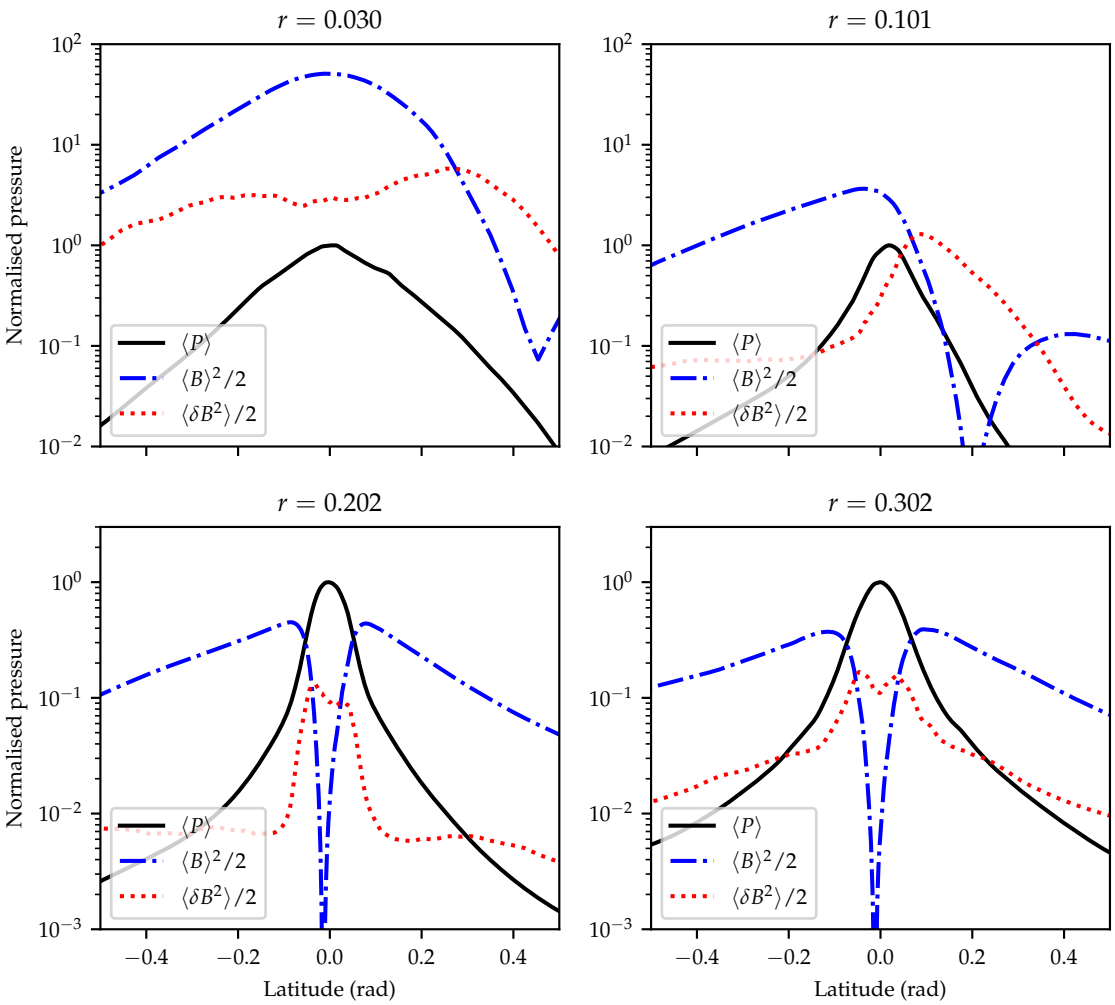

Figure 5.11 – Pressure terms contributing to the vertical structure of the disc at different radii. Averaged over 1 binary orbit of the RB3 simulation. **Top:** inner disc radii. **Bottom:** Outer disc radii. The pressure terms are normalised to the maximum value of the thermal pressure $\langle P \rangle$ at each radius.

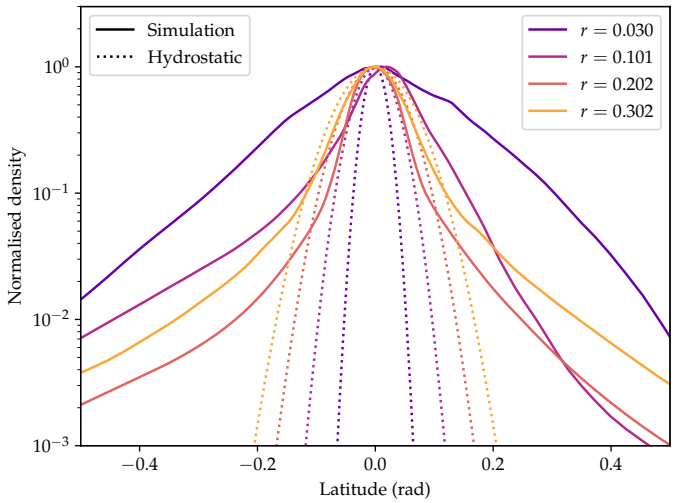

Figure 5.12 – Vertical density profile averaged over 1 binary orbit. The dotted lines show the hydrostatic equilibrium profile at each radii (gaussian). The chosen radii are the same as in figure 5.11.

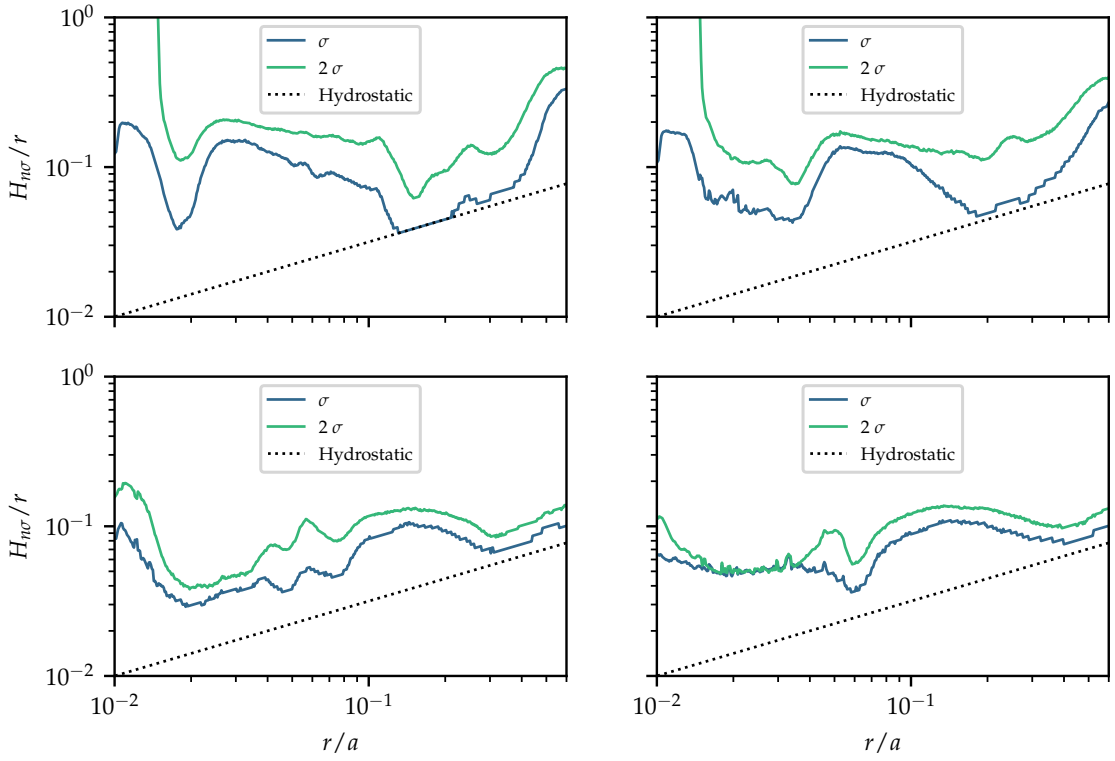

Figure 5.13 – Effective aspect ratio of the discs, averaged over 1 binary orbit. The dotted line represents the isothermal aspect ratio for the chosen disc temperature $\propto \sqrt{r}$. The regions beyond $r = 0.6$ are not shown as there can be no disc beyond the Lagrange point. **Left:** Runs with resitivity. **Right:** Ideal MHD runs. **Top:** Runs with initial $\beta = 10^3$. **Bottom:** Runs with initial $\beta = 10^4$.

define $H_{2\sigma(R)}$ corresponding to the height scale containing 95% the column density. In the case of a thin steady locally isothermal hydrostatic disc, these would coincide with the usual height scale $H = c_s/\Omega$.

On figure 5.13, we can see that the disc is puffed up in the inner regions. We see that the actual aspect ratio of the disc is approximately constant with radius, with $H/r \approx 0.1$ everywhere. with a very slight decrease with radius. This means that the disc is more than ten times thicker in the inner magnetised regions, than in the hydrostatic case. This is consistent with the pressure balance of figure 5.11; the inner regions differ from the hydrostatic picture, whereas the outer disc is more or less in hydrostatic equilibrium.

We also see that $H_{2\sigma(R)} > H_{\sigma(R)}$. This means that compared to a Gaussian vertical profile, the vertical density profile is less peaked, and more vertically spread. This is in part due to the two-temperature equation of state. With this equation of state, the hydrostatic vertical profile is a Gaussian only close to the midplane. Moreover, the presence of a magnetic wind changes the vertical density profile as matter from the disc will be carried away from the disc to its atmosphere.

We see that the inner eccentric cavity region $r < 0.02$ also strongly differs from the hydrostatic structure.

5.2.3 *Outflow and accretion*

The accretion rate plotted on 5.14, is defined as the radial mass flux integrated on spherical shells.

$$\dot{M}(r) = -\int_{\vartheta_{\min}}^{\vartheta_{\max}} \int_0^{2\pi} \langle \rho v_r \rangle_t r^2 d\theta \sin\theta d\phi \tag{5.14}$$

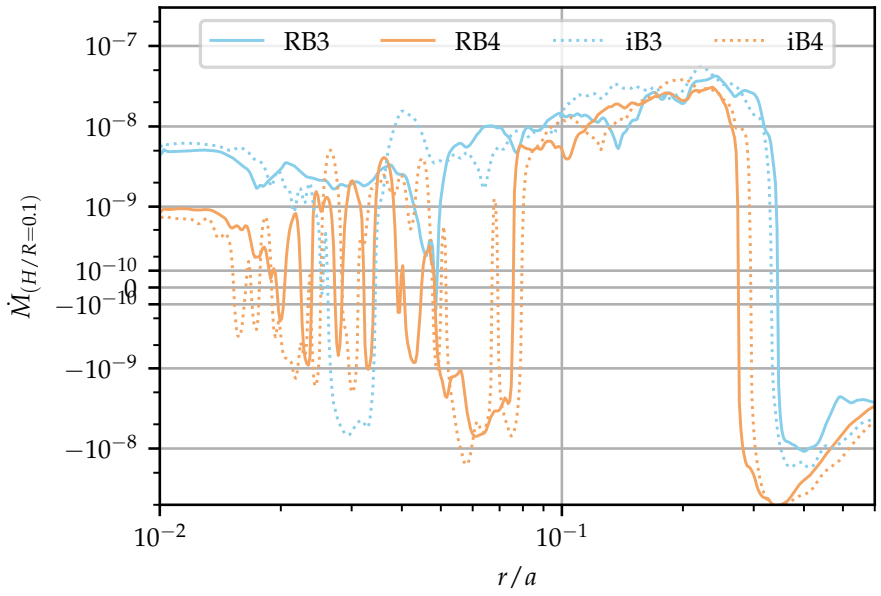

Figure 5.14 – Time-averaged accretion rate computed on spherical shells of radius r inside the disc.

where ϑ_{min} and ϑ_{max} are the latitude position of the surface of the disc. This surface is not taken from the hydrostatic scale-height H, as we saw that it did a poor job at describing the actual vertical profile of density. Rather I take these angles to be such that they form an angle corresponding to $\pm H/r = 0.1$, in agreement with the results of figure 5.13, around the local density maximum. $\langle \dots \rangle_t$ is a time average.

I take the outflow rate of the wind to be a similar integral over the complementary latitude domain $[0, \pi] \setminus [\vartheta_{\text{min}}, \vartheta_{\text{max}}]$. I show the ratio of the wind outflow rate to the accretion rate on figure 5.15. Note the wind outflow is positive when $v_r > 0$, opposite to the accretion rate. We see that the contribution of the wind to matter flow is comparable to the accretion rate inside the disc. In fact, close to 50% of the mass loss of the disc occurs through this outflow. This ratio is slightly less in the ideal simulation, closer to 30%, because in this simulation, the accretion rate is increased. This values are greater than the values inferred from observations of a few percents of the disc accretion rate (Hoare and Drew, 1993; Knigge and Drew, 1997) for outbursting dwarf novæ and nova-like.

On this figure, we also see that in the inner region of the disc, at $r < 0.1$, the mass flux above and below the disc are accretion flows rather than outflow. This is also what happens in the less magnetised $\beta = 10^4$ simulations. This is because, as discussed above, in these simulations, the winds is launched further away from the disc. This is clearly visible on figure 5.16. This figure shows the azimuthally and time-averaged radial matter flux $\langle \rho v_r \rangle_{\varphi,t}$. There, we see that for the simulations with higher magnetisation $\beta = 10^3$, this flux becomes an outflow at closer distance from the disc than in the $\beta = 10^4$ simulations. In the latter simulations, the accreting atmosphere (in blue) is more vertically extended than in the former.

5.2.4 *Disc magnetisation*

In my simulations, the initial advection of the vertical magnetic field creates a strong radial magnetic field. So much so that even though the magnetic flux remains more or less constant inside the whole disc (as shown on figure 5.7), the magnetisation increases everywhere inside the disc, as we can see on figure 5.8. In general, the midplane B_r

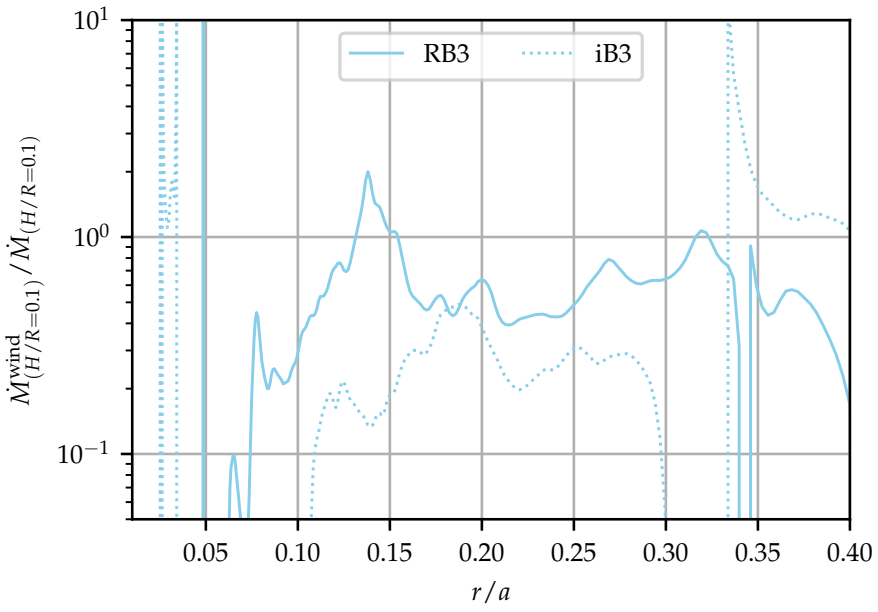

Figure 5.15 – Time-averaged outflow rate computed on spherical shells of radius r inside the disc.

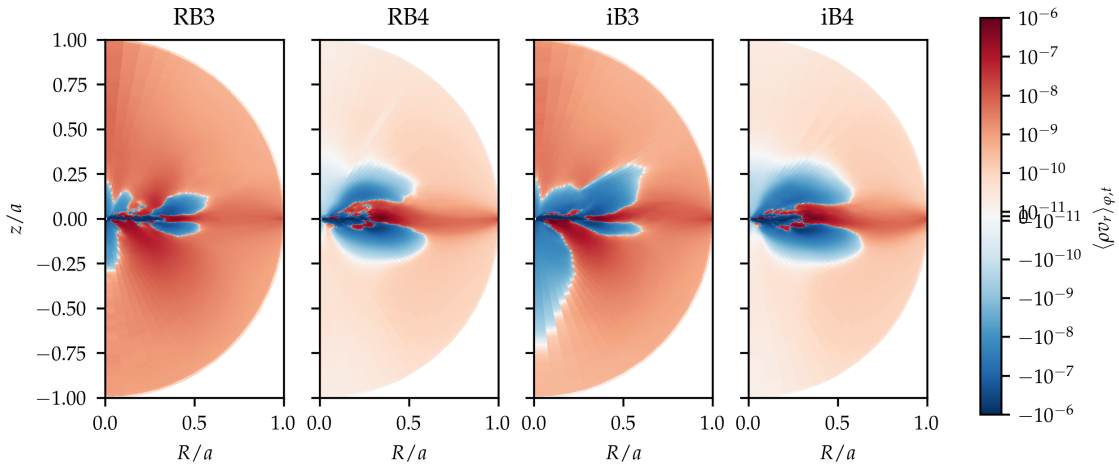

Figure 5.16 – Time-averaged of the radial matter flux $\langle \rho v_r \rangle_{\varphi,t}$.

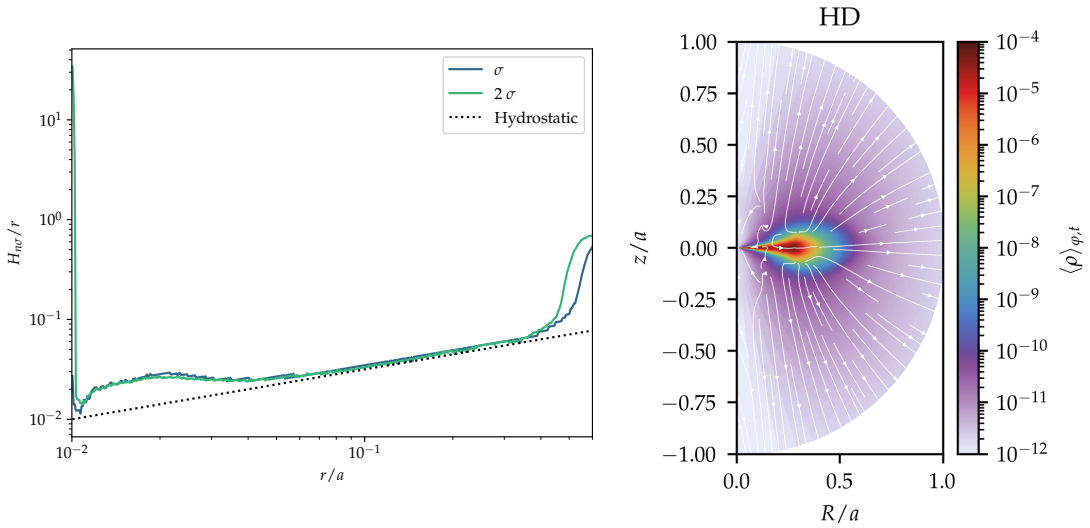

Figure 5.17 – Properties of the non-magnetic simulation. **Left:** Effective disc heightscale measured as in figure 5.13. **Right:** Density profile and poloidal velocity field as in figure 5.10.

caused by accretion is zero, because the magnetic field advection is symmetrical with respect to the midplane.

Here I observe that the magnetic configuration of the disc is not symmetrical with respect to the disc midplane. As a matter of fact, the $B_\varphi = 0$ surface does not coincide with the vertical density maximum. This asymmetry is visible on figure 5.11. On this figure, we can see that the magnetic pressure terms are not symmetrical with respect to $\theta = \frac{\pi}{2}$. A consequence of this dissymmetry is that the wind launched from either surface of the disc are not symmetrical either. This is noticeable on figure 5.10. This asymmetry is further discussed in the next section.

5.2.5 *Comparison with the non-magnetic case*

In this subsection, I compare the above simulations to the same simulation without magnetic field. This simulation is also restarted from the two-dimension hydrodynamics simulation. The third dimension and tidal potential are introduced in the same way, but no magnetic field is added.

We can see that this simulation is much closer to the hydrostatic equilibrium state as shown on figure 5.17. The disc scale-height is very close to c_s/Ω_K, except in the innermost regions, because there some matter falls back onto the disc; it is not a hydrostatic state. On the right panel of this figure, we also see that the disc density structure is less elevated than the magnetic case. This is because there is no contribution of the magnetic pressure to vertical structure. As a consequence, we only have a thermal wind, due to the chosen equation of state for the gas. The disc mass loss due to this wind is more than an order of magnitude less than in the magnetic case.

5.3 DISC TILT

After a few binary orbits, all the magnetic simulations presented above develop a tilted disc. Here I first describe the observed tilt, and then present tentative mechanisms producing the tilt.

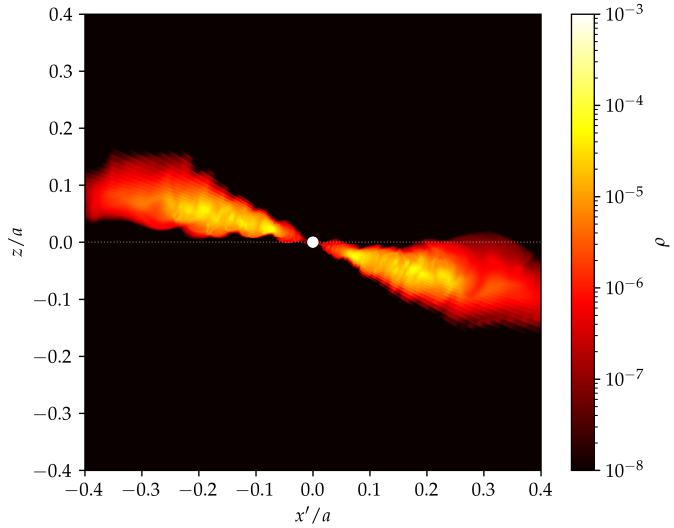

Figure 5.18 – Density slice of a snapshot of simulation RB3 at $\varphi \equiv \pi/4[\pi]$. The grey dotted line represents the orbital plane of the binary system.

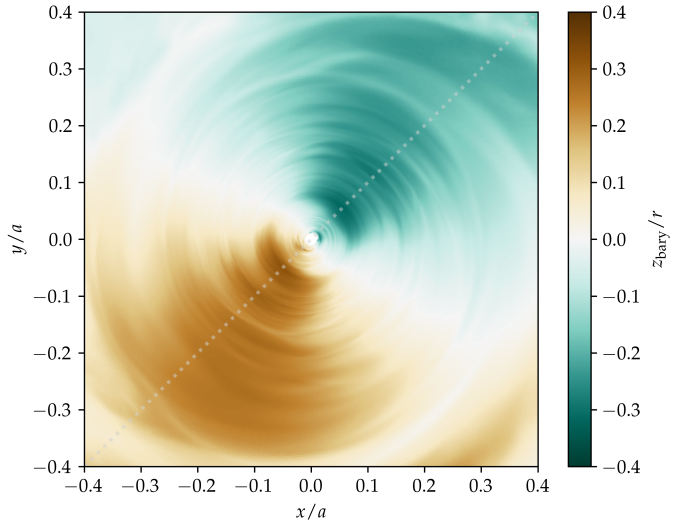

Figure 5.19 – Altitude of the barycentre of a snapshot of simulation RB3. The grey dotted line represents the slice of figure 5.18.

5.3.1 *Description of the tilt*

This tilt is illustrated by figure 5.18. On this vertical density slice, it is very clear that the disc is tilted with respect to the orbital plane of the binary system. To describe this tilt, I introduce the following quantity.

$$\theta_{\text{bary}}(r,\varphi) = \frac{\int_0^\pi \rho(r,\theta,\varphi)\theta d\theta}{\int_0^\pi \rho(r,\theta,\varphi)d\theta} \tag{5.15}$$

and the corresponding altitude is $z_{\text{bary}}(r,\varphi) = r\arctan(\frac{\pi}{2} - \theta_{\text{bary}})$. This quantity is plotted for a snapshot of simulation RB3 on figure 5.19. This figure shows us that the disc is tilted rather than warped. The disc is still planar but no longer lies in the plane of the binary system. This behaviour is observed in all simulations.

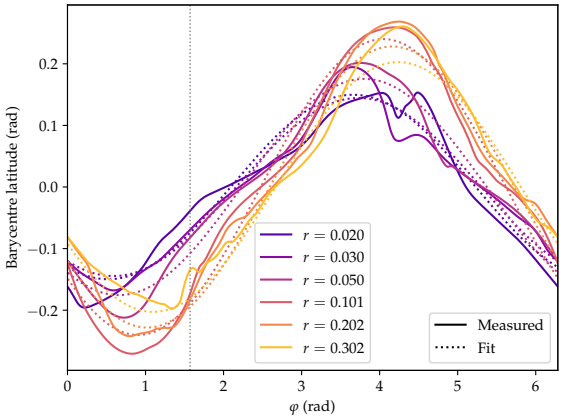

Figure 5.20 – Measure and fit of the latitude of the barycentre, from the same snapshot as figure 5.18 and 5.19. The grey dotted line corresponds to the position of the slice of figure 5.18.

In this case, where the disc remains planar, the altitude of the barycentre is easily parametrised. The following expression parametrises the latitude of a planar ring at radius r.

$$\lambda_{\text{bary}}^{\text{plane}}(r,\varphi) = \text{sign}(\sin(\varphi-\varpi)) \left[\frac{\pi}{2} - \arctan\left(\frac{\sqrt{\tan^2(\varphi-\varpi-\frac{\pi}{2})+\cos^2 A}}{\sin A}\right)\right] \tag{5.16}$$

where $\lambda_{\text{bary}}^{\text{plane}} = \frac{\pi}{2} - \theta_{\text{bary}}^{\text{plane}}$ is the latitude of the barycentre, A is the angle between the ring and the equatorial plane, and ϖ is the angular position of the ascending node of this ring, that is the azimuth at which it crosses the equatorial plane ($\theta = \frac{\pi}{2}$) and where $\partial\lambda/\partial\varphi > 0$. In general, both A and ϖ may be function of the radius. In the case where the disc is exactly planar, we have no radial dependency on these parameters $A' = \varpi' = 0$. When the tilt is small, $|A| \ll \frac{\pi}{2}$, this expression reduces to

$$\lambda_{\text{bary}}^{\text{plane}}(r,\varphi) = A(r)\sin\left(\varphi-\varpi(r)\right) \tag{5.17}$$

To quantify the disc tilt, I measure how $A(r,t)$ and $\varpi(r,t)$ evolve with radius and time across the simulations. To do so, I measure $\theta_{\text{bary}}(r,\varphi)$ for each snapshot and I fit for each time and radius to the expression of equation (5.17). As we can see on figure 5.20, the assumption that each ring is planar is a good approximation, and the position of the barycentre is well fitted by approximation (5.17).

Figure 5.21 shows the evolution of parameters A and ϖ for the simulation RB3. On this figure, rather than fitting A in $[-\frac{\pi}{2},\frac{\pi}{2}]$, I fit for its amplitude $|A|$. This means that the orientation of the tilt is not defined with 2π periodicity but rather with π periodicity as ϖ and $\varpi+\pi$ are equivalent. On this figure, we see that at early times, that is for $t < 15$, both the measured parameter values appear to be indistinguishable from noise. During this phase, the measured $A \neq 0$ can be attributed to the turbulent behaviour of the disc. For a disc with no tilt, the orientation of the tilt ϖ is ill-defined and any slight non-zero tilt value, due to noise, will produce a random ϖ.

On the contrary, after $t = 15$ a coherent behaviour emerges. The tilt angle A grows rapidly and in a coherent way at all radii. Concomitantly, the tilt orientation becomes coherent and rotates at a constant angular velocity. The coherent behaviour of the tilt direction starts around half a binary orbit earlier, but a that time the tilt angle behaviour

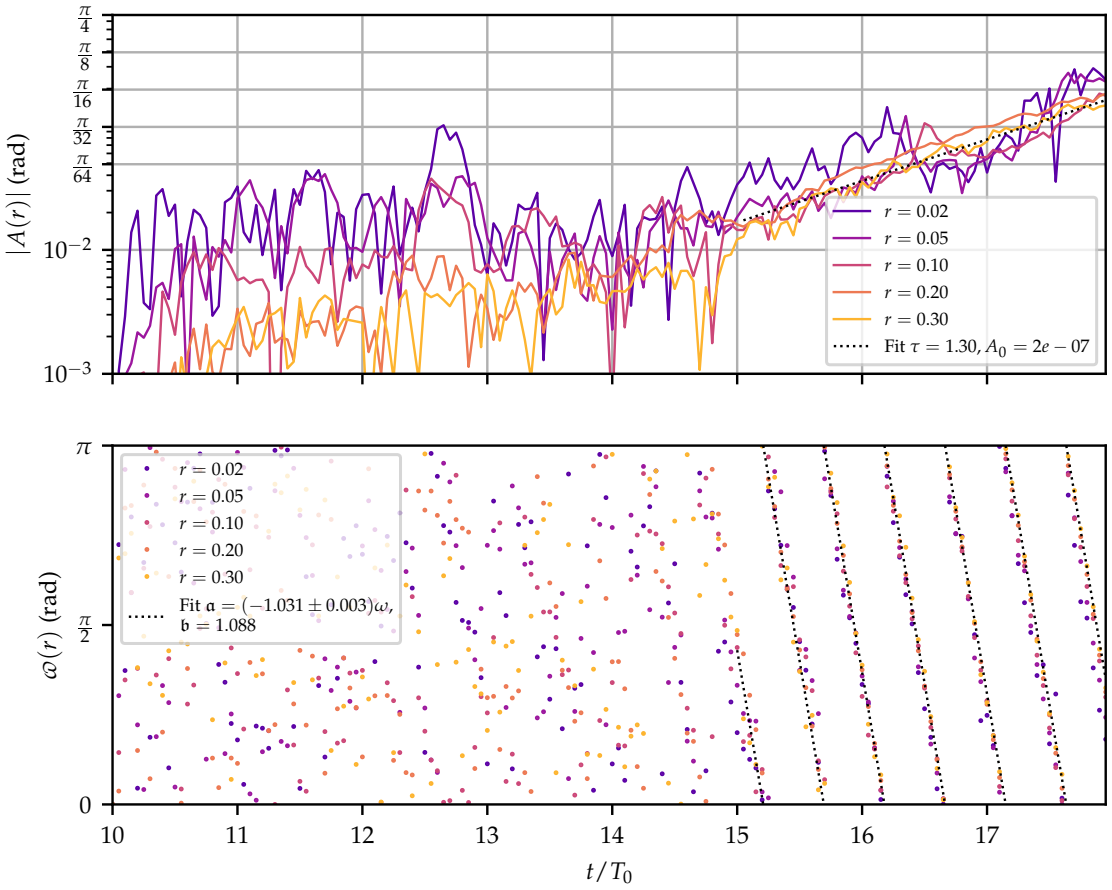

Figure 5.21 – Time evolution of the tilt parameters for the disc of simulation RB3 at different radii. The black dotted lines correspond to the fit of equation (5.18) for $t > 15\ T_0$, fitted on the measure at radius $r = 0.3$.

change is not clear-cut. During this second phase, I fit the evolution of both parameters, as shown by the black dotted lines. The fits are carried at the $r = 0.3$ radius. For the tilt angle, I fit an exponential growth, and for the tilt orientation, I fit a linear evolution of the following form.

$$\begin{cases} A_{\text{fit}}(t) = A_0 e^{-t/\tau} \\ \varpi_{\text{fit}}(t) = \mathfrak{a}t + \mathfrak{b} \end{cases} \tag{5.18}$$

The obtained values of the fitting parameters are shown on figure 5.21. On this figure, it may be argued that the tilt angle growth at $r = 0.3$ started at earlier times. It is possible, but we also have to keep in mind that the local dynamical (keplerian) timescale is longer at this radius than at more inner radii. This means that a possible transient regime, due to the idealised initial condition is expected to relax slower there. This initial growth may simply be taking longer than the initial transient growth taking place at inner radii.

The two relevant parameters to describe the tilt growth are its growth time τ and the tilt rotation speed $\mathfrak{a}$. The growth time is very short compared to the typical binary evolution time scales as it is close to one binary orbit. The fluctuation noise on the measure tilt angle prevents me from having a more precise estimate. This value of τ is similar for all four Ma $= 100$ simulations. On the other hand, $\mathfrak{a}$ can be estimated more precisely as there is little fluctuation on the behaviour of ϖ around the fit. In all simulations, the rotation of the orientation of the warp is compatible with $-\omega$, the

opposite of the binary angular frequency. This means that the tilt orientation is fixed in the non-rotating reference frame. A further refinement can be obtained thanks to the very coherent behaviour of ϖ. In fact, the tilt orientation is slightly less than $-\omega$. The tilt orientation is retrograde with respect to the binary system, at a frequency of a few precents of the binary orbital frequency. Such a frequency corresponds to a tilted disc rotating in a few tens of binary systems orbits. This frequency is reminiscent of the frequency of superhumps of SU UMa systems. One should however keep in mind that the simulations did not run for as long as this period, as such I can not conclude on the exact behaviour of the tilt on such timescales.

ANGULAR MOMENTUM MEASUREMENTS Another method to quantify the tilt of the disc is to examine its angular momentum. Using the fact that the tilt appears to be stationary in non-rotating frame, I use the frame $(\boldsymbol{a}, \boldsymbol{b}, \boldsymbol{c})$ to describe this tilt. This frame is such that it coincides with the rotating frame $(\boldsymbol{x}, \boldsymbol{y}, \boldsymbol{z})$ when $t \equiv 0[T_0]$. In each point of the disc, I use the local angular momentum per unit volume

$$\boldsymbol{\ell} = \rho \boldsymbol{r} \wedge \boldsymbol{v}. \tag{5.19}$$

This quantity can then be integrated on the disc

$$\boldsymbol{L} = \int_{r_{\text{in}}}^{r_{\text{out}}} \int_{\mathcal{S}(r)} \boldsymbol{\ell} \, dS \, dr = \int_{r_{\text{in}}}^{r_{\text{out}}} d\boldsymbol{L} \tag{5.20}$$

where I have decomposed the radial direction from the other directions, $\mathcal{S}(r)$ are the spheres of radius r. $d\boldsymbol{L}(r)/dr$ is the integral over those spheres. As the density inside the disc is much larger than outside the disc, contributions from outside the disc are negligible. As such $d\boldsymbol{L}(r)$ is the angular momentum of the disc annulus at radius r and of width dr.

Here, I assume that the disc is made of concentric planar rings, as previous results suggested. This corresponds to a warp with no azimuthal modes $m > 1$. This also corresponds to the picture of concentric misaligned circular (possibly Keplerian) orbits around the white dwarf. If the disc lies inside the orbital plane of the binary system, $\forall r,\ d\boldsymbol{L}(r) \parallel \boldsymbol{z}$. Otherwise, $d\boldsymbol{L}(r)$ will have non-zero $\boldsymbol{a}$ and $\boldsymbol{b}$ components.

Figure 5.22 shows the evolution of $d\boldsymbol{L}(r)$ for the simulation `RB3`. We see that initially, $d\boldsymbol{L} \parallel \boldsymbol{z}$ as the disc lies in the binary plane. After less than a binary orbit, the local angular momentum has non-zero components that are not aligned with the binary rotation. These values are initially small and oscillatory. As shown on this figure, the observed patterns in local angular momentum are compatible with waves propagating at half the speed of sound. This is the expected velocity of bending waves in an accretion disc (Papaloizou and Lin, 1995). On this figure, we see a first regime, up to $t = 15$, where bending waves propagate inside the disc, with non-zero tilt. Then after $t = 15$ the stationary tilt grows. We see on this figure too, that the direction of the tilt is constant in this phase. In all phases, the non $\boldsymbol{z}$ components of the angular momentum remain smaller than the $\boldsymbol{z}$ component.

NON-MAGNETIC SIMULATION Contrarily to the magnetic simulations, the non-magnetic simulation `HD` does not feature this tilt, as shown on figure 5.23. On this figure, only a very small tilt is visible and only very close to the white dwarf (see the zoomed-in region of the left panel). On the altitude plot (right panel), this tenuous tilt is also somewhat visible. The scale used in both panels is the same as on figure 5.18 and figure 5.19 for comparison purposes. We can see that the tilt of this disc is negligible compared to that of the magnetised discs.

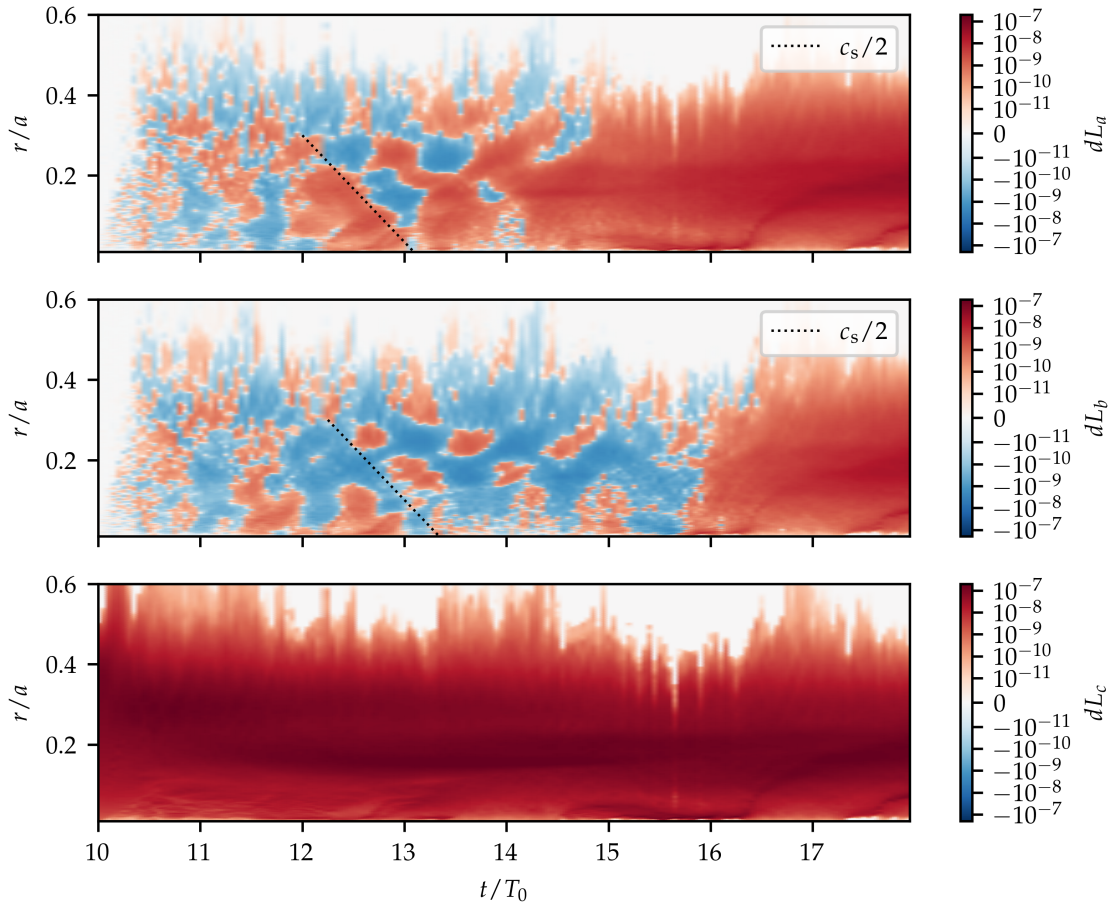

Figure 5.22 – Evolution of local angular momentum components for disc rings, with time. The black dotted lines correspond to wave characteristics propagating at half the speed of sound.

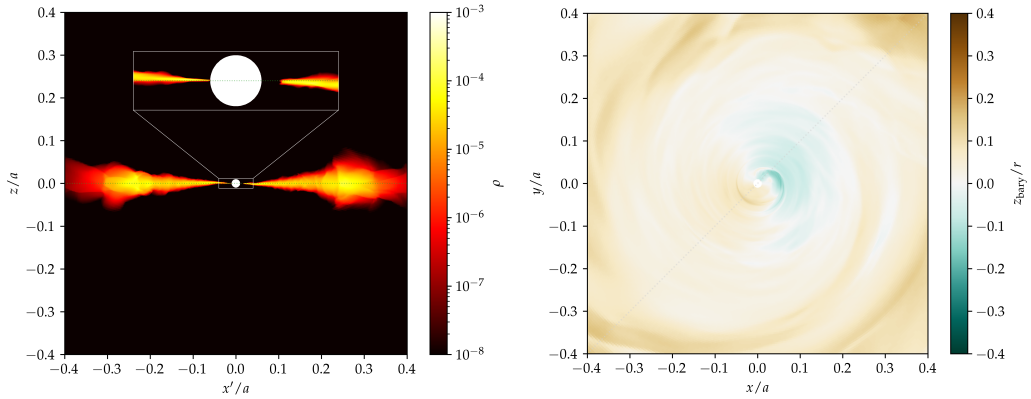

Figure 5.23 – Same as figures 5.18 and 5.19 for the non-magnetic simulation HD. The green dotted line on the left panel shows the equatorial plane. The inner region (zoomed-in inlet) features a slight tilt.

Figure 5.24 better quantifies this absence of tilt. The fitted tilt angle A remains small at all times and all radii, more precisely is $|A(r)| \ll H/r$ in most of the disc. Only in the very inner parts of the disc do we have $|A(r)| > 0.01$ rad, but even then the tilt angle is limited to $\leq \frac{\pi}{64} \approx 0.05$ rad. In these inner regions, the tilt angle A reaches values more than four times as large in the magnetised case. We also see that no coherent pattern develops in ϖ as it was the case on figure 5.21. This shows that in any case, the tilt regime in this simulation is different from the very coherent magnetised disc tilt presented above.

On figure 5.25, we see the evolution of the local angular momentum of the disc $d\boldsymbol{L}$. The disc is initially planar and axisymmetric at $t = 10$. Here too, after less than a binary orbit, bending waves propagate radially inside the accretion disc. As there are no magnetic effects on the disc, namely no MRI, the wave patterns appear more clearly than in the magnetics simulations. The chequerboard pattern that can be observed in this figure is a telltale of a standing wave inside the disc. After $t = 15$, however, no global tilt appears in this simulation. This suggests one of two things. Either the tilt growth is entirely due to the presence of a magnetic field, and this would be why it does not appear in this simulation. Or the growth of a disc tilt is possible in a non-magnetic disc, but the presence of a magnetic field shortens its growth time dramatically. Indeed, from this simulation alone, one can not exclude the possibility that a tilt grows on times scales $\tau \gg 10\ T_0$ in a non-magnetic disc.

HIGHER TEMPERATURE SIMULATION To further examine the tilt, I produce a higher temperature simulation R50. This simulation with Ma $= 50$ is aimed at understanding the effect of temperature on the tilt. For this simulation, I use the same radial and azimuthal grids as the Ma $= 100$ simulations. This means that for those directions, the number of points per disc height scale is doubled. For the latitudinal grid, I use the same number of points (64) to cover the $\pm 4H$ region, and the same number of points to reach the poles (2×64). In this direction, the number of grid points per disc height scale is kept the same. The magnetic field geometry is the same, and the atmosphere temperature is also kept to be the same. The resistivity scaling is tuned so that the magnetic Reynolds number is the same. The initial β parameter is set to 10^3.

The tilt parameters of this simulation are plotted on figure 5.26. Similarly to the Ma $=$ 100 simulation, we can observe that the disc is initially not tilted. During this phase, I also observe bending waves propagating through the disc. After $t = 15$, in this simulation too the disc becomes rapidly highly tilted. Here, it appears that the tilt first grows at inner radii. The growth time of this tilt can be measured and its value is approximately half of the growth time of the tilt in Ma $= 100$ simulations. The pattern speed of the tilt

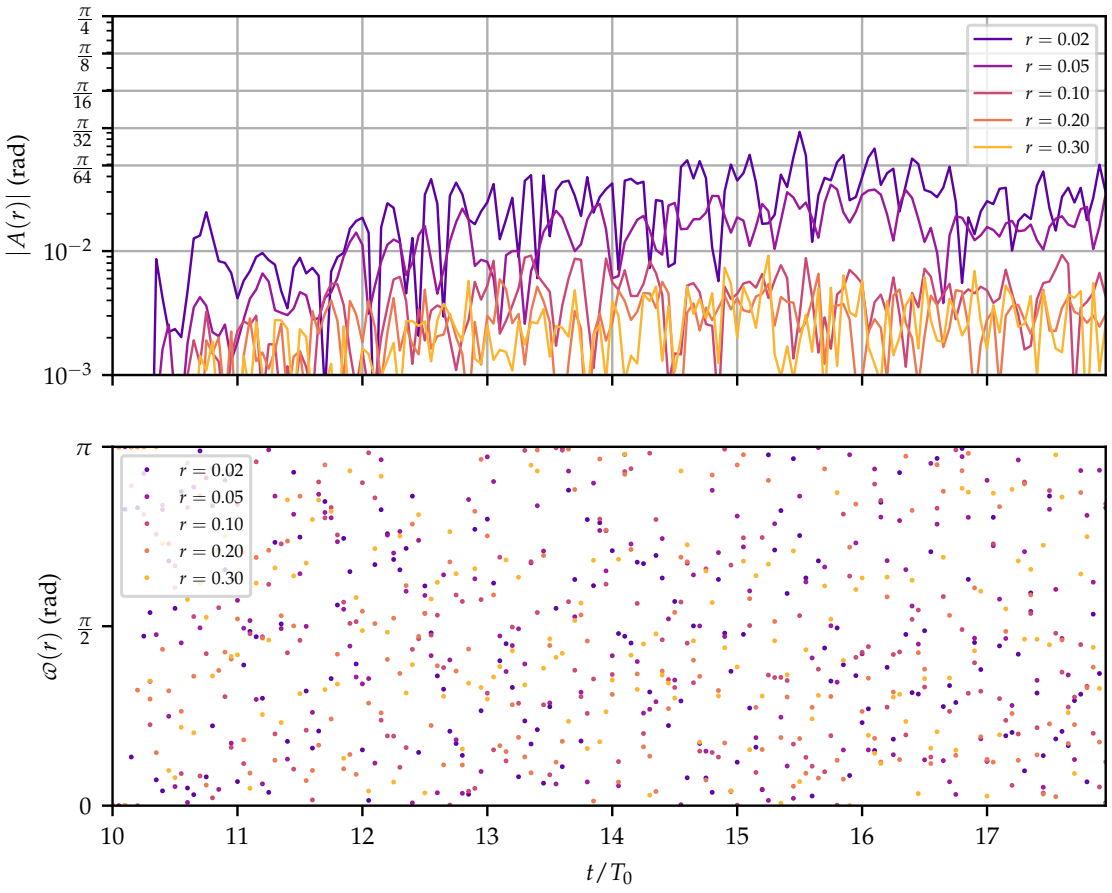

Figure 5.24 – Time evolution of the tilt parameters for the disc of the non-magnetic simulation HD at different radii.

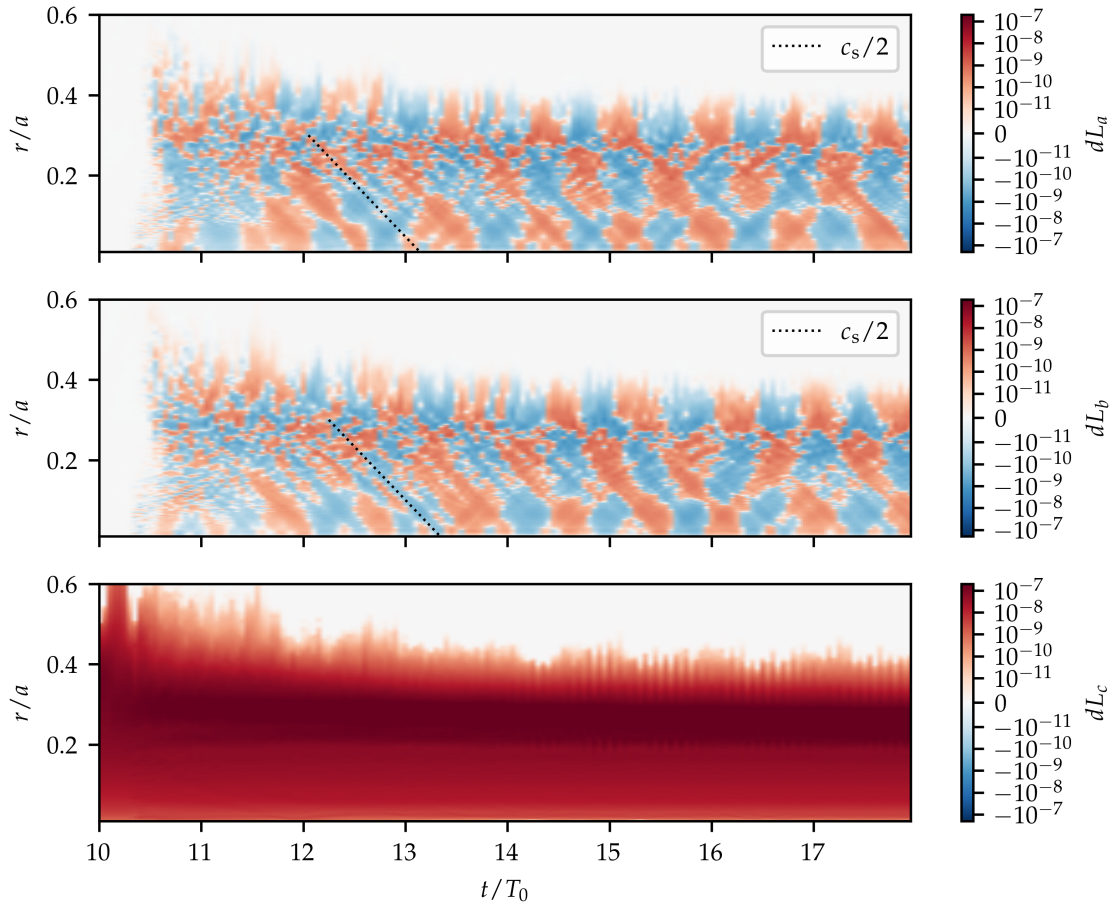

Figure 5.25 – Evolution of local angular momentum components for disc rings, with time for the non-magnetic simulation HD. The black dotted lines correspond to wave characteristics propagating at half the speed of sound.

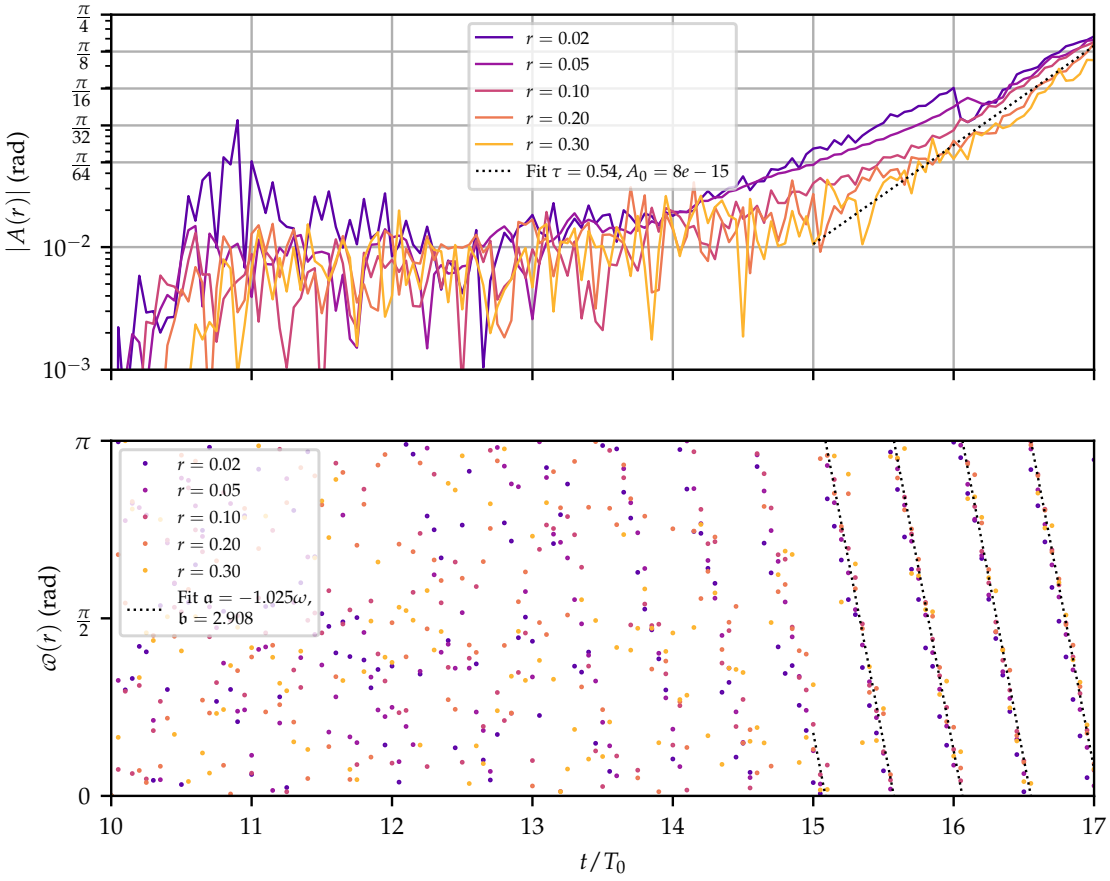

Figure 5.26 – Tilt parameters of the Ma = 50 magnetic simulation.

is similar to the one observed at higher Mach number: retrograde at approximately 3% of the binary frequency.

The growth time of the tilt appears to be related to the sound speed of the disc plasma. In both cases, the extent of the disc is approximately $r_{\text{out}}/a = 0.3$. From this length and the bending wave propagation speed $c_s/2$, one computes the radial crossing time for these waves:

$$\tau = \frac{r_{\text{out}}}{c_s/2} \approx \begin{cases} 1.1 & \text{if Ma} = 100, \\ 0.6 & \text{if Ma} = 50, \end{cases} \tag{5.21}$$

The values of these typical bending wave crossing times are very close to the measured growth time of the tilts in both Ma = 100 and Ma = 50 magnetised simulations respectively.

5.3.2 *Understanding the tilt*

Here, I present attempts at explaining the origin of the tilt observed in the magnetic simulations, and try to understand the mechanism producing it.

5.3.2.1 *Previous works*

Tilted, or more generally warped discs have been studied in different contexts in the past. Warped discs were studied because such a non-planar geometry could explain observations. For instance, such geometries are directly observed in AGN (Miyoshi et

al., 1995), and explain the behaviour of several X-Ray Binaries (Gerend and Boynton, 1976); they are also observed in younger binary systems like KH Tau (Stapelfeldt et al., 1998), AA Tau (Bouvier et al., 2013), protoplanetary disc (Marino et al., 2015), ... From an observational point of view, warped and tilted disc are often invoked.

As a consequence of these observations, some work has been carried out to understand them from a theoretical point of view. The most studied warps and tilts are those around black holes and neutron stars; these are due to relativistic frame dragging (Lense and Thirring, 1918) close to the horizon of a misaligned black hole (Bardeen and Petterson, 1975). Here, I will ignore these works as they are not relevant to the study of dwarf novæ; moreover, in my case, the spin of the white dwarf and of the binary system are aligned.

The origins of these warps differ from system to system. For instance, it is possible that the tidal influence of a companion excites a warp (Lubow, 1992), through a resonant coupling mechanism similar to the eccentricity growth I discussed in the previous chapter. The presence of a wind, may also exert a sufficiently strong torque that warps the accretion disc (Schandl and Meyer, 1994). A strong enough radiation from the accreting object may also cause the disc to develop a warp (Pringle, 1996). Finally, if the accreting object has a strong misaligned magnetic dipole, it may exert sufficient torque to warp the accretion disc around it (Lai, 1999).

The first dynamical models of warps by Papaloizou and Pringle (1983) assumed that the angular momentum transport parameter $\alpha > H/r$ the disc aspect ratio, and found that in this case, the warp is described by a diffusion-like mechanism, and is diffused on shorter times scale than the usual viscous timescale. Papaloizou and Lin (1995) then showed that when $\alpha < H/r$, the warp propagation becomes wavelike rather than diffusive. These waves are the bending waves I mentioned in the previous section, and propagate at $c_s/2$. These theories were then refined to non-linear order by Ogilvie (1999). Papaloizou and Terquem (1995) also showed that a distant companion could tidally excite a tilt in an accretion disc, and not necessarily relax towards coplanarity.

These theoretical models were confirmed by numerous numerical studies (Nelson and Papaloizou, 1999; Lodato and Pringle, 2007; Lodato and Price, 2010). During the same period, Murray et al. (2002) produced simulations where a global disc warp is excited in a close binary system by the misaligned magnetic dipole of the secondary star. They suggest that such geometry may explain negative superhump behaviours, that is superhumps with a period less than the binary orbital period. Foulkes et al. (2006, 2010) studied illumination-induced warps with numerical simulations. They concluded that this mechanism likely explains the warped disc observed in low-mass X-ray binaries.

The previous numerical models made use of the smoothed particle hydrodynamics (SPH) method. This method is well-suited to study systems with complex geometries, but as discussed earlier, it requires the input of an ad-hoc viscosity and poorly captures sharp pressure structures like shock-waves. Ogilvie and Latter (2013b) developed a *warped shearing box* framework, improving the traditional shearing box model for warped discs. This allows to locally study flow properties in a warped disc. In a joint paper, Ogilvie and Latter (2013a) used this framework to study local instabilities in this particular type of flow. They find that even discs with small warps, too small to be observable, can be unstable to a linear hydrodynamical instability. As such, they can generate turbulence and possibly enhance accretion.

More recently, Paris and Ogilvie (2018) included magnetic field in the warped shearing box framework and studied its effects. They find that the magnetic tension detunes the hydrodynamics resonance: with magnetic field the epicyclic frequency no longer matches the orbital frequency. The magnetic field, however, introduces new Alfvenic-epicyclic resonances that can be forced, but depend on the field strength and on the shear rate of

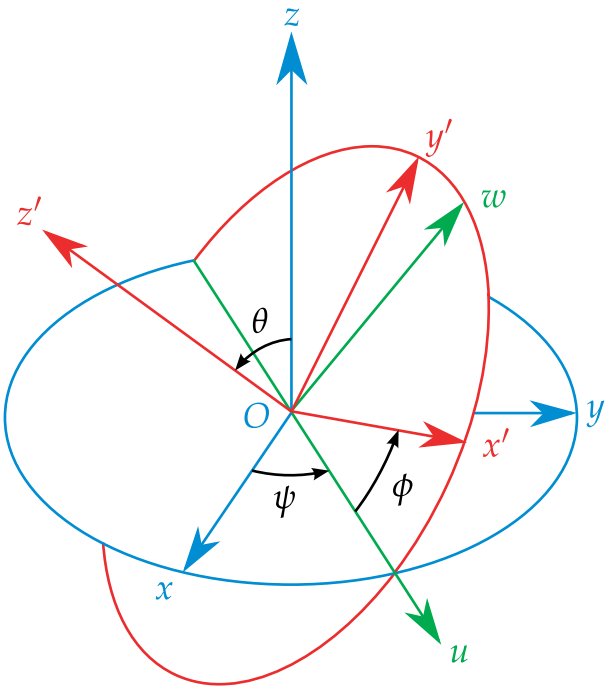

Figure 5.27 – Euler angles nutation θ, precession ψ and intrinsic rotation ϕ. The ring corresponds to the red circle. The $\boldsymbol{u}$ direction corresponds to the nutation axis.

the flow. Their work neglects the MRI and may be more relevant in high magnetisation discs with $\beta \approx 1$.

When it comes to specifically studying cataclysmic variable stars, Sheikhnezami and Fendt (2015) studied the jet launching mechanism from warped disc, but did not focus on the evolution of the disc warp. Pjanka and Stone (2020) also produced three-dimensional CV disc simulations. They noted that the disc slightly deviated from the binary plane, but did not measure any significant warp or tilt of the accretion disc.

The simulations I presented in the previous section do not fit well in the above-mentioned scenarii. The disc is initially aligned with the orbital plane of the binary system, the disc rotation is aligned with the white dwarf spin, the initial magnetic field is top–bottom symmetric, the binary mass ratio is such that the disc is truncated well below the 3:1 resonance radius, and the disc is magnetised but has $\beta \gg 1$ almost everywhere.

As mentioned above, the comparison with the non-magnetic simulation suggests that the tilt growth may be at least partly explained by the magnetic field. Magnetic simulations focusing on the global study of warp are not numerous to this day.

5.3.2.2 *Tidal disturbance*

The first scenario I explore is a possible instability mechanism solely due to the tidal potential. Here, I will describe the disc as nested circular rings centred on the white dwarf. I describe the position of this ring with the Euler angles θ, ψ, ϕ of figure 5.27 [1].

The rings at different radii are considered independent. I first assume that they have axisymmetric linear mass $\mu(r)$. I will relax this assumption further in this section.

Rather than solving the full dynamical evolution of the rings, I study their potential energy in terms of the tilt parameters. The potential, including both the tidal component and the centrifugal force reads as follows.

1. Adapted from https://commons.wikimedia.org/wiki/File:Eulerangles-alternative2.svg

$$\Psi = -\frac{GM_{\rm NB}}{|\boldsymbol{r}|} - \frac{GM_{\rm s}}{|\boldsymbol{r}-\boldsymbol{a}|} + \frac{GM_{\rm s}}{a^3}\boldsymbol{r}\cdot\boldsymbol{a} - \frac{1}{2}\omega^2\Delta^2 \tag{5.22}$$

where ω is the angular frequency of the binary systems and Δ is the distance to the z axis.

It can be expressed in a modified cylindrical frame, coinciding with the vectors $(\boldsymbol{u}, \boldsymbol{w}, \boldsymbol{z}')$ of figure 5.27. I write the corresponding cylindrical coordinates (R', ϕ', z'). As the Euler angle ϕ corresponds to ϕ' of these cylindrical coordinates, I drop the prime on this coordinate. Moreover, this coordinate is only relevant to parametrise the ring and will only appear to be integrated over.

The ring lies in the $z' = 0$ plane; in this plane, the potential is

$$\begin{aligned}\Psi'(R', \phi, z' = 0) = &-\frac{GM_{\rm WD}}{R'} - \frac{GM_{\rm s}}{\sqrt{R'^2 + a^2 - 2R'a(\cos\phi\sin\psi + \sin\phi\cos\theta\cos\psi)}} \\ &+ \frac{GM_{\rm s}}{a^2}R'(\cos\phi\sin\psi + \sin\phi\cos\theta\cos\psi) + -\frac{1}{2}\omega^2R'^2\left(\cos^2\phi + \sin^2\phi\cos^2\theta\right)\end{aligned} \tag{5.23}$$

The potential energy of the ring of radius R is thus the following integral.

$$E_{\rm p} = \int_0^{2\pi} \mu R\Psi' d\phi. \tag{5.24}$$

The first term of the potential yields a constant when integrated, as it is spherically symmetric. The third term yields zeros, by symmetry. Only the potential of the companion star and the centrifugal energy contribute non-trivially to this potential energy. The latter can be easily evaluated analytically, and yields

$$E_{\rm cfg} = \frac{\pi}{2}\mu R^3\omega^2\sin^2\theta + \text{cst} \tag{5.25}$$

The total potential energy landscape is numerically integrated and computed on figure 5.28. On this figure, we retrieve the top-bottom symmetry of the potential, which translates in $\theta \sim \pi - \theta$, and $\psi \sim \psi + \pi$. We also note that for $\theta \equiv 0[\pi]$ the system is degenerated, as in this case, ψ is ill-defined. This is exactly the same degeneracy as we saw for ϖ when $A = 0$ in the previous section.

On this figure, we see that there are two equilibrium configurations for the ring $\partial_\phi E_{\rm p} = \partial_\theta E_{\rm p} = 0$. The first one is unstable, as it corresponds to a maximum of $E_{\rm p}$ and is at $\theta = \frac{\pi}{2}$ and $\psi \cong 0[\pi]$. This configuration corresponds to a disc normal to the position of the secondary star $\boldsymbol{a}$. The other equilibrium configuration, stable this time, corresponds to a disc lying in the binary system plane with $\theta = 0[\pi]$. The stability of this configuration corresponds to the expected position of a disc in these systems.

However, if I now relax the assumption that the ring has uniform mass, this picture changes. This is motivated by the presence of spiral density wave in this kind of disc, as I extensively studied in chapter 4.

Like for spiral waves, it is natural to write the linear mass μ as a Fourier expansion.

$$\mu(\phi) = \sum_{m=0}^{\infty} \mu_m e^{im\phi} \tag{5.26}$$

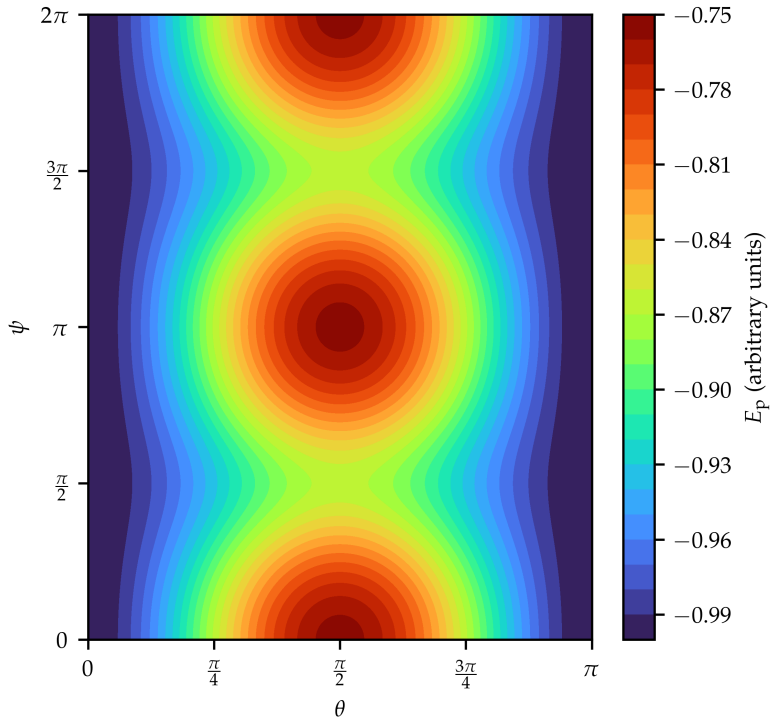

Figure 5.28 – Potential energy landscape for an uniform ring at radius $R'/a = 0.3$ and binary systems mass ratio $q = 0.4$.

with $\mu_m \in \mathbb{C}$. In fact, as μ is a real-valued function, we can write this expansion as

$$\mu(\phi) = \sum_{m=0}^{\infty} |\mu_m| \cos(m\phi - \phi_m) \tag{5.27}$$

where ϕ_m is some real phase.

With this new linear mass, we have changes in the total potential energy. The first term of the potential does not contribute, as for $m > 0$ the integral cancels out. The third term of the potential is non-vanishing only for $m = 1$ by symmetry and yields

$$E_3^m = \begin{cases} \frac{R^2}{a^2} G M_s \pi |\mu_m| \cos\phi_m & \text{if } m = 1, \\ 0 \quad \text{otherwise.} \end{cases} \tag{5.28}$$

The centrifugal energy term only contributes to the $m = 0$ and $m = 2$ modes and yields:

$$E_{\text{ctf}}^{(m)} = \begin{cases} \frac{\pi}{2} |\mu_m| R^3 \omega^2 \sin^2\theta + \text{cst}, & \text{if } m = 0 \\ -\frac{\pi}{4} |\mu_m| R^3 \omega^2 \sin^2\theta \cos\phi_m + \text{cst}, & \text{if } m = 2 \\ \text{cst}, \quad \text{otherwise.} \end{cases} \tag{5.29}$$

From the results discussed in chapter 4, I also know that the $m = 2$ spirals are in co-rotation with the companion star. As a first approximation, let us assume that this is true for all m.

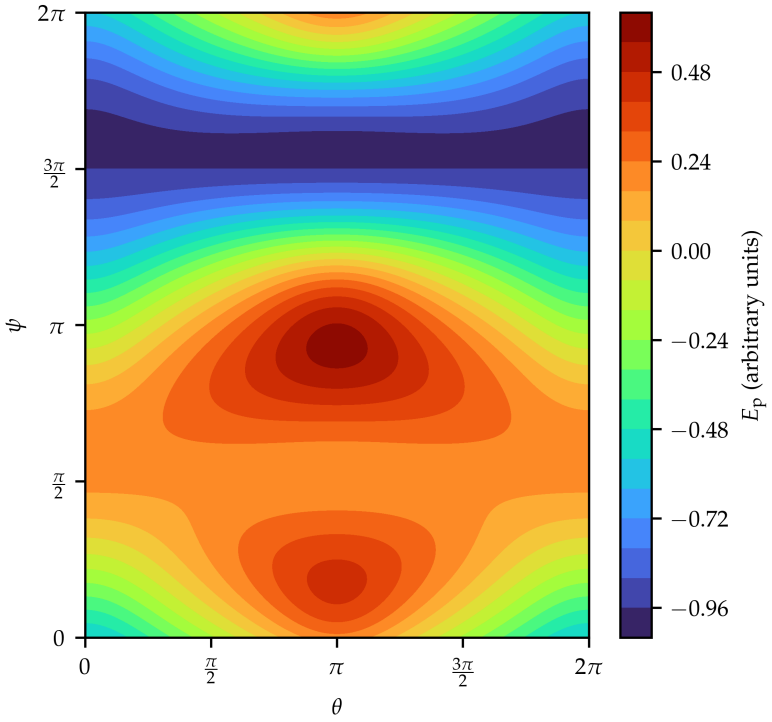

Figure 5.29 – Potential energy landscape for a non-axisymmetric ring at radius $R'/a = 0.3$ and binary systems mass ratio $q = 0.4$, for $m = 1$ and $\delta = 0.3$ rad.

This means that the phase of the m^{th} mode is

$$\phi_m = m\left(\frac{\pi}{2} + \delta - \psi\right) \tag{5.30}$$

where δ is the angle between the x axis and the first density maximum of the m^{th} mode.

Figures 5.29 and 5.30 show the potential energy landscapes for a $m = 1$ and $m = 2$ ring respectively, with $\delta = 0.3$ rad. In both cases, we see consequent changes in comparison with the uniform disc. First, we see that the $\psi \sim \psi + \pi$ symmetry is broken by the $m = 1$ mode, this is expected. We also see that the $\theta \sim \pi - \theta$ symmetry is broken in both cases. This is because when θ crosses $\frac{\pi}{2}$, the density maxima are also change in azimuth. In this case, the periodicity is 2π for θ rather than π.

On these figures, we see that $\theta \equiv 0[\pi]$ no longer is a stable equilibrium position. In the $m = 2$ case, one stable equilibrium position is reached for $\theta = \frac{\pi}{2}$, that is a maximally tilted ring. Furthermore, this configuration corresponds to the global potential energy minimum. This means that a disc with a corotating density non-axisymmetric density structure is not at gravitational equilibrium when lying in the binary system plane.

It is however unlikely that the disc will actually stabilise at $\theta = \frac{\pi}{2}$. Indeed, this simple model assumes that the spiral pattern is fixed in the disc, but as the tilt angle becomes large, this assumption is likely to be wrong. Moreover, the exact stable equilibrium configuration depends on the spiral location δ which is not constant with radius for spiral density waves. This means that interactions between the different rings of the disc will also change this picture.

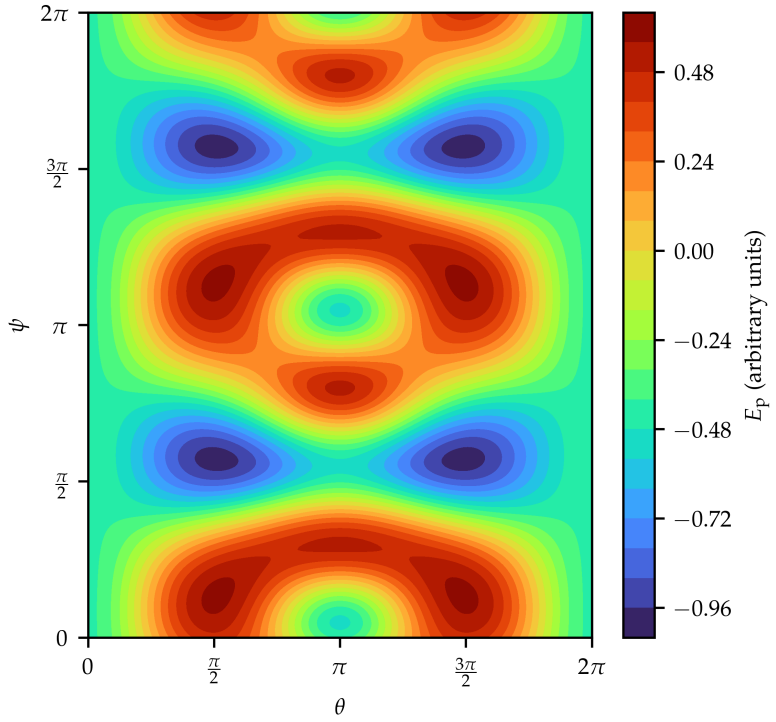

Figure 5.30 – Potential energy landscape for a non-axisymmetric ring at radius $R'/a = 0.3$ and binary systems mass ratio $q = 0.4$, for $m = 2$ and $\delta = 0.3$ rad.

It is however quite interesting that, because of the non-axisymmetric potential, first density waves are excited, and these density waves, in turn, destabilise the disc with respect to tilt.

Nevertheless, it is important to note several shortcomings of this analysis. First, the Coriolis force is not included in this energetic approach as this force does not derive from a potential, unlike the centrifugal force. Second, for the disc to find a configuration with minimal potential energy and stabilise at the bottom of the potential well, some of its energy must be lost through some dissipation process. Otherwise, the ring will merely oscillate around a potential energy minimum, and never settle. Finally, for the disc to change inclination, its angular momentum is required to change. This is actually not a problem as a tidal potential produces a non-zero torque and is not expected to conserve angular momentum, unlike a central potential. It remains to be shown, however, that this torque is compatible with leading the ring to a configuration of minimum potential energy.

5.3.2.3 *Torques on the disc*

For a disc tilt to develop, there necessarily is a torque exerted on the disc that induces its rotation. In this section, I present the diagnostic on the torques exerted on the disc. For the plane to be pushed out of the binary plane, there needs to be a non-axisymmetric force exerted on the disc at the origin of this torque.

I can compute the different forces on the disc from the MHD equations local body forces $\boldsymbol{f}$ as follows. I am only interested in their component in the θ direction, as it is what will push the disc away from the binary plane, and then induce an out-of-plane rotation of the disc.

$$\Delta F = \int_{\theta_{\min}}^{\theta_{\max}} f r d\theta \tag{5.31}$$

For the thermodynamics and magnetic pressure forces, these integrals are straightforward to evaluate:

$$\Delta F_P = P(\theta_{\min}) - P(\theta_{\max}) \tag{5.32}$$

$$\Delta F_{P_m} = P_m(\theta_{\min}) - P_m(\theta_{\max}) \tag{5.33}$$

After evaluating these forces for both pressures, the gravitational force and magnetic tension, it appears that the dynamics is mostly driven by the magnetic pressure force, as its amplitude is larger than that of the other forces. This comparison is shown on figure 5.31. There we see that the strongest torque is that of the magnetic pressure. Its general distribution corresponds to the distribution of the total torque, moreover, this torque contribution is the largest in most of the disc. In the following, I focus on the magnetic pressure contribution as it is the dominant contribution to the torque. Here the disc is defined as the regions where the density exceeds $\rho_{\max}/1000$, where $\rho_{\max}$ is the density maximum of the snapshot. This definition of the disc allows me to treat the disc in the same way whether it is tilted or not. This method is also agnostic on the shape of any possible deformation of the disc. $\theta_{\min}$ and $\theta_{\max}$ max are then detected automatically from this definition.

Figure 5.32 shows maps from these quantities. On this figure, we see that even though not rigorously axisymmetric, ΔP_m is not as polarised as a strong $m = 1$ tilt would suggest. This remains true even when the disc is very tilted, at $t = 18\ T_0$. At this time, the magnetic pressure remains mostly axisymmetric.

The origin of this non-zero net magnetic pressure force originates in the broken symmetry in the non-vertical magnetic field. The azimuthal averages of the toroidal magnetic field shown on 5.33. On this figure, we see that the altitude of the $\langle B_\varphi \rangle_\varphi = 0$ surface does not lie in the binary plane $z = 0$. Rather it is elevated above this plane. In the inner disc region, where this effect is strongest, this region is much higher than both the hydrostatic height scale c_s/Ω_K and the effective disc height scale of figure 5.13, such that $H_{\text{eff.}}/r \approx 0.1$. At further radii, this effect is less strong, and the $\langle B_\varphi \rangle_\varphi = 0$ surface is closer to the binary plane, but is still elevated by a noticeable fraction of the disc height scale. This type of magnetic configuration has been observed in the past in shearing box simulations (Lesur et al., 2014; Bai, 2015), as well as in global simulations (Béthune et al., 2017; Suriano et al., 2018). This geometry produces weak accretion and wind on the side of the $\langle B_\varphi \rangle_\varphi = 0$ surface and an enhanced outflow on the other side. This means that the wind torque exerted on the disc is not top–bottom symmetric, consistently with the difference in magnetic pressure. In previous works, this symmetry is broken because the disc is highly resistive. Here I see this effect on both resistive and ideal simulations.

This symmetry is better quantified with a Fourier decomposition of the pressure difference. This is shown on figure 5.34. In order to smooth out the rapid fluctuation, I smooth the magnetic pressure force over one binary orbit; this time is comparable to the timescale of the tilt growth. The spectra of this figure show that at both times, the axisymmetric $m = 0$ mode is larger than the higher order modes, in particular the $m = 1$ mode. This means that the effect of the magnetic pressure is mostly axisymmetric. It remains possible that an axisymmetric force still destabilises the disc with respect to tilt. As I presented above, the geometry of the potential makes it so that it is not clear that the binary plane is a stable equilibrium position for a disc with non-uniform density.

5.3.2.4 *Non-magnetic experiments*

Here I present additional simulations to explore to possibility that the disc tilt is produced by the differential magnetic pressure. To do so, I use a modified non-magnetic

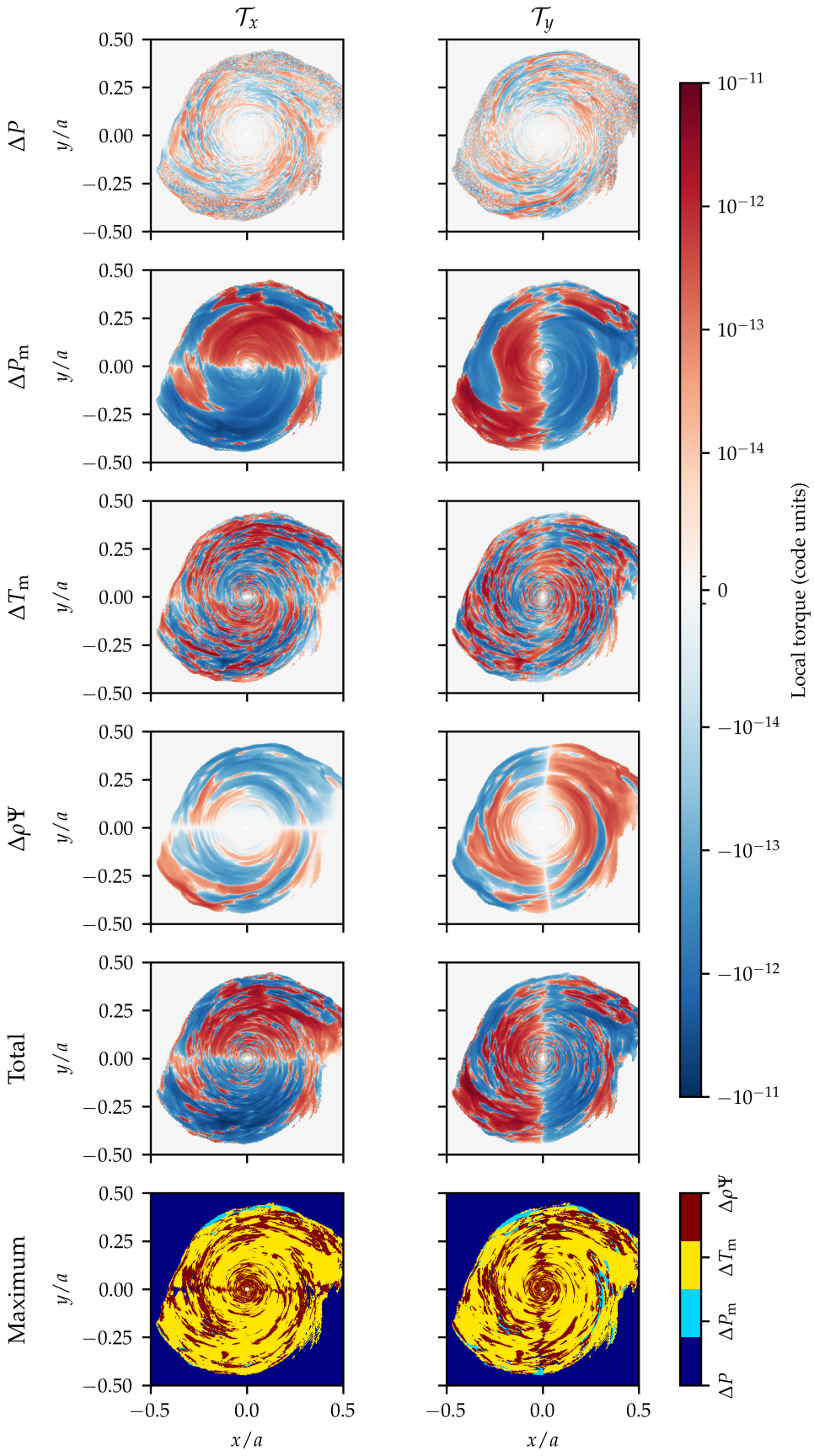

Figure 5.31 – Computed torques of corresponding to the different forces for a snapshot of RB3 at time $t = 14\ T_0$. The different rows correspond to different forces: thermodynamics pressure, magnetic pressure, magnetic tension, gravity, total torque. The last row shows which component is the larger at each point. **Left:** x component of the torque. **Right:** y component of the torque.

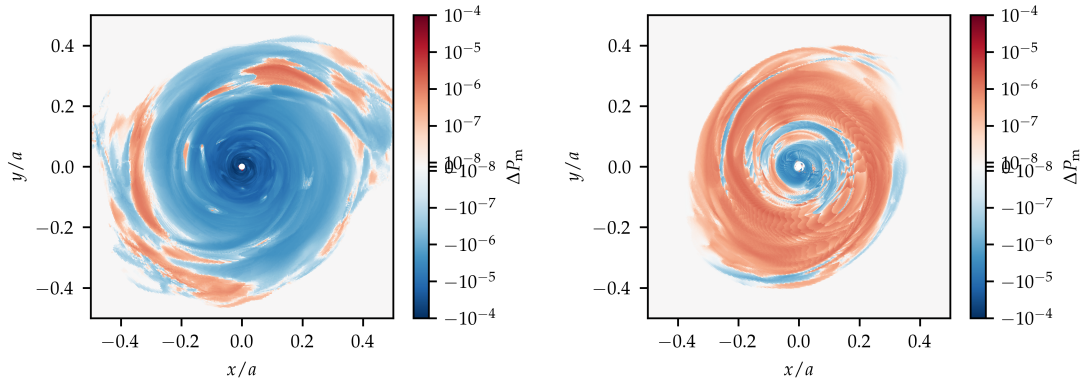

Figure 5.32 – Vertical pressure forces on the disc at for simulation RB3, before the tilt growth. **Left:** At $t = 13.6\ T_0$, when the tilt is still negligible. **Right:** $t = 18\ T_0$, when the tilt is very strong.

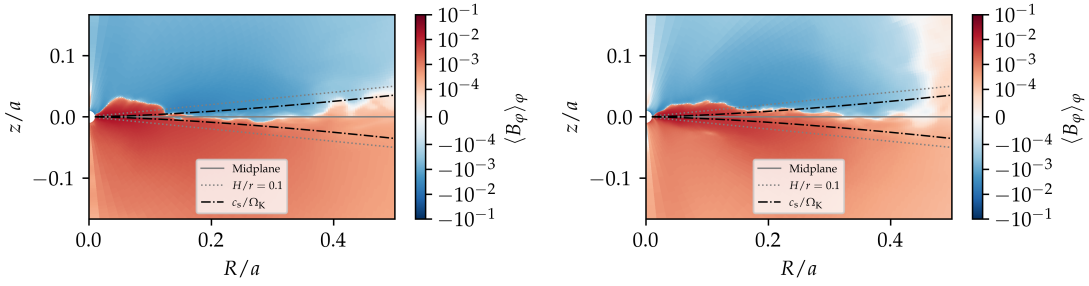

Figure 5.33 – Azimuthal average of the toroidal magnetic field for two snapshots of the RB3 simulation. The different lines show different altitudes relevant to the disc scale, which were discussed above. **Left:** At $t = 13.6\ T_0$, when the tilt is still negligible. **Right:** $t = 15\ T_0$, when the tilt is starting its rapid growth.

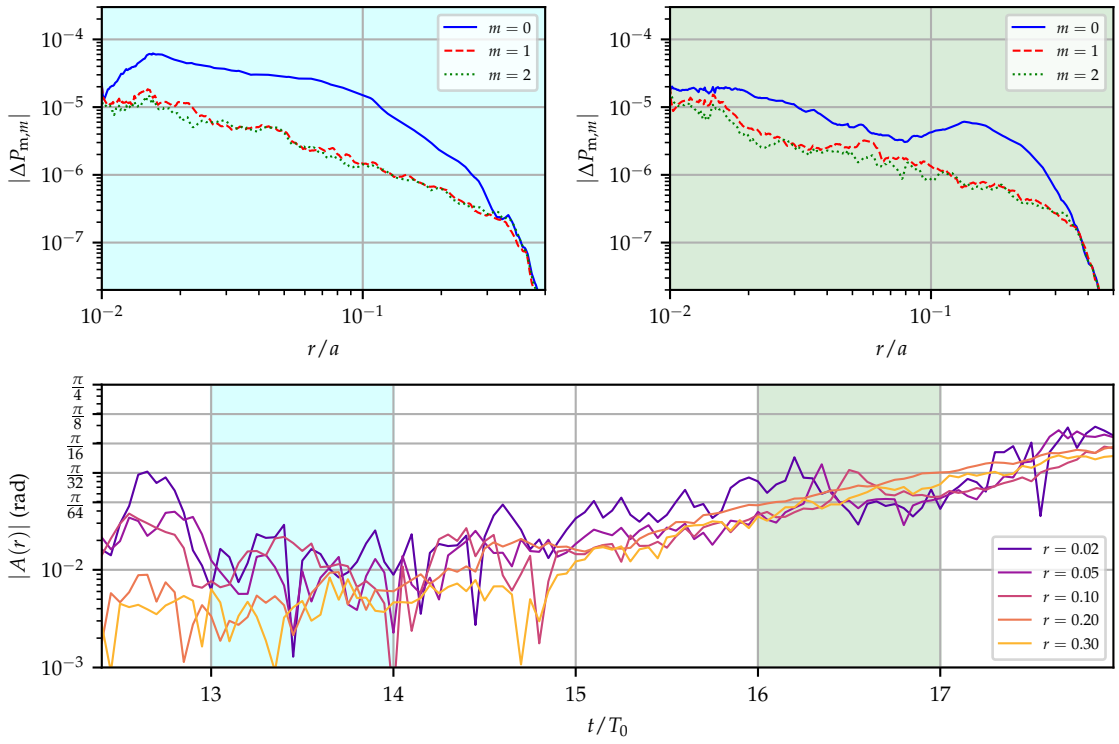

Figure 5.34 – First modes of the Fourier transform of vertical pressure forces on the disc for simulation RB3. **Top left:** Averaged between $t = 13\ T_0$ and $t = 14\ T_0$, when the tilt is still negligible. **Top right:** Averaged between $t = 16\ T_0$ and $t = 17\ T_0$, when the tilt is very strong. **Bottom:** Same a top panel of figure 5.21 with averaging time span highlighted in the same colour as the corresponding spectrum.

setup. As the non-magnetic simulation never develops a strong tilt like the magnetic ones, the aim is to manually add to these simulations magnetic-like effects to find which effect causes the tilt to grow.

MODIFIED EQUATION OF STATE In this setup I change the equation of state to have a locally isothermal disc, rather than a globally isothermal disc. This change is motivated by two reasons. First, this allows us to include the fact that H_{eff}/r is approximately constant in the magnetic simulations. This requires that $T \propto 1/r$. Second, a larger H/r at the inner radius allows me to have larger cells at this radius and thus larger integration timestep, hence shorter integration time for these experiments. The equation of state I use is the following:

$$c_s(\rho, r) = c_{\text{d}} \left(\frac{r}{r_0}\right)^{-\frac{1}{2}} + \frac{1}{2}\left[1 - \tanh\left(\frac{\log \frac{\rho}{\rho_{\text{c}}}}{\Delta}\right)\right]\left(c_{\text{c}} - c_{\text{d}}\left(\frac{r}{r_0}\right)^{-\frac{1}{2}}\right), \tag{5.34}$$

Note that here, r is the *spherical* radius and not the cylindrical radius as is usually the case for locally isothermal equation of states. This is because, if the disc tilts the cylindrical radius is no longer relevant, but the spherical radius still is. This equation of state is shown on figure 5.35.

GRID The grid for these simulations is adapted to the new $H/r = 0.1$. This allows to have a fine resolution up to higher latitudes, compared to the grid of simulations with $\text{Ma} = 100$ presented above. The new grid uses 384 radial logarithmically spaces points for $r \in [0.01, 0.6]$, and 640 uniformly spaced azimuthal points. This radial grid is the

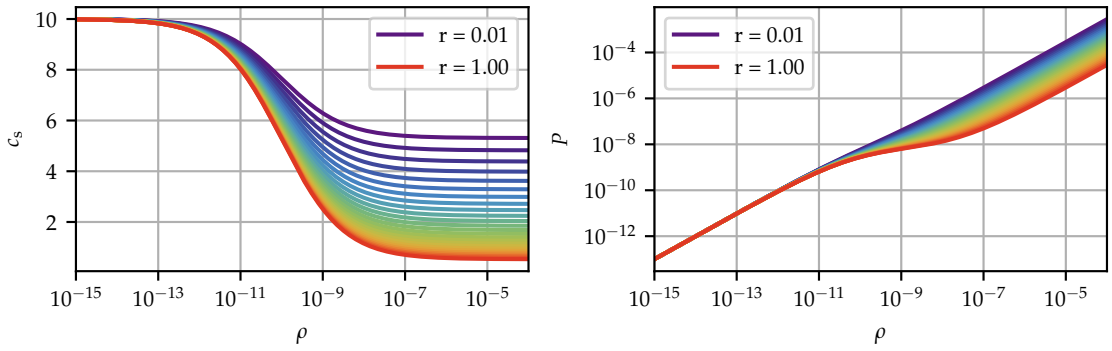

Figure 5.35 – Modified equation of state for the locally isothermal non-magnetic simulations. Different colours correspond to different radii. The minimum and maximum radii are labelled.

Name	Mach number	Resolution $(N_r, N_\theta, N_\varphi)$	Body force	Note
`NBF`	10	$(384, 144, 640)$	No	reference run
`WBFw`	10	$(384, 144, 640)$	Uniform	$\varepsilon = 0.1$
`WBFs`	10	$(384, 144, 640)$	Uniform	$\varepsilon = 1$
`WBFR2`	10	$(384, 144, 640)$	$1/r^2$	$\varepsilon = 1$
`WBF2R2`	10	$(384, 144, 640)$	$1/r^2$	$\varepsilon = 2$
`WBF4R2`	10	$(384, 144, 640)$	$1/r^2$	$\varepsilon = 4$
`WBF32R2`	10	$(384, 144, 640)$	$1/r^2$	$\varepsilon = 32$
`WBF100R2`	10	$(384, 144, 640)$	$1/r^2$	$\varepsilon = 100$
`IT`	10	$(384, 144, 640)$	No	Initial tilt
`50WBF`	50	$(512, 192, 640)$	$1/r^2$	$\varepsilon = 300$

Table 5.2 – List of the non-magnetic 3D simulations presented in this section.

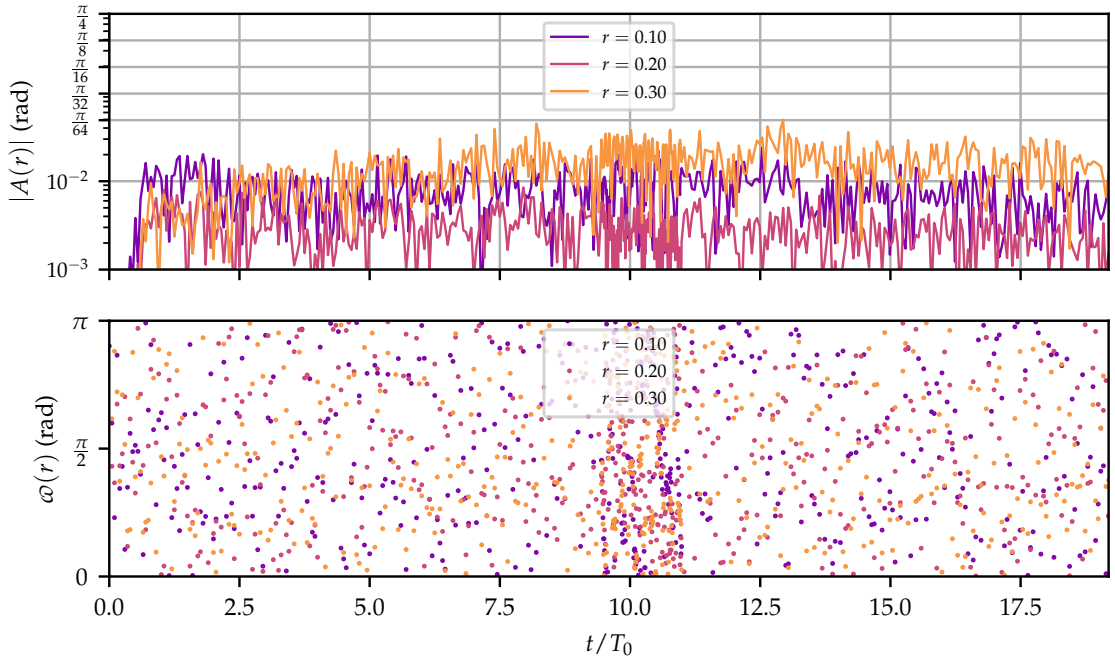

Figure 5.36 – Tilt parameters of the reference simulation NBF. The increased point density at $t = 10$ corresponds to an increased output frequency to study shorter timescale phenomena.

same as the Ma = 100 simulation, truncated at lower outer radius. In the latitudinal direction 80 points cover uniformly the $\pm 4H/r$ angular region, and 32 points on either side extend geometrically to the poles.

The list of simulations presented here is shown in table 5.2. I discuss the added physics below. Apart from the grid, the temperature, and the body force, all other parameters (initial truncation, boundary conditions, density floor) are kept identical to the simulations presented above.

REFERENCE SIMULATION For comparison purposes, I first produce a purely hydrodynamic simulation with no added physics. As expected and like the Ma = 100 non-magnetic simulation, no tilt develops in ten binary orbits, and bending waves propagate inside the disc (see figure 5.39). On the ϖ plot, we also see no coherent behaviour.

Like in the simulations of chapter 4 as well as the Ma = 100 simulations presented above, in these simulations, I observe the growth of an inner cavity at radii $r \leq 0.05\ a$. As a consequence, I ignore any tilt that may be measured in these regions as their density is negligible compared to that of the disc.

ADDING A BODY FORCE To mimic the effect of the net vertical force of the magnetic pressure measured above, I introduce a body force to the simulation. This force is as follows. This force is oriented along the latitudinal direction in hopes of producing a tilt. Note that in the equatorial plane $\boldsymbol{e}_z \parallel \boldsymbol{e}_\theta$.

$$\boldsymbol{f} = -f_0 \boldsymbol{e}_\theta = -\frac{\Delta P_0}{a \Delta\theta_0 \rho_0} \varepsilon \boldsymbol{e}_\theta \tag{5.35}$$

where f_0 is the amplitude of this force, and is computed from typical values of the pressure difference ΔP_0 and density ρ_0 taken from the Ma = 100 simulation. $\Delta\theta_0$ is taken to be 0.1 to rescale the force to the adapted Mach number. ε is a normalisation factor

to tune the amplitude of the force. I use $\rho_0 = 10^{-6}$ and $\Delta P_0 = 10^{-5}$ consistently with previous measures. Technically speaking $\boldsymbol{f}$ is an acceleration and $\rho \boldsymbol{f}$ is a body force. However, I abusively use the 'body force' terminology to match the implementation of IDEFIX for user-defined body forces, where $\boldsymbol{f}$ and not $\rho \boldsymbol{f}$ is defined by the user.

I produce two simulations with this body force, one with $\varepsilon = 1$ (`WBFs`) and one with $\varepsilon = 0.1$ (`WBFw`). The tilt parameters of these simulations are shown on figure 5.37. We see that neither simulation develops a long-lived tilt on such time scales.

I note however that in simulation `WBFw`, an initial transient tilt develops for $t \leq 2\ T_0$. This initial tilt is shown on figure 5.38. This tilt is present only in regions $r \leq 0.2\ a$. In outer regions, most of the disc is above the equatorial plane, and mostly axisymmetric. This tilt is noticeable on the top panel of figure 5.37 at early times $t \leq 2\ T_0$. It is however short-lived and is likely attributable to the relaxation from the idealised initial state.

If like above, the growth time of the tilt corresponds to the crossing time of a bending wave, we would have:

$$\tau = \int_{r_{\text{in}}}^{r_{\text{out}}} \frac{dr}{c_{\text{s}}(r)/2} = \frac{4}{3 c_{\text{d}} \sqrt{r_0}} \left[r_{\text{out}}^{3/2} - r_{\text{in}}^{3/2} \right] \tag{5.36}$$

For our value of c_{d} and assuming, $0.3 = r_{\text{out}} \ll r_{\text{in}} = r_0$, we get $\tau \approx 0.4$. This means that the tilt is expected to grow faster, because the disc is hotter. The initial tilt growth is consistent with this faster growth. The life span of this initial tilt is of only a few τ.

The `WBFs` simulation ends up with a bowl-shaped disc, as the force pushes in a uniform fashion, in regions where the gravity is less strong. There is no noticeable tilt on the disc of this simulation, even at early times.

Note that the slow tilt growth at late times that can be seen at $r = 0.3$ for the `WBFs` simulation is an artefact of my measuring method. The disc no longer lies around the equatorial plane (as it is bowl-shaped). There is no actual increase in tilt at this radius.

BENDING WAVE PROPAGATION On the simulation `WBFw`, I examine the propagation of bending waves inside the disc. I find a chequerboard pattern similar to the one observed in the Ma = 100 simulation and in the magnetic simulations.

This proves that bending waves propagate inside the disc, as expected. However, no link between these waves and the body force can be easily drawn. It is possible that they are simply a remnant of the relaxation of the idealised initial condition of the disc. Figure 5.39 shows the local angular momentum defined above for this simulation and the reference simulation. The wave characteristics at $c_{\text{s}}/2$ match the observed patterns.

$1/r^2$ BODY FORCE To refine the previous simple model, I change the radial dependency of the body force. Now I take a $1/r^2$ radial dependency, such that the ratio of the white dwarf's gravity to this body force is constant with radius. This is to prevent the disc ending up bowl-shaped like it was the case for `WBFs`. This radial profile is consistent with the actual radial dependency of the magnetic pressure difference, as can be seen on the top panels of figure 5.34.

$$\boldsymbol{f}_r = -f_0 \left(\frac{r}{r_0} \right)^{-2} \boldsymbol{e}_\theta = -\frac{\Delta P_0}{a \Delta\theta_0 \rho_0} \varepsilon \left(\frac{r}{r_0} \right)^{-2} \boldsymbol{e}_\theta \tag{5.37}$$

I produce five simulations with this force, with $\varepsilon = 1$, $\varepsilon = 2$, $\varepsilon = 4$, $\varepsilon = 32$, $\varepsilon = 100$. All these simulations have the same behaviour with respect to the tilt: that is not tilt growth.

The runs `WBF32R2` and `WBF100R2` with the strongest forces feature an initial transient tilt over a few binary orbits. After that, all runs reach a tilt $A \leq 10^{-2}$ rad everywhere.

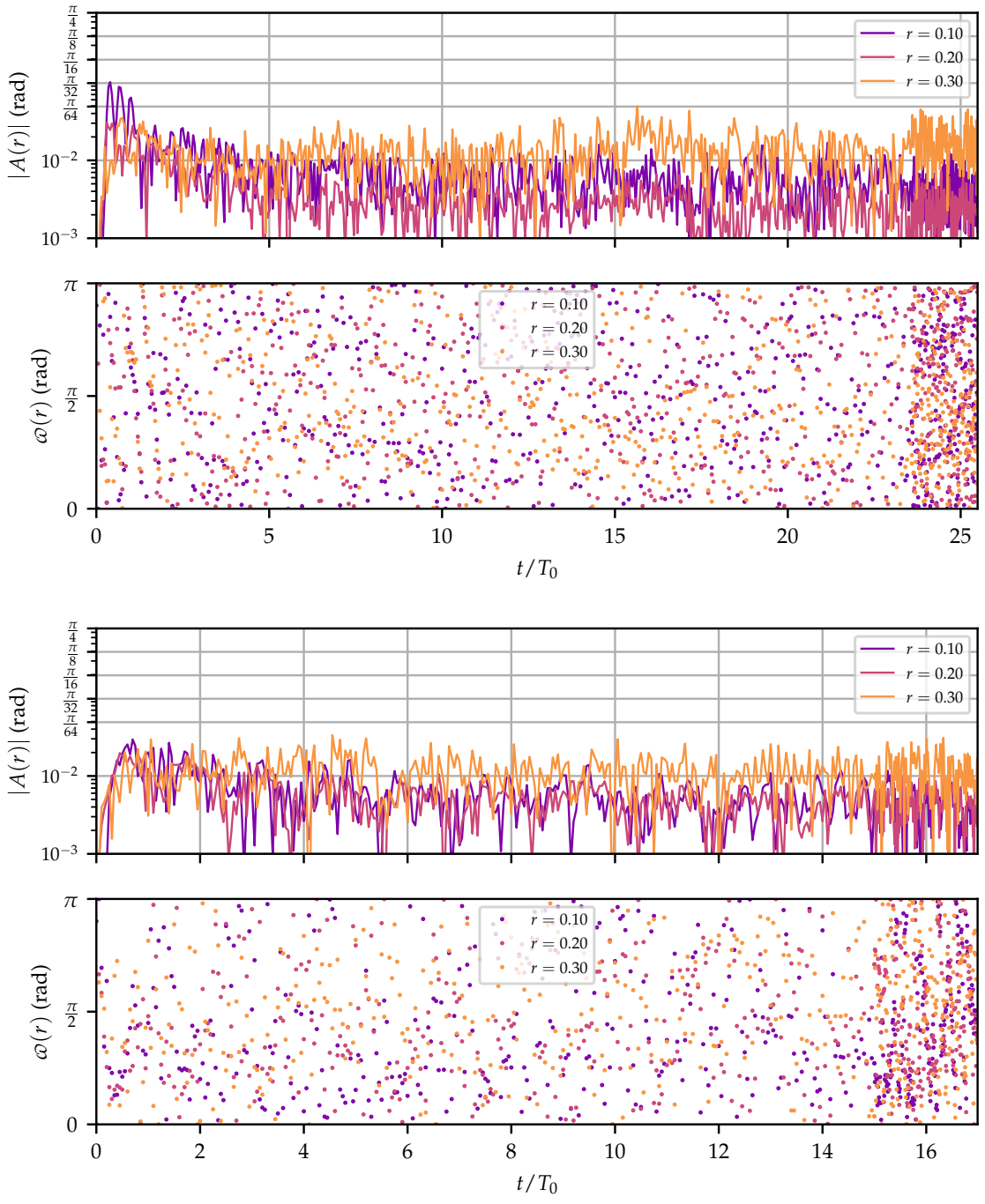

Figure 5.37 – **Top:** Tilt parameters of the simulation `WBFw`. **Bottom:** Tilt parameters of the simulation `WBFs`. The increased point density at the final times corresponds to an increased output frequency to study shorter timescale phenomena.

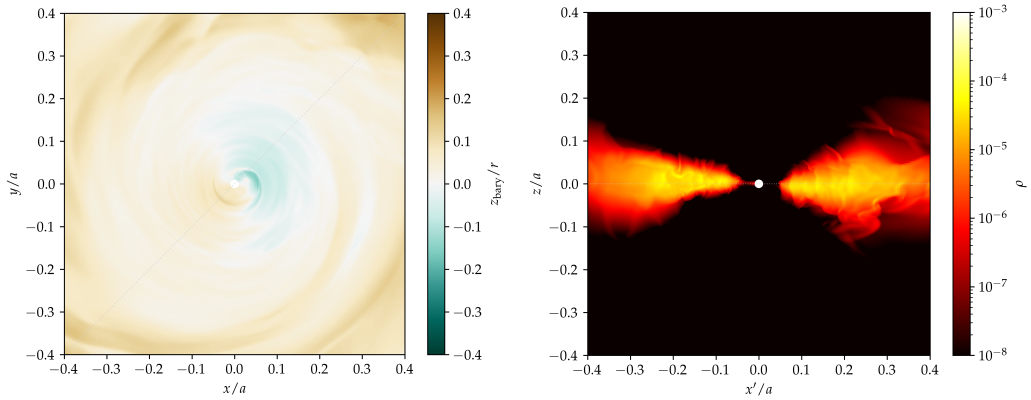

Figure 5.38 – **Left:** altitude plot of the WBFw simulation at $t = 1\ T_0$. The grey dotted line corresponds to the slice of the right panel. **Bottom:** Density slice of the WBFw simulation at $t = 1\ T_0$. The grey dotted line corresponds to the binary plane.

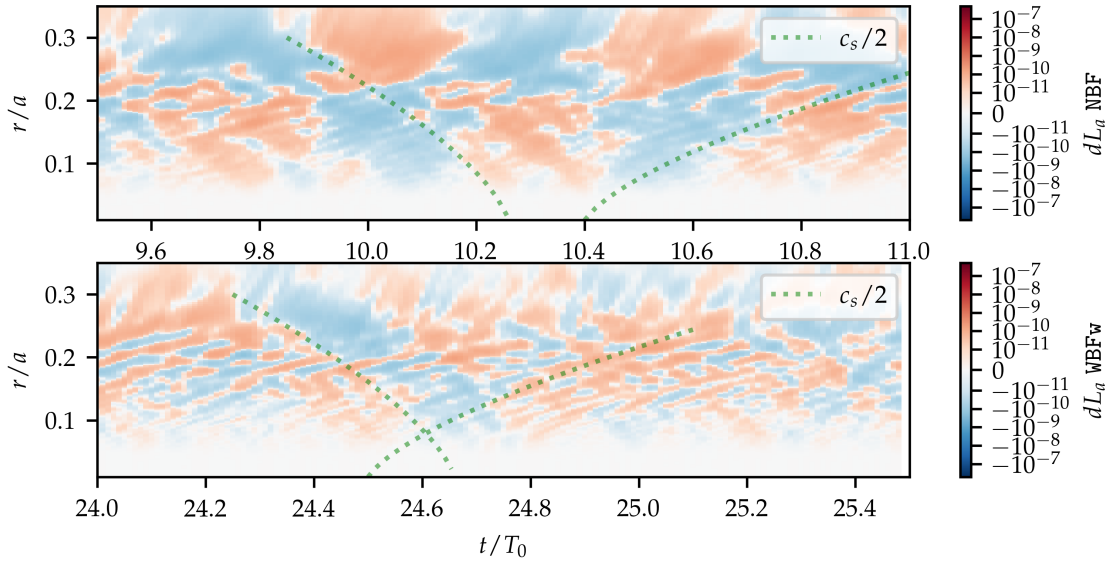

Figure 5.39 – Bending wave propagation in the non-magnetic Ma = 10 simulations. **Top:** NBF simulation. **Bottom:** WBFw simulation. The position of the characteristics is chosen by hand to match the most visible features.

This state appears to be steady for the 30 binary orbits integration time. This evolution is shown on figure 5.40 for the two extreme values of ε chosen.

With the simulations presented above, it appears that a force comparable to the magnetic pressure is not able to reproduce a disc tilt in a similar timescale, even when the force magnitude is the same. A fundamental shortcoming of the constant body force approach is that it lacks the positive feedback that the exponential growth suggests.

INITIALLY TILTED DISC I now present a simulation with no body force, but where the initial condition is a tilted disc. The aim of this simulation is to study the stability of such a state from a hydrodynamics perspective. I integrate this simulation for 30 binary orbits.

The tilt parameters are plotted on figure 5.41. There we see that on a ten-orbit timescale, the initial tilt is stable. There are small fluctuations to this tilt angle, but it remains constant. The pattern speed of the tilt ϖ can thus be very accurately measured. This tilt is retrograde in the non-rotating frame, at $2.5 \pm 0.3\%$ of the binary frequency. This pattern speed is consistent with the pattern speed measured for the magnetised tilted disc.

We can see on figure 5.41 that at later times, beginning around $t = 15$ the tilt angle start to change. Its value starts oscillating around its initial value. The amplitude of this oscillation appears to grow, but its growth time is longer than the integration time of the simulation. For instance, I can not distinguish whether this oscillation is due to some beating phenomenon and would decrease at later time, like would be the case for Kozai-Lidov type oscillations (Kozai, 1962; Lidov, 1962), or if it is a slow monotonic growth.

LOWER TEMPERATURE SIMULATION To make sure that there is not threshold effect in the temperature of the disc, and that the modified equation of state does not interfere with the growth of a tilt, I produce a last simulation. This simulation is the same as the $\mathrm{Ma} = 50$ without magnetic field and where I add the previously described body force. I use $\varepsilon = 300$.

The measured tilt parameters of this simulation are shown on figure 5.42. There we see that no large amplitude tilt develops. In fact, the disc ends up in a slight axisymmetric V shape. Here too, we see the initial tilt growth during the first binary orbit after the restart. Here we see that the growth rate of the tilt is much faster than the global tilt growth scale of figure 5.26.

With this simulation, I conclude that the tilt growth mechanism can not be simply reproduced in non-magnetic simulations, even when including an axisymmetric body force to the disc. It is possible that even though subdominant, the higher-order components of this force induce the tilt. But then, there must be some filtering mechanisms that prevent the apparition of a $m > 1$ warping mode.

5.4 SUMMARY

In this chapter, I presented the global three-dimensional MHD and non-magnetic simulations I produced during my PhD. The results I obtained can be summarised as follows.

1. A global MHD wind can be launched from low-temperature ($\mathrm{Ma} = 100$) resistive ($\mathrm{Rm} \leq 100$) dwarf novæ discs.
2. The effect of resistivity on the disc is small compared to the overall presence of magnetic field, both with respect to the MRI and to the wind launching.
3. The winds launched from these discs appear to break the top–bottom symmetry. This asymmetry exerts an axisymmetric net vertical force on the disc.

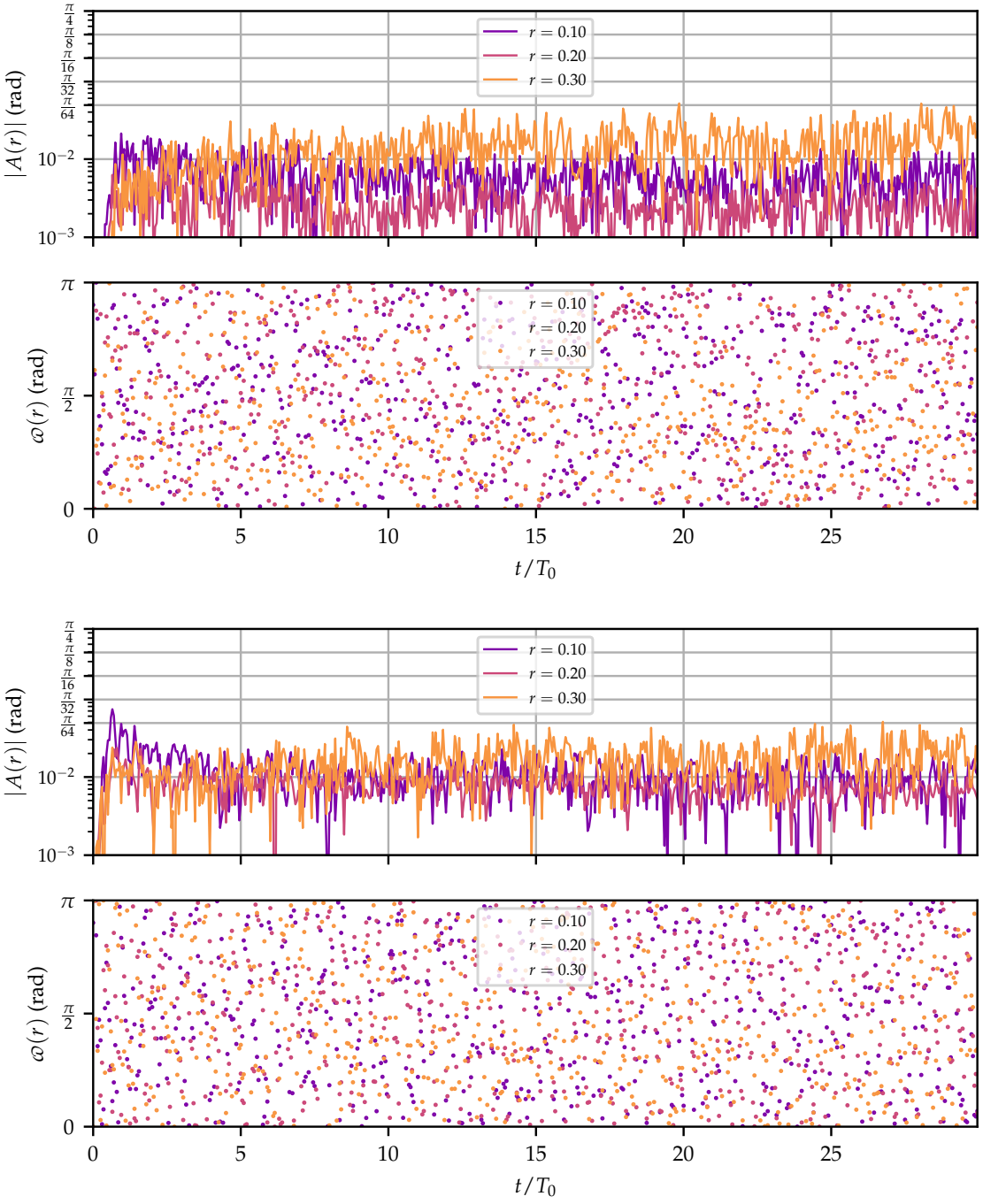

Figure 5.40 – **Top:** Tilt parameters of the reference simulation `WBFR2`. **Bottom:** Tilt parameters of the reference simulation `WBF100R2`.

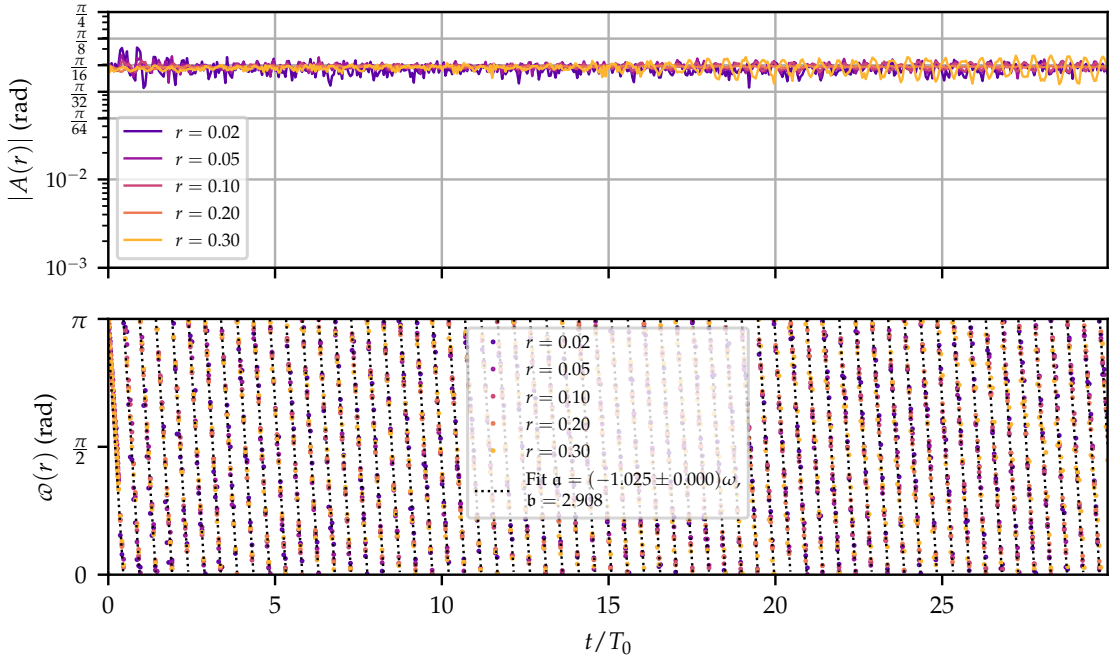

Figure 5.41 – Tilt parameters of the simulation `IT`.

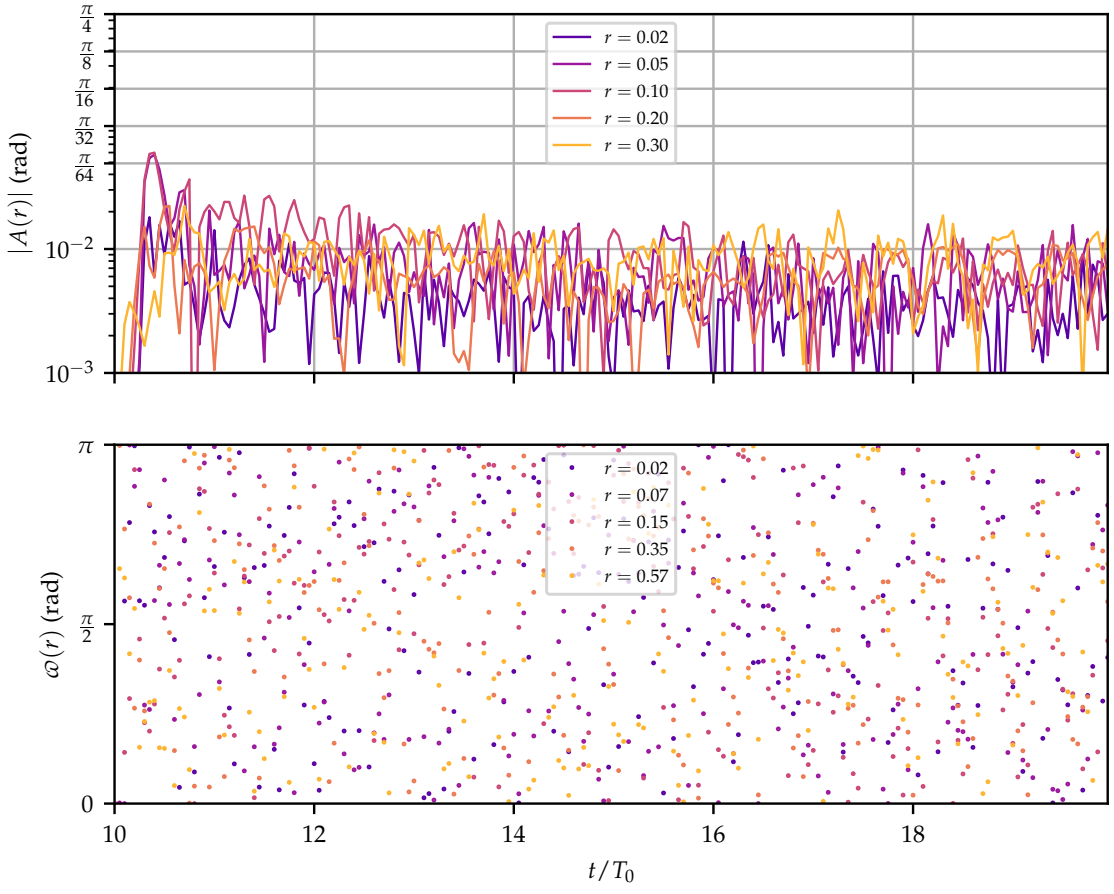

Figure 5.42 – Tilt parameters of the simulation `50WBF`.

4. After a few binary orbits time, I see an exponentially growing disc tilt. The growth timescale of this tilt appears to be related to the crossing time of bending waves.
5. The tilt is rotating much slower than the binary systems at about 3% of its angular frequency, in the opposite direction.
6. A non-axisymmetric ring (*e.g.* due to spiral density waves) is likely to be unstable when lying in the orbital plane of a binary system.
7. Using non-magnetic simulations, I was not able to determine the origin of the tilt growth. An axisymmetric net force, even when combined with the non-axisymmetry tidal potential does not drive a global disc tilt.
8. A purely hydrodynamics tilted disc is stable on bending wave crossing timescales.

The mechanism driving the tilt growth is yet to be elucidated. It is possible that in addition to the axisymmetric net force imposed by the non-top-bottom-symmetric wind, additional higher order forcing forces the tilt growth. The exponential nature of the tilt growth however suggests that an additional feedback mechanism could be present to sustain such growth.

The tilt I measure in the tilted simulations all have a very particular pattern speed. The tilt has a rotation period (in the non-rotating frame) of around 30 to 40 binary orbits. These frequencies are the frequencies at which superhumps are observed in SU UMa systems. This explanation for superhumps was originally proposed by Bonnet-Bidaud et al. (1985). Simulation works using SPH method (Wood and Burke, 2007; Thomas and Wood, 2015) showed that the precession frequencies matched the observed frequencies. The present work further confirms this possibility.

Part III

CONCLUSION AND PERSPECTIVES

6

CONCLUSION

Thanks to their short recurrence times-scale, cataclysmic variable stars, and especially dwarf novæ are key elements of accretion disc theory. They enable us to probe accretion driving mechanisms in both hot disc and cold disc regimes and put strong constraints on the efficiency of these mechanisms. The mechanisms studied in dwarf novæ disc are then often directly translatable to other accreting systems, like X-ray binaries in outburst, AGN discs or inner regions of protoplanetary disc, for the hot disc regime, and outer parts of X-ray binary discs or the dead zone of protoplanetary discs for the cold disc regime.

In this thesis, I focused on the problem of accretion during the quiescence phase of dwarf novæ. As presented, during this phase, the accretion disc of these systems is cold at temperature $T \approx 2000$K. As a first consequence, the disc is razor thin, with aspect ratio of $H/R \approx 10^{-3}$. Second, the plasma of the disc is poorly ionised and highly resistive, with magnetic Reynolds number $\mathrm{Rm} \lesssim 100$ in the disc bulk. Under these conditions, the usual accretion driving mechanism of hot discs, and of the outburst phase, the Magneto-rotational Instability is quenched inside the disc, and can not sustain sufficient turbulence to produce the anomalous viscosity required to explain recurrence times between two outbursts. Hence, I focused on other possible accretion-driving mechanisms for this phase.

First, I examined the possibility that quiescent accretion could be driven by a purely non-magnetic mechanism: the transport of angular momentum due to the presence of tidally excited spiral shocks in the accretion disc. These shocks have been extensively studied in the past through linear theory and numerical simulations. However, they were never explored the quiescence temperature regime. During this phase, the disc is very thin, and the tidally excited spirals are all the more tightly wound rendering their numerical study computationally expensive. Thanks to the new GPU-accelerated code Idefix, I was able to explore this regime down to realistic temperature regimes. In this work, I first showed that the analytical linear theory poorly describes this low-temperature regime. Indeed, the dominant spiral mode I observed in my simulation is not the two-armed mode expected by the linear theory, but rather a one-armed spiral mode. Moreover, I showed that the spiral pattern speed in my discs did not match the quasi non-linear (order two) theory either. However, the pattern speeds did not take random values, rather their values are integer multiples of the binary angular frequency. When it comes to the angular momentum transport achieved by these spiral shocks, I obtained the three following results. First, for isothermal discs, the spiral shocks drive accretion at a far weaker rate than the rate required by the Disc Instability Model for the quiescence phase. This means that in quiescent dwarf novæ, another angular momentum transport mechanism is at play. Second, I showed that at low-temperature, a very long transient regime, close to a hundred binary orbits time, takes place. This time is comparable to the recurrence time of some dwarf novæ. This suggests that the quiescence phase could be too short for a steady state to be reached, implying that there could be memory effects from one outburst to the next. Third, I showed that spiral shock heating is able to sustain a disc temperature $\geq 1,000$ K during quiescence, without requiring any other heating mechanisms. I also observed very hot regions in the disc, $T \approx 10^4$ K, namely at the external tidal truncation radius. If these very high temperatures are indeed reached in actual quiescent discs, this may have a huge impact, as the MRI could be sustained in

the outermost disc region during this phase. Most of these results are published in Van den Bossche et al. (2023).

In the second part of this work, I focused on the other relevant accretion-driving mechanism for quiescent dwarf novæ discs: magnetic wind-driven accretion. Such winds arise in a wide variety of accreting systems and exert a surface torque on the disc, allowing for accretion in the disc. Local shearing box simulations including realistic magnetic resistivity suggested that such winds could be launched even from a poorly ionised disc (Scepi et al., 2018a,b). At that time, it remained to be shown that this picture was valid for a global disc geometry. With the IDEFIX code, I was able to produce global simulations of discs that are thinner than what had been achieved before. I modelled discs with aspect ratio $H/R = 0.01$ and a realistic resistivity to describe the quiescence phase. In these simulations, I observed that a wind is indeed launched from a global, cold, resistive disc. This wind increased accretion by more than an order of magnitude compared to the non-magnetic case. I also observed that MRI is triggered at the surface of the disc, where the resistivity is lower and the magnetisation is higher. Due to the numerical cost of global simulations, however, I could not further study the MRI because of too low a resolution. Finally, I observed that the winds produced in these thin discs, both ideal and resistive, were not top-bottom symmetric. As a consequence, they exert a net vertical force on the disc.

At later times, in these magnetic simulations, I observe the rapid growth of a global disc tilt. This tilt arise in all magnetic simulations with similar properties whether the disc is resistive or ideal. However, the comparison non-magnetic simulation never develops any significant tilt. This suggests that this tilt is due to the coupling to the magnetic field. A comparison with a simulation at higher temperature allowed me to understand that the growth time of this global disc tilt is related to the disc crossing time of a bending wave, propagating at half the speed of sound. Furthermore, I observe that the disc tilt is almost stationary in the non-rotating reference frame. The disc tilt is retrograde at close to 3% of the binary system angular frequency. This frequency matched the observed period of superhumps in SU UMa systems, and tilted discs have been proposed to explain them (Bonnet-Bidaud et al., 1985). To try and understand the physical origin of this tilt growth, I examined the gravitational stability of density rings in a binary potential. From an energetic approach, I showed that a disc with non-axisymmetric density features was not always at equilibrium when lying in the binary orbital plane. Comparison to the non-magnetic simulation, however, suggests that this instability does not occur on as short a timescale as the tilt growth I observe in magnetic simulations. I then explored the effect of a net vertical force exerted by the magnetic wind by including this effect in non-magnetic simulations. I observed that an axisymmetric vertical forcing did not produce a global disc tilt even in a non-axisymmetric potential. This is possibly due to the lack of positive feedback in this simple model. As a consequence, the mechanism at the origin of the disc tilt remains to be understood. I also showed that on the timescales relevant to the propagation of bending waves, a global tilt is stable in a binary potential.

7

PERSPECTIVES

In this last chapter, I present perspectives for continuing the work presented in this thesis. Some of the perspectives presented here are projects I plan on carrying out at some point, while others are just ideas that would be interesting to explore.

First, it would be interesting to follow up on the promising results of chapter 4 on disc thermodynamics and spiral shock heating.

In order to match observations, the Disc Instability Model predict the dwarf novæ disc to have temperatures of a roughly constant 2,000 K during quiescence. However, several mechanisms like spiral shocks are expected to heat the disc, as observed by Ju et al. (2016) and myself. Yet a proper global treatment of thermodynamics in realistically thin quiescent discs has never been done; previous works (Ju et al., 2016; Pjanka and Stone, 2020; Van den Bossche et al., 2023) were limited to either isothermal discs or discs with no cooling. Preliminary unpublished results presented in chapter 4 showed that non-magnetic tidal shocks alone are able to sustain the disc at a realistic quiescent temperature of around 1,000 K. Moreover in the external parts of the disc could reach much higher temperatures of a few 10^4 K. In this regime, the magnetic instability that was thought to be quenched by low temperature could survive even in quiescence. In semi-detached binaries, this region could be sustained by the hot spot, where the matter flux from the companion star hits and heats the disc on secular times scales. Better understanding this hot region is key to understanding the transition from quiescence to outburst in variable stars, be it compact binaries or FU Orionis-type stars.

A first step to continue this study is to produce similar simulations as the one presented in chapter 4, including proper thermodynamics treatment, and including a temperature dependant viscosity. Such an $\alpha(T)$ would model the fact that when the disc temperature is low, the bulk MRI is quenched by resistivity but when the disc reaches high enough temperatures, MRI can reappear. Preliminary work using such a model has been done by a masters intern, Remi Zerna, and already show promising results. Thanks to this type of sub-grid model for turbulent viscosity, these simulations can be integrated for hundreds of binary orbits and allow for the study of several complete outburst-quiescence cycles. One of the questions that can be answered with such simulations is to know where the outburst starts. At this point in time, we have no general model to know whether outbursts are triggered in the inner regions, and produce inside-out outbursts, or if they are triggered in the outer disc, producing outside-in outbursts. These simulations will also allow me to examine possible memory effects between outbursts, suggested by the very long relaxation time observed in chapter 4.

The study of global dwarf novæ disc presented in chapter 5 can also be further explored.

During the first phase of my simulations, I observe the launching of a global MHD wind. It would be interesting to better study them. For instance, it would be possible to post-treat these simulations with a Monte Carlo radiative transfer code. Such a study could be carried out using the PYTHON code developed by Long and Knigge (2002) especially for winds of cataclysmic variables. This would allow me to compare the winds obtained in my simulations with actual observations of dwarf novæ. A such comparison is crucial to ensure the validity of theoretical and numerical models. The first parameter that should be compared with such a study is the wind loss rate estimated from observations to the wind loss rate measured in the simulation. To further refine this comparison,

it would be best to include a proper thermodynamics treatment of the fluid, rather than using a barotropic two-temperature equation of state as presented here.

Second, the geometry and amplitude of magnetic field in dwarf novæ systems is not constrained at all, and in order to launch an efficient wind, a large-scale vertical magnetic field is required. A weaker assumption for the magnetic configuration of the systems is that magnetic loops are advected from the companion star through the matter flux. Pjanka and Stone (2020) included this in their model at higher temperatures. Recent simulations by Jacquemin-Ide et al. (2023) showed that a large-scale magnetic field required to launch outflows can be produced by non-linear disc dynamo. It is not clear whether this mechanism can also play a role to produce such fields in much thinner cataclysmic variable discs. If this is the case, this would allow us to relax the very strong assumption of *ad hoc* large-scale vertical magnetic field used in most numerical works. This would also allow to apply these results to black-hole X-rays binaries, where the large-scale magnetic field can not come from the dipole of the central object and needs to be transported through the disc.

Finally, further investigating the growth of the disc tilt is key. Warped discs have been greatly studied in the non-magnetised case. Here, it appears that the presence of a magnetic field dramatically changes the picture. Such warps or disc tilt can trigger accretion-driving instabilities and modify their efficiency compared to a planar, non-warped disc (Aly et al., 2023). This can have an influence beyond the case of cataclysmic variable discs. For instance, in the context of protoplanetray discs, if the accretion driven by the warp is strong enough, the disc can empty on timescales shorter than planet formation timescales. Recent observations, relying on different techniques, have shown that such distortions are common in protoplanetary discs (*e.g.* Rosenfeld et al. (2012) and Marino et al. (2015)). To further investigate warp in cold magnetised discs, a first step would be to produce local simulations of distorted discs in the warped shearing box model (Ogilvie and Latter, 2013b). Using the recent addition of magnetic effects to this model (Paris and Ogilvie, 2018), I would examine how the warping of a magnetised disc influences the different local disc hydrodynamics and magnetohydrodynamics instabilities. To resolve these instabilities in numerical simulations, at least 50 grid points per disc height scale are required (Latter et al., 2010b). Hence, local simulations are better suited than entire disc simulations to understand how these instabilities develop and saturate. Global simulations with such fine resolution are still too expensive for current computing power. Then, the local shearing box model could be refined to better describe the effect of a secondary star's gravitational potential on the protoplanetary disc. As the shearing box model describes the shear flow at a given radius around the star, the potential of the secondary star can be included using a time-varying perturbation of the central gravitational potential. As long as the secondary star is not too close to the disc, this perturbation can be approximated by a sine function. Finally, it would be interesting to include non-ideal magnetic effects that arise because the disc's low temperature, namely Ohmic resistivity, and possibly ambipolar diffusion to use this model for protoplanetary discs. These effects are known to suppress some accretion-driving instabilities, like the MRI, but allow new instabilities to develop (Latter et al., 2010a). These shearing box simulations will provide information on which magnetic and non-magnetic instabilities can take place in cold warped discs. This would allow me to quantify how local turbulence is changed, compared to well-studied planar isolated discs.

To further hone our comprehension of warped discs, this study could be continued with global, entire disc simulations. Indeed, local simulations are a powerful tool to examine local properties of the flow but they are limited in the description of large-scale turbulence (see, for example, King et al. (2007)). Global simulations are crucial to obtain a precise picture of disc evolution. The shearing box models will provide us with values of the turbulence locally achieved in different regions of warped protoplanetary discs. These first results will then be used to produce global 3D simulations of such systems. The decrease in the resolution required to describe a full 3D disc would be compensated

for by prescriptions on the small-scale physics informed by the shearing box simulation produced beforehand. This can be done by imposing a local effective viscosity that depends on the local properties of the flow, mimicking the effects of unresolved instabilities. This way we would be able to couple the small-scale flow description of shearing box simulations with the large-scale description of entire disc simulations. A global description of such systems would also allow, in the later stages of this project, to include global effects such as radiative transfer. A strong warp in the inner region of a protoplanetary disc can cast a shadow on the outer parts of the disc (see *e.g.* Casassus et al. (2019)) or enhance irradiation. This can dramatically change the local thermodynamical properties of the disc, namely its ionisation state. Such shadowing effects can only be captured using radiative transfer. Moreover, in multiple star systems, UV irradiation from the companion stars can also heat the disc to higher temperatures than what would be the case in isolated protoplanetary discs. This can lead to increased ionisation of the disc or even increase the local sound speed of the gas above the local escape velocity (Johnstone et al., 1998), depleting the disc. Modelling radiative transfer would also furnish a quantitative way of comparing those results with observations of warped discs. This is crucial as it provides strong constraints on the validity of the theoretical models used.

To conclude, we now have a better idea of how accretion is driven in quiescent discs. The tidally excited spiral shocks can be definitely ruled out as driving enough accretion during quiescence to explain the recurrence times of dwarf novæ. Moreover, it is now clear that even in cold, highly resistive, quiescent discs magnetic field plays a crucial role. It allows surface Magneto-rotational instability to develop and produce a strong accretion-driving wind. It also appears that the presence of a magnetic field produces a highly asymmetrical torque on the disc, leading to the growth of a global disc tilt. The coupling to magnetic field, even weak, produces discs with widely different global properties compared to purely hydrodynamic discs. As a consequence, magnetic effects need to be included in more accretion disc models; magnetic winds dramatically change both the accretion properties of discs as well as their geometrical properties.

Part IV

APPENDIX

BIBLIOGRAPHY

Achten, Wouter M.J. et al. (2013). « Carbon footprint of science: More than flying ». In: *Ecological Indicators* 34, pp. 352–355. ISSN: 1470-160X. DOI: https://doi.org/10.1016/j.ecolind.2013.05.025. URL: https://www.sciencedirect.com/science/article/pii/S1470160X13002306 (cit. on p. 182).

Aly et al. (Nov. 2023). « WInDI: a Warp-Induced Dust Instability in protoplanetary discs ». In: *arXiv*. DOI: 10.48550/arXiv.2311.06182 (cit. on pp. 152, 196).

Artymowicz, Pawel and Stephen H. Lubow (Feb. 1994). « Dynamics of Binary-Disk Interaction. I. Resonances and Disk Gap Sizes ». In: *The Astrophysical Journal* 421, p. 651. DOI: 10.1086/173679 (cit. on p. 47).

Baba, Hajime et al. (Feb. 2002). « Spiral Structure in WZ Sagittae around the 2001 Outburst Maximum ». In: *Publications of the Astronomical Society of Japan* 54, pp. L7–L10. DOI: 10.1093/pasj/54.1.L7 (cit. on pp. 17, 185).

Bai, Xue-Ning (Jan. 2015). « Hall Effect Controlled Gas Dynamics in Protoplanetary Disks. II. Full 3D Simulations toward the Outer Disk ». In: *The Astrophysical Journal* 798.2, 84, p. 84. DOI: 10.1088/0004-637X/798/2/84 (cit. on pp. 29, 133).

Bai, Xue-Ning and James M. Stone (Apr. 2013a). « Local Study of Accretion Disks with a Strong Vertical Magnetic Field: Magnetorotational Instability and Disk Outflow ». In: *The Astrophysical Journal* 767.1, 30, p. 30. DOI: 10.1088/0004-637X/767/1/30 (cit. on p. 39).

Bai, Xue-Ning and James M. Stone (May 2013b). « Wind-driven Accretion in Protoplanetary Disks. I. Suppression of the Magnetorotational Instability and Launching of the Magnetocentrifugal Wind ». In: *The Astrophysical Journal* 769.1, 76, p. 76. DOI: 10.1088/0004-637X/769/1/76 (cit. on p. 43).

Balbus, Steven A. and John F. Hawley (July 1991). « A Powerful Local Shear Instability in Weakly Magnetized Disks. I. Linear Analysis ». In: *The Astrophysical Journal* 376, p. 214. DOI: 10.1086/170270 (cit. on pp. 39, 187).

Balbus, Steven A. and John C. B. Papaloizou (Aug. 1999). « On the Dynamical Foundations of α Disks ». In: *The Astrophysical Journal* 521, pp. 650–658. ISSN: 0004-637X. DOI: 10.1086/307594 (cit. on pp. 30, 31, 186).

Balbus, Steven A. and Caroline Terquem (May 2001). « Linear Analysis of the Hall Effect in Protostellar Disks ». In: *The Astrophysical Journal* 552.1, pp. 235–247. DOI: 10.1086/320452 (cit. on p. 29).

Balman, S. (Jan. 2015). « Inner Disk Structure of Dwarf Novae in the Light of X-Ray Observations ». In: *Acta Polytechnica CTU Proceedings* 2.1, pp. 116–122. DOI: 10.14311/APP.2015.02.0116 (cit. on pp. 21, 185).

Baptista, R. et al. (Aug. 2007). « A Study of the Evolution of the Accretion Disk of V2051 Ophiuchi through Two Outburst Cycles ». In: *The Astronomical Journal* 134.2, pp. 867–879. DOI: 10.1086/519762 (cit. on pp. 13, 184).

Baptista, Raymundo (Jan. 2016). « Eclipse Mapping: Astrotomography of Accretion Discs ». In: Astrophysics and Space Science Library 439. Ed. by Henri M. J. Boffin et al., p. 155. DOI: 10.1007/978-3-319-39739-9_9 (cit. on pp. 13, 14, 16, 184).

Baptista, Raymundo and M. S. Catalán (June 2001). « Changes in the structure of the accretion disc of EX Draconis through the outburst cycle ». In: *Monthly Notices of the Royal Astronomical Society* 324.3, pp. 599–611. DOI: 10.1046/j.1365-8711.2001.04320.x (cit. on pp. 13, 15, 184).

Bardeen, James M. and Jacobus A. Petterson (Jan. 1975). « The Lense-Thirring Effect and Accretion Disks around Kerr Black Holes ». In: *The Astrophysical Journal Letters* 195, p. L65. DOI: 10.1086/181711 (cit. on pp. 127, 193).

Bath, G. T. (Nov. 1969). « Dynamical Instabilities in Semidetached Close Binary Systems with Possible Applications to Novae and Novalike Variables ». In: *The Astrophysical Journal* 158, p. 571. DOI: 10.1086/150219 (cit. on p. 8).

Bath, G. T. (Apr. 1972). « Time-Dependent Studies of Dynamical Instabilities in Semidetached Binary Systems ». In: *The Astrophysical Journal* 173, p. 121. DOI: 10.1086/151405 (cit. on p. 8).

Beals, C. S. (Dec. 1929). « On the nature of Wolf-Rayet emission ». In: *Monthly Notices of the Royal Astronomical Society* 90, pp. 202–212. DOI: 10.1093/mnras/90.2.202 (cit. on pp. 18, 185).

Bell, K. R. and D. N. C. Lin (June 1994). « Using FU Orionis Outbursts to Constrain Self-regulated Protostellar Disk Models ». In: *The Astrophysical Journal* 427, p. 987. DOI: 10.1086/174206 (cit. on p. 33).

Béthune, William et al. (Apr. 2017). « Global simulations of protoplanetary disks with net magnetic flux. I. Non-ideal MHD case ». In: *Astronomy & Astrophysics* 600, A75, A75. DOI: 10.1051/0004-6361/201630056 (cit. on p. 133).

Bitner, Martin A. et al. (June 2007). « The Masses and Evolutionary State of the Stars in the Dwarf Nova SS Cygni ». In: *The Astrophysical Journal* 662.1, pp. 564–573. DOI: 10.1086/517496 (cit. on p. 106).

Blandford, R. D. and D. G. Payne (June 1982). « Hydromagnetic flows from accretion disks and the production of radio jets. » In: *Monthly Notices of the Royal Astronomical Society* 199, pp. 883–903. DOI: 10.1093/mnras/199.4.883 (cit. on p. 42).

Bodo, G. et al. (Aug. 2008). « Aspect ratio dependence in magnetorotational instability shearing box simulations ». In: *Astronomy & Astrophysics* 487.1, pp. 1–5. DOI: 10.1051/0004-6361:200809730 (cit. on p. 41).

Bodo, G. et al. (May 2014). « On the Convergence of Magnetorotational Turbulence in Stratified Isothermal Shearing Boxes ». In: *The Astrophysical Journal Letters* 787.1, L13, p. L13. DOI: 10.1088/2041-8205/787/1/L13 (cit. on pp. 45, 187).

Bonnet-Bidaud, J. M. et al. (Feb. 1985). « The continuum variability of the puzzling X-ray three-period cataclysmic variable 2A 0526-328 (TV Col). » In: *Astronomy & Astrophysics* 143, pp. 313–320 (cit. on pp. 145, 150, 195).

Bouvier, J. et al. (Sept. 2013). « AA Tauri's sudden and long-lasting deepening: enhanced extinction by its circumstellar disk ». In: *Astronomy & Astrophysics* 557, A77, A77. DOI: 10.1051/0004-6361/201321389 (cit. on p. 127).

Brahe, Tycho (1573). *De Stella Nova* (cit. on pp. 3, 175).

Brio, M. and C. C. Wu (Apr. 1988). « An Upwind Differencing Scheme for the Equations of Ideal Magnetohydrodynamics ». In: *Journal of Computational Physics* 75.2, pp. 400–422. DOI: 10.1016/0021-9991(88)90120-9 (cit. on p. 52).

Cannizzo, J. K. et al. (Sept. 1982). « Convective accretion disks and the onset of dwarf nova outbursts. » In: *The Astrophysical Journal Letters* 260, pp. L83–L86. DOI: 10.1086/183875 (cit. on pp. 33, 186).

Cannizzo, J. K. et al. (Jan. 1985). « Accretion Instability Models for Dwarf Novae and X-Ray Transients ». In: *Cataclysmic Variables and Low-Mass X-ray Binaries*. Ed. by D. Q. Lamb and J. Patterson, p. 307. DOI: 10.1007/978-94-009-5319-2_36 (cit. on p. 33).

Cannizzo, John K. et al. (Oct. 1988). « On the Outburst Recurrence Time for the Accretion Disk Limit Cycle Mechanism in Dwarf Novae ». In: *The Astrophysical Journal* 333, p. 227. DOI: 10.1086/166739 (cit. on pp. 38, 186).

Cannizzo, John K. et al. (Mar. 2012). « The Kepler Light Curves of V1504 Cygni and V344 Lyrae: A Study of the Outburst Properties ». In: *The Astrophysical Journal* 747.2, 117, p. 117. DOI: 10.1088/0004-637X/747/2/117 (cit. on pp. 38, 186).

Caplar, Neven et al. (June 2017). « Quantitative evaluation of gender bias in astronomical publications from citation counts ». In: *Nature Astronomy* 1, 0141, p. 0141. DOI: 10.1038/s41550-017-0141. arXiv: 1610.08984 [astro-ph.IM] (cit. on p. 179).

Casassus et al. (June 2019). « Cooling in the shade of warped transition discs ». In: *Monthly Notices of the Royal Astronomical Society* 486.1, pp. L58–L62. DOI: 10.1093/mnrasl/slz059 (cit. on p. 153).

Chandrasekhar, S. (July 1931). « The Maximum Mass of Ideal White Dwarfs ». In: *The Astrophysical Journal* 74, p. 81. DOI: 10.1086/143324 (cit. on p. 23).

Chandrasekhar, Subrahmanyan (1961). *Hydrodynamic and hydromagnetic stability* (cit. on p. 39).

Cimerman, Nicolas P. and Roman R. Rafikov (Jan. 2024). « Gravitational torque in circumbinary discs: global radial oscillations ». In: *Monthly Notices of the Royal Astronomical Society*. DOI: 10.1093/mnras/stae134 (cit. on p. 99).

Coppejans, Deanne L. and Christian Knigge (Sept. 2020). « The case for jets in cataclysmic variables ». In: *New Astronomy Reviews* 89, 101540, p. 101540. DOI: 10.1016/j.newar.2020.101540 (cit. on pp. 19, 185).

Coppejans, Deanne L. et al. (Aug. 2015). « Novalike cataclysmic variables are significant radio emitters ». In: *Monthly Notices of the Royal Astronomical Society* 451.4, pp. 3801–3813. DOI: 10.1093/mnras/stv1225 (cit. on pp. 19, 185).

Coppejans, Deanne L. et al. (Dec. 2016). « Dwarf nova-type cataclysmic variable stars are significant radio emitters ». In: *Monthly Notices of the Royal Astronomical Society* 463.2, pp. 2229–2241. DOI: 10.1093/mnras/stw2133 (cit. on pp. 19, 185).

Cordova, F. A. and K. O. Mason (Sept. 1982). « High-velocity winds from a dwarf nova during outburst. » In: *The Astrophysical Journal* 260, pp. 716–721. DOI: 10.1086/160291 (cit. on pp. 18, 185).

Courant, R. et al. (Jan. 1928). « Über die partiellen Differenzengleichungen der mathematischen Physik ». In: *Mathematische Annalen* 100, pp. 32–74. DOI: 10.1007/BF01448839 (cit. on pp. 54, 188).

Court, J. M. C. et al. (June 2020). « EX draconis: using eclipses to separate outside-in and inside-out outbursts ». In: *Monthly Notices of the Royal Astronomical Society* 494.4, pp. 4656–4664. DOI: 10.1093/mnras/staa1042 (cit. on p. 15).

Cowling, T. G. (Jan. 1941). « The non-radial oscillations of polytropic stars ». In: *Monthly Notices of the Royal Astronomical Society* 101, p. 367. DOI: 10.1093/mnras/101.8.367 (cit. on p. 46).

Cox, Arthur N. and John N. Stewart (Jan. 1970). « Rosseland Opacity Tables for Population II Compositions ». In: *The Astrophysical Journal Supplement* 19, p. 261. DOI: 10.1086/190208 (cit. on pp. 34, 35).

Crutcher, Richard M. and Athol J. Kemball (Oct. 2019). « Review of Zeeman Effect Observations of Regions of Star Formation K Zeeman Effect, Magnetic Fields, Star formation, Masers, Molecular clouds ». In: *Frontiers in Astronomy and Space Sciences* 6, 66, p. 66. DOI: 10.3389/fspas.2019.00066 (cit. on p. 24).

Cúneo, V. A. et al. (Nov. 2023). « Unveiling optical signatures of outflows in accreting white dwarfs ». In: *Astronomy & Astrophysics* 679, A85, A85. DOI: 10.1051/0004-6361/202347265 (cit. on p. 18).

Darwin, G. H. (July 1879). « A tidal theory of the evolution of satellites ». In: *The Observatory* 3, pp. 79–84 (cit. on p. 46).

Davidson, Kris and Jeremiah P. Ostriker (Jan. 1973). « Neutron-Star Accretion in a Stellar Wind: Model for a Pulsed X-Ray Source ». In: *The Astrophysical Journal* 179, pp. 585–598. DOI: 10.1086/151897 (cit. on p. 10).

Davis, S. F. (1988). « Simplified Second-Order Godunov-Type Methods ». In: *SIAM Journal on Scientific and Statistical Computing* 9.3, pp. 445–473. DOI: 10.1137/0909030 (cit. on p. 54).

Davis, Shane W. et al. (Apr. 2010). « Sustained Magnetorotational Turbulence in Local Simulations of Stratified Disks with Zero Net Magnetic Flux ». In: *The Astrophysical Journal* 713.1, pp. 52–65. DOI: 10.1088/0004-637X/713/1/52 (cit. on pp. 45, 187).

de Val-Borro, M. et al. (Aug. 2006). « A comparative study of disc-planet interaction ». In: *Monthly Notices of the Royal Astronomical Society* 370.2, pp. 529–558. DOI: 10.1111/j.1365-2966.2006.10488.x (cit. on p. 84).

Done, C. and J. P. Osborne (July 1997). « The X-ray spectrum of the dwarf nova SS CYG in quiescence and outburst ». In: *Monthly Notices of the Royal Astronomical Society* 288.3, pp. 649–664. DOI: 10.1093/mnras/288.3.649 (cit. on p. 12).

Drew, J. E. (1990). « Winds from Disks ». In: *IAU Colloq. 122: Physics of Classical Novae*. Ed. by Angelo Cassatella and Roberto Viotti. Vol. 369, p. 228. DOI: 10.1007/3-540-53500-4_130 (cit. on pp. 18, 185).

Dubus, Guillaume et al. (Sept. 2018). « Testing the disk instability model of cataclysmic variables ». In: *Astronomy & Astrophysics* 617, A26, A26. DOI: 10.1051/0004-6361/201833372 (cit. on p. 39).

Ductor, Lorenzo et al. (Nov. 2023). « Gender and Collaboration ». In: *The Review of Economics and Statistics* 105.6, pp. 1366–1378. ISSN: 0034-6535. DOI: 10.1162/rest_a_01113. eprint: https://direct.mit.edu/rest/article-pdf/105/6/1366/2178684/rest_a_01113.pdf. URL: https://doi.org/10.1162/rest%5C_a%5C_01113 (cit. on p. 177).

Echevarría, J. (Jan. 2012). « Doppler tomography in cataclysmic variables: an historical perspective ». In: *Memorie della Societa Astronomica Italiana* 83, p. 570. DOI: 10.48550/arXiv.1201.3075 (cit. on pp. 17, 184).

Euler, Leonhard (1757). « Principes généraux du mouvement des fluides ». In: pp. 274–315. URL: http://eulerarchive.maa.org//docs/originals/E226.pdf (cit. on p. 27).

Euler, Leonhard (1768). *Institutiones calculi integralis*. Imperial Acadamy of Science (St Petersbourg). URL: http://catalogue.bnf.fr/ark:/12148/cb37341158h (cit. on p. 50).

Evans, Charles R. and John F. Hawley (Sept. 1988). « Simulation of Magnetohydrodynamic Flows: A Constrained Transport Model ». In: *The Astrophysical Journal* 332, p. 659. DOI: 10.1086/166684 (cit. on pp. 57, 188).

Faulkner, J. et al. (Oct. 1983). « On the evolution of accretion disc flow in cataclysmic variables- I.The prospect of a limit cycle in dwarf nova systems. » In: *Monthly Notices of the Royal Astronomical Society* 205, pp. 359–375. DOI: 10.1093/mnras/205.2.359 (cit. on pp. 33, 186).

Fender, Rob et al. (Nov. 2019). « Late-outburst radio flaring in SS Cyg and evidence for a powerful kinetic output channel in cataclysmic variables ». In: *Monthly Notices of the Royal Astronomical Society* 490.1, pp. L76–L80. DOI: 10.1093/mnrasl/slz145 (cit. on pp. 19, 185).

Ferguson, Jason W. et al. (Apr. 2005). « Low-Temperature Opacities ». In: *The Astrophysical Journal* 623.1, pp. 585–596. DOI: 10.1086/428642 (cit. on p. 96).

Fertig, D. et al. (Sept. 2011). « The Fall and the Rise of X-Rays from Dwarf Novae in Outburst: RXTE Observations of VW Hydri and WW Ceti ». In: *Publications of the Astronomical Society of the Pacific* 123.907, p. 1054. DOI: 10.1086/661949 (cit. on pp. 21, 185).

Fleming, Timothy P. et al. (Feb. 2000). « The Effect of Resistivity on the Nonlinear Stage of the Magnetorotational Instability in Accretion Disks ». In: *The Astrophysical Journal* 530.1, pp. 464–477. DOI: 10.1086/308338 (cit. on p. 43).

Foulkes, Stephen B. et al. (Mar. 2006). « Three-dimensional smoothed particle hydrodynamics simulations of radiation-driven warped accretion discs ». In: *Monthly Notices of the Royal Astronomical Society* 366.4, pp. 1399–1409. DOI: 10.1111/j.1365-2966.2005.09910.x (cit. on pp. 127, 193).

Foulkes, Stephen B. et al. (Jan. 2010). « SPH simulations of irradiation-driven warped accretion discs and the long periods in X-ray binaries ». In: *Monthly Notices of the Royal Astronomical Society* 401.2, pp. 1275–1289. DOI: 10.1111/j.1365-2966.2009.15721.x (cit. on pp. 127, 193).

Fromang, S. and J. Papaloizou (Dec. 2007). « MHD simulations of the magnetorotational instability in a shearing box with zero net flux. I. The issue of convergence ». In:

Astronomy & Astrophysics 476.3, pp. 1113–1122. DOI: 10.1051/0004-6361:20077942 (cit. on pp. 41, 45, 187).

Fromang, S. et al. (Dec. 2007). « MHD simulations of the magnetorotational instability in a shearing box with zero net flux. II. The effect of transport coefficients ». In: *Astronomy & Astrophysics* 476.3, pp. 1123–1132. DOI: 10.1051/0004-6361:20077943 (cit. on pp. 45, 187).

Gaia Collaboration et al. (Aug. 2018). « Gaia Data Release 2. Summary of the contents and survey properties ». In: *Astronomy & Astrophysics* 616, A1, A1. DOI: 10.1051/0004-6361/201833051 (cit. on p. 39).

Gammie, Charles F. (Jan. 1996). « Layered Accretion in T Tauri Disks ». In: *The Astrophysical Journal* 457, p. 355. DOI: 10.1086/176735 (cit. on pp. 40, 43).

Gammie, Charles F. and Kristen Menou (Jan. 1998). « On the Origin of Episodic Accretion in Dwarf Novae ». In: *The Astrophysical Journal* 492.1, pp. L75–L78. DOI: 10.1086/311091 (cit. on pp. 40, 43, 45, 99).

Gardiner, Thomas A. and James M. Stone (May 2005). « An unsplit Godunov method for ideal MHD via constrained transport ». In: *Journal of Computational Physics* 205.2, pp. 509–539. DOI: 10.1016/j.jcp.2004.11.016 (cit. on p. 57).

Gerend, D. and P. E. Boynton (Oct. 1976). « Optical clues to the nature of Hercules X-1 / HZ Herculis. » In: *The Astrophysical Journal* 209, pp. 562–573. DOI: 10.1086/154751 (cit. on p. 127).

Gibbs, J. Willard (Dec. 1898). « Fourier's Series ». In: *Nature* 59.1522, p. 200. DOI: 10.1038/059200b0 (cit. on p. 55).

Gibbs, J. Willard (Apr. 1899). « Fourier's Series ». In: *Nature* 59.1539, pp. 606–606. DOI: 10.1038/059606a0 (cit. on p. 55).

Gingold, R. A. and J. J. Monaghan (Nov. 1977). « Smoothed particle hydrodynamics: theory and application to non-spherical stars. » In: *Monthly Notices of the Royal Astronomical Society* 181, pp. 375–389. DOI: 10.1093/mnras/181.3.375 (cit. on pp. 46, 187).

Godon, Patrick and Edward M. Sion (June 2023). « White Dwarf Photospheric Abundances in Cataclysmic Variables. III. Five Dwarf Novae with an Evolved Secondary Donor Star ». In: *The Astrophysical Journal* 950.2, 139, p. 139. DOI: 10.3847/1538-4357/accb94 (cit. on p. 12).

Godunov, Sergei K. (1959). « Finite difference method for numerical computation of discontinuous solutions of the equations of fluid dynamics ». In: *Matematičeskij sbornik* 47(89).3. Translated by Bohachevsky, I., pp. 271–306. URL: https://hal.science/hal-01620642 (cit. on pp. 50, 52, 175, 188).

Godunov, Sergei K. et al. (Jan. 1976). « Numerical solution of multidimensional problems of gas dynamics ». In: *Moscow Izdatel Nauka* (cit. on p. 52).

Goldreich, P. and S. Tremaine (Oct. 1980). « Disk-satellite interactions. » In: *The Astrophysical Journal* 241, pp. 425–441. DOI: 10.1086/158356 (cit. on p. 46).

Goldreich, Peter and Gerald Schubert (Nov. 1967). « Differential Rotation in Stars ». In: *The Astrophysical Journal* 150, p. 571. DOI: 10.1086/149360 (cit. on p. 26).

Goodman, Jeremy and Guohong Xu (Sept. 1994). « Parasitic Instabilities in Magnetized, Differentially Rotating Disks ». In: *The Astrophysical Journal* 432, p. 213. DOI: 10.1086/174562 (cit. on p. 41).

Grevesse, N. and A. J. Sauval (May 1998). « Standard Solar Composition ». In: *Space Science Reviews* 85, pp. 161–174. DOI: 10.1023/A:1005161325181 (cit. on pp. 12, 29, 59, 188).

Groot, P. J. (Apr. 2001). « Evolution of Spiral Shocks in U Geminorum during Outburst ». In: *The Astrophysical Journal Letters* 551.1, pp. L89–L92. DOI: 10.1086/319826 (cit. on pp. 17, 185).

Guilet, Jérôme et al. (Nov. 2022). « MRI-driven dynamo at very high magnetic Prandtl numbers ». In: *Monthly Notices of the Royal Astronomical Society* 516.3, pp. 4346–4353. DOI: 10.1093/mnras/stac2499 (cit. on pp. 45, 187).

Hakala, P. et al. (June 2004). « XMM-Newton observations of the dwarf nova YZ Cnc in quiescence ». In: *Astronomy & Astrophysics* 420, pp. 273–281. DOI: 10.1051/0004-6361:20035843 (cit. on pp. 18, 185).

Hameury, J. -M. et al. (Mar. 2009). « The thermal-viscous disk instability model in the AGN context ». In: *Astronomy & Astrophysics* 496.2, pp. 413–421. DOI: 10.1051/0004-6361/200810928 (cit. on p. 33).

Hameury, J. M. (Sept. 2020). « A review of the disc instability model for dwarf novae, soft X-ray transients and related objects ». In: *Advances in Space Research* 66.5, pp. 1004–1024. DOI: 10.1016/j.asr.2019.10.022 (cit. on pp. 33, 39, 48).

Hameury, Jean-Marie et al. (Aug. 1998). « Accretion disc outbursts: a new version of an old model ». In: *Monthly Notices of the Royal Astronomical Society* 298.4, pp. 1048–1060. DOI: 10.1046/j.1365-8711.1998.01773.x (cit. on pp. 37, 38, 70, 98, 107).

Harrison, Thomas E. (Aug. 2014). « The WISE Light Curves of Z Camelopardalis during Outburst: Evidence for Synchrotron Emission? » In: *The Astrophysical Journal Letters* 791.1, L18, p. L18. DOI: 10.1088/2041-8205/791/1/L18 (cit. on pp. 19, 185).

Harrison, Thomas E. (Dec. 2016). « Abundance Derivations for the Secondary Stars in Cataclysmic Variables from Near-infrared Spectroscopy ». In: *The Astrophysical Journal* 833.1, 14, p. 14. DOI: 10.3847/0004-637X/833/1/14 (cit. on p. 12).

Harrison, Thomas E. and Rachel E. Marra (July 2017). « Determinations of the $^{12}C/^{13}C$ Ratio for the Secondary Stars of AE Aquarii, SS Cygni, and RU Pegasi ». In: *The Astrophysical Journal* 843.2, 152, p. 152. DOI: 10.3847/1538-4357/aa7946 (cit. on p. 12).

Harten, Amiram et al. (2021/07/24/ 1983). « On Upstream Differencing and Godunov-Type Schemes for Hyperbolic Conservation Laws ». In: *SIAM Review* 25.1, pp. 35–61. URL: http://www.jstor.org/stable/2030019 (cit. on pp. 52, 188).

Hartley, Louise E. et al. (Oct. 2005). « Spiral waves and the secondary star in the nova-like variable V3885 Sgr ». In: *Monthly Notices of the Royal Astronomical Society* 363.1, pp. 285–292. DOI: 10.1111/j.1365-2966.2005.09447.x (cit. on pp. 17, 185).

Hawley, John F. et al. (Feb. 1995). « Local Three-dimensional Magnetohydrodynamic Simulations of Accretion Disks ». In: *The Astrophysical Journal* 440, p. 742. DOI: 10.1086/175311 (cit. on pp. 41, 44, 187).

Hawley, John F. et al. (June 1996). « Local Three-dimensional Simulations of an Accretion Disk Hydromagnetic Dynamo ». In: *The Astrophysical Journal* 464, p. 690. DOI: 10.1086/177356 (cit. on p. 41).

Held, Loren E. and Henrik N. Latter (Nov. 2018). « Hydrodynamic convection in accretion discs ». In: *Monthly Notices of the Royal Astronomical Society* 480.4, pp. 4797–4816. DOI: 10.1093/mnras/sty2097 (cit. on p. 46).

Held, Loren E. and Henrik N. Latter (June 2021). « Magnetohydrodynamic convection in accretion discs ». In: *Monthly Notices of the Royal Astronomical Society* 504.2, pp. 2940–2960. DOI: 10.1093/mnras/stab974 (cit. on p. 46).

Hernández Santisteban, J. V. et al. (June 2019). « From outburst to quiescence: spectroscopic evolution of V1838 Aql imbedded in a bow-shock nebula ». In: *Monthly Notices of the Royal Astronomical Society* 486.2, pp. 2631–2642. DOI: 10.1093/mnras/stz798 (cit. on pp. 19, 185).

Hind, J. R. (Jan. 1856). « On a new Variable Star ». In: *Monthly Notices of the Royal Astronomical Society* 16, pp. 56–56. DOI: 10.1093/mnras/16.3.56 (cit. on p. 4).

Hirose, Shigenobu et al. (May 2014). « Convection Causes Enhanced Magnetic Turbulence in Accretion Disks in Outburst ». In: *The Astrophysical Journal* 787.1, 1, p. 1. DOI: 10.1088/0004-637X/787/1/1 (cit. on pp. 17, 39, 45, 46, 187).

Hoare, Melvin G. and Janet E. Drew (Feb. 1993). « The ionization of the winds from cataclysmic variables without classical boundary layers. » In: *Monthly Notices of the Royal Astronomical Society* 260, pp. 647–662. DOI: 10.1093/mnras/260.3.647 (cit. on pp. 18, 115, 185).

Horne, K. (Mar. 1985). « Images of accretion discs -I. The eclipse mapping method. » In: *Monthly Notices of the Royal Astronomical Society* 213, pp. 129–141. DOI: 10.1093/mnras/213.2.129 (cit. on p. 13).

Horne, K. (Jan. 1991). « Variability and Structure of Accretion Disks in Cataclysmic Variables. » In: *IAU Colloq. 129: The 6th Institute d'Astrophysique de Paris (IAP) Meeting: Structure and Emission Properties of Accretion Disks*. Ed. by C. Bertout et al., p. 3 (cit. on p. 12).

Horne, K. and M. C. Cook (May 1985). « UBV images of the Z Cha accretion disc in outburst. » In: *Monthly Notices of the Royal Astronomical Society* 214, pp. 307–317. DOI: 10.1093/mnras/214.3.307 (cit. on pp. 13, 15).

Horne, K. and R. F. Stiening (Oct. 1985). « Eclipse maps of the accretion disc in RW Trianguli. » In: *Monthly Notices of the Royal Astronomical Society* 216, pp. 933–948. DOI: 10.1093/mnras/216.4.933 (cit. on pp. 13, 184).

Hōshi, R. (May 1979). « Accretion Model for Outbursts of Dwarf Nova ». In: *Progress of Theoretical Physics* 61.5, pp. 1307–1319. DOI: 10.1143/PTP.61.1307 (cit. on pp. 33, 35, 186).

Huang, Junming et al. (2020). « Historical comparison of gender inequality in scientific careers across countries and disciplines ». In: *Proceedings of the National Academy of Sciences* 117.9, pp. 4609–4616. DOI: 10.1073/pnas.1914221117. eprint: https://www.pnas.org/doi/pdf/10.1073/pnas.1914221117. URL: https://www.pnas.org/doi/abs/10.1073/pnas.1914221117 (cit. on p. 177).

Hugoniot, H (1889). « Sur la propagation du mouvement dans les corps et spécialement dans les gaz parfaits ». In: *Journale de l'école polytechnique*. URL: http://catalogue.bnf.fr/ark:/12148/cb34378280v (cit. on p. 54).

Iglesias, Carlos A. and Forrest J. Rogers (June 1996). « Updated Opal Opacities ». In: *The Astrophysical Journal* 464, p. 943. DOI: 10.1086/177381 (cit. on p. 96).

Jacquemin-Ide, J. et al. (Mar. 2021a). « Magnetic outflows from turbulent accretion disks. I. Vertical structure and secular evolution ». In: *Astronomy & Astrophysics* 647, A192, A192. DOI: 10.1051/0004-6361/202039322 (cit. on p. 42).

Jacquemin-Ide, J. et al. (Mar. 2021b). « Magnetic outflows from turbulent accretion disks. I. Vertical structure and secular evolution ». In: *Astronomy & Astrophysics* 647, A192, A192. DOI: 10.1051/0004-6361/202039322. arXiv: 2011.14782 [astro-ph.HE] (cit. on pp. 111, 112).

Jacquemin-Ide, Jonatan et al. (Oct. 2023). « Magnetorotational dynamo can generate large-scale vertical magnetic fields in 3D GRMHD simulations of accreting black holes ». In: *arXiv e-prints*, arXiv:2311.00034, arXiv:2311.00034. DOI: 10.48550/arXiv.2311.00034 (cit. on pp. 152, 195).

Janiuk, Agnieszka et al. (Feb. 2004). « On the Turbulent α-Disks and the Intermittent Activity in Active Galactic Nuclei ». In: *The Astrophysical Journal* 602.2, pp. 595–602. DOI: 10.1086/381159 (cit. on p. 33).

Jetsu, L. et al. (Aug. 2013). « Did the Ancient Egyptians Record the Period of the Eclipsing Binary Algol—The Raging One? » In: *The Astrophysical Journal* 773.1, 1, p. 1. DOI: 10.1088/0004-637X/773/1/1 (cit. on p. 3).

Johnstone et al. (May 1998). « Photoevaporation of Disks and Clumps by Nearby Massive Stars: Application to Disk Destruction in the Orion Nebula ». In: *The Astrophysical Journal* 499.2, pp. 758–776. DOI: 10.1086/305658 (cit. on p. 153).

Joy, Alfred H. (Nov. 1954). « Spectroscopic Observations of AE Aquarii. » In: *The Astrophysical Journal* 120, p. 377. DOI: 10.1086/145928 (cit. on pp. 6, 184).

Joy, Alfred H. (Sept. 1956). « Radial-Velocity Measures of SS Cygni at Minimum Light. » In: *The Astrophysical Journal* 124, p. 317. DOI: 10.1086/146226 (cit. on pp. 6, 184).

Ju, Wenhua et al. (June 2016). « Global MHD Simulations of Accretion Disks in Cataclysmic Variables. I. The Importance of Spiral Shocks ». In: *The Astrophysical Journal* 823.2, 81, p. 81. DOI: 10.3847/0004-637X/823/2/81 (cit. on pp. 18, 47, 70, 75–77, 79–82, 89, 95, 151, 185, 187, 190).

Ju, Wenhua et al. (May 2017). « Global MHD Simulations of Accretion Disks in Cataclysmic Variables (CVs). II. The Relative Importance of MRI and Spiral Shocks ». In: *The Astrophysical Journal* 841.1, 29, p. 29. DOI: 10.3847/1538-4357/aa705d (cit. on p. 47).

Kansas, Nick (2007). *Star maps*. Praxis New York, NY. DOI: 10.1007/978-0-387-71669-5 (cit. on pp. 3, 183).

Kato, S. et al. (2008). *Black-Hole Accretion Disks — Towards a New Paradigm* — (cit. on p. 26).

King, A. R. et al. (Apr. 2007). « Accretion disc viscosity: how big is alpha? » In: *Monthly Notices of the Royal Astronomical Society* 376.4, pp. 1740–1746. DOI: 10.1111/j.1365-2966.2007.11556.x (cit. on pp. 38, 45, 152, 186, 187).

Kley, W. et al. (Aug. 2008). « Simulations of eccentric disks in close binary systems ». In: *Astronomy & Astrophysics* 487.2, pp. 671–687. DOI: 10.1051/0004-6361:200809953 (cit. on pp. 46, 77, 86, 88, 90, 190).

Knigge, Christian and Janet E. Drew (Sept. 1997). « Eclipse Mapping of the Accretion Disk Wind in the Cataclysmic Variable UX Ursae Majoris ». In: *The Astrophysical Journal* 486.1, pp. 445–456. DOI: 10.1086/304519 (cit. on pp. 18, 115, 185).

Knödlseder, Jürgen et al. (Mar. 2022). « Estimate of the carbon footprint of astronomical research infrastructures ». In: *Nature Astronomy* 6, pp. 503–513. DOI: 10.1038/s41550-022-01612-3. arXiv: 2201.08748 [astro-ph.IM] (cit. on p. 182).

Kong, Hyunsik et al. (Dec. 2022). « Influence of the first-mover advantage on the gender disparities in physics citations ». In: *Communications Physics* 5.1, 243, p. 243. DOI: 10.1038/s42005-022-00997-x. arXiv: 2110.02815 [physics.soc-ph] (cit. on p. 179).

Körding, Elmar et al. (June 2008). « A Transient Radio Jet in an Erupting Dwarf Nova ». In: *Science* 320.5881, p. 1318. DOI: 10.1126/science.1155492 (cit. on pp. 19, 185).

Kotko, I. and J. -P. Lasota (Sept. 2012). « The viscosity parameter α and the properties of accretion disc outbursts in close binaries ». In: *Astronomy & Astrophysics* 545, A115, A115. DOI: 10.1051/0004-6361/201219618 (cit. on pp. 38, 186).

Kozai, Yoshihide (Nov. 1962). « Secular perturbations of asteroids with high inclination and eccentricity ». In: *The Astronomical Journal* 67, pp. 591–598. DOI: 10.1086/108790 (cit. on p. 142).

Kraft, Robert P. (Mar. 1962). « Binary Stars among Cataclysmic Variables. I. U Geminorum Stars (dwarf Novae). » In: *The Astrophysical Journal* 135, p. 408. DOI: 10.1086/147280 (cit. on pp. 6, 10, 184).

Kraft, Robert P. (Jan. 1963). « Cataclysmic Variables as Binary Stars ». In: *Advances in Astronomy and Astrophysics* 2, pp. 43–85. DOI: 10.1016/B978-1-4831-9920-7.50006-4 (cit. on p. 8).

Kraft, Robert P. et al. (July 1962). « Binary Stars among Cataclysmic Variables. II. Nova WZ Sagittae: a Possible Radiator of Gravitational Waves. » In: *The Astrophysical Journal* 136, pp. 312–315. DOI: 10.1086/147381 (cit. on pp. 8, 184).

Krzeminski, W. (Oct. 1964). « Eclipsing Binary U Geminorum. » In: *The Astronomical Journal* 69, p. 549. DOI: 10.1086/109493 (cit. on p. 8).

Krzeminski, W. (Oct. 1965). « The Eclipsing Binary U Geminorum. » In: *The Astrophysical Journal* 142, p. 1051. DOI: 10.1086/148375 (cit. on p. 8).

Kunz, Matthew W. and Geoffroy Lesur (Sept. 2013). « Magnetic self-organization in Hall-dominated magnetorotational turbulence ». In: *Monthly Notices of the Royal Astronomical Society* 434.3, pp. 2295–2312. DOI: 10.1093/mnras/stt1171 (cit. on p. 30).

Kunze, S. et al. (Aug. 1997). « Reproducing superhumps and gamma-shifts of SU UMa stars with SPH simulations ». In: *Monthly Notices of the Royal Astronomical Society* 289.4, pp. 889–897. DOI: 10.1093/mnras/289.4.889 (cit. on p. 46).

Kutta, W. (1901). « Beitrag zur näherungweisen Integration totaler Differentialgleichungen ». In: *Zeitschift für Mathematik und Physik* 46, pp. 435–456. URL: https://archive.org/stream/zeitschriftfrma12runggoog#page/n449/mode/2up (cit. on p. 50).

Lai, Dong (Oct. 1999). « Magnetically Driven Warping, Precession, and Resonances in Accretion Disks ». In: *The Astrophysical Journal* 524.2, pp. 1030–1047. DOI: 10.1086/307850 (cit. on pp. 127, 193).

Lamb, F. K. et al. (Aug. 1973). « A Model for Compact X-Ray Sources: Accretion by Rotating Magnetic Stars ». In: *The Astrophysical Journal* 184, pp. 271–290. DOI: 10.1086/152325 (cit. on p. 10).

Lasota, Jean-Pierre (June 2001). « The disc instability model of dwarf novae and low-mass X-ray binary transients ». In: *New Astronomy Reviews* 45.7, pp. 449–508. DOI: 10.1016/S1387-6473(01)00112-9 (cit. on p. 33).

Latter et al. (July 2010a). « Resistive double-diffusive instability in the dead zones of protostellar discs ». In: *Monthly Notices of the Royal Astronomical Society* 405.3, pp. 1831–1839. DOI: 10.1111/j.1365-2966.2010.16556.x (cit. on p. 152).

Latter, H. N. and J. C. B. Papaloizou (Oct. 2012). « Hysteresis and thermal limit cycles in MRI simulations of accretion discs ». In: *Monthly Notices of the Royal Astronomical Society* 426.2, pp. 1107–1120. DOI: 10.1111/j.1365-2966.2012.21748.x (cit. on pp. 45, 187).

Latter, Henrik N. et al. (Aug. 2010b). « MRI channel flows in vertically stratified models of accretion discs ». In: *Monthly Notices of the Royal Astronomical Society* 406.2, pp. 848–862. DOI: 10.1111/j.1365-2966.2010.16759.x (cit. on pp. 111, 152).

Lense, Josef and Hans Thirring (Jan. 1918). « Über den Einfluß der Eigenrotation der Zentralkörper auf die Bewegung der Planeten und Monde nach der Einsteinschen Gravitationstheorie ». In: *Physikalische Zeitschrift* 19, p. 156 (cit. on pp. 127, 193).

Lerman, Kristina et al. (Oct. 2022). « Gendered citation patterns among the scientific elite ». In: *Proceedings of the National Academy of Science* 119.40, e2206070119, e2206070119. DOI: 10.1073/pnas.2206070119 (cit. on p. 179).

Lesur, G. (Feb. 2021). « Magnetohydrodynamics of protoplanetary discs ». In: *Journal of Plasma Physics* 87.1, 205870101, p. 205870101. DOI: 10.1017/S0022377820001002 (cit. on pp. 32, 41, 43, 44, 186).

Lesur, G. et al. (Feb. 2013). « The magnetorotational instability as a jet launching mechanism ». In: *Astronomy & Astrophysics* 550, A61, A61. DOI: 10.1051/0004-6361/201220395 (cit. on p. 39).

Lesur, G. R. J. et al. (Sept. 2023). « IDEFIX: A versatile performance-portable Godunov code for astrophysical flows ». In: *Astronomy & Astrophysics* 677, A9, A9. DOI: 10.1051/0004-6361/202346005 (cit. on pp. 49, 106, 188).

Lesur, Geoffroy et al. (June 2014). « Thanatology in protoplanetary discs. The combined influence of Ohmic, Hall, and ambipolar diffusion on dead zones ». In: *Astronomy & Astrophysics* 566, A56, A56. DOI: 10.1051/0004-6361/201423660 (cit. on pp. 29, 133).

Lesur, Geoffroy et al. (Oct. 2015). « Spiral-driven accretion in protoplanetary discs. I. 2D models ». In: *Astronomy & Astrophysics* 582, L9, p. L9. DOI: 10.1051/0004-6361/201526734 (cit. on pp. 92, 94).

Levy, David H. (2005). *David Levy's Guide to Variable Stars* (cit. on p. 3).

Lidov, M. L. (Oct. 1962). « The evolution of orbits of artificial satellites of planets under the action of gravitational perturbations of external bodies ». In: *Planetary and Space Science* 9.10, pp. 719–759. DOI: 10.1016/0032-0633(62)90129-0 (cit. on p. 142).

Lightman, Alan P. and Douglas M. Eardley (Jan. 1974). « Black Holes in Binary Systems: Instability of Disk Accretion ». In: *The Astrophysical Journal Letters* 187, p. L1. DOI: 10.1086/181377 (cit. on p. 35).

Lin, D. N. C. and J. E. Pringle (Jan. 1976). « Numerical Simulation of Mass Transfer and Accretion Disc Flow in Binary Systems ». In: *Structure and Evolution of Close Binary Systems*. Ed. by Peter Eggleton et al. Vol. 73, p. 237 (cit. on p. 46).

Lindegren, L. et al. (Aug. 2018). « Gaia Data Release 2. The astrometric solution ». In: *Astronomy & Astrophysics* 616, A2, A2. DOI: 10.1051/0004-6361/201832727 (cit. on p. 39).

Liu, Tai-Ping (Jan. 1993). « Nonlinear stability and instability of overcompressive shock waves ». In: *Institute for Mathematics and Its Applications* 52, p. 159 (cit. on p. 52).

Lodato, Giuseppe and Daniel J. Price (June 2010). « On the diffusive propagation of warps in thin accretion discs ». In: *Monthly Notices of the Royal Astronomical Society* 405.2, pp. 1212–1226. DOI: 10.1111/j.1365-2966.2010.16526.x (cit. on p. 127).

Lodato, Giuseppe and J. E. Pringle (Nov. 2007). « Warp diffusion in accretion discs: a numerical investigation ». In: *Monthly Notices of the Royal Astronomical Society* 381.3, pp. 1287–1300. DOI: 10.1111/j.1365-2966.2007.12332.x (cit. on p. 127).

Londrillo, P. and L. del Zanna (Mar. 2004). « On the divergence-free condition in Godunov-type schemes for ideal magnetohydrodynamics: the upwind constrained transport method ». In: *Journal of Computational Physics* 195.1, pp. 17–48. DOI: 10.1016/j.jcp.2003.09.016 (cit. on p. 58).

Long, Knox S. and Christian Knigge (Nov. 2002). « Modeling the Spectral Signatures of Accretion Disk Winds: A New Monte Carlo Approach ». In: *The Astrophysical Journal* 579.2, pp. 725–740. DOI: 10.1086/342879 (cit. on pp. 151, 195).

Lovelace, R. V. E. et al. (Mar. 1999). « Rossby Wave Instability of Keplerian Accretion Disks ». In: *The Astrophysical Journal* 513.2, pp. 805–810. DOI: 10.1086/306900 (cit. on p. 93).

Lubow, Stephen H. (Nov. 1991a). « A Model for Tidally Driven Eccentric Instabilities in Fluid Disks ». In: *The Astrophysical Journal* 381, p. 259. DOI: 10.1086/170647 (cit. on pp. 46, 87).

Lubow, Stephen H. (Nov. 1991b). « Simulations of Tidally Driven Eccentric Instabilities with Application to Superhumps ». In: *The Astrophysical Journal* 381, p. 268. DOI: 10.1086/170648 (cit. on pp. 46, 86, 187, 190).

Lubow, Stephen H. (Oct. 1992). « Tidally Driven Inclination Instability in Keplerian Disks ». In: *The Astrophysical Journal* 398, p. 525. DOI: 10.1086/171877 (cit. on pp. 127, 193).

Lucy, L. B. (Dec. 1977). « A numerical approach to the testing of the fission hypothesis. » In: *The Astronomical Journal* 82, pp. 1013–1024. DOI: 10.1086/112164 (cit. on pp. 46, 187).

Lucy, L. B. and P. M. Solomon (Mar. 1970). « Mass Loss by Hot Stars ». In: *The Astrophysical Journal* 159, p. 879. DOI: 10.1086/150365 (cit. on p. 42).

Lynden-Bell, D. and J. E. Pringle (Sept. 1974). « The Evolution of Viscous Discs and the Origin of the Nebular Variables ». In: *Monthly Notices of the Royal Astronomical Society* 168.3, pp. 603–637. ISSN: 0035-8711. DOI: 10.1093/mnras/168.3.603 (cit. on pp. 21, 30, 186).

Marino, S. et al. (Jan. 2015). « Shadows Cast by a Warp in the HD 142527 Protoplanetary Disk ». In: *The Astrophysical Journal Letters* 798.2, L44, p. L44. DOI: 10.1088/2041-8205/798/2/L44 (cit. on pp. 127, 152).

Marsh, T. R. (2001). « Doppler Tomography ». In: *Astrotomography, Indirect Imaging Methods in Observational Astronomy*. Ed. by H. M. J. Boffin et al. Vol. 573, p. 1. DOI: 10.48550/arXiv.astro-ph/0011020 (cit. on pp. 17, 184).

Martin, Pierrick et al. (Apr. 2022). « The carbon footprint of IRAP ». In: *arXiv e-prints*, arXiv:2204.12362, arXiv:2204.12362. DOI: 10.48550/arXiv.2204.12362. arXiv: 2204.12362 [astro-ph.IM] (cit. on p. 182).

Masset, F. (Jan. 2000). « FARGO: A fast eulerian transport algorithm for differentially rotating disks ». In: *Astronomy & Astrophysics Supplement* 141, pp. 165–173. DOI: 10.1051/aas:2000116 (cit. on pp. 56, 57, 60, 188).

Mauche, Christopher W. and John C. Raymond (Dec. 1987). « IUE Observations of the Dwarf Nova HL Canis Majoris and the Winds of Cataclysmic Variables ». In: *The Astrophysical Journal* 323, p. 690. DOI: 10.1086/165865 (cit. on pp. 18, 185).

Maury, Antonia C. and Edward C. Pickering (Jan. 1897). « Spectra of bright stars photographed with the 11-inch Draper Telescope as part of the Henry Draper Memorial. » In: *Annals of Harvard College Observatory* 28, pp. 1–128 (cit. on pp. 18, 185).

Maxwell, J. C. (1861). « XXV. On physical lines of force ». In: *The London, Edinburgh, and Dublin Philosophical Magazine and Journal of Science* 21.139, pp. 161–175. DOI: 10.1080/14786446108643033 (cit. on p. 28).

McCrea, W. H. (May 1929). « Emissionslinien als Begleiter von Absorptionslinien in Sternspektren ». In: *Zeitschrift fur Physik* 57.5-6, pp. 367–379. DOI: 10.1007/BF01339623 (cit. on pp. 18, 175, 185).

McGowan, K. E. et al. (Feb. 2004). « On the Correlated X-Ray and Optical Evolution of SS Cygni ». In: *The Astrophysical Journal* 601.2, pp. 1100–1108. DOI: 10.1086/380758 (cit. on pp. 19, 21, 185).

McNally, Colin P. et al. (Mar. 2019). « Migrating super-Earths in low-viscosity discs: unveiling the roles of feedback, vortices, and laminar accretion flows ». In: *Monthly Notices of the Royal Astronomical Society* 484.1, pp. 728–748. DOI: 10.1093/mnras/stz023 (cit. on p. 60).

Meheut, Heloise et al. (July 2015). « Angular momentum transport and large eddy simulations in magnetorotational turbulence: the small Pm limit ». In: *Astronomy & Astrophysics* 579, A117, A117. DOI: 10.1051/0004-6361/201525688 (cit. on pp. 45, 187).

Mestel, L. and H. C. Spruit (May 1987). « On magnetic braking of late-type stars ». In: *Monthly Notices of the Royal Astronomical Society* 226, pp. 57–66. DOI: 10.1093/mnras/226.1.57 (cit. on pp. 8, 184).

Meyer, F. and E. Meyer-Hofmeister (Jan. 1981). « On the elusive cause of cataclysmic variable outbursts. » In: *Astronomy & Astrophysics* 104, pp. L10–L12 (cit. on pp. 33, 186).

Mignone, A. and L. Del Zanna (Jan. 2021). « Systematic construction of upwind constrained transport schemes for MHD ». In: *Journal of Computational Physics* 424, 109748, p. 109748. DOI: 10.1016/j.jcp.2020.109748 (cit. on p. 58).

Mignone, A. et al. (May 2007). « PLUTO: A Numerical Code for Computational Astrophysics ». In: *The Astrophysical Journal Supplement* 170.1, pp. 228–242. DOI: 10.1086/513316 (cit. on p. 56).

Mignone, A. et al. (Sept. 2012a). « A conservative orbital advection scheme for simulations of magnetized shear flows with the PLUTO code ». In: *Astronomy & Astrophysics* 545, A152, A152. DOI: 10.1051/0004-6361/201219557 (cit. on p. 56).

Mignone, A. et al. (Jan. 2012b). « The PLUTO Code for Adaptive Mesh Computations in Astrophysical Fluid Dynamics ». In: *The Astrophysical Journal Supplement* 198.1, 7, p. 7. DOI: 10.1088/0067-0049/198/1/7 (cit. on p. 56).

Mineshige, S. and Y. Osaki (Jan. 1983). « Disk-instability model for outbursts of dwarf novae Time-dependent formulation and one-zone model ». In: *Publications of the Astronomical Society of Japan* 35.3, pp. 377–396 (cit. on pp. 33, 186).

Miyoshi, Makoto et al. (Jan. 1995). « Evidence for a black hole from high rotation velocities in a sub-parsec region of NGC4258 ». In: *Nature* 373.6510, pp. 127–129. DOI: 10.1038/373127a0 (cit. on p. 126).

Miyoshi, Takahiro and Kanya Kusano (Sept. 2005). « A multi-state HLL approximate Riemann solver for ideal magnetohydrodynamics ». In: *Journal of Computational Physics* 208.1, pp. 315–344. DOI: 10.1016/j.jcp.2005.02.017 (cit. on pp. 54, 59, 106, 188).

MPI Forum (June 2021). *MPI: A Message-Passing Interface Standard Version 4.0*. URL: https://www.mpi-forum.org/docs/mpi-4.0/mpi40-report.pdf (cit. on pp. 56, 175).

Murray, J. R. (June 1998). « Simulations of superhumps and superoutbursts ». In: *Monthly Notices of the Royal Astronomical Society* 297.1, pp. 323–333. DOI: 10.1046/j.1365-8711.1998.01504.x (cit. on p. 46).

Murray, James R. et al. (Sept. 2002). « Magnetically warped discs in close binaries ». In: *Monthly Notices of the Royal Astronomical Society* 335.2, pp. 247–255. DOI: 10.1046/j.1365-8711.2002.05628.x (cit. on pp. 127, 193).

Nelson, Richard P. and John C. B. Papaloizou (Nov. 1999). « Hydrodynamic simulations of propagating WARPS and bending waves in accretion discs ». In: *Monthly Notices*

of the Royal Astronomical Society 309.4, pp. 929–940. DOI: 10.1046/j.1365-8711.1999.02894.x (cit. on p. 127).

Neustroev, V. V. et al. (July 2004). « Searching evidences for spiral shocks in the quiescent accretion disk of U Gem ». In: *Revista Mexicana de Astronomia y Astrofisica Conference Series*. Ed. by G. Tovmassian and E. Sion. Vol. 20. Revista Mexicana de Astronomia y Astrofisica Conference Series, pp. 162–163. DOI: 10.48550/arXiv.astro-ph/0402050. arXiv: astro-ph/0402050 [astro-ph] (cit. on p. 18).

Neustroev, V. V. et al. (Jan. 2011). « Dark spot, spiral waves and the SW Sextantis behaviour: it is all about UX Ursae Majoris ». In: *Monthly Notices of the Royal Astronomical Society* 410.2, pp. 963–977. DOI: 10.1111/j.1365-2966.2010.17495.x (cit. on pp. 17, 185).

Nixon, C. J. et al. (Jan. 2024). « On the role of numerical diffusivity in MHD simulations of global accretion disc dynamos ». In: *Journal of Plasma Physics* 90.1, 905900101, p. 905900101. DOI: 10.1017/S002237782300140X (cit. on p. 60).

Ogilvie, G. I. (Apr. 1999). « The non-linear fluid dynamics of a warped accretion disc ». In: *Monthly Notices of the Royal Astronomical Society* 304.3, pp. 557–578. DOI: 10.1046/j.1365-8711.1999.02340.x (cit. on p. 127).

Ogilvie, Gordon I. and Henrik N. Latter (Aug. 2013a). « Hydrodynamic instability in warped astrophysical discs ». In: *Monthly Notices of the Royal Astronomical Society* 433.3, pp. 2420–2435. DOI: 10.1093/mnras/stt917 (cit. on pp. 127, 193, 195).

Ogilvie, Gordon I. and Henrik N. Latter (Aug. 2013b). « Local and global dynamics of warped astrophysical discs ». In: *Monthly Notices of the Royal Astronomical Society* 433.3, pp. 2403–2419. DOI: 10.1093/mnras/stt916 (cit. on pp. 127, 152, 193, 195).

Osaki, Y. (Jan. 1974). « An Accretion Model for the Outbursts of U Geminorum Stars ». In: *Publications of the Astronomical Society of Japan* 26, p. 429 (cit. on pp. 8, 10, 11, 184).

Osaki, Y. (Mar. 1985). « Irradiation-induced mass-overflow instability as a possible cause of superoutbursts in SU UMa stars. » In: *Astronomy & Astrophysics* 144, pp. 369–380 (cit. on pp. 46, 187).

Osaki, Yoji (Nov. 1970). « A Mechanism for the Outbursts of U Geminorum Stars ». In: *The Astrophysical Journal* 162, p. 621. DOI: 10.1086/150694 (cit. on pp. 8, 10).

Osaki, Yoji and Taichi Kato (Oct. 2013). « Study of Superoutbursts and Superhumps in SU UMa Stars by the Kepler Light Curves of V344 Lyrae and V1504 Cygni ». In: *Publications of the Astronomical Society of Japan* 65, 95, p. 95. DOI: 10.1093/pasj/65.5.95 (cit. on p. 7).

Oyang, Bryance et al. (July 2021). « Investigating lack of accretion disc eccentricity growth in a global 3D MHD simulation of a superhump system ». In: *Monthly Notices of the Royal Astronomical Society* 505.1, pp. 1–17. DOI: 10.1093/mnras/stab1212 (cit. on pp. 86, 190).

Paczyński, B. (Jan. 1965). « Cataclysmic Variables among Binary Stars I. U Geminorum Stars ». In: *Acta Astronomica* 15, p. 89 (cit. on p. 8).

Paczyński, B. (Sept. 1977). « A model of accretion disks in close binaries ». In: *The Astrophysical Journal* 216, pp. 822–826. ISSN: 0004-637X. DOI: 10.1086/155526 (cit. on pp. 46, 68, 77, 107).

Pandel, Dirk et al. (June 2005). « X-Ray Observations of the Boundary Layer in Dwarf Novae at Low Accretion Rates ». In: *The Astrophysical Journal* 626.1, pp. 396–410. DOI: 10.1086/429983 (cit. on pp. 21, 185).

Papaloizou, J. and D. N. C. Lin (Oct. 1984). « On the tidal interaction between protoplanets and the primordial solar nebula. I - Linear calculation of the role of angular momentum exchange ». In: *The Astrophysical Journal* 285, pp. 818–834. DOI: 10.1086/162561 (cit. on p. 46).

Papaloizou, J. C. B. and D. N. C. Lin (Jan. 1995). « On the Dynamics of Warped Accretion Disks ». In: *The Astrophysical Journal* 438, p. 841. DOI: 10.1086/175127 (cit. on pp. 121, 127).

Papaloizou, J. C. B. and J. E. Pringle (Mar. 1983). « The time-dependence of non-planar accretion discs ». In: *Monthly Notices of the Royal Astronomical Society* 202, pp. 1181–1194. DOI: 10.1093/mnras/202.4.1181 (cit. on p. 127).

Papaloizou, John C. B. and Caroline Terquem (June 1995). « On the dynamics of tilted discs around young stars ». In: *Monthly Notices of the Royal Astronomical Society* 274.4, pp. 987–1001. DOI: 10.1093/mnras/274.4.987 (cit. on p. 127).

Paris, J. B. and G. I. Ogilvie (June 2018). « A local model of warped magnetized accretion discs ». In: *Monthly Notices of the Royal Astronomical Society* 477.2, pp. 2406–2418. DOI: 10.1093/mnras/sty596 (cit. on pp. 127, 152, 193, 195).

Parker, E. N. (Nov. 1958). « Dynamics of the Interplanetary Gas and Magnetic Fields. » In: *The Astrophysical Journal* 128, p. 664. DOI: 10.1086/146579 (cit. on p. 41).

Patterson, J. (Mar. 1981). « Rapid oscillations in cataclysmic variables. VI. Periodicities in erupting dwarf novae. » In: *The Astrophysical Journal Supplement* 45, pp. 517–539. DOI: 10.1086/190723 (cit. on pp. 13, 184).

Patterson, J. and J. C. Raymond (May 1985a). « X-ray emission from cataclysmic variables with accretion disks. I. Hard X-rays. » In: *The Astrophysical Journal* 292, pp. 535–549. DOI: 10.1086/163187 (cit. on pp. 20, 21, 185).

Patterson, J. and J. C. Raymond (May 1985b). « X-ray emission from cataclysmic variables with accretion disks. II. EUV/soft X-ray radiation. » In: *The Astrophysical Journal* 292, pp. 550–558. DOI: 10.1086/163188 (cit. on pp. 21, 185).

Pearson, K. J. et al. (June 1997). « The effect of the magnetic field of the secondary star in dwarf novae ». In: *Monthly Notices of the Royal Astronomical Society* 288.2, pp. 421–430. DOI: 10.1093/mnras/288.2.421 (cit. on pp. 24, 30).

Perna, Rosalba et al. (Nov. 2003). « Chandra Observations of the Dwarf Nova WX Hydri in Quiescence ». In: *The Astrophysical Journal* 598.1, pp. 545–552. DOI: 10.1086/378855 (cit. on pp. 18, 185).

Pjanka, Patryk and James M. Stone (Dec. 2020). « Stratified Global MHD Models of Accretion Disks in Semidetached Binaries ». In: *The Astrophysical Journal* 904.2, 90, p. 90. DOI: 10.3847/1538-4357/abbe07 (cit. on pp. 47, 75, 106, 128, 151, 152, 187, 195).

Pringle, J. E. (July 1996). « Self-induced warping of accretion discs ». In: *Monthly Notices of the Royal Astronomical Society* 281.1, pp. 357–361. DOI: 10.1093/mnras/281.1.357 (cit. on p. 127).

Pringle, J. E. and M. J. Rees (Oct. 1972). « Accretion Disc Models for Compact X-Ray Sources ». In: *Astronomy & Astrophysics* 21, p. 1 (cit. on p. 10).

Rankine, William John Macquorn (1870). « XV. On the thermodynamic theory of waves of finite longitudinal disturbance ». In: *Philosophical Transactions of the Royal Society of London* 160, pp. 277–288. DOI: 10.1098/rstl.1870.0015 (cit. on p. 54).

Riemann, Bernhard (1860). « Ueber die Fortpflanzung ebener Luftwellen von endlicher Schwingungsweite ». In: *Abhandlungen der Königlichen Gesellschaft der Wissenschaften zu Göttingen*. URL: https://www.maths.tcd.ie/pub/HistMath/People/Riemann/Welle/Welle.pdf (cit. on pp. 50, 188).

Riols, A. and G. Lesur (May 2019). « Spontaneous ring formation in wind-emitting accretion discs ». In: *Astronomy & Astrophysics* 625, A108, A108. DOI: 10.1051/0004-6361/201834813. arXiv: 1904.07910 [astro-ph.EP] (cit. on p. 108).

Ritter, H. (Sept. 2008). « Formation and Evolution of Cataclysmic Variables ». In: *arXiv e-prints*, arXiv:0809.1800, arXiv:0809.1800. DOI: 10.48550/arXiv.0809.1800. arXiv: 0809.1800 [astro-ph] (cit. on pp. 6, 8, 184).

Roe, P. L. (Jan. 1986). « Characteristic-based schemes for the euler equations ». In: *Annual Review of Fluid Mechanics* 18, pp. 337–365. DOI: 10.1146/annurev.fl.18.010186.002005 (cit. on p. 55).

Rohlf, James William (1994). *Modern Physics from aα to Zo* (cit. on p. 25).

Rosenfeld et al. (Oct. 2012). « Kinematics of the CO Gas in the Inner Regions of the TW Hya Disk ». In: *The Astrophysical Journal* 757.2, 129, p. 129. DOI: 10.1088/0004-637X/757/2/129 (cit. on p. 152).

Ross, Clara et al. (2020). *The Leaky Pipeline in Physics Publishing*. arXiv: 2010.08912 [physics.soc-ph]. URL: https://arxiv.org/abs/2010.08912 (cit. on p. 177).

Ruiz-Carmona, R. et al. (Jan. 2020). « A systematic study of spiral density waves in the accretion discs of cataclysmic variables ». In: *Monthly Notices of the Royal Astronomical Society* 491.2, pp. 2217–2253. DOI: 10.1093/mnras/stz2992 (cit. on pp. 18, 99, 185).

Runge, C. (June 1895). « Ueber die numerische Auflösung von Differentialgleichungen ». In: *Mathematische Annalen* 46.2, pp. 167–178. ISSN: 1432-1807. DOI: 10.1007/BF01446807. URL: https://doi.org/10.1007/BF01446807 (cit. on p. 50).

Russell, T. D. et al. (Aug. 2016). « The reproducible radio outbursts of SS Cygni ». In: *Monthly Notices of the Royal Astronomical Society* 460.4, pp. 3720–3732. DOI: 10.1093/mnras/stw1238 (cit. on pp. 19, 185).

Rutten, R. G. M. et al. (Nov. 1992a). « OY Carinae revisited: development of the accretion disk during a normal outburst. » In: *Astronomy & Astrophysics* 265, pp. 159–167 (cit. on pp. 13, 184).

Rutten, R. G. M. et al. (July 1992b). « Reconstruction of the accretion disk in six cataclysmic variable stars. » In: *Astronomy & Astrophysics* 260, pp. 213–226 (cit. on pp. 13, 184).

Ryan, Benjamin R. et al. (May 2017). « Resolution Dependence of Magnetorotational Turbulence in the Isothermal Stratified Shearing Box ». In: *The Astrophysical Journal* 840.1, 6, p. 6. DOI: 10.3847/1538-4357/aa6a52 (cit. on pp. 45, 187).

Saha, Megh Nad (1920). « LIII. Ionization in the solar chromosphere ». In: *The London, Edinburgh, and Dublin Philosophical Magazine and Journal of Science* 40.238, pp. 472–488. DOI: 10.1080/14786441008636148 (cit. on pp. 29, 59).

Salvesen, Greg et al. (Mar. 2016). « Accretion disc dynamo activity in local simulations spanning weak-to-strong net vertical magnetic flux regimes ». In: *Monthly Notices of the Royal Astronomical Society* 457.1, pp. 857–874. DOI: 10.1093/mnras/stw029 (cit. on p. 39).

Sano, Takayoshi and James M. Stone (Sept. 2002). « The Effect of the Hall Term on the Nonlinear Evolution of the Magnetorotational Instability. II. Saturation Level and Critical Magnetic Reynolds Number ». In: *The Astrophysical Journal* 577.1, pp. 534–553. DOI: 10.1086/342172 (cit. on p. 30).

Savonije, G. J. and J. C. B. Papaloizou (May 1983). « On the tidal spin up and orbital circularization rate for the massiveX-ray binary systems. » In: *Monthly Notices of the Royal Astronomical Society* 203, pp. 581–593. DOI: 10.1093/mnras/203.3.581 (cit. on pp. 18, 70, 72, 185, 189).

Savonije, G. J. et al. (May 1994). « On Tidally Induced Shocks in Accretion Discs in Close Binary Systems ». In: *Monthly Notices of the Royal Astronomical Society* 268, p. 13. DOI: 10.1093/mnras/268.1.13 (cit. on pp. 18, 47, 70, 185, 187, 189).

Sawada, K. et al. (Aug. 1986a). « Accretion shocks in a close binary system ». In: *Monthly Notices of the Royal Astronomical Society* 221, pp. 679–686. DOI: 10.1093/mnras/221.3.679 (cit. on p. 47).

Sawada, K. et al. (Mar. 1986b). « Spiral shocks on a Roche lobe overflow in a semi-detached binary system. » In: *Monthly Notices of the Royal Astronomical Society* 219, pp. 75–88. DOI: 10.1093/mnras/219.1.75 (cit. on p. 47).

Scepi, N. et al. (Jan. 2018a). « Impact of convection and resistivity on angular momentum transport in dwarf novae ». In: *Astronomy & Astrophysics* 609, A77, A77. DOI: 10.1051/0004-6361/201731900 (cit. on pp. 19, 29, 30, 45, 61, 150, 187, 188).

Scepi, N. et al. (Dec. 2018b). « Turbulent and wind-driven accretion in dwarf novae threaded by a large-scale magnetic field ». In: *Astronomy & Astrophysics* 620, A49, A49. DOI: 10.1051/0004-6361/201833921 (cit. on pp. 39, 45, 48, 150, 185, 187).

Scepi, Nicolas (June 2019). « Accrétion dans les disques de novae naines ». Theses. Université Grenoble Alpes. URL: https://theses.hal.science/tel-02444294 (cit. on pp. 36, 59, 96).

Scepi, Nicolas et al. (June 2019). « Magnetic wind-driven accretion in dwarf novae ». In: *Astronomy & Astrophysics* 626, A116, A116. DOI: 10.1051/0004-6361/201834781 (cit. on pp. 19, 39, 48, 185, 186).

Schandl, S. and F. Meyer (Sept. 1994). « Herculis X-1: coronal winds producing the tilted shape of the accretion disk. » In: *Astronomy & Astrophysics* 289, pp. 149–161 (cit. on p. 127).

Shafter, A. W. and K. A. Misselt (June 2006). « Modeling Eclipses in the Classical Nova V Persei: The Role of the Accretion Disk Rim ». In: *The Astrophysical Journal* 644.2, pp. 1104–1117. DOI: 10.1086/503764 (cit. on pp. 13, 184).

Shakura, N. I. and R. A. Sunyaev (Jan. 1973). « Black holes in binary systems. Observational appearance. » In: *Astronomy & Astrophysics* 24, pp. 337–355 (cit. on pp. 10, 15, 30, 32, 82, 90, 186).

Sheikhnezami, Somayeh and Christian Fendt (Dec. 2015). « Wobbling and Precessing Jets from Warped Disks in Binary Systems ». In: *The Astrophysical Journal* 814.2, 113, p. 113. DOI: 10.1088/0004-637X/814/2/113 (cit. on p. 128).

Sheltzer, Jason M. and Joan C. Smith (2014). « Elite male faculty in the life sciences employ fewer women ». In: *Proceedings of the National Academy of Sciences* 111.28, pp. 10107–10112. DOI: 10.1073/pnas.1403334111. eprint: https://www.pnas.org/doi/pdf/10.1073/pnas.1403334111. URL: https://www.pnas.org/doi/abs/10.1073/pnas.1403334111 (cit. on p. 177).

Shi, Ji-Ming et al. (Mar. 2016). « Saturation of the magnetorotational instability in the unstratified shearing box with zero net flux: convergence in taller boxes ». In: *Monthly Notices of the Royal Astronomical Society* 456.3, pp. 2273–2289. DOI: 10.1093/mnras/stv2815 (cit. on pp. 45, 187).

Smak, J. (Jan. 1969). « On the Period of SS Cygni ». In: *Acta Astronomica* 19, p. 287 (cit. on p. 8).

Smak, J. (Jan. 1971). « Eruptive Binaries. II. U Geminorum ». In: *Acta Astronomica* 21, p. 15 (cit. on pp. 8, 184).

Smak, J. (Jan. 1982). « Accretion in cataclysmic binaries. I - Modified alpha-disks with convection ». In: *Acta Astronomica* 32.3-4, pp. 199–211 (cit. on pp. 33, 186).

Smak, J. (Jan. 1984). « Eruptive binaries. XI. Disk-radius variations un U Gem. » In: *Acta Astronomica* 34, pp. 93–96 (cit. on pp. 13, 184).

Smak, J. (Sept. 1999). « Dwarf Nova Outbursts. III. The Viscosity Parameter alpha ». In: *Acta Astronomica* 49, pp. 391–401 (cit. on pp. 38, 186).

Smith, Amanda J. et al. (July 2007). « Comprehensive simulations of superhumps ». In: *Monthly Notices of the Royal Astronomical Society* 378.3, pp. 785–800. DOI: 10.1111/j.1365-2966.2007.11840.x (cit. on p. 46).

Spitzer, L. (1956). *Physics of Fully Ionized Gases* (cit. on p. 25).

Spruit, H. C. (Oct. 1987). « Stationary shocks in accretion disks ». In: *Astronomy & Astrophysics* 184.1-2, pp. 173–184 (cit. on p. 47).

Stapelfeldt, Karl R. et al. (July 1998). « An Edge-On Circumstellar Disk in the Young Binary System HK Tauri ». In: *The Astrophysical Journal Letters* 502.1, pp. L65–L69. DOI: 10.1086/311479 (cit. on p. 127).

Steeghs, D. et al. (Sept. 1997). « Spiral structure in the accretion disc of the binary IP Pegasi ». In: *Monthly Notices of the Royal Astronomical Society* 290.2, pp. L28–L32. DOI: 10.1093/mnras/290.2.L28 (cit. on pp. 17, 185).

Suriano, Scott S. et al. (June 2018). « The formation of rings and gaps in magnetically coupled disc-wind systems: ambipolar diffusion and reconnection ». In: *Monthly Notices of the Royal Astronomical Society* 477.1, pp. 1239–1257. DOI: 10.1093/mnras/sty717 (cit. on p. 133).

Suzuki, Takeru K. (Nov. 2023). « MHD in a Cylindrical Shearing Box. II. Intermittent Bursts and Substructures in MRI Turbulence ». In: *The Astrophysical Journal* 957.2, 99, p. 99. DOI: 10.3847/1538-4357/acfb88 (cit. on p. 46).

Teich, Erin G. et al. (Oct. 2022). « Citation inequity and gendered citation practices in contemporary physics ». In: *Nature Physics* 18.10, pp. 1161–1170. DOI: 10.1038/s41567-022-01770-1. arXiv: 2112.09047 [physics.soc-ph] (cit. on p. 179).

Terquem, C. E. J. M. L. J. (Jan. 2002). « Theory of Turbulent Accretion Disks ». In: *EAS Publications Series*. Ed. by Jerome Bouvier and Jean-Paul Zahn. Vol. 3. EAS Publications Series, pp. 203–228. DOI: 10.1051/eas:2002051 (cit. on p. 26).

Tetarenko, Bailey et al. (July 2018). « Strong disc winds traced throughout outbursts in black-hole X-ray binaries ». In: *42nd COSPAR Scientific Assembly*. Vol. 42, E1.4-62-18, E1.4-62–18 (cit. on p. 39).

Thomas, David M. and Matt A. Wood (Apr. 2015). « The Emergence of Negative Superhumps in Cataclysmic Variables: Smoothed Particle Hydrodynamics Simulations ». In: *The Astrophysical Journal* 803.2, 55, p. 55. DOI: 10.1088/0004-637X/803/2/55 (cit. on p. 145).

Toomre, A. (May 1964). « On the gravitational stability of a disk of stars. » In: *The Astrophysical Journal* 139, pp. 1217–1238. DOI: 10.1086/147861 (cit. on p. 27).

Toro, E. F. (1999). *Riemann Solvers and Numerical Methods for Fluid Dynamics*. Springer-Verlag (cit. on pp. 52, 55).

Toro, E. F. et al. (July 1994). « Restoration of the contact surface in the HLL-Riemann solver ». In: *Shock Waves* 4.1, pp. 25–34. DOI: 10.1007/BF01414629 (cit. on pp. 54, 188).

Turner, H. H. (Dec. 1906). « U Geminorum, Pogson's observations of, edited ». In: *Monthly Notices of the Royal Astronomical Society* 67, p. 119. DOI: 10.1093/mnras/67.2.119 (cit. on p. 6).

Van den Bossche, M. et al. (Sept. 2023). « Spiral-wave-driven accretion in quiescent dwarf novæ ». In: *Astronomy & Astrophysics* 677, A10, A10. DOI: 10.1051/0004-6361/202346090 (cit. on pp. 67, 88, 91, 92, 150, 151).

van Leer, B. (July 1979). « Towards the Ultimate Conservative Difference Scheme. V. A Second-Order Sequel to Godunov's Method ». In: *Journal of Computational Physics* 32.1, pp. 101–136. DOI: 10.1016/0021-9991(79)90145-1 (cit. on p. 54).

van Leer, Bram (Mar. 1974). « Towards the Ultimate Conservation Difference Scheme. II. Monotonicity and Conservation Combined in a Second-Order Scheme ». In: *Journal of Computational Physics* 14.4, pp. 361–370. DOI: 10.1016/0021-9991(74)90019-9 (cit. on p. 55).

van Paradijs, J. (June 1996). « On the Accretion Instability in Soft X-Ray Transients ». In: *The Astrophysical Journal Letters* 464, p. L139. DOI: 10.1086/310100 (cit. on p. 33).

van Paradijs, Jan and Frank Verbunt (May 1984). « A comparison of soft x-ray transients and dwarf novae ». In: *High Energy Transients in AstroPhysics*. Ed. by S. E. Woosley. Vol. 115. American Institute of Physics Conference Series, pp. 49–62. DOI: 10.1063/1.34556 (cit. on p. 33).

Velikhov, Evgeny Pavlovich (Nov. 1959). « Stability of an Ideally Conducting Liquid Flowing between Cylinders Rotating in a Magnetic Field ». In: *Soviet Journal of Experimental and Theoretical Physics* 9.5, pp. 995–998 (cit. on p. 39).

Verbunt, F. (Dec. 1982). « Accretion Disks in Stellar X-Ray Sources ». In: *Space Science Reviews* 32.4, pp. 379–404. DOI: 10.1007/BF00177448 (cit. on p. 9).

Verbunt, F. and C. Zwaan (July 1981). « Magnetic braking in low-mass X-ray binaries. » In: *Astronomy & Astrophysics* 100, pp. L7–L9 (cit. on pp. 8, 184).

Vogt, N. (Dec. 1974). « Photometric study of the dwarf nova VW Hydri. » In: *Astronomy & Astrophysics* 36, pp. 369–378 (cit. on p. 6).

Vogt, N. (Jan. 1982). « Z Chamaeleontis : evidence for an eccentric disk during supermaximum ? » In: *The Astrophysical Journal* 252, pp. 653–667. DOI: 10.1086/159592 (cit. on pp. 46, 187).

Vrielmann, Sonja and Warren Offutt (Jan. 2003). « The disc evolution of V2051 Oph on decline from superoutburst ». In: *Monthly Notices of the Royal Astronomical Society* 338.1, pp. 165–175. DOI: 10.1046/j.1365-8711.2003.06030.x (cit. on pp. 13, 184).

Vrielmann, Sonja et al. (Aug. 2002). « Physical parameter eclipse mapping of the quiescent disc in V2051 Ophiuchi ». In: *Monthly Notices of the Royal Astronomical Society* 334.3, pp. 608–620. DOI: 10.1046/j.1365-8711.2002.05544.x (cit. on pp. 13, 184).

Walker, Merle F. (Oct. 1954). « Nova DQ Herculis (1934): an Eclipsing Binary with Very Short Period ». In: *Publications of the Astronomical Society of the Pacific* 66.392, p. 230. DOI: 10.1086/126703 (cit. on pp. 6, 184).

Walker, Merle F. (Jan. 1956). « A Photometric Investigation of the Short-Period Eclipsing Binary, Nova DQ Herculis (1934). » In: *The Astrophysical Journal* 123, p. 68. DOI: 10.1086/146132 (cit. on pp. 6, 184).

Warner, B. and R. E. Nather (Jan. 1971). « Observations of rapid blue variables - II. U Geminorum. » In: *Monthly Notices of the Royal Astronomical Society* 152, p. 219. DOI: 10.1093/mnras/152.2.219 (cit. on pp. 8, 184).

Warner, Brian (2003). *Cataclysmic Variable Stars*. DOI: 10.1017/CBO9780511586491 (cit. on pp. 4, 6, 183).

Way, Samuel F. et al. (2016). « Gender, Productivity, and Prestige in Computer Science Faculty Hiring Networks ». In: *Proceedings of the 25th International Conference on World Wide Web*. WWW '16. Montréal, Québec, Canada: International World Wide Web Conferences Steering Committee, pp. 1169–1179. ISBN: 9781450341431. DOI: 10.1145/2872427.2883073. URL: https://doi.org/10.1145/2872427.2883073 (cit. on p. 177).

Webb, Natalie A. (Mar. 2023). « Accreting white dwarfs ». In: *arXiv e-prints*, arXiv:2303.10055, arXiv:2303.10055. DOI: 10.48550/arXiv.2303.10055 (cit. on pp. 19, 185).

Weizsäcker, Carl Friedrich von (1948). « Die Rotation kosmischer Gasmassen ». In: *Zeitschrift für Naturforschung A* 3.8-11, pp. 524–539. URL: https://www.degruyter.com/view/journals/zna/3/8-11/article-p524.xml (cit. on pp. 30, 186).

Wells, Louisa D. (Jan. 1896). « South Pole Reductions ». In: *Project PHAEDRA: Preserving Harvard's Early Data and Research in Astronomy (https://library.cfa.harvard.edu/project-phaedra). Harvard College Observatory observations*, p. 1670 (cit. on pp. 6, 183).

Wheatley, P. J. and C. W. Mauche (Aug. 2005). « Chandra X-ray Observations of WZ Sge in Superoutburst ». In: *The Astrophysics of Cataclysmic Variables and Related Objects*. Ed. by J. -M. Hameury and J. -P. Lasota. Vol. 330. Astronomical Society of the Pacific Conference Series, p. 257. DOI: 10.48550/arXiv.astro-ph/0412166 (cit. on pp. 21, 185).

Wheatley, P. J. et al. (Mar. 1996). « The X-ray and EUV spectrum of the dwarf nova VW Hydri in outburst and quiescence. » In: *Astronomy & Astrophysics* 307, p. 137 (cit. on pp. 21, 185).

Wheatley, Peter J. et al. (Oct. 2003). « The X-ray and extreme-ultraviolet flux evolution of SS Cygni throughout outburst ». In: *Monthly Notices of the Royal Astronomical Society* 345.1, pp. 49–61. DOI: 10.1046/j.1365-8711.2003.06936.x (cit. on pp. 20, 21, 185).

Whitehurst, Robert (May 1988a). « Numerical simulations of accretion discs - I. Superhumps : a tidal phenomenon of accretion discs. » In: *Monthly Notices of the Royal Astronomical Society* 232, pp. 35–51. DOI: 10.1093/mnras/232.1.35 (cit. on pp. 46, 187).

Whitehurst, Robert (Aug. 1988b). « Numerical simulations of accretion discs. II. Design and implaementation of a new numerical method. » In: *Monthly Notices of the Royal Astronomical Society* 233, pp. 529–551. DOI: 10.1093/mnras/233.3.529 (cit. on pp. 46, 187).

Wilbraham, H. (1848). « On a certain periodic function ». In: *Cambridge Dublin Math. J.* 3, pp. 198–201 (cit. on p. 55).

Williams, R. E. and D. H. Ferguson (June 1982). « He I line emission and the helium abundance in cataclysmic variables ». In: *The Astrophysical Journal* 257, pp. 672–685. DOI: 10.1086/160022 (cit. on p. 12).

Wood, J. et al. (Apr. 1986). « High-speed photometry of the dwarf nova Z Cha in quiescence. » In: *Monthly Notices of the Royal Astronomical Society* 219, pp. 629–655. DOI: 10.1093/mnras/219.3.629 (cit. on pp. 12, 13).

Wood, J. H. et al. (Aug. 1989a). « The ephemeris and variations of the accretion disc radius in IP Pegasi. » In: *Monthly Notices of the Royal Astronomical Society* 239, pp. 809–824. DOI: 10.1093/mnras/239.3.809 (cit. on pp. 13, 184).

Wood, Janet H. et al. (June 1989b). « Eclipse Studies of the Dwarf Nova OY Carinae in Quiescence ». In: *The Astrophysical Journal* 341, p. 974. DOI: 10.1086/167557 (cit. on pp. 13, 184).

Wood, Matt A. and Christopher J. Burke (June 2007). « The Physical Origin of Negative Superhumps in Cataclysmic Variables ». In: *The Astrophysical Journal* 661.2, pp. 1042–1047. DOI: 10.1086/516723 (cit. on p. 145).

Yamaguchi, Natsuko et al. (Sept. 2023). « Sodium enhancement in evolved cataclysmic variables ». In: *Monthly Notices of the Royal Astronomical Society* 524.1, pp. 740–758. DOI: 10.1093/mnras/stad1878 (cit. on p. 12).

Zanni, C. et al. (July 2007). « MHD simulations of jet acceleration from Keplerian accretion disks. The effects of disk resistivity ». In: *Astronomy & Astrophysics* 469.3, pp. 811–828. DOI: 10.1051/0004-6361:20066400 (cit. on p. 108).

Zhu, Zhaohuan and James M. Stone (Apr. 2018). « Global Evolution of an Accretion Disk with a Net Vertical Field: Coronal Accretion, Flux Transport, and Disk Winds ». In: *The Astrophysical Journal* 857.1, 34, p. 34. DOI: 10.3847/1538-4357/aaafc9 (cit. on p. 106).

Zorotovic, M. et al. (Dec. 2011). « Post common envelope binaries from SDSS. XI. The white dwarf mass distributions of CVs and pre-CVs ». In: *Astronomy & Astrophysics* 536, A42, A42. DOI: 10.1051/0004-6361/201116626 (cit. on p. 24).

Zorotovic, Monica and Matthias R. Schreiber (Sept. 2020). « Cataclysmic variable evolution and the white dwarf mass problem: A Review ». In: *Advances in Space Research* 66.5, pp. 1080–1089. DOI: 10.1016/j.asr.2019.08.044 (cit. on pp. 6, 184).

Zuckermann, Marie-Claire (Feb. 1961). « Observations et interprétation de l'étoile variable SS Cygn ». In: *Annales d'Astrophysique* 24, p. 431 (cit. on pp. 8, 175).

A

STATISTIC ON THE BIBLIOGRAPHY

This PhD thesis cites 311 articles (not including references of the appendixes), all listed in the bibliography. The statistics of a sample of this size can hint at general trends of the domain. In this appendix, I present and discuss some of the statistics I was able to draw from this article pool.

FIRST AUTHOR. Here, I focus on properties of the first author of each paper only. I do so for two main reasons. The first reason is that a paper is often associated, and even assimilated to the first author's name & publication year pair. As a matter of fact, in most of the articles I cited throughout this thesis, and in this thesis the citation format is this one, *e.g.* (Zuckermann, 1961). This means that, in most cases, the results presented in the paper will be associated with this author, while the following ones may be often forgotten, or less strongly mentally associated with the results. This effect is even stronger when the authors are unknown to the reader. The second reason is that other authors are strongly correlated to the first author and would not increase the sample size of 'independent' items.

PUBLICATION YEAR. Figure A.1 shows the time distribution of the articles of the bibliography. Most articles (286 articles, or 92%) I cite are published in 1950 or more recently. 25% of the citations date from before 1980. The median citation year is 1998, and the third quartile of the distribution is 2012.

AFFILIATION COUNTRY. A second easily accessible piece of data of the bibliography is the affiliation country of the first author. Here, I only look at the first affiliation of the first author in case of multiple affiliation. Note that the affiliation of the author may be correlated to their nationality, but is in no way a measure of the nationality of the authors.

I did not look into the language in which the articles are written, since almost all of them are written in English. Notable exception are older articles written in French (*e.g.* Zuckermann (1961)), in German (*e.g.* McCrea (1929)), in Latin (*e.g.* Brahe (1573)) and Russian (*e.g.* Godunov (1959), although the cited reference is actually an English translation).

The country distribution is plotted on figure A.2. There 'N' stands for Not Applicable. This is the case for consortium papers like for example MPI Forum (2021), with no geographic affiliation.

JOURNAL. The last easily accessible information I looked into is the journal in which the article is published. Here, a lot of small journals have a few publications while most are shared between a few journals. These few are *The Astrophysical Journal* (APJ), *Monthly Notices of the Royal Astronomical Society* (MNRAS), *Astronomy & Astrophysics* (AnA) and their affiliated journals for letters and supplements. The distribution is plotted on figure A.3. There 'N' stands for Not Applicable. This is the case for online published papers like for example MPI Forum (2021), or books.

ASSUMED GENDER. Finally, I also looked into the gender of the first author. Contrarily to the previous information, this one is not easily accessible as it is not written on the article. To determined out the gender of the first author I used the following method.

— If the first name of the author is gendered, I use this gender. Note that this only works with Western European names I am familiar with.

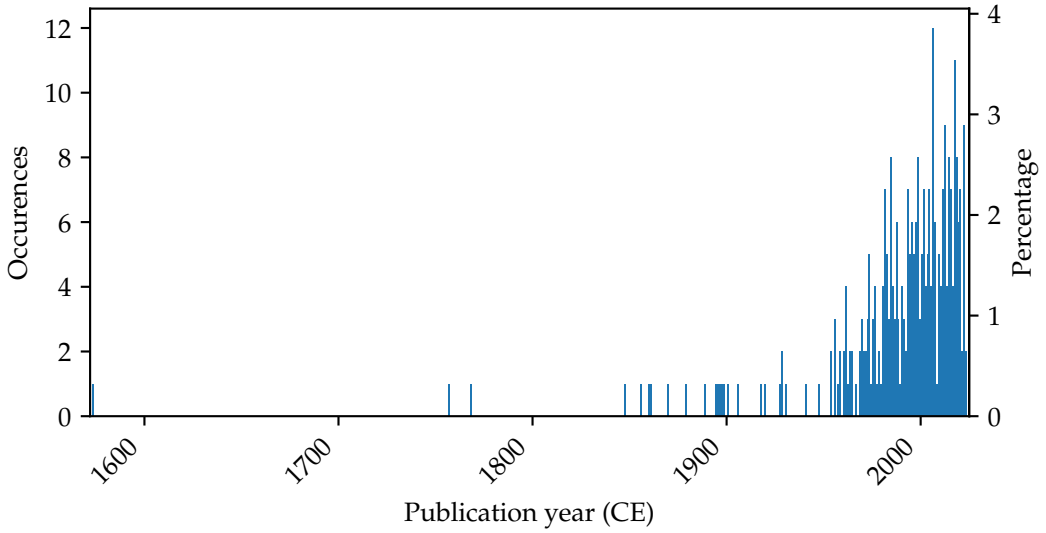

Figure A.1 – Histogram of the publication year of the articles of the Bibliography.

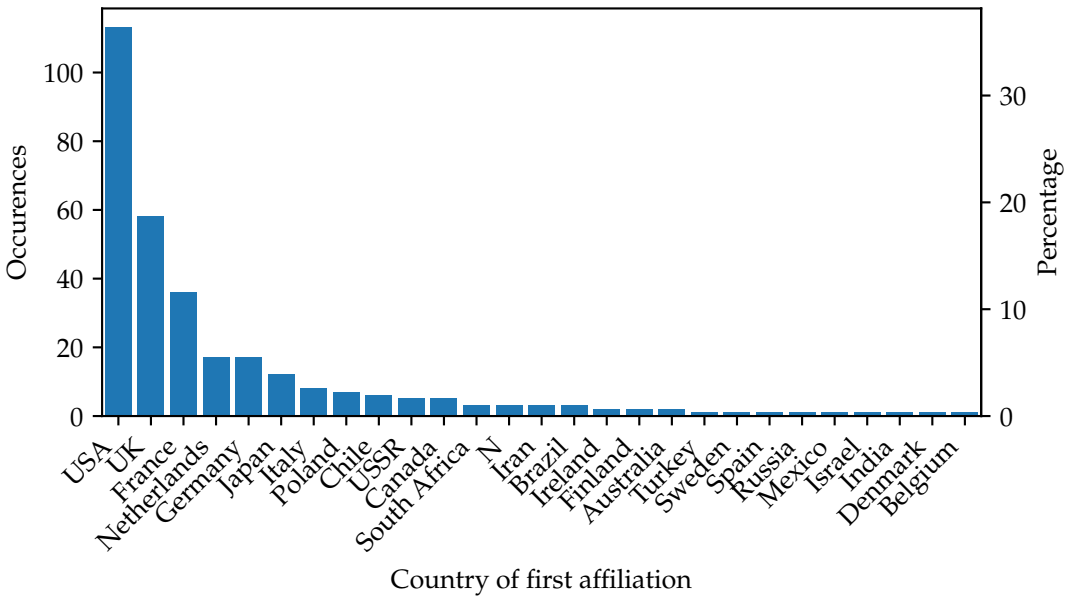

Figure A.2 – Histogram of the affiliation of the first author of the articles of the Bibliography.

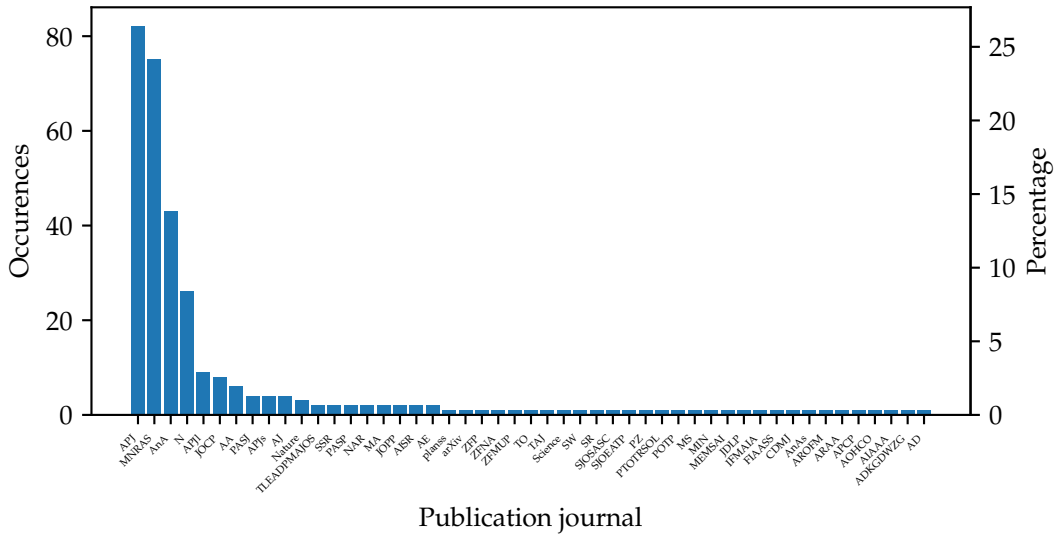

Figure A.3 – Histogram of the journal of the articles of the Bibliography.

— If I was able to determine the gender from a photo from a reliable source, like a personal webpage, or an institutional webpage, I use this gender.
— If a colleague (from the Sherpas team at IPAG) knows the gender of the author, I use this gender.
— If all previous methods do not yield satisfactory result, I remain agnostic on the gender.

There is no priority order in the above points. Because, I stopped as soon as I obtained a satisfactory answer, I am not able to obtain contradictory genders. Note also that the gender I determine with this method may differ from the gender to which the author identifies, as I never found a first hand (from the author themselves) indication of the gender. Note also that for sake of simplicity, I only used two binary gender. This means that any non-binary or gender-fluid authors will be incorrectly labelled as either female or male. This is why I refer to this gender as the *assumed* gender. Finally, I can not confidently rule out mistakes on either points of my determination method.

All things considered, this should give us an estimate in gender representation amongst the first authors of the cited articles. Figure A.4 shows the assumed gender distribution. '?' stands for unknown gender, that is authors for which I was not able to determine a gender. 'N' stands for Not Applicable, for example for large consortia.

Note that when I cite multiple articles from a same first author, they are counted as many times as the number of different articles. I assume that each article represent a different contribution to physics and a counting authors individually would produce a poor estimation of gender representation in the domain.

On figure A.4, we see that 83 % (258) of first authors are males (M), while only 12.5 % (39) of first authors are females (F). This is much less than the $\approx$ 50 % of females in the general population. This stark under-representation has been well studied and is mostly due to sexist and gender-associated educations starting at least from primary school all the way up to university, and then awarding faculty positions (Sheltzer and Smith, 2014; Way et al., 2016; Huang et al., 2020; Ross et al., 2020; Ductor et al., 2023)

On figure A.5, we can see that since the 1990s, the proportion of cited female first authors is strongly increasing. There are even a few years in the last decades with 50% of female first authors. Note however, that the sample size are very small here ($\leq$ 5) meaning that the measure frequencies may strongly depart from what can be observed in the global astrophysics community.

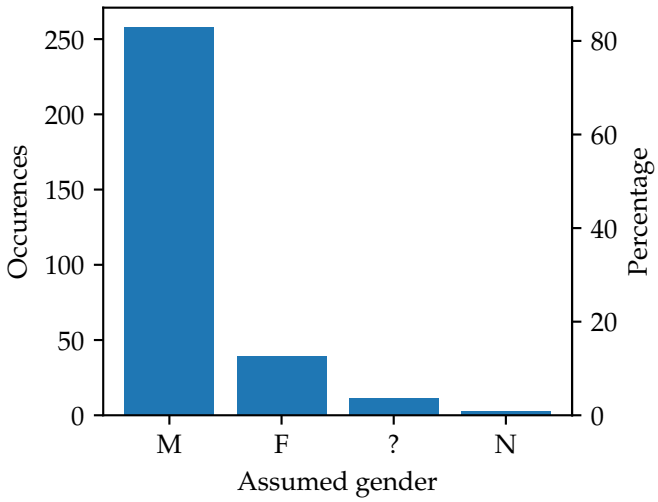

Figure A.4 – Histogram of the assumed gender of the first authors of the articles of the Bibliography. Non-binary authors are incorrectly assigned a gender for this plot.

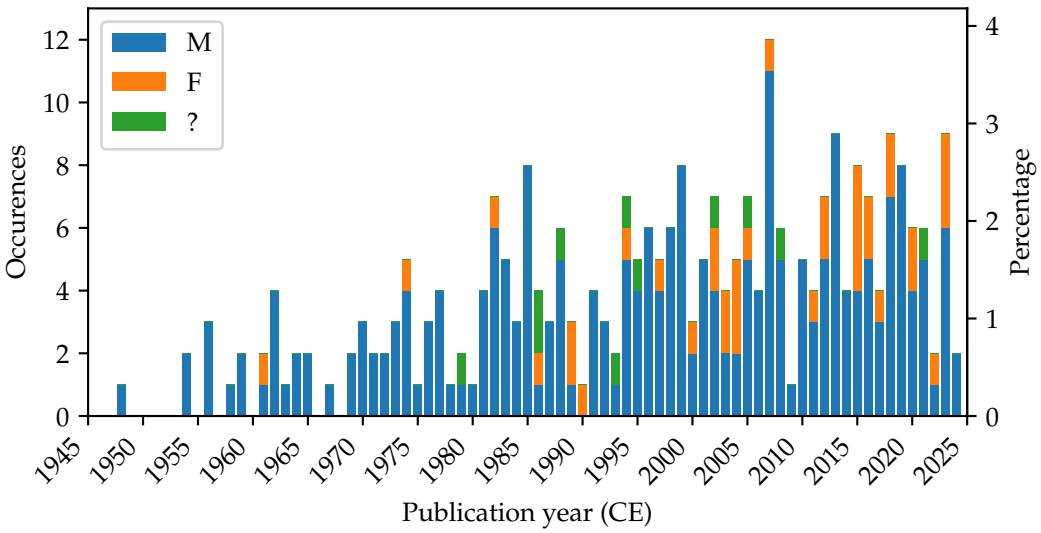

Figure A.5 – Histogram of the assumed gender of the first authors of the articles of the Bibliography as a function of publication year, for recent articles only. Non-binary authors are incorrectly assigned a gender for this plot.

Note that the choice in the articles I cite in this work may result from an involuntarily biased bibliographical choice, by reproducing the bias of the community. For instance, I used several reviews and textbooks to find appropriate references, and I reproduce the bias of these here.

The aim of this short appendix is to establish a lie of the land at the scale of the bibliography of this work. It would be very interesting, but much more difficult, to compare this to the actual population of researchers contributing to this field. This could, for example, further highlight the fact that women are less cited than men (Caplar et al., 2017; Kong et al., 2022; Lerman et al., 2022; Teich et al., 2022).

The csv file containing the bibliography, with added country of first affiliation of first author, and assumed gender of first author is available on my personal webpage `http://vandenbossche.eu`. This way, mistakes can be corrected and this study can be carried further by anyone eager to do so.

B

CARBON FOOTPRINT

NUMERICAL SIMULATIONS

The work presented in this thesis mostly relies on results obtained by large scale numerical simulations. The use of High-Performance Computing (HPC) methods, like the ones presented in this work, requires a large amount of energy, and as such has a significant environmental footprint. Here, I present the total amount of energy consumed for the simulations of this work, and estimate the carbon footprint of this PhD work.

Simulations	**Consumption** (GPUh)	**Cluster** (Architecture)
Spiral shocks simulations of chapter 4	370,000	GRICAD (Nvidia V100)
MHD wind simulations ofchapter 5	345,000	IDRIS (Nvidia V100)
	517,000	CINES (AMD Mi250)

Table B.1 – Amount of computing time used for the simulations of this work.

As mentioned in section 3.4, this work was carried out on different computing clusters. Table B.1 lists the total amount of GPU hours (GPUh) used on the different computing centres. From these values, we can estimate the amount of energy consumed. GENCI (Grand équipement national de calcul intensif), the French national entity in charge of HPC centres, estimated that one hour of computation using Nvidia V100 GPU produces 32.18 gCO_2 [1]. They also estimate that one hour of computation with AMD Mi250 GPU produces twice this amount.

These estimates take into account all other required infrastructure to compute of those GPUs, namely the associated CPU, networking interfaces, and other less consuming components. Note however, that these estimates do not include the environmental footprint of the creation of these component, nor does it include the environmental footprint of building the computing centre. As such, these estimates provide only a lower estimate of the footprint of this work.

From those values, I estimate that the carbon footprint of the simulations presented in this work is approximately **56 tCO_2**, that is approximately **19 tCO_2/year**.

CONFERENCES

Flight	**Emission** (tCO_2)
CDG-HER	0.9
LYS-FCO	0.4
LYS-FRA-BER	0.7

Table B.2 – Carbon footprint of professional flight (round trip) taken for this PhD.

As a comparison, table B.2 lists the carbon footprint of the flights I took to go to different conferences during my PhD. Professional travels by train are not listed as their carbon footprint is negligible in comparison.

1. This value is specific to France, where the produced electricity has a relatively low carbon footprint.

The total carbon footprint due to professional flights is approximately **2 tCO_2**, that is approximately **0.7 tCO_2/year**.

Note that the carbon footprint due to simulations is almost 30 times larger than the footprint due to professional flights over the same time period. The fact that most of the carbon footprint can be attributed to research activity rather than to travels has been shown in previous works (Knödlseder et al., 2022; Martin et al., 2022). This is a further illustration of that fact, here for numerical work. This means that further reducing the number of professional flights can only help us reduce the carbon footprint down to a certain point (Achten et al., 2013).

C

RÉSUMÉ EN FRANÇAIS

CONTEXTE

C.1 INTRODUCTION

L'observation du ciel a depuis longtemps été un passe-temps des êtres humains. En effet, les plus anciennes cartes du ciel que nous avons retrouvées datent de la même époque que les premières traces d'écriture, il y a environ 5000 ans (Kansas, 2007). Disposer de telles cartes est souvent pratique puisque les positions de la plupart des étoiles sont facilement prédictibles, et ces positions n'évoluent que sur des échelles de temps de dizaines de milliers d'années.

Cette régularité avait déjà été remarqué empiriquement à l'époque, et les cartes du ciel étaient employées pour établir des calendriers et voyager de nuit. Cette régularité a même inspiré des traditions philosophiques et religieuses, mais aussi les premières tentatives de modélisation du ciel comme l'*Harmonie des sphères* des pythagoriciens.

Dans cette thèse de doctorat, je vais au contraire m'intéresser à certains objets qui sortent de cette constance, dont les propriétés observationnelles changent bien plus rapidement, et dont les variations sont appréciables à l'échelle d'une vie humaine.

Je me concentre sur un type particulier d'étoiles variables, les *variables cataclysmiques*. Ces systèmes sont un type de système à deux étoiles dont l'une d'entre elles est une naine blanche. Ces systèmes ont des variations de luminosités telles qu'ils peuvent devenir visibles à l'œil nu alors qu'ils sont invisibles le reste du temps. Les variations de luminosité dans ces systèmes sont dus à l'interaction entre la naine blanche et l'autre étoile, dite *secondaire*. Les augmentations soudaines de luminosité sont en général dues à de la matière de la secondaire qui tombe sur la naine blanche ; c'est ce qu'on appelle l'*accrétion*.

Le type particulier de variables cataclysmiques sur lequel je me penche dans cette thèse est appelé *novæ naines*. Ces systèmes ont des éruptions régulières avec un contraste de 2 à 5 magnitudes. Chaque système possède un motif éruptif propre, mais de manière générale, le temps entre deux éruptions varie d'une dizaine de jours à une dizaine d'années. Un exemple de courbe de lumière d'une nova naine est montré sur la figure 1.1. Les novæ naines sont séparées en trois sous-catégories dont le nom d'usage est celui du système prototypique (Warner, 2003). Premièrement les *Z Cam*, qui possèdent restent parfois bloquées dans un état de luminosité intermédiaire pendant des jours à des années, comme sur la figure 1.2. Ensuite, les *SU UMa* entrent occasionnellement en *super-éruption* qui sont plus brillantes que les éruptions normales et environs cinq fois plus longues, comme sur la figure 1.3. Durant ces super-éruptions, on observe aussi des épi-éruptions appelées *super-bosses* qui sont de plus faibles amplitudes et à plus haute fréquence. Enfin, les *U Gem* sont la catégorie qui rassemble toutes les autres novæ naines. Ces systèmes ont été observés en continu depuis Wells (1896) et sont assez brillants pour être observés par des astronomes amateurs, comme celles et ceux de l'AAVSO.

Dans ce travail, je m'intéresse tout particulièrement aux U Gem ; ces systèmes qui ne possèdent que deux états de luminosité qui diffèrent d'environ quatre magnitudes. L'état

de faible luminosité est appelé la phase de *quiescence*, tandis que l'état brillant est appelé *éruption*.

Dès les années 1920, le défi principal pour ces systèmes a été de comprendre l'origine physique des variations régulières de luminosité. Dans les années 1950 et 1960, Joy (1954), Walker (1954), Joy (1956), Walker (1956) et Kraft (1962) proposèrent que toutes les variables cataclysmiques puissent être en réalité des systèmes binaires composés d'une naine blanche et d'une étoile rouge, plus froide. Cette hypothèse fait maintenant consensus (Ritter, 2008 ; Zorotovic et Schreiber, 2020).

Une conséquence de la binarité de ces systèmes est que lorsque ces systèmes évoluent, ils finissent par tant se rapprocher (Kraft et al., 1962 ; Verbunt et Zwaan, 1981 ; Mestel et Spruit, 1987) que les couches externes de la secondaires sont aspirées par la gravité de la naine blanche ; on parle alors de *débordement du lobe de Roche* de la secondaire. Comme illustré sur la figure 1.4, cette matière forme ensuite un disque autour de la naine blanche. La région où le flux de matière de la secondaire tombe sur ce disque est appelé le *point chaud* (Smak, 1971 ; Warner et Nather, 1971).

Après plusieurs aller-retour dans les théories, il a finalement été établi par Osaki (1974) que l'origine des éruptions dans ces systèmes était le disque d'accrétion et non la secondaire. Il propose qu'avec un flux de matière constant en provenance de la secondaire, la matière s'accumulerait dans le disque jusqu'à qu'« une sorte d'instabilité » y soit déclenchée et que cette instabilité permettrait au disque de se déverser sur la naine blanche rapidement, libérant ainsi une grande quantité d'énergie potentielle.

En effet, lorsque qu'une particule massive descend dans le puits de potentiel de la naine blanche, elle perd de l'énergie potentielle. Une partie de cette énergie potentielle est transformée en énergie cinétique, mais il est possible qu'une partie de cette énergie libérée soit aussi relâchée sous la forme de lumière ; la lumière que l'on observe lors des éruptions. Ainsi la luminosité mesurée nous renseigne sur le taux d'accrétion, c'est-à-dire le flux de matière qui tombe sur la naine blanche.

En supposant que la quantité de matière accrétée pendant une éruption correspond à la quantité de matière accumulée entre deux éruptions (équation (1.3)), et en estimant le taux d'accrétion de la secondaire grâce à la luminosité du point chaud (équation (1.4)), on peut obtenir une prédiction théorique du contraste éruption/quiescence. L'équation (1.6) montre que cette valeur théorique correspond aux valeurs observées. C'est seulement dans les années 1980, que l'on comprendra l'origine physique de l'instabilité supposée par Osaki (1974), comme je le présente au chapitre 2.

Pour étudier la structure des novæ naines, il existe deux principales méthodes observationnelles qui sont propres à ce type de système.

La première est l'imagerie par éclipse (Horne et Stiening, 1985 ; Baptista, 2016). Le principe de base de cette méthode est, sur un système donné, d'utiliser l'évolution temporelle de la luminosité mesurée due à l'éclipse du disque et de la naine blanche par la secondaire. Cette méthode n'est applicable que sur les systèmes vu sous une inclinaison assez grande. Cette technique a permis de confirmer les changements de tailles supposés du disque d'accrétion entre la quiescence et l'éruption (Patterson, 1981 ; Smak, 1984 ; Wood et al., 1989a ; Wood et al., 1989b ; Rutten et al., 1992a,b ; Baptista et Catalán, 2001 ; Vrielmann et al., 2002 ; Vrielmann et Offutt, 2003 ; Shafter et Misselt, 2006 ; Baptista et al., 2007). De plus, en supposant que la température effective du disque est une fonction de la distance à l'étoile et du taux d'accrétion (équation 1.7) il est alors possible d'obtenir une estimation du taux d'accrétion dans ces systèmes. Ainsi on estime que le taux d'accrétion pendant la quiescence est d'environ $10^{-14} M_\odot$/an à $10^{-10} M_\odot$/an, et d'environ $10^{-9} M_\odot$/an à $10^{-8} M_\odot$/an pendant les éruptions. La figure 1.8 est une observation avec cette méthode.

La deuxième méthode est la tomographie Doppler (Marsh, 2001 ; Echevarría, 2012). Cette technique repose sur le décalage Doppler des lignes d'émission ou d'absorption

des spectres de ces systèmes pendant une période de rotation dans les systèmes inclinés. Avec cette méthode, on obtient une carte du système dans un espace vitesse-vitesse, que l'on peut traduire en espace réel à condition de connaitre les paramètres géométrique du système. Cette méthode a permis de découvrir la présence de structures en spirale dans les disques de ces objets (Steeghs et al., 1997 ; Groot, 2001 ; Baba et al., 2002), mais aussi dans d'autres type de variables cataclysmiques (Hartley et al., 2005 ; Neustroev et al., 2011). Ces spirales pourraient être liées aux ondes spirales étudiées par la théorie et les simulations (Savonije et Papaloizou, 1983 ; Savonije et al., 1994 ; Ju et al., 2016) et pourraient jouer un rôle déterminant dans l'accrétion durant la phase de quiescence. Ces spirales ne sont cependant pas présentes dans tous les systèmes observés (Ruiz-Carmona et al., 2020).

En plus de l'accrétion observée à l'intérieur du disque d'accrétion dans les novæ naines, des écoulements cohérents s'échappant du système ont été observés dans plusieurs systèmes. Ces écoulements sont généralement observés grâce à leur signature Doppler caractéristique (Maury et Pickering, 1897 ; Beals, 1929 ; McCrea, 1929). Un type de tels écoulements sont les vents, peu collimatés, observés pendant les éruptions (Cordova et Mason, 1982 ; Mauche et Raymond, 1987 ; Drew, 1990), et les vitesses mesurées correspondent aux vitesses d'échappement de ces systèmes. Hoare et Drew (1993) et Knigge et Drew (1997) ont estimé que quelques pourcents de la masse accrétée s'échappent dans ces écoulements.

Durant la phase de quiescence, aucune observation directe de vent n'a été réalisée. Perna et al. (2003), Hakala et al. (2004) et Hernández Santisteban et al. (2019) proposent, par des conséquences indirectes, que des vents pourraient être présents tout de même pendant cette phase. De plus, les simulations de Scepi et al. (2018b) et Scepi et al. (2019), par exemple, suggèrent que les conditions pour qu'un tel vent soit lancé sont réunies durant la quiescence.

Enfin, les jets, c'est-à-dire de tels écoulements collimatés, sont en général détectés dans les longueurs d'onde radio. En effet, ces émissions sont généralement attribuées à de l'émission synchrotron dans les jets. Körding et al. (2008), Harrison (2014), Coppejans et al. (2015, 2016), Russell et al. (2016), Fender et al. (2019) et Webb (2023) ont détecté des émissions dans ces longueurs d'onde pour des novæ naines et d'autres types de variables cataclysmiques. Cependant, la présence de tels écoulements n'est absolument pas certaine pour la majorité des systèmes (Coppejans et Knigge, 2020).

Enfin, on observe aussi dans ces systèmes des rayonnements à plus haute énergie. Pendant la phase de quiescence, quand le taux d'accrétion est faible, on observe des rayons X. Cette émission est remplacée par une émission a plus faible énergie pendant les éruptions, dans les Ultra-Violet Extrêmes (Patterson et Raymond, 1985a,b ; Wheatley et al., 1996 ; Wheatley et al., 2003 ; McGowan et al., 2004 ; Wheatley et Mauche, 2005 ; Fertig et al., 2011 ; Balman, 2015). Les conditions pour chacun de ces deux types d'émission permet d'avoir une nouvelle estimation des taux d'accrétion pendant chacune des phases. Par exemple, pour le système SS Cyg, Wheatley et al. (2003) et Pandel et al. (2005) estime un taux d'accrétion de $10^{-12} M_\odot$/an à $10^{-10} M_\odot$/an pendant la quiescence, et d'environ $10^{-8} M_\odot$/an pendant les éruptions.

C.2 Hydrodynamique et magnétohydrodynamique des disques d'accrétion

Comme vu ci-dessus, l'objet de mon étude est le disque de matière formé autour de la naine blanche dans les novæ naines.

Le cadre adapté à l'étude de ces disques est celui de la mécanique des fluides, considérés comme étant un milieu continu et collisionnel. En particulier, quand il existe un

couplage entre le fluide du disque et un champ magnétique extérieur, les approximations de la magnéto-hydrodynamique (MHD) sont vérifiées pour ces systèmes. En effet

, les échelles de temps et d'espaces étudiées sont des ordres de grandeur plus grandes que celles de la microphysique électrostatique. Ainsi les équations pertinentes pour décrire l'évolution des disques de novæ naines sont les équations d'Euler, avec force de Lorentz, et les équations de Maxwell, et Ohm (résistive) pour décrire l'évolution d'un possible champ magnétique. Ce sont les équations (2.14) à (2.27). En réalité, dans les disques d'accrétion froids, le niveau d'ionisation des particules peut être assez faible. C'est pour cette raison qu'est inclue une résistivité Ohmique dans les équations de la MHD, dite MHD résistive. Il peut exister d'autres effets dits non-idéaux dans les disques froids, mais pour les disques de novæ naines, seule la résistivité est pertinente.

Depuis Weizsäcker (1948), ces équations ont été appliquées aux disques d'accrétions. La difficulté principale rencontrée dans les modèles de disques d'accrétion est depuis les premiers modèles de comprendre comment le moment cinétique est redistribué au sein du disque. Sans cette redistribution, il ne peut pas y avoir d'accrétion. Shakura et Sunyaev (1973) et Lynden-Bell et Pringle (1974) comprirent que cette redistribution pouvait être due à une viscosité turbulente dans le disque d'accrétion, et qu'elle pouvait être quantifiée par un paramètre adimensionné α (équation (2.32)). Avec le formalisme de la turbulence faible, pour les disques minces, Balbus et Papaloizou (1999) ont montré que ce paramètre α pouvait être rapporté aux différentes contraintes hydrodynamique et magnétiques dans le fluide (équation (2.40)). Plus récemment, Lesur (2021) propose un paramètre analogue υ pour quantifier l'importance des vents dans le transport de moment cinétique du disque.

Plus précisément pour les novæ naines, il existe un modèle théorique unidimensionnel pour décrire l'alternance entre les phases de quiescence et d'éruption comme un cycle d'hystérésis thermo-visqueux, c'est le Modèle d'Instabilité du Disque, ou DIM (Hōshi, 1979 ; Meyer et Meyer-Hofmeister, 1981 ; Cannizzo et al., 1982 ; Smak, 1982 ; Faulkner et al., 1983 ; Mineshige et Osaki, 1983). Ce modèle est une description axisymétrique du disque d'accrétion auquel est ajouté une description de la thermodynamique des disques de novæ naines, ainsi que l'apport de matière par la secondaire. D'une part, est ajouté un terme de chauffage visqueux du disque, lié à α, et d'autre part est ajouté un terme de refroidissement pour modéliser les pertes radiatives aux surfaces du disque, lié à l'opacité du gas du disque.

La particularité du régime des novæ naines réside dans ce terme de refroidissement. En effet, comme illustré sur la figure 2.1, l'hydrogène du gas s'ionise dans la plage de températures typiques pour les disque de novæ naines. Cela a pour conséquence une abrupte variation de l'opacité avec la température et produit ainsi non pas un mais trois états d'équilibre pour le disque à une température donnée (figure 2.2). Seulement deux de ces trois états sont stables, et ils correspondent respectivement aux phases de quiescence et d'éruption.

En estimant les temps caractéristiques de chacune des phases de ces systèmes, il est possible d'évaluer le paramètre α pour chacune d'elles. Ainsi on obtient $\alpha_{\text{quiescence}} = 0.02 - 0.04$ (Cannizzo et al., 1988, 2012) et $\alpha_{\text{outburst}} = 0.1 - 0.2$ (Smak, 1999 ; King et al., 2007 ; Kotko et Lasota, 2012).

Grâce à ce modèle, il est possible de reproduire des cycles quiescence-éruption (figure 2.4) et de les comparer aux observations pour en ajuster les paramètres. Par exemple, Scepi et al. (2019) ajouta l'effet d'un vent au DIM et mesura son effet sur les courbes de lumières ainsi obtenues.

Un des manques du DIM est cependant qu'il ne fournit pas d'origine physique à la viscosité α ad-hoc que l'on doit y inclure. Cette question dépasse les novæ naine et le

DIM, et l'origine physique de cette viscosité turbulente est commune à tous les disques d'accrétion.

C'est seulement Balbus et Hawley (1991) qui identifièrent analytiquement une instabilité linéaire comme possible origine de cette turbulence ; c'est l'instabilité magnéto-rotationnelle (MRI). Elle repose sur un couplage entre le disque d'accrétion et un champ magnétique extérieur vertical de faible amplitude. Dans cette instabilité, la tension magnétique agit comme un ressort entre deux particules fluide et permet un transport radial de moment cinétique (figure 2.5). Cette instabilité sature en turbulence dont la viscosité effective dépend de l'amplitude du champ magnétique (équation (2.60)).

Comment mentionné plus haut, un vent magnétique peut aussi contribuer au transport de moment cinétique dans le disque. Un tel vent est lancé par une suite de dynamo Ω puisant son énergie dans la rotation différentielle du disque d'accrétion.

Cependant, dans les disques froids et peu ionisés, ces deux effets peuvent être modérés par la résistivité. En l'occurrence, la MRI ne peut pas se développer dans les disques trop résistifs.

Pour aller plus loin que le modèle unidimensionnel qu'est le DIM, il est possible de réaliser des simulation bi- ou tridimensionnelles de l'écoulement du disque d'accrétion.

Notamment, pour étudier les propriétés locales du l'écoulement turbulent et de la MRI, a été développé un paradigme de simulation local : la boîte de cisaillement (Hawley et al., 1995). Ce modèle correspond à une version numérique de l'approximation de Hill. Cependant, il a été constaté que des effets numériques pouvaient influencer les résultats de telles simualtions, comme une dépendance du paramètre α dans la résolution de la simulation (Fromang et Papaloizou, 2007 ; King et al., 2007 ; Davis et al., 2010 ; Bodo et al., 2014 ; Shi et al., 2016 ; Ryan et al., 2017). Il a aussi été constaté que les valeurs du nombre de Prantl magnétique de ces simulations n'était pas comparables aux valeurs dans les systèmes réels et que les résultats des simulations changeait avec ce nombre (Fromang et al., 2007 ; Meheut et al., 2015 ; Guilet et al., 2022). Cependant, les résultats de ce genre de simulations sont satisfaisant et permettent de reproduire les observations de novæ naines (Latter et Papaloizou, 2012 ; Hirose et al., 2014) et ce, même dans des régimes très résistifs (Scepi et al., 2018a,b).

Il est aussi possible de réaliser des simulations dites *globales* de l'entièreté du disque d'accrétion, en sacrifiant cependant la physique aux petites échelles de la turbulence. La première génération de simulations de systèmes binaire utilisa une méthode à base de macro-particles de fluide, le SPH (Gingold et Monaghan, 1977 ; Lucy, 1977) pour étudier les propriétés géométriques générales de ces disques (Vogt, 1982 ; Osaki, 1985 ; Whitehurst, 1988a,b ; Lubow, 1991b). Ensuite, pour étudier des propriétés comme chocs spiraux dans les disques, les simulations changèrent de paradigme en faveur des méthodes aux volumes finis. Ces études montèrent notamment que la contribution à l'accrétion par les ondes spirales décroissait quand la température diminuait (Savonije et al., 1994 ; Ju et al., 2016). Cependant, parce que simuler des disques froids donc fins est extrêmement coûteux, les régimes étudiés n'ont jamais atteint les température de la phase de quiescence. Ainsi produire des simulations tridimensionnelles de disque entier avec un champ magnétique comme celles de Pjanka et Stone (2020) ne permet à ce stade pas d'étudier la quiescence.

C'est dans ce contexte que se place mon travail de thèse : Le régime de quiescence n'a jamais été étudié quantitativement avec des simulations globales. Avec les méthodes présentées au chapitre suivant, c'est le problème auquel je m'attèle ici.

C.3 Méthode des volumes finis pour la mécanique des fluides

Les méthodes dites des volumes finis sont des méthodes utilisées pour résoudre des systèmes d'équation différentielles de la forme d'équation de conservation (équation

3.1). Dans ce travail de thèse, j'utilise le code IDEFIX (LESUR et al., 2023) qui est une implémentation numérique d'une méthode au volumes finis de type Godunov.

Le principe de ces méthodes est de discrétiser le domaine d'études en une collection de volumes de tailles finies et de s'intéresser aux quantités contenues dans ces volumes ainsi qu'un flux aux interfaces de cellules. Les quantités dans ces volumes, comme la vitesse ou la densité du fluide, sont approximées. La méthode originale de Godunov GODUNOV (1959) choisit d'utiliser la valeur moyenne dans la cellule comme approximation. De nos jours, on utilise des approximations d'ordre supérieur, plus raffinées, ici une approximation affine de ces quantités dans les cellules (figure 3.1). Ensuite, calculer les flux aux interfaces des calculer revient à se ramener au problème idéaliser de RIEMANN (1860). Un fluide étant séparés en deux états à une interface : la question est de trouver l'état final du fluide.

Pour ce faire, on utilise des solutioneurs de Riemann approchés. Ces algorithmes permettent d'obtenir une solution approchée pour l'état du fluide à l'interface de la discontinuité initiale. Il existe différentes approximations comme HLL, ou HLLC (HARTEN et al., 1983 ; TORO et al., 1994), mais le principe de base de ces solutionneurs est le même : On suppose que des ondes se propagent depuis la discontinuité initiale, et que l'état du fluide entre deux fronts d'ondes consécutifs est uniforme. Par exemple, le solutionneur HLL utilise deux ondes, tandis que le solutioneur HLLC en utilise trois. Pour la MHD,il faut inclure les ondes liées au couplage avec le champ magnétique et le solutionneur HLLD utilise cinq ondes (MIYOSHI et KUSANO, 2005). Dans ces solutionneurs, pour assurer la stabilité du schéma numérique, il faut respecter la condition Courant-Friedrichs-Lewy (CFL) condition (COURANT et al., 1928) (équation 3.15). Elle permet de s'assurer qu'aucun front d'onde ne parcourt plus que la taille d'une cellule en un pas de temps (figure 3.3).

Plus particulièrement pour les disques d'accrétion, il est aussi possible d'utiliser l'algorithme d'advection orbitale FARGO (MASSET, 2000). Cela est utile pour modérer l'effet de la condition CFL lorsque l'écoulement dévie peu par rapport à une advection orbitale connue, en pratique képlerienne. J'utilise cette méthode pour accélérer les simulations présentées au chapitre 4.

Dans le cas de la MHD, en plus de l'évolution du fluide, il faut aussi faire évoluer le champ magnétique comme l'équation d'induction le dicte. Pour ce faire tout en conservant une divergence nulle, le code utilise l'algorithme du transport contraint (EVANS et HAWLEY, 1988). Ici contrairement à la méthode des volumes finis présentée ci-dessus, les valeurs des champs ne correspondent pas aux valeurs au centre des cellules. En effet, le champ magnétique est défini sur les surfaces des cellules tandis que le champ électrique est défini sur les arêtes des cellules. Cependant, cette méthode ne conserve pas parfaitement la divergence du champ magnétique lorsque le nombre de pas de temps d'intégration est très grand. Pour compenser cet effet, je choisis pour mes simulations MHD d'évoluer le potentiel vecteur plutôt que le champ magnétique. Pour modéliser la résistivité du plasma dans mes simulations, j'utilise une table pré-calculée de valeurs que j'utilise en fonctions des conditions locales du fluide (GREVESSE et SAUVAL, 1998 ; SCEPI et al., 2018a).

La force principale de ce type de méthode pour la mécanique des fluides est sa capacité à résoudre des écoulements très compressibles comme c'est le cas des disques d'accrétion. Cependant, les solutionneurs de Riemann n'offrent pas une grande précision lorsque le plasma est fortement magnétisé, ce qui peut mener à des solutions non-physiques.

J'ai d'ailleurs rencontré des difficultés numériques liées aux limitations des algorithmes que j'utilisais. La première a été liée à l'utilisation de l'algorithme d'advection FARGO. En effet, dans les disques de système binaires, les régions les plus externes du disque sont tronquées par les forces de marée de la secondaire. Dans cette région, le gas n'a aucune raison d'être à une vitesse proche de la vitesse képlérienne associée à la naine

blanche. J'ai donc souhaité inclure cette dépendance radiale à la vitesse d'advection de FARGO. Cependant, bien que les conditions théoriques sur cette vitesse soient réunies, j'ai obtenu des résultats non-physiques d'excitations d'ondes parasites (figure 3.4).

Ensuite, dans les simulations MHD, dans les régions de forte magnétisation, j'ai constaté l'excitation de structures oscillantes non résolues (figure 3.5). Une solution usuelle pour résoudre ce problème est de changer le solutionneur de Riemann dans ces zones. Cela n'étant pas possible avec IDEFIX à ce stade, j'ai implémenté une condition de lissage de chocs qui peut cibles les régions de forte magnetisation uniquement.

RÉSULTATS

À présent, on comprend bien le problème : les observations montrent qu'il y a de l'accrétion pendant la phase froid et sombre de quiescence, mais nous ne connaissons pas de mécanisme physique capable de l'expliquer.

Dans cette partie, je présente deux mécanismes pertinents pour l'accrétion en quiescence. Le premier est un effet non-magnétique : l'excitation de chocs spiraux dans le disque d'accrétion par les forces de marées de la secondaire. Le second nécessite la présence d'un champ magnétique vertical à grande échelle : le lancement de vents magnétiques depuis le disque.

C.4 CHOCS SPIRAUX DANS LES DISQUES MINCES DE SYSTÈMES BINAIRE

Durant la phase de quiescence le disque est froid, peu ionisé, et mal couplé au champ magnétique extérieur. Ici, je néglige, en première approximation, complètement tout couplage au champ magnétique.

L'effet de la présence d'une secondaire est la présence d'importantes forces de marée dans la région du disque d'accrétion autour de la naine blanche. En effet, il est possible que dans les régions externes du disque, les forces de marée atteignent un tiers de la gravité de la naine blanche.

Le premier effet de la présence de la secondaire et de ces forces de marées est que le disque d'accrétion va être tronqué avec une extension radiale maximale. En pratique pour étudier ce genre de systèmes, il est pratique de se placer dans le référentiel en rotation synchrone avec la secondaire, afin d'avoir un potentiel gravitationnel constant.

Ensuite, comme vu plus haut, la secondaire va aussi fournir continuellement de la matière au disque d'accrétion. En pratique lorsque que l'on étudie l'écoulement du disque sur des échelles plus courte que la durée d'une phase de quiescence, l'influence de ce flux de matière est assez faible. La seule façon de mesurer son effet dans des simulations et d'artificiellement augmenter le flux de matière par des ordres de grandeurs. Je choisis donc de ne pas inclure ce flux de matière dans cette étude.

La présence de la secondaire va aussi exciter des ondes spirales stationnaires dans le disque. Ces ondes sont des ondes de choc stationnaire et contribuent à redistribuer le moment cinétique dans le disque. Pour les étudier, j'utilise d'abord l'approche analytique de SAVONIJE et PAPALOIZOU (1983) et SAVONIJE et al. (1994).

Cette approche est une approche perturbative dans laquelle on résout les équations d'Euler bidimensionnelles polaire autour d'un état « moyen ». Cet état correspond à un état d'équilibre hydrostatique radial du disque, dans lequel l'écoulement est quasi-képlerien. On choisit alors de trouver une solution perturbative à l'écoulement lorsqu'on ajoute la secondaire. On décompose les solutions perturbatives en modes de Fourier azimutaux – ces modes correspondent aux différents modes de spirales – et on se limite

au premier ordre dans les perturbations. Avec une approximation WKB dans le rapport d'aspect du disque, supposé petit, on peut trouver des solutions analytiques aux équations.

Une fois cette méthode établie, je commence par vérifier la validité des hypothèses faites dans le contexte du régime de quiescence. Il s'avère qu'en réalité, dans le régime de quiescence, quand le disque est très froid et très mince, l'approximation linéaire n'est plus valide. En effet, l'amplitude de la perturbation, supposée petite par rapport à celle de l'état moyen, devient comparable à celle de l'état moyen. Cela signifie que les effets non-linéaires, négligés par cette approximation, ne seront en fait pas négligeable. Physiquement, cela est dû au fait qu'à basse température, les spirales sont des structures de plus en plus fines, et que les chocs correspondants sont de plus en plus raides.

C'est pour cette raison que je continue l'étude de ces ondes avec le code Idefix, qui reflète intrinsèquement les effets non-linéaires. Pour la suite de cette étude, je réalise des simulations bidimensionnelles polaires.

Je choisis de discrétiser la région qui contient le disque d'accrétion de manière uniforme en azimut, et de manière logarithmique en rayon, avec des cellules plus fines proche de la naine blanche. Je prends SS Cyg comme système de référence et utilise ce système pour définir les unités de base.

Pour les conditions aux limites, j'impose un flux sortant avec une vitesse azimutal keplérienne incluant la rotation du référentiel.

Pour l'état initial des simulations, je chois de pré-tronquer le disque au rayon de troncation attendu. Cela permet de gagner du temps d'intégration en raccourcissant le régime transitoire initial.

Je réalise des simulations de disques à différentes températures, partant des travaux de la littérature jusqu'au températures de quiescence, ainsi que des simulations avec des masses de secondaire différentes.

La première étape de ce travail est de vérifier que le code Idefix est en mesure de reproduire les résultats établis avec d'autres codes. Ici, je reproduis une partie des simulations de Ju et al. (2016) obtenues avec le code Athena++. Les figures 4.4 et 4.5 sont des reproductions de l'article en question avec le code Idefix. On y constate que les résultats obtenus avec les deux codes sont très proches tant pour la simulation isotherme que pour la simulation adiabatique. Notamment, les valeurs mesurées du paramètres α sont en adéquations.

Une fois cette vérification effectuée, je me concentre sur les simulations à plus basses températures (figure 4.7) et à différents rapports de masse (figure 4.10). Avec ces simulations, j'observe tout d'abord que les spirales excitées ne correspondent pas à celles étudiées par la théorie linéaire discutée plus haut. En effet, les spirales dans mes simulations sont des spirales à un bras, tandis que la théorie linéaire n'étudie que les spirales à deux bras. En effet, c'est ce second mode qui est le plus fortement excité par les forces de marée.

J'observe que les spirales à deux bras sont présentes seulement dans les régions externes des disques de mes simulations, tandis que les régions internes sont dominées par des spirale à un bras. De plus plus la température du disque est basse, plus la région dominée par les spirales à deux bras est réduite. Dans la simulation la plus froide que je réalise – correspondant à la quiescence–, la quasis-totalité du disque est dominée par une spirale à un bras.

Une spirale à un bras peut être interprétée comme un mode excentrique de spirale. La croissance d'excentricité ayant déjà étudiée dans ce type de disque (Lubow, 1991b ; Kley et al., 2008 ; Oyang et al., 2021), je compare mes résultats aux travaux précédents. Cependant, la croissance d'excentricité, selon les mécanismes étudiés précédemment, n'est

possible que si la masse de la secondaire est suffisamment faible par rapport à celle de la naine blanche, de sorte qu'une résonance orbitale puisse se situer dans le disque. Or, j'observe ces spirales excentriques dans toutes mes simulations, indépendamment du rapport de masse. Je constate aussi, que dans les régimes de rapport de masse où cette croissance a été observée par le passé, je ne l'observe pas. La différence principale avec mes simulations étant qu'elles sont plus froides. Je constate aussi que les vitesses de phases des spirales ne sont pas cohérentes avec le mécanisme de croissance de l'excentricité usuel.

Je m'intéresse ensuite au transport de moment cinétique produit par ces ondes spirales. Le premier résultat que j'obtiens concerne le temps de relaxation par rapport à l'état initial. Je constate que les simulations à basse température n'atteignent pas d'état stationnaire en une centaine d'orbite de système binaire. Cette durée est comparable à la durée d'une phase de quiescence dans les systèmes réels. Cela signifie que le disque n'atteint peut-être jamais d'état stationnaire avant de revenir en éruption. Cela suggère qu'il pourrait y avoir des effets de mémoires entre plusieurs éruptions consécutives.

Ensuite, je mesure la valeur du paramètre α. Pour ce faire, j'attends quatre-vingts orbites de système binaire afin d'être aussi peu influencé que possible par l'état initial. Dans toutes mes simulations je mesure des valeurs de α significativement plus faible que les valeurs estimées pour les systèmes quiescents réels. Cela signifie que pendant la phase de quiescence, l'accrétion est due à un autre phénomène que ces ondes spirales.

Les simulations effectuées avec un petit rapport de masse ont cependant montré des valeurs de α plus grandes que celles avec une secondaire plus lourde. La gravité de la secondaire étant à l'origine de ces spirales, ce résultat semble contre-intuitif. Pour m'assurer de leur sens, je réalise une simulation sans secondaire, et je constate que l'accrétion est bien réduite à nouveau. Cependant, lorsque je redémarre la simulation en enlevant la secondaire en cours de route, je redémarre un état transitoire pendant lequel l'accrétion est augmentée.

Je réalise aussi des simulations additionnelles afin de vérifier que l'excitation des ondes spirales à un seul bras n'était pas un artéfact ni dû à la résolution de la simulation, ni aux conditions aux bords. Notamment, j'implémente une condition au bord de relaxation des ondes incidentes. Malgré une grande extension radiale de cette zone, les ondes excentriques subsistent.

Enfin, j'ai réalisé des simulations additionnelles afin d'étudier les conséquences des ondes spirales sur la thermodynamique du disque. Pour ce faire, je résous désormais l'équation de conservation de l'énergie. Pour compenser de manière cohérente le chauffage dû aux spirales j'implémente une fonction de refroidissement pour modéliser les pertes par rayonnement de corps noir. J'approxime d'abord l'opacité du disque comme étant constante, mais cela mène à un refroidissement trop rapide du disque. Ensuite, je choisis d'utiliser des valeurs tabulées de l'opacité avec un modèle simplifié de transfert radiatif vertical. Avec cette simulation, j'obtiens qu'à des températures réalistes de quiescence, les ondes spirales fournissent un chauffage suffisant pour compenser les pertes radiatives. Cela signifie que la température du disque en quiescence est possible due uniquement aux chocs spiraux.

C.5 DISQUES MINCES MAGNÉTIQUES DANS LES SYSTÈMES BINAIRES

Dans ce chapitre, je présente les simulations tridimensionnelles de disques magnétisés que j'ai réalisé, afin d'étudier le lancement d'un vent magnétique et ses propriétés.

Le paramètre de contrôle pertinent pour réaliser des simulations MHD de vent, pour quantifier l'importance du champ magnétique est le paramètre addimentionné β correspondant au champ moyen poloïdal (équation 5.2).

Pour compléter les équations d'Euler tridimensionnelles, j'utilise une équation d'état barotropique (équation (5.5)) afin de modéliser le changement de température du gas quand sa densité change.

La résistivité Ohmique que j'utilise provient de tables, comme présenté dans l'introduction. Ces valeurs sont cependant re-dimmensionnées afin d'avoir un nombre de Reynolds magnétique réaliste même si le disque est plus épais qu'un disque réel en quiescence.

Ici, aussi j'utilise une grille uniforme pour la dimension azimutale, et des grilles non uniformes pour les autres dimensions. Ces grilles non-uniformes sont concentrées sur la région d'intérêt de la simulation : le plan équatorial du système binaire, là où le disque se situe (5.3). Cela est couplé à un algorithme de dé-raffinement proche de l'axe des coordonnées sphériques.

Les conditions aux limites sont des conditions d'écoulement sortant, en imposant une densité inférieure à l'extérieur du domaine pour que le gradient de pression soit toujours dirigé vers l'extérieur.

Le disque initial est le résultat d'une simulation non-magnétique antisymétrique sans secondaire, afin que l'équilibre hydrostatique associé à l'équation d'état choisi soit d'abord atteint avant l'introduction simultanée du champ magnétique et de la secondaire en trois dimensions. Comme au chapitre précédent, le disque hydrodynamique initial est aussi pré-tronqué, et le champ magnétique imposé au redémarrage est purement poloïdal.

Dans la première phase d'évolutions des simulations magnétiques, j'observe la création d'une cavité intérieur à basse densité au voisinage de la naine blanche. Cette cavité est comparable à celles observées dans les simulations du chapitre précédent. Une grande partie du champ magnétique initial est advecté dans cette zone, qui devient par conséquent très fortement magnétisée. J'obtiens ainsi une région interne avec $\beta \approx 1$ et un disque externe avec $\beta \ll 1$.

J'observe aussi que dans ces simulations, des modes propres à la MRI se développent malgré la grande résistivité du disque d'accrétion. En réalité, ces modes ne se développent pas dans le plan médian du disque car la résistivité y est en effet trop grande, ils se développent aux surfaces du disques là où, la densité étant plus faible, le gas est plus magnétisé et moins résistif (figure 5.9)).

Dans ces simulations, un vent magnétique est lancé depuis les surfaces des disques. La surface de lancement est cependant à plus haute altitude que l'échelle de hauteur caractéristique hydrostatique du disque. De manière concomitante, les disques sont plus épais que ce que l'équilibre hydrostatique dicte. Cela est dû à la contribution additionnelle du champ magnétique. La composante de pression magnétique de la force de Lorentz s'ajoute à la pression thermodynamique pour compenser la gravité verticale. Dans les régions internes de mes simulations, c'est cette pression magnétique qui domine le bilan des forces vertical. Cela a pour conséquence de produire un disque bien plus épais. En quantifiant ce changement d'épaisseur, je constante que le rapport d'aspect du disque est à peu près constant et vaux un dixième à tous les rayons ; pour les rayons internes, cela correspond à un disque dix fois plus épais que le profil hydrostatique.

Je mesure que le taux d'accrétion de ces simulations, comparé à une simulation de référence non-magnétique, est augmenté d'un facteur mille. Je constate aussi que les simulation idéales et résistives ne diffèrent que peu. Par contre varier le paramètre β produit des taux d'accrétion différent, avec un plus grand taux d'accrétion pour un champ magnétique plus important.

Ainsi je constate qu'un vent magnétique global parvient à être lancé même depuis un disque d'accrétion très mince et très résistif. Ce vent augmente significativement l'accré-

tion, mais produit aussi un disque interne fortement magnétisé et très épais par rapport au profil hydrostatique.

Après environ cinq orbites de système binaire après le redémarrage tridimensionnel des simulations, je constate que tous les disque de mes simulations magnétisées s'inclinent. Cette inclinaison est globale, de telle sorte que le disque n'est pas gauchi et reste quasi-plan.

La façon dont je quantifie cette inclinaison est la suivante. Je calcule pour tous les rayons et tous les azimuts la latitude du barycentre du disque. Ensuite, je fait une régression sinusoidale de cette latitude en fonction de l'azimut ; une sinusoïde est la forme attendue pour une faible inclinaison de disque. J'observe ainsi que la croissance de cette inclinaison globale du disque par rapport au plan du système binaire est exponentielle et quasi-simultanée à tous les rayons. Une fois cette croissance exponentielle lancée, tous les rayons sont en phase et le disque précesse. L'orientation azimutale de l'inclinaison n'est pas synchrone avec la secondaire, au contraire elle est quasi-stationnaire dans le référentiel non-tournant. Cette croissance prend la même forme exponentielle dans toutes les simulations magnétiques que je réalise. Indépendamment de la résistivité et du paramètre plasma. Dans toutes les simulations cette croissance démarre à un temps similaire, après quatre à cinq orbites de système binaire, après le redémarrage en trois dimensions, et l'ajout du champ magnétique.

Une autre façon d'étudier cette inclinaison est de regarder l'orientation du vecteur moment cinétique local, qui est relié au vecteur d'inclinaison. Dans les diagrammes espace-temps de cette quantité (figure 5.22), on peut voir cette inclinaison à la fin de la simulation. Cependant, on y voit aussi la propagation d'ondes de flexions dans la phase initiale durant laquelle le disque n'est pas incliné. La simulation de référence sans champ magnétique, quant à elle, ne s'incline jamais de la sorte, mais la propagation d'ondes de flexions est clairement visible. Je réalise une simulation magnétisée à plus haute température, avec un disque deux fois plus épais, et je constate la croissance de l'inclinaison du disque aussi. Avec cette simulation je constate que le temps de croissance de l'inclinaison des disques de toutes les simulations semble correspondre au temps de traversée du disque pour les ondes de flexion.

Après avoir décrit l'inclinaison des disques, je m'attèle maintenant à comprendre son origine. Les travaux sur de telles géométries de disques sont rares et il existe à ce jour peu de mécanismes connus qui permettent d'expliquer ces inclinaisons, et encore moins dans le contexte des novæ naines. Par exemple, il est connu qu'un disque de binaire X autour d'un trou noir non-aligné avec l'axe du système binaire peut produire une inclinaison du disque interne (Lense et Thirring, 1918 ; Bardeen et Petterson, 1975). De même si le champ magnétique de l'objet central n'est pas aligné avec le disque, une inclinaison peut se développer (Lai, 1999 ; Murray et al., 2002). Mais mes simulations ne correspondent à aucun de ces scénarios. Lubow (1992) propose un mécanisme d'inclinaison du disque à partir des forces de marées de la secondaire, semblable à la croissance d'excentricité discutée au chapitre précédent. Cependant, ici aussi le régime dans lequel ce mécanisme est possible est à petit rapports de masse, or je ne suis pas dans ce régime. Foulkes et al. (2006, 2010) propose un autre mécanisme d'inclinaison produit par l'illumination de l'objet central, cependant les luminosités nécessaires à cet effets ne sont pas atteignable dans les disques de novæ naines. Enfin, Ogilvie et Latter (2013a,b) ont développé un nouveau paradigme pour étudier ces disques gauchis. Ils proposent une version modifiée de la boîte de cisaillement, avec des conditions aux limites adaptées aux disque non-plans. Paris et Ogilvie (2018) ajoutent les effets du couplage au champ magnétique à ce modèle, mais ne se concentrent que sur les disque très fortement magnétisés. Ces différents scénarios ne s'appliquant pas à mes simulations, je cherche alors un mécanisme de croissance différent.

Premièrement, je réalise un étude de stabilité des disques inclinés. J'étudie l'énergie potentielle d'un anneau de matière à rayon fixée par rapport au potentiel gravitationnel total du système. Je confirme que pour un anneau axisymétrique, le plan du système binaire est un point d'équilibre stable. Ensuite, j'étudie le cas d'un anneau dont la distribution azimutale de masse n'est pas uniforme, comme c'est le cas quand il y a des ondes spirales de densité dans le disque. Dans ce cas, le plan du système binaire n'est plus le minimum global d'énergie. Cependant, comme la simulation sans champ magnétique ne s'incline jamais, cela suggère que le temps liée à cette instabilité est plus long que celui de la croissance que j'observe.

J'explore ensuite la possibilité que la croissance de l'inclinaison soit due à une asymétrique du vent magnétique. Cette asymétrie entre le haut et le bas du disque est clairement visible et mesurable. Une telle dissymétrie implique que le vent exerce une force nette sur le disque, qui tend à le sortir localement du plan du système binaire. Je constate que cette force est largement axisymmétrique et est due à la pression magnétique. Même si l'inclinaison est un effet non-axisymétrique, il est possible qu'avec le potentiel de la secondaire, cet effet produise un inclinaison. Je réalise donc une série de simulations additionnelle. Ces simulations sont non-magnétiques, mais inclue une force modélisant la différence de pression magnétique mesurée dans les simulations magnétiques. Ces simulations sont tridimensionnelles et incluent la secondaire. Avec ces simulations, je ne parviens pas à reproduire l'inclinaison mesurée dans les disques magnétisée. Ce qui confirme que l'effet purement axisymmétrique ne permet pas d'obtenir une inclinaison globale. Enfin je réalise une simulation avec un disque initialement incliné, afin d'étudier la stabilité de cette configuration. Je constate qu'un tel disque est stable sur les échelles de propagation des ondes de flexion. L'origine de cette inclinaison reste donc à comprendre.

C.6 CONCLUSION

La question à laquelle cette thèse propose une réponse est celle de l'accrétion pendant la phase de quiescence des novæ naines. Les travaux présentés ici, sont cependant applicable à une plus grande variété d'objets. En effet l'accrétion dans les disques froids reste une grande question de l'astrophysique aussi bien pour les binaires X, les AGN ou les disques protoplanétaires.

Dans ce travail, j'ai commencé par explorer la piste du transport de moment cinétique pas les ondes spirales excitées par le potentiel de marée. Les résultats de cette partie peuvent être résumés comme suit :

1. Le mode de spiral dominant est le mode de spirales à un bras, contrairement au mode à deux bras que la théorie linéaire étudiait.
2. Les vitesses de phase de ces ondes spirales ne sont pas en accord avec la théorie quasi-non linéaire, mais prennent des valeurs qui sont des multiples entiers de la fréquence du système binaire.
3. Les chocs spiraux produise de l'accrétion, mais des ordre de grandeur en dessous des valeurs nécessaire pour reproduire les observation en quiescence.
4. J'observe un temps de relaxation très long pour les disques avec des températures de quiescence réalistes. Cela suggère qu'il pourrait y avoir des effets de mémoire d'une éruption à la suivante dans ces systèmes.
5. Les chocs spiraux sont capables de maintenir une température réaliste pour la quiescence dans ces disques.

Ainsi les chocs spiraux sont définitivement éliminés comme explication de l'accrétion en quiescence.

Dans la deuxième partie, j'ai étudié la possibilité que l'accrétion soit dominée par des vents magnétisés. Les résultats de cette partie sont les suivants :

1. Il est possible de lancer des vents magnétique depuis un disque froid, mince et résistifs en quiescence.
2. L'effet de la résistivité s'avère petit par rapport à l'ajout du champ magnétique, en ce qui concerne la MRI et le lancement du vent.
3. Les vents ainsi lancés depuis des disques minces sont dissymétriques haut-bas, exerçant ainsi une force nette axisymmétrique sur le disque.
4. Après quelques orbites de systèmes binaires, les disques s'inclinent de manière globale. Le temps de croissance de cette inclinaison semble lié au temps de traversée des ondes de flexion.
5. L'orientation de l'inclinaison est quasi-stationnaire dans le référentiel non-tournant. Plus précisément, elle est rétrograde à environ 3% de la fréquence du système binaire.
6. Un anneau de matière non-axisymmétrique (par exemple dû à des ondes spirales) n'est pas stable dans le plan du système binaire.
7. En réalisant des simulations non-magnétiques, je n'ai pas pu déterminer l'origine de la croissance exponentielle de l'inclinaison. Il apparaît qu'un force axisymmétrique couplé au potentiel de marée n'est pas suffisant.
8. Un disque non-magnétique incliné est stable sur les échelles de temps de propagation des ondes de flexion.

Ainsi l'origine de l'inclinaison reste incomprise à ce stade. Cependant, la fréquence de rotation de l'orientation de l'inclinaison des disques est compatible avec les observations de super-bosses dans certains systèmes (Bonnet-Bidaud et al., 1985).

C.7 PERSPECTIVES

Dans cette dernière partie, je présente rapidement des perspectives pour les travaux de cette thèse.

Premièrement, il serait intéressant de continuer la piste ouverte par l'étude thermodynamique des ondes spirales. L'idée serait de réaliser des simulations telles que celle présenté à la fin du chapitre 4 mais sur des échelles de temps plus longues, en incluant le flux de matière de la secondaire. Cela permettrait d'étudier des cycles quiescence-éruption complets. Cela permettrait aussi de mesurer précisément les possibles effets de mémoire évoqués plus haut. Des simulations préliminaires ont été réalisées avec un stagiaire de M1, en incluant un α ajouté à la main qui dépend de la température locale du disque. Cela permet de modéliser le lancement de la MRI quand le disque devient assez chaud et ionisé.

Ensuite, il serait intéressant de comparer les résultats des simulations magnétiques avec des observations de systèmes réels. Cela peut être fait, en traitant les sorties du code Idefix avec un logiciel de transfert radiatif, comme par exemple python (Long et Knigge, 2002).

Réaliser des simulations avec une hypothèse moins forte sur la géométrie initiale du champ magnétique permettrait aussi de généraliser ces résultats. Jacquemin-Ide et al. (2023) a récemment montré qu'un champ vertical peut être généré dans les disques à partir de champ magnétique sans flux net. La question se pose donc de savoir si les résultats serait les mêmes avec un champ magnétique initialement advecté par la secondaire, comme dans Pjanka et Stone (2020).

Enfin, continuer à explorer la dynamique des disques inclinés et gauchis est nécessaire. Une façon de procéder est de poursuivre l'étude de Ogilvie et Latter (2013a,b) et Paris et Ogilvie (2018) avec la boîte de cisaillement gauchie. Il s'agirait de continuer à inclure les effets magnétique afin d'explorer des régimes plus proches de ceux des disques d'accrétion faiblement magnétisés. Ensuite, il serait possible d'inclure les effets non idéaux

pertinent, comme la résistivité Ohmique pour les novæ naines. Une deuxième partie de ce projet serait d'utiliser les résultats obtenus par cette première étude avec la boîte de cisaillement gauchie pour réaliser des simulations globales. Les résultats de la première parties pourraient être incorporées comme un modèle sous-maille des simulations globales. Cela permettrait d'étudier plus précisément l'effet d'une inclinaison ou d'un gauchissement du disque sur la dynamique de l'accrétion. En effet, il a été montré qu'un tel changement de géométrie pouvait changer les instabilités qui se développent dans le disque (Aly et al., 2023).

En conclusion, nous avons maintenant une meilleure idée de l'origine de l'accrétion dans les disques quiescents. Les chocs spiraux excités par les forces de marée peuvent être définitivement écartés comme étant à l'origine d'une accrétion suffisante pendant la quiescence pour expliquer les temps de récurrence des novæ naines. De plus, il est maintenant clair que même dans les disques froids, fortement résistifs et quiescents, le champ magnétique joue un rôle crucial. Il permet à l'instabilité magnéto-rotationnelle de se développer aux surfaces du disque et de lancer un fort vent magnétique. Il apparaît également que la présence d'un champ magnétique produit un couple fortement asymétrique sur le disque, conduisant à l'apparition d'une inclinaison globale du disque. Le couplage avec le champ magnétique, même faible, produit des disques dont les propriétés globales sont très différentes de celles des disques purement hydrodynamiques. En conséquence, les effets magnétiques doivent être inclus dans un plus grand nombre de modèles de disques d'accrétion. Les vents magnétiques modifient considérablement les propriétés d'accrétion des disques ainsi que leurs propriétés géométriques.

COLOPHON

This document was typeset using the typographical look-and-feel `classicthesis` developed by André Miede. The style was inspired by Robert Bringhurst's seminal book on typography "*The Elements of Typographic Style*". `classicthesis` is available for both LaTeX and LyX:

https://bitbucket.org/amiede/classicthesis/